ESMRMB

European Society for Magnetic Resonance in Medicine and Biology

ESMRMB 2013 Congress

October 3–5, Toulouse/FR

Book of Abstracts

EPOS™ Poster / Paper Poster / Clinical Review Poster / Software Exhibits

DOI: 10.1007/s10334-013-0385-4

EPOS™ Poster

Animal brain MRI

523

Neuroimaging characterization of a mouse model of vascular cognitive impairment.

T.D. Farr[1], M.-P. Brinckmann[1], M. Foddis[1], A. Kunz[1], C. Po[2], U. Dirnagl[1,3], M. Füchtemeier[1,3]
[1]*Department for Experimental Neurology, Center for Stroke Research Berlin (CSB), Charité University Hospital, Berlin/GERMANY,* [2]*Imagerie par Résonance Magnétique Médicale et Multi-Modalités, Université Paris-Sud, Paris/FRANCE,* [3]*Partner site, German Center for Neurodegenerative Diseases (DZNE), Berlin/GERMANY*

Purpose/Introduction: Vascular cognitive impairment (VCI) is the second leading cause of dementia. However, very little attention has been given to this disease by preclinical researchers. Chronic hypoperfusion to the brain has been proposed as a potential animal model for VCI and several groups have reported spatial and working memory impairments, hippocampal atrophy, and white matter damage in a relatively new mouse model of chronic hypoperfusion (1-3). Our group is currently working to characterize this model with magnetic resonance imaging and preliminary results are presented here.
Subjects and Methods: Chronic brain hypoperfusion was induced by wrapping microcoils (180µm diameter) around both carotid arteries in male C57/BL6 mice. Cerebral blood flow (CBF) was monitored using a 7T system (Bruker) prior to- and at 4 and 24hrs and 11, 17 and 25 days post microcoil implantation using arterial spin labeling: a FAIR EPI sequence (TR/TE: 10000/10ms, 10 TIs, resolution: 195µm^2). Degeneration of the white matter was examined using an EPI DTI sequence (TR/TE: 4000/29ms, 4 shots, 6 B values, 30 directions, resolution: 156µm^2). T_2 sequences: MSME (TR/TE: 3000/10ms, 16 echoes, resolution: 98µm^2) and RARE (TR/TE: 5000/10ms, 8 echoes, RARE factor: 2, 2 averages, resolution: 156µm^2) were also employed and alterations in the major cerebral vessels characterized at 28 days using a 3D TOF angiography sequence (TR/TE: 15/2.5ms, α: 20˚, resolution: 98µm^3). At the conclusion of the experiments, tissue was harvested for immunohistochemistry.
Results: Half of the mice exhibited a substantial decrease in CBF following microcoil implantation. From these animals, half exhibited increases in CBF within 2 weeks, while CBF in the other half remained unchanged. Some animals also exhibited evidence of vascular remodeling in the angiography image, such as dilation and growth of the Circle of Willis and other major cerebral vessels in response to shear stress. Detailed analysis of the DTI data and histology is currently pending.
Discussion/Conclusion: These preliminary results indicate that this model might be more variable than previously reported. Ongoing work aims to establish selection criteria for model success and gain mechanistic insight into the observed pathology.
References:
1) Shibata, 2004, Stroke. 35: 2598-03
2) Holland, 2011. NeurobiolAge. 2325: 1-6
3) Yoshizaka, 2008. ExpNeurol. 210: 585-91

524

Molecular imaging of selectin expression after stroke.

T.D. Farr[1], D. Grünstein[2], C.-H. Lai[2], P. Boehm-Sturm[1], A. Barandov[2], C.-C. Wang[2], G. Orts-Gil[2], G. Laettig[1], P.H. Seeberger[2], C. Harms[2]
[1]*Department of Experimental Neurology, Center for Stroke Research (CSB), Charité University Medicine, Berlin/GERMANY,* [2]*Department of Biomolecular Systems, Max-Planck Institute of Colloids and Interfaces, Potsdam/GERMANY*

Purpose/Introduction: Non-invasive imaging of the inflamed brain endothelium during disease is of high interest. E and P selectin are endothelial transmembrane proteins that participate in leukocyte adherence to blood vessels during inflammation. Selectins bind to carbohydrates, which can in turn be coupled to iron oxide nanoparticles for visualization with MRI (1,2). The purpose of the study was to examine nanoparticles coupled to Sialyl Lewis ^{X} (SiaLe^X).
Subjects and Methods: Magnetic nanoparticles (MNPs) were coated with silica and rendered neutral for *in vivo* administration. Sub-populations of MNPs were covalently bound to sugar moieties that contain ligands with no targets (MNPs + L^X) or the ligand sialyl Lewis^X (MNPs + sLe^X), which targets E and P selectin. Male C57/BL6 mice (n=18) received 60min of middle cerebral artery occlusion (MCAO) and 4hrs later randomly received one of the 3 types of MNPs (n=6, each) i.v. (1000µmol Fe/kg). T_1, T_2, and T_2* weighted images were acquired and tissues processed for immunohistochemistry and Prussian blue staining.
Results: All of the iron formulations exhibited a strong blood pool effect immediately after injection and 24hrs later the brains contained many small punctate regions of signal loss. There were no differences between groups in overall brain signal to noise ratios (SNRs), and no differences in SNRs between the infarcted volumes when compared to the mirrored regions in the intact hemisphere. To account for partial volume effects, the number of dark voxels in each volume of interest was measured. A greater number of dark voxels were present in the infarcted volumes of all groups when compared to the intact hemisphere (MNP: 237.5 ± 109.7 vs 142.9 ± 76; MNPs + L^X: 95.3 ± 81.7 vs 46.5 ± 32.3; MNPs + sLe^X: 246.1 ± 95 vs 122 ± 35). The greatest effect was in the MNPs + sLe^X treated animals, though this failed to reach statistical significance on account of the high degree of variability. Interestingly, in 3 of the 5 mice that received naked MNPs, there was a large region of iron accumulation. Furthermore, Prussian blue staining was only observed in the vasculature of one of these animals, though intense staining was observed in the livers and spleens of all mice.
Discussion/Conclusion: These preliminary results indicate that functionalized magnetic nanoparticles for E and P selectin may not bind in sufficient amounts to the injured tissue to be detectable beyond the appropriate control particles.
References:
1) Jin, 2009. CMMI. 4: 305-11
2) van Kasteren, 2009. PNAS. 106: 18-23

525

Fluctuations in cerebral blood flow and arterial changes in a rat model of vascular cognitive impairment.

C. Po, C. Sebrie
Imagerie par Résonance Magnétique Médicale et Multi-Modalités, Université Paris-Sud, Orsay/FRANCE

Purpose/Introduction:
Vascular dementia is the second leading of dementia after Alzheimer's disease; its prevalence will increase, which will make it a priority for health services. The aim of this study is to observe and understand the evolution of neuroanatomical in a standard animal model using MRI.
Subjects and Methods:
Permanent bilateral common carotid occlusion (BCCAo) was performed in male Wistar rats (n=9) and parameters compared to healthy animals (n=2). In all animals, anatomical images, angiography, cerebral blood flow (CBF), and O_2-saturation maps were obtained prior to BCCAo as well as 24hrs after and weekly for 5 weeks at 7T. T2maps were acquired using a RARE sequence: TR = 5000 ms, 8 TEs, RARE factor = 2, resolution = 0.156x0.156x1 mm^3. Angiography was performed using FLASH 2D: TR/TE = 18/4.5 ms; resolution = 0.156x0.156x0.4 mm^3. CBF maps were acquired with FAIR-EPI: TR/TE = 10000/10.7 ms, 10 T1, 2 shots, resolution = 0.375x0.375x1 mm^3. To obtain the O_2-saturation, periods of 5 min under 20% or 100% oxygen were interleaved during a single shot GE-EPI sequence: TR/TE = 3000/15 ms, 500 repetitions, resolution = 0.2 x0.2x1 mm^3.
Results:
In some BCCAo rats (n=4), lesion was observed on the T2maps from 24hr after BCCAo. Despite this, changes in the major cerebral vessels, as assessed with angiography, evolved in a comparable manner. Thus, the angiography showed a modification of the posterior vessels of the Willis circle from 1 week after BCCAo (white arrows): density of vessels was more important and disorganized locally.

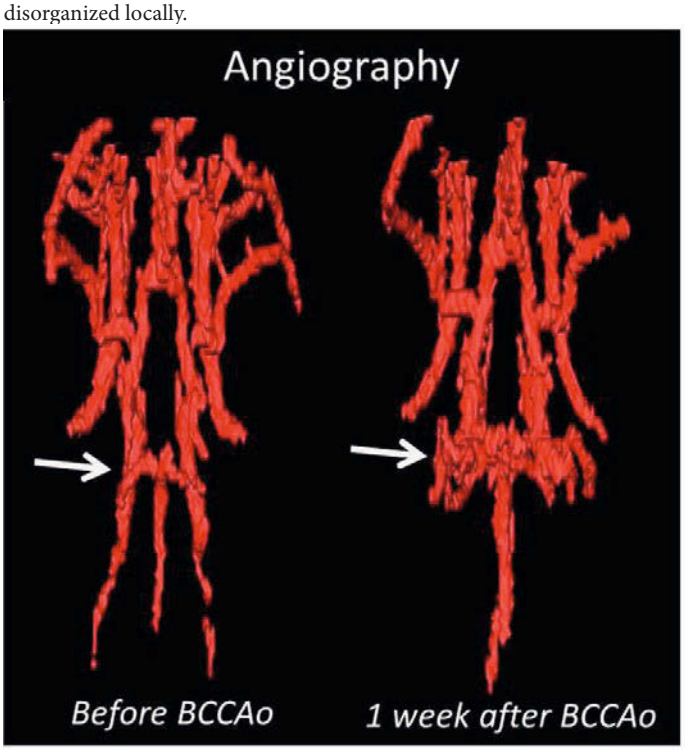

Before surgery, there was a high degree of inter-individual variation in CBF while the O_2-saturation remained comparable; both parameters were stable in the two healthy rats. 24h after BCCAo, in all rats, cortical CBF decreased significantly irrespective of edema while the O_2-saturation increased. Both returned to presurgical values after 1 week.
Discussion/Conclusion:
The BCCAo model showed a high degree of variability with respect to the development of edema. Despite this, homogeneity was observed in terms of arterial vasculature modulation in response to sheer stress, as demonstrated with angiography. CFB and O_2-saturation changes were independent of edema formation and their recovery indicates that the structural change in vessels are relatively rapid and capable of compensating. This MRI study demonstrates the importance of imaging protocols for the study of neurovascular diseases.
References:
Acknowledgements: This study was funded under the ERA-NET Neuron scheme (ANR2011-NEUR-001-03)

526

WITHDRAWN

527

Application of cryo-coil and modified pulse sequences for relaxation study of the mouse brain in vivo at 9.4T.

W.I. Pięd zia, K. Jasinski, K. Kalita, B. Tomanek, W.P. Węglarz
Department of Magnetic Resonance Imaging, Institute of Nuclear Physics PAN, Kraków/POLAND

Purpose/Introduction: Limited experimental time available during in vivo experiments using standard coils often results in SNR which is too low for quantitative analysis of the resulted images. Moreover, standard pulse sequences currently available on preclinical MRI scanners are not specific enough to identify tissues with short T1 and T2. Therefore the aim of this work was to assess the capability of using a cryo-coil [1] combined with the inversion recovery ultra-short echo time (IR-UTE) pulse sequence [2] as well as composed refocusing pulses [3] to image and quantify T1 and T2 relaxation times of the brain structures containing various amount of myelin (i.e. white matter (WM) and gray matter (GM)) in healthy mouse brain at 9.4T.
Subjects and Methods: The Bruker CryoProbe [1], UTE 2D pulse sequence with and without inversion pulse, and CPMG pulse sequence with Mao and the composed Levitt-Freeman refocusing pulses were used for coronal brain images of a healthy C57BL/6J mouse and the assessment of short T1 and T2 relaxation times. A volume room temperature coil was also used for SNR comparison. The IR-UTE 2D pulse sequence was optimized for maximum WM and GM Contrast-to-Noise Ratio (CNR).
Results: The results showed 3 to12 fold improvement in SNR for the cryo-coil comparing to the volume coil depending on the area (Fig. 1, 2). The inversion times providing optimum CNR for WM and GM were found to be between 500 and 1000 ms for the echo time of 351 μs (Fig. 3). The study also demonstrated that sequence utilizing composed refocusing pulses allows reliable assessment of short T2 component in case of bi-exponential fitting.

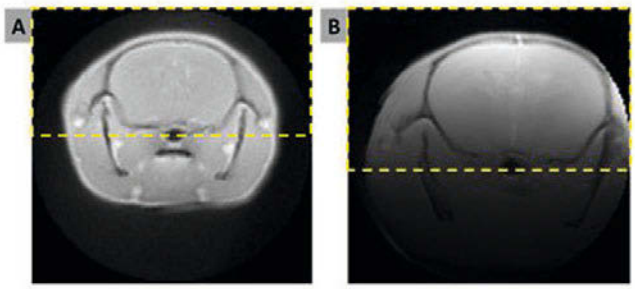

Fig. 1. Comparison of axial MR images of the mouse brain *in vivo* using the 2D UTE pulse sequence A. Birdcage B. CryoProbe.

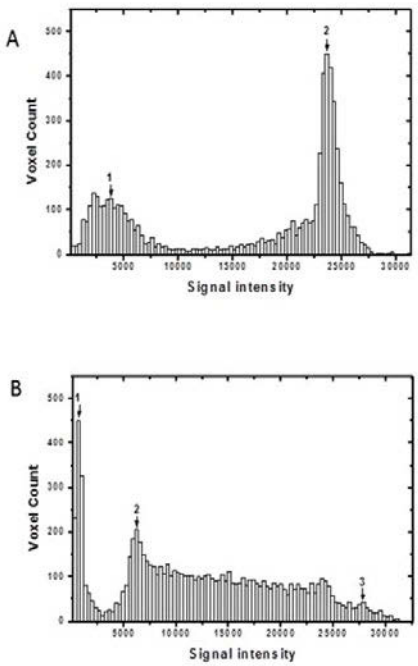

Fig. 2. Histograms for the birdcage (A.) and the cryo-coil (B.) from the selected regions of the axial MR images (Fig. 1). 1 – background signal (noise); 2, 3 – range of signal values used for SNR calculation.

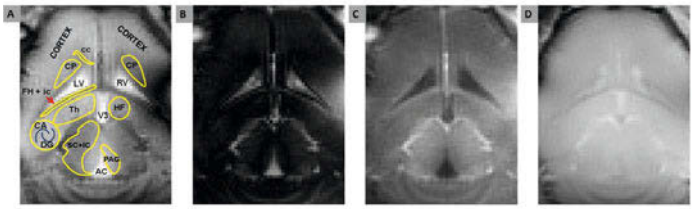

Fig. 3. Coronal IR-UTE MR images of a mouse brain *in vivo*: **A.** TI = 500 ms **B.** TI = 750 ms **C.** TI = 1000 ms **D.** no inversion pulse. **LV** - left ventricle, **RV** - right ventricle, **V3** - dorsal third ventricle, **AC** - cerebral aqueduct, **cc** – corpus callosum, **ic** - internal capsule, **FH** – fimbria hippocampi, **CP** – caudoputamen, **HF** – hippocampal formation, **SC** – superior colliculus, **IC** – inferior colliculus, **CA** - Cornu Ammonis, **DG** - Dentate Gyrus, **PAG** - periaqueductal gray, **Th** – Thalamus; LV+RV+V3+AC = CSF. (FOV=1.5 × 1.5 cm, slice thickness = 1 mm).

Discussion/Conclusion: Using cryo-coil allows for significant SNR gain and thus shortening of the experimental time. The results indicate that the optimized IR-UTE pulse sequence at 9.4T allows for one order in magnitude enhancement of the CNR for WM and GM as compared to standard UTE. The application of composed refocusing pulses allows improved T2 measurements when compared to standard CPMG pulse sequence.

References:

1. Baltes C, Radzwill NI, Bosshard S, Marek D, Rudin M. Micro MRI of the mouse brain using a novel 400 MHz cryogenic quadrature RF probe. NMR in Biomedicine 2009;22(8):834-842.
2. Larson PE, Conolly SM, Pauly JM, Nishimura DG. Using adiabatic inversion pulses for long-T2 suppression in ultrashort echo time (UTE) imaging. Magn Reson Med 2007;58:952–61.
3. Poon CS, Henkelman RM. Practical T2 quantitation for clinical applications. J Magn Reson Imaging 1992;2:541-553.

528

Aging induces different T2 relaxometry changes in brains of SHR rats compared to Wistar

R. Tudela[1, 2], T. Petrova[3], X. López-Gil[2], G. Soria[2]
[1]Group of Biomedical Imaging of the University of Barcelona, CIBER de Bioingenieria, Biomateriales y Nanomedicina (CIBER-BBN), Barcelona/SPAIN, [2]Experimental 7T MRI Unit, IDIBAPS, Barcelona/SPAIN, [3]Erasmus program, University of Leicester, Leicester/UNITED KINGDOM

Purpose/Introduction: It is known that aging-induced memory loss and the increase of the risk of nerve disorders are accompanied by tissue dehydration. [1]. In addition to aging, hypertension is a risk factor for neurodegenerative disease such as vascular cognitive impairment [2, 3]. Magnetic resonance imaging (MRI) and specially T2 relaxometry maps are highly sensitive to water content changes in different tissues including the brain. Our objective in this study was to evaluate the effect of both aging and hypertension in brain water content as assessed by T2 relaxometry in spontaneous hypertensive rats (SHR) compared to Wistar.

Subjects and Methods: Longitudinal MRI scans were performed under isofluorane anaesthesia in a BioSpec 70/30 horizontal animal scanner (Bruker BioSpin, Ettlingen, Germany), equipped with a 12 cm inner diameter actively shielded gradient system (400 mT/m) and a phased array surface coil for rat brain. Male Wistar (n=12) and SHR (n=12) rats were scanned at gradients at 10, 14, 18, 22, 26 and 40 weeks after birth with multislice multi echo MRI sequence T2 mapping of coronal slices acquired with a multislice-multi-echo (MSME) sequence by applying 16 different TEs, from 11 to 176 ms, TR = 4764 ms, slice thickness = 1 mm, number of slices = 18, FOV = 40 x 40 mm, and matrix size = 256 x 256 pixels, resulting in a spatial resolution of 0.156 x 0.156 mm in 1.00 mm slice thickness.

Results: A significant effect of time was observed in T2 relaxometry in different regions of interest (ROI). Indeed, a significant decrease in the T2 relaxation times was observed in all analysed ROIS (striatum, cortex, prefrontal cortex

and corpus callosum) 40 weeks after birth compared to 10 weeks in the control group. SHR rats did not show this significant decrease although a tendency was observed. Therefore, 40 weeks after birth T2 times were significantly different between the 2 rat strains. Voxel based analysis and statistical parametric maps are currently being performed to identify other brain structures related to vascular cognitive impairment.

Discussion/Conclusion: Our results revealed increased T2 times in aged SHR rat brains compared to aged Wistar rats, suggesting a brain edema which might be related to the neurocognitive deficits shown by these animals in López-Gil et al. ESMRMB 2013 (abstract submitted).

References:

[1] Ayrapetyan et al., J Bioequiv Availab 2012, 4:5
[2] O'Brien et al. Lancet Neurol 2003; 2(2):89-98.
[3] Sabbatini M et al. Ageing Dev 2002; 123(5):547-559.

529

Complex Networks for the discrimination of Inflammation processes using multi-parametric MRI

A.B. Martin-Recuero[1], M. Zanin[2], S. Cerdan[1]
[1]*Alberto Sols, Consejo de Investigaciones Cientificas, Madrid/SPAIN,*
[2]*Computer Science, Universidad Nova de Lisboa, Lisboa/PORTUGAL*

Purpose/Introduction: Cerebral inflammatory responses underlie the most morbid and prevalent neurological disorders, including cancer, ischemia, or neurodegeneration[1]. In most cases, current bioimaging methods are not able to discriminate unambiguously between the primary pathology and the associated inflammatory response. To this end, we report here the use of complex network representations on raw MR dataset maps, aiming at discriminating between inflamed and healthy mouse brain, and at identifying relationships between measurements enabling more accurate diagnoses and therapies.

Subjects and Methods: Adult male mice C57BL/6 (n=6) received an i.p. injection of LPS from Escherichia Coli Serotype 0127:B8 (5mg/kg). MRI studies of the mouse brain were carried out in a horizontal 7T/16 scanner. DWI in the head-foot (H-F), left-right (L-R) and the antero-posterior (A-P) directions with b=0, 100, 400, 800 s/mm² (two basals), T1 (7 TR), T2 (50 TE), and MT maps were acquired before and three days after the LPS administration, when maximal inflammation develops[2]. The dimension of resulting images has been reduced by averaging data in 256 bins (Figure 1).

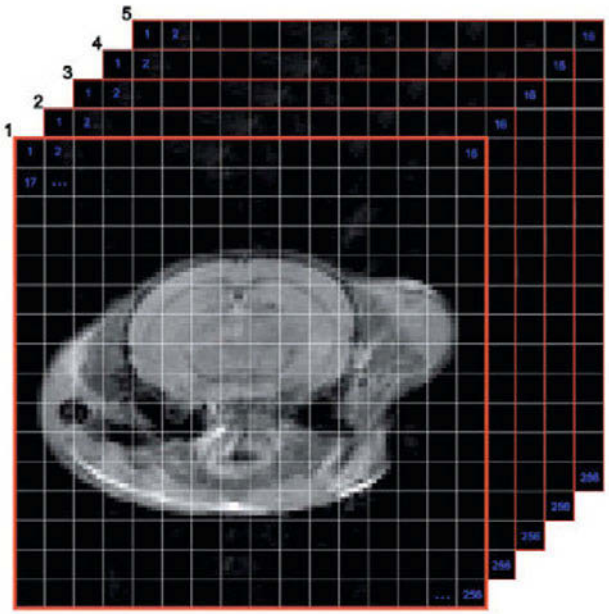

Figure 1: Example of data bin division in a sequence of MR map data set. The dimension of resulting images has been reduced by averaging data in 256 bins

A complex network representation has been created for each subject following the procedure proposed in (3), where each node represents one of the bins of an image, and pairs of them are connected with a link when the values of the corresponding bins follow a model found in inflammation. See figure 2 for a representation of the reconstruction method, and figure 3 for an example of the resulting networks. Different structural metrics are then extracted from the resulting networks, and their values used to discriminate control subjects and patients.

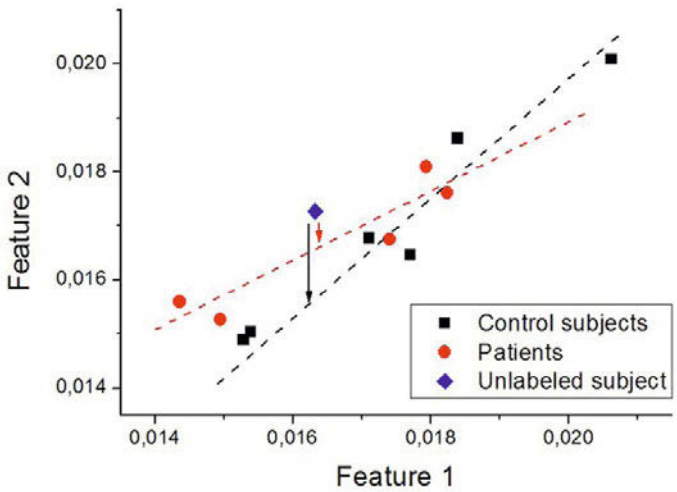

Figure 2. *Calculating link weights. Black squares (red circles) represent values of two features for the set of control subjects (patients). Black and red dashed lines respectively represent the two linear regressions modeling the expected behavior of both features in the control and patient groups. An unlabeled subject is represented by a blue diamond, and its distance from both regression lines by two arrows: when the distance from the patient fit is lower than the distance from the control subjects fit, a link between the corresponding nodes is created.*

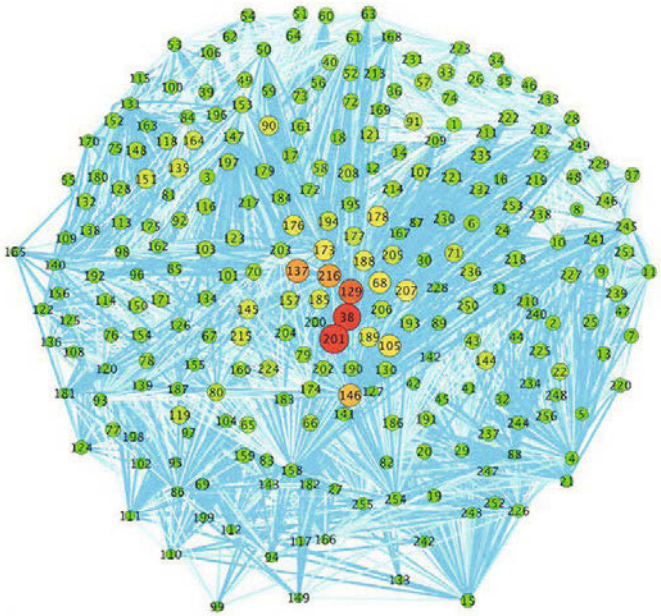

Figure 3. Example of resulting networks. The figure depicts the network corresponding to a mouse inflamed. Size and color of nodes represent their centrality, i.e. their relative inflammation importance in brain by using datasets of MR maps .

Results: Figure 4 reports the classification score obtained for each map dataset considered. Classification has been performed by analyzing two network structural metrics by means of Support Vector Machines, specifically Clustering Coefficient and Efficiency. In three cases, a 100% score is achieved: ADC(9), T1W(4) and T2W(23). In both cases, the most important feature characterizing patients is a reduction of the Clustering Coefficient in their networks.

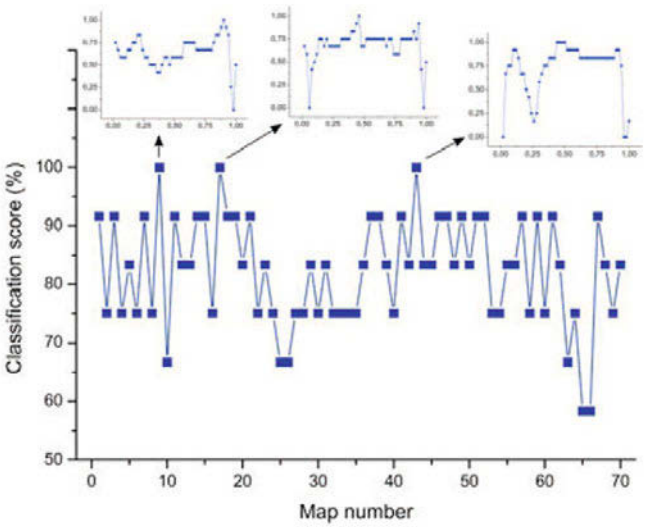

Figure 3. *Classification score obtained with each MR map. Insets show, for the three maps achieving a 100% classification score, the evolution of the score as a function of network link densities.*

Discussion/Conclusion: We propose the use of network representations to analyze MR raw dataset maps and extract global features. By analyzing the resulting network topologies, it is possible to detect relevant relationships between features, i.e. different inflamed regions, that allow discriminating patients between control and inflamed with a 100% precision score. In turn, this sheds light on the mechanisms behind the disease and their most convenient imaging protocols.

References:

(1)Scrivo R. et al.2011,Autoimmun Rev.10(7):369-74.
(2)Martin-Recuero, ISMRM 2012
(3)Zanin, M. et al,2011. Chaos:21(3), 033103-033103.

530

Donepezil prevents the effect of scopolamine in phMRI provocation model

N. Hegedüs, P. Kocsis, D. Gajári, S. Dávid, L. Deli, Z. Pozsgay, K. Tihanyi
Preclinical Imaging Center, Gedeon Richter Plc., Budapest/HUNGARY

Purpose/Introduction: The effective treatment of cognitive decline is a major therapeutic area in drug research. Several animal models are known to test the cognitive effect of drugs; however these models lack translational power. Recently evolved small animal fMRI is a powerful translational method; data obtained in animals or humans are suitable for translation. Unfortunately, the direct examination of drug effects is not always possible by fMRI. These problems can be overcome if drugs are tested in a proper provocation model. In order to establish a phMRI based animal model, first we studied the effect of scopolamine on BOLD responses in rat brain as a provocation drug, and the reversibility of its effect by donepezil.

Subjects and Methods: Male Wistar rats weighing 240-260 g anaesthetized with isoflurane were used in the experiments. Radiofrequency (RF) pulses were transmitted using a volume coil. A receive-only phased array rat brain coil was placed on the dorsal surface of the rat's head. After 1000 second control period scopolamine were administered as a challenge agent. The test drug was administered one hour before scopolamine. ROI analysis was performed comparing the effect of scopolamine on BOLD responses in drug pretreated or in vehicle treated animals in various brain regions.

Results: Scopolamine strongly decreased the BOLD responses in the prefrontal cortex but had no visible effect on hippocampus and other brain areas. Donepezil pretreatment fully prevented the effect of scopolamine in the prefrontal cortex.

Discussion/Conclusion: Functionally, the prefrontal cortex (PFC) of rats has been implicated in working-memory, attention, response initiation and management of autonomic control and emotion. The strong negative effect of scopolamine on PFC well explains its memory disturbing effect. The pretreatment of animals with the procognitive compound donepezil caused a full reversal of the effect of scopolamine. Based on these results the model is suitable to test procognitive agents and also can help to elucidate the mechanism of action of various centrally acting drugs via the analysis of their effects on various brain regions. Further validation of the model with various procognitive and memory disturbing agents is in progress.

References:

I. Klinkenberg, A. Blokland (2010) The validity of scopolamine as a pharmacological model for cognitive impairment: A review of animal behavioral studies; Neuroscience and Biobehavioral Reviews 34 1307–1350

EPOS™ Poster

Cardiovascular MRI

531

4D PC-MRI for the quantification and visualisation of peripheral arterial flow

A. Watson[1], K. Lanaghan[2], C. Mccomb[3], T. Steedman[2], K. Forbes[4], J. Foster[3]
[1]Clinical Physics, NHS Greater Glasgow and Clyde, Glasgow/UNITED KINGDOM, [2]MRI, BHF Glasgow Cardiovascular Research Centre, Glasgow/UNITED KINGDOM, [3]Clinical Physics (MRI), BHF Glasgow Cardiovascular Research Centre, Glasgow/UNITED KINGDOM, [4]NeuroRadiology, Institute for Neurological Sciences, Glasgow/UNITED KINGDOM

Purpose/Introduction: The emergence of 4D PC-MRI techniques(1), with the ability to obtain a volume of time resolved velocity data, offers an exciting analogue to the use of colour and spectral Doppler ultrasound in vascular diagnosis. This raises the possibility of the provision of flow velocities and velocity ratios, for the assessment of arterial stenosis, in regions such as the subclavian artery or aorto-iliac arterial segment where ultrasound imaging is difficult.
This study aimed to evaluate a 4D flow work-in-progress package as a potential tool for the quantification and visualisation of peripheral vascular blood flow.
Subjects and Methods: MRI studies were performed on a 3T Siemens Verio with 4-D flow work-in-progress package. Standard 2D PC-MRI slices ware also acquired. Doppler ultrasound studies used a GE Logiq-e with a 12L-RS linear transducer. MRI scan parameters were optimised to obtain best spatial resolution within the temporal resolution constraints. For some studies the 3D velocity encoding parameter was varied between spatial dimensions.
Test phantoms consisted of: a silicone-elastomer carotid vessel with a 70% stenosis and a rigid silicone 8mm diameter tube with a 50% stenosis. A dual-modality, computer-controlled system was used to pump a blood mimic with constant or pulsatile flow patterns.
The carotid arteries of two healthy volunteers were scanned using both MRI and ultrasound.
Results: Both the phantom and in-vivo studies revealed PC-MRI techniques underestimated peak maximum velocity values when compared with Doppler ultrasound; particularly in the case of 4D PC-MRI (mean bias, of -71cms^{-1}, p = 0.02) which, as shown for the carotid phantom, would underestimate the degree of stenosis(2). The underestimation of maximum velocities by 4D PC-MRI remained even when Doppler spectral broadening effects were considered. The 50% stenosis phantom was better able to quantify and resolve the stenosis due to a higher pixel per lumen ratio. 4D flow visualisation of these smaller vessels appeared to improve by reducing velocity sensitivity in the non-dominant flow directions.
Discussion/Conclusion: In comparison with 2D PC-MRI and spectral Doppler, 4D flow considerably underestimates velocity values due to the limited spatial resolution that can be achieved within reasonable clinical scanning times. However, visualisation of the smaller peripheral vessels appears promising and can be enhanced by reducing the velocity sensitivity in the non-dominant flow direction.
References:
(1) Markl M, et al. 4D flow MRI. J Magn Reson Imaging 2012; 36(5):1015-1036.
(2) Oates CP, et al. Joint recommendations for reporting carotid ultrasound investigations in the United Kingdom. Eur J Vasc Endovasc Surg 2009; 37(3):251-261.

532

Right Ventricular Function and Different Patterns of Delayed Cardiac Enhancement Assessed by Cardiac MRI in Symptomatic Patients with Post Total Correction of Tetralogy of Fallot : A Report From Iran

F. Akhavan[1], M. Motevalli[1], M. Razaghy Ghasrodashty[2]
[1]Radiology, Tehran medical university, Tehtan/IRAN, [2]Radiology, Shahed medical university, Tehran/IRAN

Purpose/Introduction: Tetralogy of Fallot (TOF) is the most common type of cyanotic congenital heart disease. The underlying mechanisms that contribute to global right ventricular (RV) dysfunction in patients with repaired tetralogy of fallot are incompletely understood. We therefore sought to quantify delayed enhancement (DE) after repairing tetralogy of fallot by cardiac magnetic resonance (CMR) to evaluate possible correlation between delayed enhancement and RV function.
Subjects and Methods: In a retrospective cohort study, the clinical and cardiac magnetic resonance data were collected for 110 consecutive symptomatic patients with repaired TOF during 35 years ago. Cardiac function indexes were compared in two groups of patients with and without delayed enhancement.
Results: Pateints' mean age was 21.9±6.9 years. 65 (59.1%) patients were male and 45 (40.9%) were female. DE was positive in 103 (93.6%) and negative in 7 (6.4%) patients. The position of DE was "right ventricualr outflow tract (RVOT) without other sites" in 81 (78.6%) and "RVOT with the other sites" in 22 (21.4%) patients. Mean regurgitation fraction in DE positive and DE negative was 38.1%±13.9 and 22.3%±16.7 respectively (P=0.010). Mean right ventricle end diastolic volume (RVEDV) in DE positive and DE negative was 258.2 mL/m2±91.8 and 185.5 mL/m2 ±38.2 respectively (P=0.047). Mean of right ventricle end systolic volume (RVESV) in DE positive and DE negative was 162.8 mL/m2±71.1 and 103.3 mL/m2±35.9 respectively (P=0.045) and mean of right ventricle ejection fraction (RVEF) in DE positive and DE negative was 38.2% ±7.7 and 44.8%±9.1 respectively (P=0.010).
Discussion/Conclusion: DE is a common finding in patients with repaired tetralogy of fallot and it can correlate with RV function. We found delayed enhancement as an indicative of ventricular scarring or fibrosis in theses patients showing a direct correlation with RV dysfunction.
References:
1-Oosterhof T, Mulder BJM, Vliegen HW, Roos A. Corrected Tetralogy of Fallot:Delayed Enhancement in Right Ventricular Outflow Tract. Radiology. 2005; 237:868–871.
2-Al Habib HF, Jacobs JP, Mavroudis C, Tchervenkov CI, O'Brien SM, Mohammadi S, et al. Contemporary patterns of management of tetralogy of Fallot: data from the Society of Thoracic Surgeons Database.Ann Thorac Surg. Sep 2010; 90(3):813-9; discussion 819-20.
3-Nielsen JC, Powell AJ. Cardiovascular MRI applications in congenital heart disease.Indian J Radiol Imaging.2007 (May); 17, 2:86-97.
4-Wald RM, Haber I, Wald R, Valente AM, Powell AJ,Geva T. Effects of Regional Dysfunction and Late Gadolinium Enhancement on Global Right Ventricular Function and Exercise Capacity in Patients With Repaired Tetralogy of Fallot. Circulation. 2009; 119:1370-1377

533

Assesment of Undefined Myocardial Infarction Using Cardiac MRI in Patients with End-stage Renal Disease.

I. Yuce[1], M. Keles[2], M. Kantarci[3]
[1]*Radiology, Erzurum Regional Research Hospital, Erzurum/TURKEY,*
[2]*Nephrology, Ataturk University School of Medicine, Erzurum/TURKEY,*
[3]*Radiology, Ataturk University School of Medicine, Erzurum/TURKEY*

Purpose/Introduction:
Undefined myocardial infarction (UMI) is characterized with presence of myocardial scarring in subjects who had no history of myocardial infarction (MI) (1). Data derived from population-based studies showed that mortality rate of patients with UMI is nearly 45-55 % (1). This rate is high as of patients with MI or may be higher. Nevertheless, end-stage renal disease (ESRD) comprises high risk of UMI. In our study, we assessed the cardiac viability of patients with ESRD. We aimed to detect the UMI frequency, to reveal the other ischemic events, to introduce the effectiveness of cardiac magnetic resonance (CMR) imaging in the risk population and to compare the imaging findings with electrocardiography (ECG) and laboratory results.
Subjects and Methods:
Our study consisted of 20 patients referred to radiology department from nephrology clinic for CMR examination between June 2010 and December 2011. Sixty percent of the patients were female (n: 12, mean age: 44.5) and forty percent of were male (n: 8, mean age: 52.6). In all patients, resting left ventricle (LV) functions and assessment of myocardial early and late contrast enhancement were evaluated and risk groups were determined. All examinations were performed with a 1.5 Tesla magnetic resonance imaging (MRI) scanner (Siemens, Magnetom Avanto, Forchheim, Germany). ECG and laboratory test were also performed in all patients. Patients were followed clinically for an average of 18 ± 4 months.
Results:
In our study group, pathological findings were detected in six patients (30%). Scar tissue was (high risk) detected in three (15%), hibernation was (moderate risk) detected in three (15%) patients. There were no pathology (low risk) detected in the remaining 14 patients. There was a statistically significant difference in terms of mortality between patients in high and low risk groups ($p<0.05$). Comparing ECG and troponin levels did not show significant difference.
Discussion/Conclusion:
In conclusion, our study showed that in patient population, CMR is successfully able to make risk group classification and reveal the ischemic events even those can not be demonstrated with ECG and laboratory tests. CMR, which is capable of demonstrating the coronary ischemia and defining the UMI, now emerges as a non-invasive imaging technique in patients with ESRD.
References:
1. Andrade JM, Gowdak LH, Giorgi MC, et al. Cardiac MRI for detection of unrecognized myocardial infarction in patients with end-stage renal disease: comparison with ECG and scintigraphy. Am J Roentgenol 2009; 193: 25-32.

534

Intersite reproducibility of myocardial assessment of T1 and partition coefficient on phantom and one volunteer at 1.5T and 3.0T.

C. Falque[1], P. Viout[2], M. Bernard[3], F. Kober[2], A. Jacquier[1]
[1]*Radiology, Hopital La Timone, Marseille/FRANCE,* [2]*CRMBM UMR CNRS 7339, Aix Marseille Université, Marseille/FRANCE,* [3]*CRMBM UMR 7339, Aix Marseille Université - CNRS, Marseille/FRANCE*

Purpose/Introduction: Extracellular matrix expansion may represent a clinical relevant surrogate marker for cardiac morbidity and mortality. Several technical limits have been raised about accuracy and reproducibility of partition coefficient calculation, especially because there is sparse information on inter site reproducibility of T1 mapping sequence at 1.5T and 3.0T. The aim of our study was to evaluate inter sites reproducibility of partition coefficient (λ) using ShMOLLI sequences on phantom, and to assess reproducibility of T1 mapping performed among different sites on one volunteer at 1.5T and 3.0T.
Subjects and Methods: Phantoms were built to produce similar T1 and T2 of myocardium and blood before and after gadolinium. Phantom was brought on 12 different sites (13 magnets), and ShMOLLI schemes (1) were performed at 1.5T (α:35°, sampling:5-2 and 4-3-2; pause: 3 HB) and 3.0T (α:20°; sampling:5-2 and 4-3-2; pause: 4 HB) at 40, 60, 90 and 120bpm. T1 reference was assessed ones using IR-GRE (TR/TE=13000/18; 17 inversions between 30-9000 ms). Four different λ were simulated as close as possible to reality (myocardium with high, moderate and low level of fibrosis and normal myocardium). Same ShMOLLI schemes were performed on one volunteer in 6 sites; 5 at 1.5T and 2 at 3.0T.
Results: Partition coefficient was overestimated in agreement with the predominant T1 underestimation of tubes with high T1 value. For 1.5T, median error of λ was equal to 2.9%(1.8; 3.4) at 40bpm, 3.4%(3.0; 4.2) at 60bpm, 2.5%(1.7; 3.4) at 90bpm and 2.0%(1.1; 3.3) at 120bpm. At 3.0T, median error of λ was equal to 3.7% (2.4; 5.0) at 40bpm; 3.3% (2.3; 4.9) at 60bpm; 3.4% (2.0; 4.8) at 90bpm; 2.0% (0.5; 4.2) at 120 bpm. Comparing 1.5T and 3.0T, there were no significant difference in λ value between all heart rates. For the volunteer, there was no significant difference in T1 value, obtained in fat, skeletal muscle, myocardium and blood at 1.5T. Results obtained on the 2 magnets 3.0T were similar.
Discussion/Conclusion: Partition coefficient estimation is precise and reproducible between different sites on 1.5T and 3.0T using ShMOLLI sequences. On one volunteer, intersites reproducibility was good.
References:
(1) Piechnick SK, 2010, JCMR

535

The effect of gradient temperature stabilization on the spatio-temporal field stability of a high field MRI system

I. Markuerkiaga, **D. Padro**, T. Reese
Molecular Imaging Unit, CICbiomaGUNE, Donostia/SPAIN

Purpose/Introduction: Modern high field preclinical MRI systems are built compact, with gradient coils that fit tightly in the magnet bore. Heat generated during operation can be transferred directly from the gradient coil surface to the passive shims. Generally, gradient use is generating heat which in turn can cause undesired field drifts by indirectly [1, 2] or directly [3] heating the passive shims. Under different experimental conditions we measured the field stability at 11.7T with and without making use of a temperature control unit that is designed to stabilize the gradient surface temperature well above room temperature.
Subjects and Methods: Measurements were made on a Bruker Biospec 11.7T system with a 16 cm bore diameter using an actively shielded 750 mT/m gradient. The 9 cm gradient insert is equipped with four heating elements on the surface, that can be switched on/off by a gradient control temperature unit (GCTU) [4] to maintain the temperature of four individual temperature sensors at a preset level (our system 42.5 °C). The 1H-resonance frequency of a "point source" (30 ul water) placed in the isocentre was determined every 15 seconds. Gradients were applied at different gradient strengths (Figure1) and gradient switching frequencies (Figure2). In our system, the maximum allowed duty cycle is achieved by individually pulsing at full power 6.5% of the time the X or Y gradients and the Z gradient 11% of the time.
Results: A direct comparison of gradient use both when the GCTU is switched off and on is made in Figure1. The magnitude of the induced field changes

is around ten times smaller when the GCTU is on. Eddy currents do not significantly contribute to these changes in either case (Figure2). Full system description will be given in the presentation.

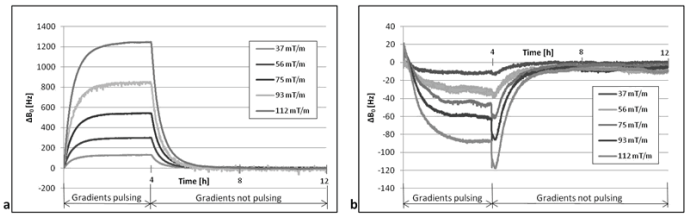

Figure 1: B_0 drift measured pulsing gradients for 4 hours at different gradient strengths and the field drift during 8h thereafter with **(a)** GCTU off and **(b)** GCTU on.

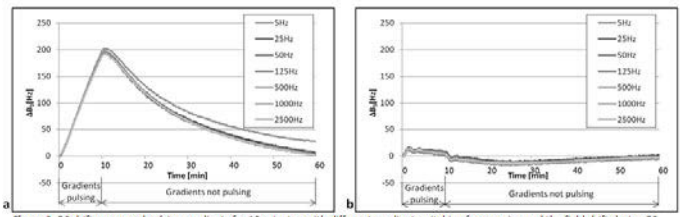

Figure 2: B0 drift measured pulsing gradients for 10 minutes with different gradient switching frequencies and the field drift during 50 minutes thereafter with **(a)** GCTU off and **(b)** GCTU on.

Discussion/Conclusion: The implementation of the GCTU effectively reduces the magnitude of the field variation due to heating of passive shims by over 90%. Nevertheless, corrective measures may still be necessary for fMRI, MR thermometry, MRS or spectroscopic imaging, especially when they are interleaved or run immediately after gradient intensive sequences. In these cases, users will have to bear in mind that the field can be spatially dependent and that the field curve may present discontinuities, like in the system studied here.

References:

[1] El-sharkawy et al. MAGMA 2007;19(5), 223–236.
[2] Foerster et al. Magn Reson Med 2005;54(5), 1261–7
[3] Nakabayashi et al. US Patent 2010
[4] Jakovcic K., GCTU Service Manual

536

Fully automated left ventricular myocardium segmentation from CINE MR using feature extraction and active contours.

V.J. Garcia-Gomez[1], **A. Alberich-Bayarri**[2], R. Sanz-Requena[2], L. Martí-Bonmatí[3], V. Naranjo-Ornedo[4]
[1]Telecommunications Engineering, Polytechnic University of Valencia, Valencia/SPAIN, [2]Radiology, Hospital Quiron Valencia, Valencia/SPAIN, [3]Radiology, Hospital Quirón Valencia, Valencia/SPAIN, [4]Telecommunications, Polytechnic University of Valencia, Valencia/SPAIN

Purpose/Introduction: The aim of this work was to develop a new fully automated methodology for left ventricular (LV) myocardium segmentation from cardiac MR CINE images without human interaction based on figures detection and adaptive contours.

Subjects and Methods: All the algorithms were implemented in Matlab R2012a (Mathworks, Natick, USA).

Initial image preparation steps were developed, first the images were cropped a 20% from each side in order to minimize the number of non-heart voxels and improve the posterior figure detection algorithms. A median filtering (3-by-3 neighborhood) and histogram equalization were then applied in order to enhance the contrast between the myocardium and left ventricle maintaining the edges sharpness. A gradient to the image was finally applied in order to increase the energies of the adaptive contours algorithms to be used.

For the segmentation algorithm, a level-set method for shape recognition was used[1]. Due to morpohological characteristics of the LV myocardium, a Hough transform was used in order to detect circular patterns. The inner contour of the myocardium was automatically fitted to an initial circumference, which was considered as an input to the adaptive snakes algorithm for contour detection[2]. The designed snakes parameters were α=0.001; β=0.4; γ=100; κ=0.05; κp=5; niter=500 for the inner contours and α=1; β=0.00001; γ=500; κ=0.00001; κp=7; niter=500 for the outer contours.

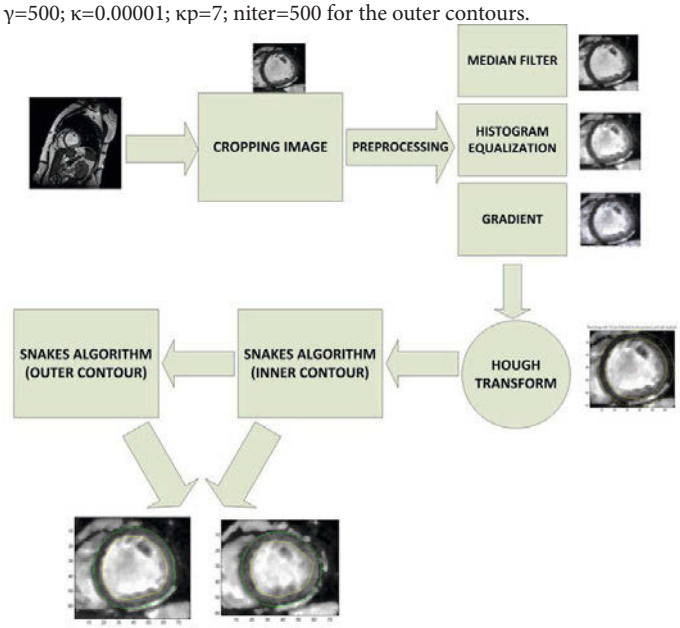

Results: The method was preliminary applied to a set of 5 cardiac 3T MR CINE examinations with a high similarity of the segmentations if compared to the corresponding ground truths. The computational burden of the method developed was low, with a total execution time average < 1 minute.

Discussion/Conclusion: The method developed for the automated myocardium segmentation from CINE MR images shows a clear benefit over the existing processes that require human interaction. Further research is currently being performed in order to quantitatively evaluate the similarity of the method if compared to manual delineations in a large dataset. Also, the method can be properly adapted to perfusion and late gadolinium enhanced acquisitions.

References:

[1] Ballard DH, Generalizing the Hough Transform to Detect Arbitrary Shapes, Pattern Recognition, 1981; 13:111-122.
[2] Kass M, Witkin A, Terzopoulos d. Snakes: active contours models. International Journal of Computer Vision 1987; 1:321-331.

537

Clinical Usefulness of Real-Time Cardiac Cine Imaging With the No-Training-Scan k-t Method

T. Kariyasu[1], K. Yokoyama[1], T. Nitatori[1], R. Ishimura[1], M. Imai[1], I. Miyazaki[1], T. Yoshioka[1], W. Yamamura[1], H. Takeshima[2], S. Nitta[2], T. Shiodera[2], T. Takeguchi[2], S. Bannae[3], S. Kuhara[3]
[1]Department of Radiology, Kyorin University, Faculty of Medicine, Tokyo/JAPAN, [2]Corporate Research & Development Center, Toshiba Corporation, Kanagawa/JAPAN, [3]MRI Systems Development Department, Toshiba Medical Systems Corporation, Otawara-shi/JAPAN

Purpose/Introduction: We have developed a method for acquiring partial two-dimensional time-series data in the same manner as with k-t SENSE and reconstructing images in a shorter time without the use of training data. The

present study was conducted to evaluate the clinical usefulness of real-time cardiac cine imaging with this method.

Subjects and Methods: A 1.5-T MRI system was used (EXCELART VantageTM Powered by Atlas, Toshiba Medical Systems Corporation, Japan). Cine imaging with the no-training-scan t-k method was performed using an SSFP sequence (TR/TE = 3.4/1.7 ms, FA = 60°, matrix = 96´256, slice thickness =10 mm, and FOV = 35´35 cm) during free breathing without ECG gating. Three types of images with different temporal resolutions of 81.6 ms, 54.4 ms, and 40.8 ms were acquired with the reduction factor set to 4, 6, and 8, respectively. The subjects were patients who underwent cardiac MRI in April 2013. Images acquired using our method were compared against images acquired by conventional retrospective ECG-gated cine imaging (ECG-gated scanning during breath holding, TR/TE = 4.2/2.1 ms, FA = 70° [approx.], matrix = 192´256, and FOV = 35´35 cm), and the image quality and reliability of left ventricular function analysis (end-diastolic and end-systolic areas and area change rate) were evaluated.

Results: Compared with the conventional method, cardiac wall motion was visualized more smoothly using our method, although the SNR decreased as the reduction factor was increased. Especially in patients with arrhythmias, in whom wall motion is difficult to evaluate using the conventional method, wall motion could be more clearly evaluated. With regard to left ventricular function analysis, the analysis results were close to those obtained using the data acquired with the conventional method.

Discussion/Conclusion: The method we have developed does not require breath holding or ECG gating and allows cardiac cine imaging to be performed for patients with breathing difficulties or arrhythmias, in whom cardiac cine imaging is difficult using the conventional method. The results of the present study indicate that our method is clinically useful. Further research is needed to determine the optimal reduction factor.

References:

None

EPOS™ Poster

Clinical body MRI

538

WITHDRAWN

539

Significance of MRI in diagnostics, outcome prognosis and definition the therapeutic tactics for cases of aseptic necrosis of the femoral head

O.Y. Medvedeva[1], V. Fokin[2]
[1]Department of Roentgenology and Radiology, S.M. Kirov Military-medical academy, St. Petersburg/RUSSIAN FEDERATION, [2]Radiology, Medical Military Academy, Saint-Petersburg/RUSSIAN FEDERATION

Purpose/Introduction: Avascular necrosis of the femoral head is a widespread pathologic process in the hip joint, leading to the decrease quality of life. Every year approximately 11000 new cases of the disease are being registered. The most susceptible age group is 35-55 y.o. persons. In 40-50% of all the cases patients are admitted for a medical consultation with an advanced stage of a disease, which increases the risk of forming secondary osteoarthritis.
Subjects and Methods: MRI data sets of forty two patients were analyzed (28 males and 14 females, mean age – 42.3 y.o.) in cases of avascular necrosis of the femoral head. Parameters analyzed – the volume and the surface of necrosis area comparing to the total volume and surface of the femoral head. The MRI-scanning was performed using 1.5 T MRI-scanner. A standardized MRI protocol was used for all examinations. The following sequences were obtained: axial and coronal proton density–weighted fast spin-echo sequence with fat saturation, coronal T1-weighted spin-echo sequence, axial T2-weighted spin-echo sequence.
Results: The MRI-scanning allowed defining the necrotic phase of the pathologic process in 20 patients (47.6%), fragmentation phase was detected in 22 patients (52.4%). For the necrotic phase the specific feature was that the necrotic surface/total femoral head surface ratio was approximately 6%. The same parameter in the second group of patients was 25-30%. The differences were statistically significant: $p<0.001$, $F = 2.5$. The correlation between the risk of the compression fracture and the volume of the osteonecrosis was less significant.
Discussion/Conclusion: A ratio of the surface area of the necrotic lesion help defining the risk of developing a compression fracture within the osteonecrosis zone, which can influence the disease prognosis and treatment tactics.
References:
1.Rajpura A, Wright AC, Board TN. The role of MR imaging in avascular necrosis of the femoral head. Semin Musculoskelet Radiol. 2011 Jul;15(3):281-300.
2. Yoon-Seok Youm, Soo-Youn Lee, Soo-Ho Lee. Apoptosis in the Osteonecrosis of the Femoral Head. Clinics in Orthopedic Surgery. - 2010. – Vol. 2. – P. 250-255.

540

Reliability and repeatability of apparent diffusion coefficient value of normal prostate

I. Jambor[1], T. Kauko[2], H. Merisaari[3], J. Järvinen[1], J. Saunavaara[4], M. Pesola[1], H.J. Aronen[1]
[1]Department of Diagnostic Radiology, University of Turku, Turku/FINLAND, [2]Department of Biostatistics, University of Turku, Turku/FINLAND, [3]Turku PET Centre, University of Turku, Turku/FINLAND, [4]Medical Imaging Centre of Southwest Finland, Turku University Hospital, Turku/FINLAND

Purpose/Introduction: To investigate the reliability and repeatability of apparent diffusion coefficient (ADC) values calculated using low b-values (lower than 100 s/mm^2) compared with ADC values calculated excluding low b-values. Moreover, the reliability and repeatability of ADC values calculated using different number of b-values was examined.
Subjects and Methods: Ten healthy volunteers (mean age 53 ± 8) underwent in total four repeated 3T single-shot spin-echo epi based DWI examinations performed on two separate days using surface coils only. The following parameters were used: TR/TE 7000 ms/87 ms, FOV 260×260 mm, matrix size 128x128, slice thickness 5 mm and 16 equally distributed b-values ranging from 0 to 2000 s/mm^2. All possible b-value combinations containing at least one of the first 4 b-values (0, 50, 100, 200 s/mm^2) were used for ADC calculation. ADC values were calculated using monoexponential fit. Reliability and repeatability of ADC values, calculated using different b-value combinations, was assessed using Shrout-Fleiss analysis (1). In addition, Bland-Altman analysis was used for each pair of ADC values calculated using or excluding low b-values.
Results: In total 61436 b-value combinations were evaluated. Removal of 0 and 50 s/mm^2 b-values improved the reliability and repeatability of ADC values of normal prostate. The effect was mainly prominent when only 2 or 3 b-values were used for ADC calculation. ADC values calculated using combinations without b-values of 0 and 50 s/mm^2 had better reliability and repeatability than ADC values calculated using b-value combinations without 0, 50 and 100 s/mm^2 b-values. In the subset of ADC values calculated using b-value combinations with the highest b-value of 650 s/mm^2, 139 observations were out of 2 standard deviations (SD) in Bland-Altman analysis when 4 b-values were used while only 8 when 7 b-values were used. In the same subset, 51 observations were out of 2 SD for the b-value combinations without use of 0, 50 s/mm^2 while 46 for the b-value combinations without use of 0, 50 and 100 s/mm^2 when 6 b-values were used. The use of more than 5 b-values led to only minor further improvement in the reliability and repeatability of ADC values.
Discussion/Conclusion: ADC values calculated without the use of 0 and 50 s/mm^2 b-values had better reliability and repeatability than ADC values calculated using low b-values. Our findings support the use of non-0 b-values for ADC calculation.
References:
1. Shrout PE, Fleiss JL. Intraclass correlations: uses in assessing rater reliability. Psychol Bull 1979; 86:420-428.

541

Imaging of composite mesh used in Ventral Hernia Repair with Amide Proton Transfer MRI.

F. Franconi[1], J. Roux[2], X. Garric[3], L. Lemaire[4]
[1]PRIMEX (CIFAB), Université d'Angers, Angers Cedex/FRANCE, [2]SCAHU, Pavillon Ollivier, UFR Sciences Médicales, Université d'Angers, Angers Cedex / FRANCE, [3]Artificial Biopolymer Department UMR CNRS 5247, Université de Montpellier 1&2, Montpellier/FRANCE, [4]UMR-S INSERM 1066, Université d'Angers, Angers Cedex /FRANCE

Purpose/Introduction: The implantation of synthetic meshes is widely used in ventral hernia repair. The lack of non-invasive imaging techniques to visualize these prostheses leads to late diagnostic of possible complications (prosthesis displacement or shrinkage, infection, or abdominal adhesion). In this study, the potential of the amide proton transfer (APT) (1) contrast to visualize commercial composite mesh was explored in vitro and in vivo. Indeed, some reinforcement prostheses are coated with an absorbable protein films to reduce visceral adhesion that can be visualized by APT.
Subjects and Methods: All MR studies were performed with a Biospec Avance III MR scanner (Bruker Biospin, Wissembourg, France) using a 20 cm bore 7T magnet. A 72 mm diameter volume coil was used for in vitro experiment and an 87 mm diameter volume coil was used as a transmitting coil and a 4x1 element phased-array coil was used in receive-only mode for in vivo experiment. Magnetization transfer asymmetry ratio (MTR_{asym}) images of composite meshes (Parietex ™ composite mesh, Covidien, Trévoux, France) were obtained in vitro and in vivo from fast-spin echo acquisitions with frequency saturation offsets of ± 3.5 ppm with respect to water frequency and no saturation. Saturation was achieved with a train of 120 spectrally selective Gaussian saturation pulses (peak B1 amplitude 5 µT, duration 36 ms).
For in vitro experiments, the collagen-coated meshes were embedded in agarose gel and images were acquired at 37°C.
In vivo, rats were assessed with APT each week for one month after the intraperitonal implantation of two meshes, one on each side of the incision. One mesh was coated with collagen and the other was not.
Results: In vitro, meshes were delineated with APT as a thin continuous linear hypersignal located on one side of the mesh. Unlike collagenfree meshes, collagen-coated meshes were easily identified in vivo with APT during the first three weeks post-implantation. The composite meshes MTR_{asym} were significantly different from the muscle MTR_{asym} value. After a month, muscle and mesh MTR_{asym} values were not significantly different and mesh conspicuity was no longer possible.
Discussion/Conclusion: The results suggest that APT-MRI is a promising technique for non-invasive, early post-surgical visualization of composite meshes used in ventral hernia repair.
References:
1 Zhou J, Lal B, Wilson DA, Laterra J, van Zijl PC. Amide proton transfer (APT) contrast for imaging of brain tumors. Magn Reson Med 2003;50(6):1120-1126.

542

WITHDRAWN

543

Using Intravoxel Incoherent Motion (IVIM) MR Imaging to Evaluate the Cortical Defect in the first episode of Acute Febrile Upper Urinary Tract Infection (UTI): A Preliminary Result

C.H. Lee, Y.S. Park, C.M. Park, J. Lee, J.W. Choi, K.A. Kim
Radiology, Korea University Guro Hospital, Seoul/KOREA

Purpose/Introduction: Introduction: Febrile upper urinary tract infection (UTI) is common in pediatric patients. Especially, upper UTI in association with vesicoureteral reflux (VUR) would lead to renal scarring, which was eventually associated with long term sequel such as hypertension, renal impairment or chronic renal failure. Therefore, early detection of perfusion defect is important because this defect can be reversible by prompt treatment.
Purpose: To compare the predictive value of diffusion weighted kidney MR (IVIM model) with DMSA for the diagnosis of febrile upper UTI in pediatric patients.
Subjects and Methods: A total 43 kidneys of 22 pediatric patients with clinical findings consistent with first episode of febrile upper UTI were evaluated from June 2011 to January 2012. Diffusion weighted sequence using IVIM model was performed with multiple b factors (b=0, 25, 50, 75, 100, 200, 500, 800) at 3.0 T MRI. The presence of low signal intensity lesion, so called defect, was evaluated by two experienced radiologists on ADC map. DMSA scintigraphy was regarded as a standard of reference. At DWI, ADC, true diffusion coefficient (D), pseudo-diffusion coefficient (D*), and perfusion fraction (F) in both defect and non-defect renal tissue were calculated using post-processing program and compared with each other.
Results: Defect was found by DWI in 14 kidneys. One case of equivocal photon defect on DMSA was missed on DWI. Sensitivity, specificity, positive predictive value, and negative predictive value for the detection of parenchymal defect were 93.3%, 100%, 100%, and 96.5%, respectively, comparing DMSA as a standard of reference. Mean value of ADC, D, D*, and F were 1.12±0.15, 1.05±0.10, 33±0.17 ($\times 10^{-3}$ mm^2/sec), and 0.14±0.09 in foci of defect. In the normal foci, mean value of ADC, D, D*, and F were 1.37±0.09, 1.31±0.10, 43±0.19 ($\times 10^{-3}$ mm^2/sec), and 0.12±0.04, respectively. ADC and D diffusion parameters were lower in renal parenchymal defect group ($p < 0.01$). D* parameter was tended to be lower in renal parenchymal defect group ($p = 0.095$).
Discussion/Conclusion: Conclusion: In spite of preliminary results, IVIM-DWI can allow both direct visualization and quantitative measurement of cortical defects. Because of its simplicity and free of radiation, IVIM-DWI may be considered as a new standard to replace a DMSA scintigraphy.
References:
1. N Engl J Med 2003;348:195-202.
2. J Am Soc Nephrol 2011;22:1429-1434.
3. Radiology 2005;235:911-917.
4. Radiology 1988;168:497-505.
5. Radiology 2008;249:891-899.

544

Histopathological verification of MR-guided breast biopsy findings - preliminary results

S. Heinze-Paluchowska, E. Luczynska, J. Aniol, S. Dyczek
Department of Radiology, Oncology Center, Krakow/POLAND

Purpose/Introduction: The purpose of our study was to present preliminary results of our experience with MR-guided breast biopsy of suspicious enhancing breast lesions identified only at MR imaging, invisible in US, MG (digital mammography) or CESM (contrast enhanced spectral mammography).
Subjects and Methods: 8G and 11G (115/145 mm) needle biopsy of 28 lesions visible at MR imaging only was performed with MR imaging guidance

in 27 patients, aged 31-72 years. The study was approved by the Local Ethics Committee and prior written informed consent was obtained from all patients. All included patients received a diagnosis of malignant, high-risk, or benign breast tissue (according to BI-RADS scale) and undergone subsequent surgery or follow-up imaging. To avoid difficulties due to the poor quality of earlier breast MR imaging - all patients had repeated breast MRI examination on 1.5T Siemens Avanto (16ch Breast coil, Noras) before the intervention.
Lesion characteristics (morphology, size, enhancement) were recorded. MR–guided breast biopsy findings were compared with histopathological or follow-up imaging results.
Results: Histological verification from MRI-guided breast biopsy was possible in 27 (96%) of 28 lesions. Malignancy was identified in 12 (44%) lesions: 7 invasive cancers and 5 ductal carcinoma in situ (DCIS) lesions. 2 (40%) of DCIS lesions were upgraded to invasive cancer after mastectomy. A high-risk lesion (atypical lobular/ductal hyperplasia, lobular carcinoma in situ) was identified in 6 (22%) cases. 9 (33%) lesions were supposed to be benign.
Discussion/Conclusion: MR–guided breast biopsy is sufficiently appropriate for obtaining histological validation of lesions invisible in other imaging techniques (i.e. US, MG, CESM) or physical examination. It is feasible, safe and can reduce treatment by eliminating unnecessary surgical biopsy.
References:
P. Crystal, A. Sadaf , K. Bukhanov, et al. High-risk lesions diagnosed at MRI-guided vacuum-assisted breast biopsy: can underestimation be predicted? Eur Radiol (2011) 21:582–589
Liberman L, Bracero N, Morris E, Thornton C, Dershaw DD MRI-guided 9-gauge vacuum-assisted breast biopsy: initial clinical experience. AJR Am J Roentgenol (2005)185:183–193
Han BK, Schnall MD, Orel SG, Rosen M Outcome of
MRI-guided breast biopsy. AJR Am J Roentgenol (2008) 191:1798–1804

545

Preoperative MRI in rectal cancer: accuracy in the prediction of T staging and circumferential resection margins (CRM) involvement with histologic correlation

R. Danzi[1], E. Soscia[2], C. Sirignano[2], M. Pannullo[3], M. Danzi[3], M. Salvatore[1]
[1]Radiology, università Federico II di Napoli, naples/ITALY, [2]CNR, IBB, Naples/ITALY, [3]Surgery, Università Federico II di Napoli, Naples/ITALY

Purpose/Introduction: Pre-operative rectal cancer staging include endorectal ultrasonography (EUS), computed tomography (CT) and magnetic resonance imaging (MRI). MRI with phased-array was reported as more reliable than EUS in staging advanced (stage ≥ II) rectal cancer. MRI gives information about the depth of rectal wall tumor infiltration, the involvement of mesorectal fascia (MRF), the presence of lymph node and extramural vascular invasion[1]. The aim of this study is to determinate the accuracy preoperative staging with phased-array MRI and predict "clear" circumferential resection margins (CRM), compared with histology.
Subjects and Methods: Between 2007 and 2012, 28 patients (57% male and 43% female; median age was 64,4) who underwent surgery for rectal cancer and did not received chemio-radiotherapy were selected. We reviewed the preoperative MRI evaluation of tumour stage (T stage) and involvement of MRF. Pelvic MRI were acquired by a 3T apparatus (Somatom Trio, Siemens, Erlangen, Germania) using a pelvic phased-array coil. High resolution transverse, coronal and sagittal planes T2 weighted images were acquired with the follow parameters: Tr 5900, Te 95, FA 124, matrix 256x230, fov 350x350. The lesions were classified T1-T2 (limited to submucosa or to the rectal wall), T3-T4 (extended through all wall layers, into the perirectal fat tissue or to surrounding organs). CRM has been defined as the non-peritonealized surface of a resection specimen created by dissection of the subperitoneal aspect at surgery. Curative Primary surgery was performed including low anterior resection with TME. Histology considered the CRM involved if the tumor was extended to within 1 mm of circumferential excision margin.
Results: The MRI found 24 T1-T2 tumours and 4 T3-T4 tumours, the histology found 22 T1-T2 tumours and 6 T3-T4 tumours. We assessed concordance between MRI and Histopatology with a McNemar test (P = 0,2500). The CRM was accurately staged in all patients
Discussion/Conclusion: MRI is a sensitive and specific tool for T staging and evaluation of recurrence of rectal cancer[1-2]. Our study showed high diagnostic accuracy rate of preoperative MRI in the prediction of T stage and CRM. The agreement rate between MRI and Histology was about 90% for the T stage and 100% for the CRM involvement. High quality pelvic MRI can achieve accurate preoperative loco regional decision staging, , with subsequent positive effect on prognosis, morbidity and mortality.
References:
1.Regina G.H.Beets-Tan,MD,PhD Geerard L. Beets, MD,PhD .Rectal Cancer:Review with Emphasis on MR Imaging.Radiology 2004;232,335-346
2.GiustiS, BucciantiP, CastagnaM, FruzzettiE, FattoriS, CastelluccioE, CaramellaD, BartolozziC.Preoperative rectal cancer staging with phased-array MR. RadiatOncol.2012 Mar 5;7:29.

546

WITHDRAWN

547

Diffusion Weighted Imaging and ADC in Whole Body MRI for multiple myeloma

S. Merigeaud[1], C. Exbrayat[2], E. Decoux[3], S. Aufort[3], D. Donadio[2], C. Plassot[4], S. Auger[2]
[1]Centre de Radiologie et Physiothérapie, Clinique du PARC, Castelnau Le Lez/FRANCE, [2]Hématologie, Clinique du Parc, Castelnau Le Lez/FRANCE, [3]Centre de Radiologie et Physiothérapie (CRP), Clinique du Parc, Castelnau Le Lez/FRANCE, [4]Biostatistique, INSERM Languedoc-Roussillon, Montpellier Cedex/FRANCE

Purpose/Introduction: In myeloma, recent studies have shown the interest of whole-body MRI (WB-MRI) to replace the MRI of spine and pelvis (SP-MRI) in initial and follow-up assessment. The aims of this study are to show:
- the greater sensitivity of WB-MRI compared with SP-MRI, including through the use of diffusion weighted imaging (DWI);
- the improved specificity of this examination using ADC (apparent diffusion coefficient) to exclude begnin or sequelar lesions.
Subjects and Methods: This retrospective study includes 22 patients (multiple myeloma, initial assessment or relapse) who had a Whole body MRI (including a MRI of spine and pelvis) before treatment. The examinations consisted in:
- a T1 sagittal acquisition on the whole spine,
- Coronal T2 STIR and axial diffusion (b50, b800, ADC) acquisitions on the whole body, from vertex to mid-thigh (total duration: 23 to 30 min).
Bone marrow infiltration (BI) pattern and the number of **focal lesions** (FL) were assessed with different MRI techniques by two experienced radiologists :
- first, they used images of the spine and pelvis MRI (T1 and STIR),
- then they looked at the whole body with diffusion weighted imaging but without ADC,
- and finally they interpreted the whole body with diffusion and ADC.
Results: DWI-MRI showed 50 more FL than SP-MRI, including 8 sequelae lesions identified by ADC. Diffusion identified 2 extra medullary lesions. BI was upstaged for 8 patients, and down staged for 3 patients with diffusion sequence and ADC.

The clinical follow up showed that for one patient, WB-MRI allowed to perform preventive femoral nailing on a bone lesion with cortical rupture. Three patients wouldn't have been treated without the discovery of bone lesions on MRI.
Discussion/Conclusion: DWI-MRI increases the number of visible lesions and therefore the sensitivity of WB-MRI compared to SP-MRI. ADC improves the specificity of the technique to distinguish non-active lesions.
References:
Hillengass et al. Challenges and opportunities of novel imaging techniques in monoclonal plasma cell disorders: imaging "early myeloma". Leuk Lymphoma. 2013 Jan 28.
Walker RC et al. Imaging of multiple myeloma and related plasma cell dyscrasias. J Nucl Med. 2012 Jul;53(7):1091-101.
Bäuerle T et al. Multiple myeloma and monoclonal gammopathy of undetermined significance: importance of whole-body versus spinal MR imaging. Radiology. 2009 Aug;252(2):477-85.
Durie BG. The role of anatomic and functional staging in myeloma: description of Durie/Salmon plus staging system. Eur J Cancer. 2006 Jul;42(11):1539-43.

548

Registration of T2, DWI and DCE to a normalized space for the automated analysis and structured reporting in breast MR examinations

M. Medina[1], **A. Alberich-Bayarri**[2], R. Sanz-Requena[2], L. Martí-Bonmatí[2], V. Naranjo-Ornedo[3]
[1]Telecommunications Engineering, Polytechnics University of Valencia, Valencia/SPAIN, [2]Radiology, Hospital Quiron Valencia, Valencia/SPAIN, [3]Telecommunications, Polytechnic University of Valencia, VALENCIA/SPAIN

Purpose/Introduction:
Nowadays, the MR breast acquisitions for tumors diagnosis and characterization require a huge amount of images, mainly consisting of the high temporal resolution perfusion, multiple b-values diffusion and anatomical – T2 sequences. As a consequence, the multivariate analysis including all the data and its integration in structured reports becomes intricate.
Our purpose was to develop a new image preparation methodology in order to build a spatially registered domain for all the techniques and ease the breast cancer structured report generation.
Subjects and Methods:
All the methods were developed in MATLAB r2012a (Mathworks Inc, Natick, USA). An initial segmentation was performed to the breast images by applying an automated Otsu's thresholding algorithm to the T2 images, a 3D mask of the breasts was then generated. Then, the T2, diffusion weighted (DW) and dynamic contrast enhanced (DCE) images were semi-automatically registered to a common space structured by regions (figure1). The method consisted in an automatic superimposition of the dividing lines of the breast on T2, DW and DCE images. After the fitting, the coordinates transformation was calculated for each sequence and were considered an input to the different post-processing DW and DCE pipelines, which consisted of intra-voxel incoherent motions (IVIM) modeling and pharmacokinetics (PKM) modeling of the signals, respectively.

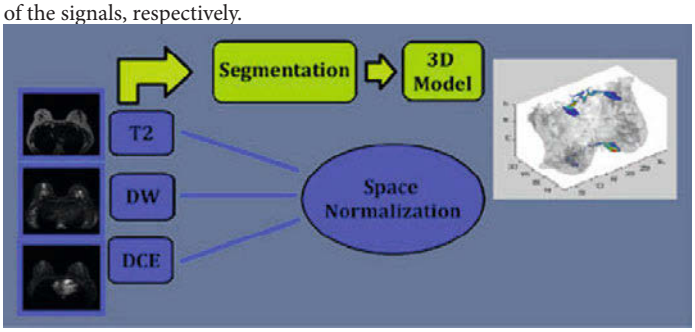

Results:
The method has been preliminary evaluated in 5 patients and the images from T2, DW and DCE acquisitions were properly registered in all cases. The DW and DCE post-processing pipelines were optimized with this information in terms of time and relevancy of the information generated.
Discussion/Conclusion: Developed methodology permits the multivariate processing of breast MR acquisitions in a common space for the extraction of imaging biomarkers from diffusion and perfusion acquisitions.
Furthermore, the registration to a common structured space permits the automated integration of the imaging biomarkers results with the routines for structured reports generation in imaging biomarkers.
References:
[1] Otsu N (1979). A threshold selection method from gray-level histograms. IEEE Trans. Sys., Man., Cyber. 9 (1): 62–66.

549

Registration of T2, DWI and DCE to a normalized space for the automated analysis and structured reporting in prostate MR examinations

J. Gavara[1], **A. Alberich-Bayarri**[2], R. Sanz-Requena[2], L. Martí-Bonmatí[2], V. Naranjo-Ornedo[2]
[1]Telecommunications Engineering, Polytechnics University of Valencia, Valencia/SPAIN, [2]Radiology, Hospital Quiron Valencia, Valencia/SPAIN

Purpose/Introduction:
Today, the MR prostate acquisition for the diagnosis and characterization of carcinoma consists primarily of T2, high temporal resolution perfusion and multiple b-values diffusion sequences. However, the spatial registration of the prostate among sequences is not straigthforward and as a result, the segmentation and multivariate analysis integration in structured reports integrating all imaging biomarkers becomes intricate.
Our objective was to develop a new image processing methodology to spatially register all the images in a structured region and ease the multivariate analysis process.
Subjects and Methods: All the methods were developed in MATLAB r2012a (Mathworks Inc, Natick, USA). A semi-automatic Bezier segmentation was initially applied to T2 images in order to obtain a 3D binary mask of the prostate. Then, the T2, diffusion weighted (DW) and dynamic contrast enhanced (DCE) images were semi-automatically registered, through an automatic superimposition of the diving lines on the prostate T2, DW and DCE images, in a common space structured by regions recommended by the European Society of Urology for the prostate diagnosis PI-RADS. After the alignment, the coordinates transformation was calculated for each sequence and were considered an input to the different post-processing DW and DCE pipelines, which consisted of intra-voxel incoherent motions (IVIM) modeling and pharmacokinetics (PKM) modeling of the signals, respectively.
Results:
The method has been preliminary evaluated in 5 patients and the images from T2, DW and DCE acquisitions were correctlly registered in all cases. The DW and DCE post-processing pipelines were optimized with this information in terms of time and relevancy of the information generated.
Discussion/Conclusion:
Developed methodology permits the multivariate processing of prostate MR acquisitions in a common space for the extraction of imaging biomarkers from diffusion and perfusion acquisitions.
Furthermore, the registration to a common structured space permits the automated integration of the imaging biomarkers results with the routines for structured reports generation in imaging biomarkers.

References:
[1] Pierre E. Bézier, The First Years of CAD/CAM and the UNISURF CAD System, in Fundamental Developments of Computer-Aided Geometric Modeling, edited by Les Piegl, Academic Press, 1993, pp. 13-26.

550

MRI of anterior cruciate ligament tears and associated findings with tibial plateau fractures

N.S. Fedorova[1], V. Fokin[2], G. Trufanov[2]
[1]Radiology, Military Academy, Saint Petersburg/RUSSIAN FEDERATION, [2]Radiology, Medical Military Academy, Saint-Petersburg/RUSSIAN FEDERATION

Purpose/Introduction: The objective of our study was to evaluate the MRI characteristics of anterior cruciate ligament (ACL) tears and associated findings relative to tibial piateau fractures.
Subjects and Methods: Ninety eight patients with tibial plateau fractures associated with ACL tears (partial tear and sprain, or complete tear) were examined (age range: 22 to 73 years old). Patients were grouped according to Schatzker classification, the type of ACL tear.
Results: Among tibial condyles fractures ACL tears were more common in III type (n=37; 37,8%) – ACL was damaged in 25 cases, 13 – complete tears, 12 – partial tears ($p < 0,05$). V type (n=26; 26,5%) – ACL complete tears were examined in 8 patients, partial – 7 ($p<0,05$). I type (n=8; 8,1%) – ACL complete tears were examined in 2 patients. II type (n=6; 6,1%) – ACL tears had 4 (2%) patients, 3 of them had complete tears, 1 – partial tears. IV type (n=12; 12,2%) – 6 case of ACL partial tear ($p=0,05$). VI (n=9; 9,3%) – ACL complete tears in 5 cases. All MRI results were confirmed by arthroscopy.
Discussion/Conclusion: ACL tears in patients with tibial condyles fractures are seen more often in III and VI types of fractures, according to Schatzker classification. There is the logical dependence of the ACL tears of the types of tibial plateau fractures.
References:

- Markhardt B, Gross J, Monu J. Schatzker Classification of Tibial Plateau Fractures: Use of CT and MR Imaging Improves Assessment1. Radiographics. 2009;29 (2): 585-597.
- Gardner MJ, Geller D, Suk M, et al. The incidence of soft tissue injury in operative tibial plateau fractures: a magnetic resonance imaging analysis of 103 patients. J Orthop Trauma 2005;19(2):79–84.
- Crawford R, Walley G, Bridgman S, Maffulli N. Magnetic resonance imaging versus arthroscopy in the diagnosis of knee pathology, concentrating on meniscal lesions and ACL tears: a systematic review. Br Med Bull 2007;84:5–23.
- Mui LW, Engelsohn E, Umans H. Comparison of CT and MRI in patients with tibial plateau fracture: can CT findings predict ligament tear or meniscal injury? Skeletal Radiol 2007;36(2):145–151.
- Yacoubian SV, Nevins RT, Sallis JG, Potter HG, Lorich DG. Impact of MRI on treatment plan and fracture classification of tibial plateau fractures. J Orthop Trauma 2002;16(9):632–637.
- Schatzker J, McBroom R, Bruce D. The tibial plateau fracture: the Toronto experience, 1968–1975. Clin Orthop Relat Res 1979;138:94–104.
- Schatzker J. Compression in the surgical treatment of fractures of the tibia. Clin Orthop Relat Res 1974;105:220–239.

551

T2, DWI, ADC and DCE in the diagnosis of prostate cancer and exclusion of local relapse after prostatectomy

G. Hagverdiyeva[1], E. Sanay[2], V. Panov[1], I. Tyurin[1], V. Matveev[2], B. Kamolov[2]
[1]radiology, Russian cancer research center named after N.N. Blokchin, Moscow/RUSSIAN FEDERATION, [2]Urological, Russian Cancer Research Center named after NN Blohin, Moscow/RUSSIAN FEDERATION

Purpose/Introduction: To evaluate the role of multiparametric MRI (T2, DWI, ADC and DCE) without NMR-spectroscopy in prostate biopsy, as a means of exclusion of local relapse after radical prostatectomy in patients suitable for salvage radiotherapy, and to compare MRI findings with postoperative prostate pathology.
Subjects and Methods: Prostate T2WI, DWI with ADC, and dynamic contrast enhanced (DCE) T1WI were obtained on Magnetom Espree 1.5T, Magnetom Skyra 3.0T and Magnetom Verio 3.0T in patients before prostate biopsy (1 group), before radical treatment (2 group), and before salvage radiotherapy after radical prostatectomy (3 group).
Results: Multiparametric MRI (mpMRI) was done in 30 patients before prostate biopsy. In 25 of them suspicious areas were found. 19 patients with suspicious areas on mpMRI had biopsies and 8 cases (42%) were positive. 12 of them (63%) had previous biopsies. The range of previous biopsies was one to three. The median number of biopsy cores was 9 in both positive and negative biopsy groups. The median number of cores from suspicious areas was 4 and 5 in the 2 groups respectively.
Just 5 (18%) of 28 suspicious areas in the transitional zone were positive on biopsy whereas 3 (30%) of 10 suspicious peripheral zone lesions were positive. In all 11 patients with biopsy confirmed PC before prostatectomy suspicious lesions were identified by mpMRI. DCET1WI was not specific in 1 patient. Median age of htese patients was 55 years, median PSA 12,8 ng/ml and median prostate volume 44,5 cm3.
mpMRI was done in 41 patient with biochemical relapse after radical prostatectomy. Median PSA in this group of patients was 0.58 ng/ml, median age 62 years, and median time from prostatectomy 583 days. Local recurrence was diagnosed in 27 patients with subsequent salvage radiotherapy and PSA decline.
Discussion/Conclusion: Multiparametric MRI followed by TRUS-guided biopsy is comparable to saturation biopsy [1] in precision of prostate cancer detection but requires significantly less biopsy cores. The specificity of mpMRI is low, especially in central lesions where benign hyperplasia is common. Its sensitivity in detection of clinically significant prostate cancer is high. Different methods of mpMRI seem to be complimentary in the detection of prostate cancer. mpMRI also has role in exclusion of local relapse before salvage radiotherapy after radical prostatectomy.
References:

1. Walz J, Graefen M, Chun FK, et al. High incidence of prostate cancer detected by saturation biopsy after previous negative biopsy series. Eur Urol 2006 Sep:50(3):498-505.

EPOS™ Poster

Clinical neuro MRI

552

Influences in regional homogeneity of parieto-temporal regions in remitted first-episode, medication-naïve and late-onset panic disorder patients

C.-H. Lai[1], Y.-T. Wu[2]
[1]*Department of Psychiatry, Cheng Hsin General Hospital, Taipei/TAIWAN,* [2]*Department of Biomedical Imaging and Radiological Sciences,, National Yang-Ming University, Taipei/TAIWAN*

Purpose/Introduction: This study was aimed to focus on the treatment effects of antidepressant for regional homogeneity (ReHo), an indicator of synchronization of brain function, in panic disorder patients.
Subjects and Methods: Twenty-one remitted PD patients with a 6-week escitalopram treatment, who were compared to twenty-one healthy controls within 6 weeks. Patients and controls all received 3-Tesla magnetic resonance imaging scanning at baseline and 6th week. We utilized REST (Resting State FMRI Data Analysis Toolkit, version 1.4) to calculate regional homogeneity (ReHo) in the two groups at baseline and 6 weeks. We compared ReHo of patients and controls at baseline and 6th week to estimate the differences of ReHo in remitted patient group and time-related effects in controls by paired t test. ReHo outputs of remitted patients and controls were compared by independent t test.
Results: Remitted PD patients had increases of ReHo in right Heschl gyrus (superior temporal lobe) and decreases of ReHo in right angular gyrus (parietal lobe). The improvements of severity of panic symptoms have been negatively correlated with changes of ReHo in right superior parietal lobe. However, remitted patients still had lower ReHo in right Heschl gyrus and left thalamus when compared to controls.
Discussion/Conclusion: Changes in ReHo of temporo-parietal regions might represent state-dependent brain changes of remission in panic disorder. Residual alterations of ReHo in temporo-thalamic regions might represent trait-like brain changes of panic disorder.
References:
Asami, T., Yamasue, H., Hayano, F., Nakamura, M., Uehara, K., Otsuka, T., Roppongi, T., Nihashi, N., Inoue, T., Hirayasu, Y., 2009. Sexually dimorphic gray matter volume reduction in patients with panic disorder. Psychiatry Res 173, 128-134.
Boshuisen, M.L., Ter Horst, G.J., Paans, A.M., Reinders, A.A., den Boer, J.A., 2002. rCBF differences between panic disorder patients and control subjects during anticipatory anxiety and rest. Biol Psychiatry 52, 126-135.
Brunoni, A.R., Lopes, M., Fregni, F., 2008. A systematic review and meta-analysis of clinical studies on major depression and BDNF levels: implications for the role of neuroplasticity in depression. Int J Neuropsychopharmacol 11, 1169-1180.

553

WITHDRAWN

554

Longitudinal white matter changes of remitted first-episode medication-naïve panic disorder patients after antidepressant treatment

C.-H. Lai[1], Y.-T. Wu[2]
[1]*Department of Psychiatry, Cheng Hsin General Hospital, Taipei/TAIWAN,* [2]*Department of Biomedical Imaging and Radiological Sciences,, National Yang-Ming University, Taipei/TAIWAN*

Purpose/Introduction: We designed this study to investigate neural correlates of WM microintegrity after remission of panic symptoms in patients with first-episode, medication-naïve and very late-onset PD.We designed this study to investigate neural correlates of WM microintegrity after remission of panic symptoms in patients with first-episode, medication-naïve and very late-onset panic disorder.
Subjects and Methods: Twenty-one patients completed treatment course with remission under escitalopram dose range around 5-15 mg/d. Twenty-one healthy controls were also enrolled into this study. Patients and controls all received 3-Tesla magnetic resonance imaging diffusion tensor imaging scanning at baseline and 6th week. We utilized FDT (FMRIB's Diffusion Toolbox v2.0) function of FSL (FMRIB Software Library) to calculate fractional anisotropy (FA). We compared FA of patients and controls at baseline and 6th week to estimate the differences of FA after treatment with remission in patient group and time-related effects in controls. FA outputs of remitted patients and controls were compared by independent t test.
Results: We found increased FA in specific areas of right uncinate fasciculi and left FOF after remission in patient group (corrected $p < 0.05$). Reduced FA of different regions of right UF was still observed in remitted patients when they were compared to the control group.
Discussion/Conclusion: Subtle changes of WM microintegrity after remission might represent neural correlates of a treatment effect in first-episode, medication-naïve and very late-onset panic disorder.
References:
Alexopoulos, G.S., Glatt, C.E., Hoptman, M.J., Kanellopoulos, D., Murphy, C.F., Kelly, R.E., Jr., Morimoto, S.S., Lim, K.O., Gunning, F.M., 2010. BDNF val66met polymorphism, white matter abnormalities and remission of geriatric depression. J Affect Disord 125, 262-268.
Alexopoulos, G.S., Murphy, C.F., Gunning-Dixon, F.M., Glatt, C.E., Latoussakis, V., Kelly, R.E., Jr., Kanellopoulos, D., Klimstra, S., Lim, K.O., Young, R.C., Hoptman, M.J., 2009. Serotonin transporter polymorphisms, microstructural white matter abnormalities and remission of geriatric depression. J Affect Disord 119, 132-141.
Allaman, I., Fiumelli, H., Magistretti, P.J., Martin, J.L., 2011. Fluoxetine regulates the expression of neurotrophic/growth factors and glucose metabolism in astrocytes. Psychopharmacology (Berl) 216, 75-84.

555

Characteristics hippocampus under case of the asymmetry of the temporal horns of the lateral ventricles

N.V. Gunicheva
radiology, Krasnoyarsk medical university, Krasnoyarsk/RUSSIAN FEDERATION

Purpose/Introduction:
The purpose was to clarify the characteristics of the hippocampi on the native MRI and the diffusion-weighted MRI (DWI) in the asymmetry of the temporal horns (TH) of the lateral ventricles (LV).
Subjects and Methods: The results were obtained with MRI Brivo-355 (GE USA), 1.5 T. Group of studies consisted from 9 patients aged 17 to 61 years (mean age 43 years) with asymmetry of the TH of the LV. That was found by

the native MRI. Of the group of studies excluded patients with asymmetric TH, as result of the scar changes.
Were analyzed the native MRI and DWI obtained in the axial plane at the level of the hippocampuses. Characteristics of the hippocampuses were estimated at the T1-weighted images (T1WI), T2-weighted images (T2WI) and DWI. Maps of the apparent diffusion coefficients (ADC) were studied too. Determination of ADC was made on both sides in the hippocampi.
Results:
The expansion TH of the rights LV was found in seven (77.8%) наблюдениях, the TH of the left LV - in two (22.2%). Changes signal›s in the hippocampuses as foci of the intensive signal on the T2WI defined in the eight (88.9%) cases. Reduction size of the hippocampuses was observed in the three (33.3%) patients.
Absolute values ADC of all patients studied were within age norm. In all cases distribution of absolute values of the ADC the hippocampuses were an asymmetric.
The relative increase of the ADC in the hippocampus on side extension of the TH of the LV detected in eight (88.9%) observations, decrease - in one (11.1%). In cases where was fixed the relative increase in the values of ADC difference between the maximum values ADC of each side was 5% to 61%, average - 22.75%. In case decrease the ADC this difference was 11%.
Discussion/Conclusion: Asymmetry of the TH of the LV of the brain in the native MRI in most cases accompanied signal changes in the hippocampus. ADC adds diagnostic information and may have of prognostic value.
References:
1. Förster A., Griebe M., Gass A., Kern R., Hennerici M.G., Szabo K. (2012) Diffusion-Weighted Imaging for the Differential Diagnosis of Disorders Affecting the Hippocampus. Cerebrovasc Dis 33: 104–115.
2. Mascalchi M, Filippi M, Floris R, Fonda C, Gasparotti R, Villari N. (2005) Diffusion-weighted MR of the brain: methodology and clinical application. Radiol Med 109(3):155-97.

556

Longitudinal gray matter changes of responding fresh major depressive disorder patients under aripiprazole monotherapy

C.-H. Lai[1, 2], Y.-T. Wu[1]
[1]Department of Biomedical Imaging and Radiological Sciences,, National Yang-Ming University, Taipei/TAIWAN, [2]Department of Psychiatry, Cheng Hsin General Hospital, Taipei/TAIWAN

Purpose/Introduction: We investigated the treatment efficacy of aripiprazole monotherapy on first-episode medication-naïve major depressive disorder patients (MDD) in this study. The accompanying gray matter volume (GMV) changes were also observed.
Subjects and Methods: Nineteen patients received aripiprazole monotherapy for treatment of MDD symptoms and clinical rating scales for MDD. Fifteen patients completed the trails and they all received 3-Tesla magnetic resonance imaging structural scans at baseline and remitted state at 6th week. To account for the inter-scanner bias, twenty-seven healthy controls were also scanned twice within 6 weeks. We utilized optimized voxel-based morphometry with global brain volume, age, and gender as covariates. We also estimated the correlation between improvements of MDD symptoms and changes in total gray matter volumes.
Results: The clinical responses after aripiprazole monotherapy were observed. MDD patients had higher GMV in the left middle frontal gyrus and left superior parietal gyrus at remitted status. Besides, they had lower GMV in the right orbitofrontal gyrus and right inferior temporal gyrus after remission. A positive correlation between improvements of MDD symptoms and changes in total gray matter volumes were observed. Remitted MDD patients still had residual GMV deficits in right superior frontal gyrus.
Discussion/Conclusion: Fronto-parieto-temporal GMV changes and residual superior frontal gyrus might represent "state-dependent brain changes" "trait-like brain changes" respectively for aripiprzole treatment for MDD.
References:
Ballmaier, M., Toga, A.W., Blanton, R.E., Sowell, E.R., Lavretsky, H., Peterson, J., Pham, D., Kumar, A., 2004. Anterior cingulate, gyrus rectus, and orbitofrontal abnormalities in elderly depressed patients: an MRI-based parcellation of the prefrontal cortex. Am J Psychiatry 161, 99-108.
Cheng, M.C., Liao, D.L., Hsiung, C.A., Chen, C.Y., Liao, Y.C., Chen, C.H., 2008. Chronic treatment with aripiprazole induces differential gene expression in the rat frontal cortex. Int J Neuropsychopharmacol 11, 207-216.
Frodl, T., Scheuerecker, J., Albrecht, J., Kleemann, A.M., Muller-Schunk, S., Koutsouleris, N., Moller, H.J., Bruckmann, H., Wiesmann, M., Meisenzahl, E., 2009. Neuronal correlates of emotional processing in patients with major depression. World J Biol Psychiatry 10, 202-208.
Lai, C.H., Hsu, Y.Y., 2011. A subtle grey-matter increase in first-episode, drug-naive major depressive disorder with panic disorder after 6 weeks‘ duloxetine therapy. Int J Neuropsychopharmacol 14, 225-235.
Lai, C.H., Hsu, Y.Y., Wu, Y.T., 2010. First episode drug-naive major depressive disorder with panic disorder: gray matter deficits in limbic and default network structures. Eur Neuropsychopharmacol 20, 676-682.

557

New Generation Biomarkers for characterization of Focal cortical Dysplasias on Diffusion tensor Imaging

R.S. Vadapalli[1], A.S. Vadapalli[2]
[1]Department of MR imaging, Vijaya diagnostics and research, Hyderabad AP India/INDIA, [2]Department of Pathology, AFMC armed forces medical college, Pune/INDIA

Purpose/Introduction: Purpose
To evaluate the role of new generation Diffusion tensor imaging Biomarkers for characterization of Focal cortical dysplasias, especially the Radial (perpendicular)Diffusivity(λ2+ λ3);λ3 maps , Radial diffusivity:FA ratio by depicting the microstructural patterns.
Subjects and Methods: fifty six patients in age group of 6 -38 years with M: F ratio of 3:2 with refractory epilepsy had undergone a MRI study on a 3T MRI(achieva Philips) TLE+ETLE protocol (T2 relaxometry, volumetry and MRS of Hippocampi with MRS,3D T1,3D T2 followed by a Medium to high resolution DTI(diffusion Tensor Imaging) with following parameters. Axial Plane B value: 1000 Number of directions 15 ,TR 6248 TE 60 Slice thickness 2mm with 0.5 inter slice gap,NSA 2,Matrix 112x112 bandwidth 29.8 .These data were post processed.using Fibertrack and Intrasense (Myrian) SW to generate FA maps, Eigen vector Maps λ 1,2 ,3 Radial diffusivity maps with ROI and mirror ROI in contralateral side. Areas of Focal cortical dysplasia were mapped and analysed.
Results: Qualitative biomarkers like asymmetry,Fiber architecture in region of dysplasia and Quantitative Parameters like FA, Mean Diffusivity,Fiber density count were studied.
Type 1B FCD(n=11)
1.reduced FA
2. Increased MD
3.Mean value of Radial Diffusivity(Perpendicular Diffusivity) Increased
4.Fiber architecture appeared normal with Normal fiber density.
5. λ3 is significantly Increased.
Type IIA ,IIB ((n=24).
-reduced FA
- abnormal color coded directionality maps due to disroganized fiber structure in dysplasia(n=24).

-radial or Perpndiclar diffusivity is signficantly Increased with RD :FA ratio of >10.
Type III: showed Ipsilateral MTS(n=26),Bilateral MTS(n=5).
In all the cases of associated FCD with Secondary MTS reduced FA,Increased perpendicular diffusivity and fiber architectural abnormalities are evident
Discussion/Conclusion:
1.FCD Type IB are better seen on Radial Diffusivity maps.
2.Radial diffusivity is Increased in TypeIIB>IIA>IB(p=<.001)
3. λ3 Maps delineate FCD and its extent Better >MD or FA >Conventional MR sequences
4.FA/RD ratio is a specific biomarker of Type II FCD.(p=<.001)
CLINICAL RELEVANCE/APPLICATION
Dysplastic cortex is known to be extending beyond MR visible abnormality and DTI visible subtle White matter abnormaities also extend beyond ,hence these Biomarkers can map the true extent of FCD.
References:
Diffusion-Tensor MR Imaging and Tractography: Exploring Brain Microstructure and Connectivity
Paolo G. P. Nucifora, MD, PhD et al.
November 2007 Radiology, 245, 367-384
Diffusion tensor imaging of cryptogenic and acquired partial epilepsies Brain (2001) 124(3): 627-636
Characterization of Cerebral White matter using quantitative Magnetic Resonance Imaging Stains. Brain Connectivity :Alexander et.al(2012)

558

Angiographic Diagnosis of Serious Head Injury and drawbacks

S.A. Babu
radiology, narayana hrudayalaya, health, shimoga/INDIA

Purpose/Introduction: to study the Aadiobogic configuration of cerebral vessels, as well as their apparent position in the skull, which are readily altered by changes in the position of the patient's head.
Subjects and Methods: Cerebral angiography is still commonly used for the diagnosis of intracranial hematomas as these hematomas displace the intracranial blood vessels from their expected positions. When the skull is not rotated, the position of the anterior cerebral artery (ACA) is in midline, coinciding with the pineal gland. At 5 rotation, the ACA deviated 9 mm from midline in the direction of rotation, and the pineal body shifted 1 mm. At 10, the ACA deviated 11 mm, with a pineab shift of 2 mm in the direction of rotation. The 15 rotation resulted in an ACA deviation of 16 mm, with a pineal shift of 2.7 mm.
Results: When the skull is not rotated, the position of the anterior cerebral artery (ACA) is in midline, coinciding with the pineal gland. At 5 rotation, the ACA deviated 9 mm from midline in the direction of rotation, and the pineal body shifted 1 mm. At 10 , the ACA deviated 11 mm, with a pineab shift of 2 mm in the direction of rotation. The 15 rotation resulted in an ACA deviation of 16 mm, with a pineal shift of 2.7 mm. The effect of skull rotation on middle meningeal artery (MMA)displacement from 0 to 15#{176} showed the MMA closer to the inner table of the skull. Rotation to the affected side in the modified hyperextended anteroposterior (AP) view was less effective in correcting apparent deviation. Nonrotated radio- graphs demonstrated a medial convexity or pseudoshift (displacement of the MMA from the inner table accompanied by medially directed convexity) in 60% of the skulls in both the transocular portion of the modified hyperextended projection and the convexity of the carotid projection.
Discussion/Conclusion: In the temporal region, the smallest error was seen in the modified Towne projection just superior to the petrous-calvarial junction. The greatest overall error was seen in the area of convexity pseudoshift on the vertebral projection. Difficulties in the interpretation of emergency cerebral angiograms have been discussed as to apparent deviations of standard angiographic landmarks produced by rotation and positioning of the patient's head in the AP position.
References:
Arthur M. Gerber, and Stephen F. Nowak. J Neurosurg 54:53-57, Jul 1986. (Medical College of Ohio at Toledo, Toledo, Ohio 43699)

EPOS™ Poster

Contrast agents

559

19F-oximetry with semifluorinated alkanes

S. Kegel[1], C. Tsagogiorgas[2], B. Theisinger[3], G. Glatting[1], L.R. Schad[4]
[1]Medical Radiation Physics/Radiation Protection, Faculty of Medicine Mannheim University of Heidelberg, Mannheim/GERMANY, [2]Department of Anaesthesiology and Surgical Intensive Care Medicine, University Medical Centre Mannheim, Mannheim/GERMANY, [3]Research & Development, Novaliq GmbH, Heidelberg/GERMANY, [4]Computer Assisted Clinical Medicine, Faculty of Medicine Mannheim University of Heidelberg, Mannheim/GERMANY

Introduction: The efficacy of cancer therapy, e.g. radiotherapy or chemotherapy, could be improved by considering oxygen partial pressure (pO2). The ideal technique for assessing oxygen tension in vivo is not or minimally invasive and indicates the temporal and spatial heterogeneity of the oxygenation. 19F has an MR sensitivity comparable to hydrogen, is 100% naturally abundant, and allows in vivo measurements without the interference of any background signal. Since a linear correlation between pO2 and the relaxation rate of the longitudinal relaxation for fluorine compounds has already been described and used for imaging [1], this work demonstrates a similar feasibility for semifluorinated alkanes (SFA) as reporter probe of tissue oxygenation. The linear correlation between R1(=1/T1) and pO2 has already been confirmed [2] for SFA. Contrary to other fluorine compounds, SFA are amphiphilic and can carry lipoproteins and lipid based drugs. Emulsions of SFA show long term stability and low Ostwald ripening [3].
Cases: The correlation of T1 and pO2 of perfluorohexyloctane (C14F13H17, „F6H8“) provided by Novaliq (Heidelberg, Germany) was calibrated [2] using a Bruker 9.4 T animal scanner (Bruker, Ettlingen, Germany) and a lab-built 1H/19F volume resonator. Samples (1 ml) of F6H8 were bubbled with mixtures of air and oxygen in an Eppendorf vial. 19F T1-maps were obtained using a RARE sequence (FOV 3,2x3,2 cm^2; 0,5x0,5x2mm^3, 7 measurements with TR100...5500ms in 4:36min). Only the single signal of the CF3-group in the molecule was detected (bandwidth 16kHz) and used for imaging [4]. Accordingly, each pixel in T1 with a standard deviation higher than 20% was dismissed. Oxygen tension maps have been calculated from measured T1-maps by calibration curves as mentioned above.
Figure 1 shows T1 map for 21%-O2 measured with F6H8. The relation between pO2 [mmHg] and T1 [s] is given by [pO2=855mmHg·s·(1/T1)-802mmHg]. pO2 maps for each oxygen level have been calculated (Figure 2).

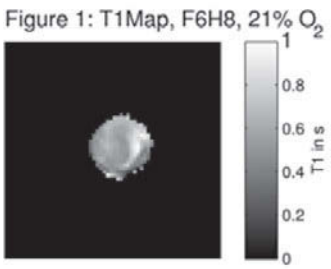

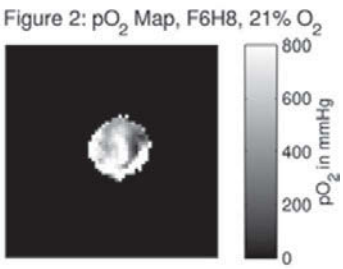

Discussion:
The aim of this study was to explore the suitability of SFA for oxygen mapping. Monitoring the distribution of oxygen partial pressure with this method showed consistent values, evidencing the feasibility of semifluorinated alkanes for 19F-oximetry.

References:
[1] Mignion, L. et al. Magn Reson Med. 2012; 69(1): 248-254
[2] Kegel, S. et al. 43. Jahrestagung der DGMP 2012, P91
[3] Meinert, H. et al. Biomat., Artif. Cells & Immob Biotech 1993, 21, 583-595
[4] Giraudeau, C. et al. Magn Reson Med. 2010; 63(4): 1119-1124

560

A New Multimodal Platform of Nanodiamond for Molecular Imaging

S. Laurent[1], S. Montante[1], L. Vander Elst[1], R.N. Muller[1, 2]
[1]General, Organic and Biomedical Chemistry, NMR and Imaging Molecular Laboratory, University of Mons, Mons/BELGIUM, [2]Center for Microscopy and Molecular Imging, CMMI, Gosseies/BELGIUM

Purpose/Introduction: Nanoparticles are currently the subject of active researches in the context of medical imaging because of their nanoscale size and their intrinsic properties differing from those of conventional materials. The possibilities of applications are numerous and the versatility of these nanoparticles allows their modulations to serve as imaging probes (diagnostic), drug-delivery vectors (therapeutic) or both (theranostic).
The main objective of this work is to develop and characterize an effective multimodal nanodiamond-based probe for medical imaging and specific of apoptosis. The functionalization of the platform involves the grafting of an apoptosis-specific vector (TLVSSL peptide), an optical agent (fluorescein trifluoroacetate or methyl violet) and a paramagnetic complex.

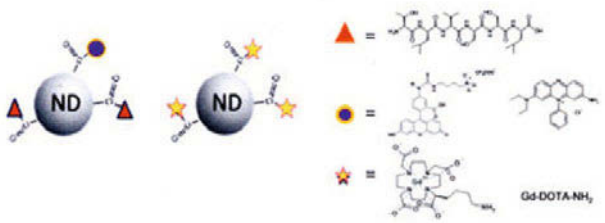

Subjects and Methods: The nanodiamond suspension was purchased from NanoCarbon Research Institute (Japan). All chemical compounds were purchased from Sigma-Aldrich (Belgium) and used as received.
Results: The first part of this work consisted in the characterization of the platform based on nanodiamond powder with size (DLS, TEM and XRD), morphology (SEM), stability and physicochemical analysis methods (turbidimetry and FTIR). Then, an oxidation step was performed in order to increase the number of carboxylic groups on the surface of nanoparticles. The analysis of the TEM pictures confirmed that the oxidative treatment induced a size-reduction of nanodiamonds in solution.
The second part concerned the preparations of the specific vector and the paramagnetic gadolinium complex. The synthesis of the peptide was carried out using an automated synthesizer and its structure was confirmed by mass spectrometry and NMR. The DOTA derivative was synthesized starting from N_6-carbobenzyloxy-L-Lysine and cyclen and then complexed with gadolinium chloride to provide the paramagnetic complex. The characterization by relaxometry and NMRD profiles has proved the efficiency of this new complex as T_1 agent.

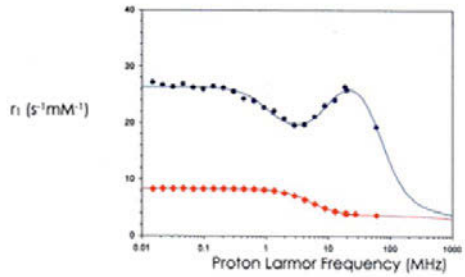

Figure 1 : NMRD profiles of Gd-DOTA-NH_2 (red) and ND-Gd-DOTA-NH_2 (blue)

The last step has been dedicated to the development and characterization of the new multimodal probes. Two samples of oxidized diamond nanoparticles have been reserved for the grafting of the apoptosis-specific vector and one of the optical agents. The coupling of the platform with fluorescein has been demonstrated by fluorescence spectroscopy. Optical microscopy study conducted on cell cultures gave evidence of the efficiency of graftings (peptide and fluorophores). Indeed, the experiments demonstrated the affinity of nanoparticles with Jurkat cells stimulated by anti-Fas. A third sample of oxidized nanoparticles has been reserved for the grafting of the MRI contrast agent previously characterized.

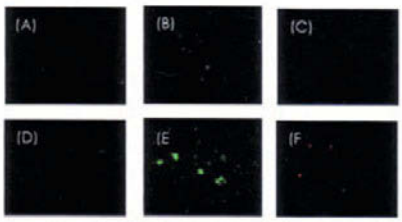

Figure 2: Fluorescence microscopy - Marking of Jurkat cells by functionalized nanodiamonds further incubated for 2 hours in absence (A,B,C) or in presence (D, E, F) of anti-Fas

(A) Non-stimulated by anti-Fas and non-incubated cells with nanodiamonds (= control)
(B) Non-stimulated by anti-Fas and incubated cells with nanodiamonds (+ fluorescein trifluoroacetate)
(C) Non-stimulated by anti-Fas and incubated cells with nanodiamonds (+ methyl violet)
(D) Anti-Fas-stimulated and non-incubated cells with nanodiamonds (= control)
(E) Anti-Fas-stimulated and incubated cells with nanodiamonds (+ fluorescein trifluoroacetate)
(F) Anti-Fas-stimulated and incubated cells with nanodiamonds (+ methyl violet)

Discussion/Conclusion: Results demonstrated clearly the effectiveness of the MRI nanodiamond-based probe for medical imaging.

References:

no reference

561

Polymer-grafted USPIO as Thermosensitive Contrast Agents for MRI

A. Hannecart[1], D. Stanicki[1], L. Vander Elst[1], S. Lecommandoux[2], J. Thévenot[2], C. Bonduel[2], A. Trotier[3], P. Massot[3], S. Miraux[3], O. Sandre[2], R.N. Muller[1,4], S. Laurent[1]

[1]General, Organic and Biomedical Chemistry, NMR and Imaging Molecular Laboratory, University of Mons-Hainaut, Mons/BELGIUM, [2]Laboratory of organic polymer chemistry, Université de Bordeaux 1, Pessac/FRANCE, [3]Magnetic Resonance Center of Biological Systems, Université de Bordeaux 2, Bordeaux/FRANCE, [4]Center for Microscopy and Molecular Imging, CMMI, Gosseies/BELGIUM

Purpose/Introduction:

This study reports the synthesis of thermosensitive polymer-grafted ultrasmall superparamagnetic iron oxide nanoparticles (USPIO) with temperature-dependent magnetic resonance imaging (MRI) signal at low field.

Subjects and Methods: Two thermosensitive polymers characterized by a lower critical solution temperature (LCST) in water, Jeffamine® M-2005 (PEO_5-st-PPO_{37}) and M-2070 (PEO_{46}-st-PPO_{13}), were grafted onto the surface of USPIO by a silanization reaction and a amide-bond coupling.

Results:

The LCSTs of Jeffamine® were measured by a ^{1}H NMR spectroscopic method and are respectively near 25°C and 85°C for the Jeffamine® M-2005 and M-2070, in accordance with the composition of EO *vs.* PO.

USPIO surrounded by a thermosensitive polymer exhibit a temperature-responsive behavior, their surface reversibly changing from hydrophilic below LCST to hydrophobic above it. This phenomenon was use to prove that iron oxide nanoparticle relaxivity is influenced by the hydrophobicity of their surface [1]. Transverse relaxivity (r_2) of the USPIO@PEO_5-st-PPO_{37} core-shell nanoparticles was measured at frequencies 8.25, 20, 60, and 300 MHz and longitudinal relaxivity (r_1) was acquired between 0.01 and 300 MHz at temperatures ranging from 15 to 50°C. A decrease of these relaxivities vs. temperature with an inflection point at the LCST was observed at low field (<60MHz) (Fig. 1).

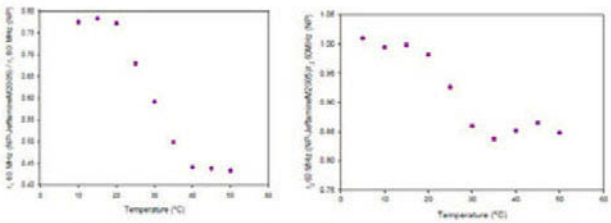

Figure 1. Plots of normalized relaxivities r_1 (A) and r_2 (B) at 60 MHz as a function of temperature

To illustrate the interest of such nanoparticles for their use as smart contrast agents, MR images were realized at low field (8.25 MHz) with either T_1-or T_2-weighted spin echo sequences. USPIO@PEO_5-st-PPO_{37} shows a perfect linearity of the signal with temperature with a change of contrast from negative below the LCST to positive above it with the T_2-weighted sequence (Fig. 2).

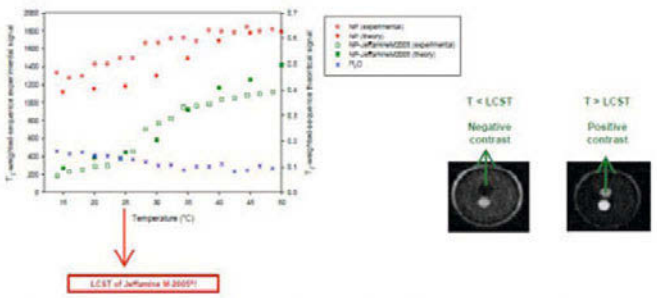

Figure 2. Plot of T_2-weighted sequence MRI signal (8.25 MHz) as a function of temperature

Discussion/Conclusion:

The decrease of relaxivities above the LCST of the thermosensitive polymer-coated USPIO clearly shows the influence of iron oxide nanoparticles surface's hydrophobicity on relaxivity.

Combining a USPIO core with a thermosensitive shell offers the possibility of modulate the MRI contrast with temperature. The perfect linearity of the signal with temperature with a T_2-weighted sequence at low field demonstrated unequivocally the interest of such nanosystems for the design of a temperature responsive contrast agent. For this purpose, it would be necessary to use a thermosensitive polymer with a LCST near 37°C.

References:

[1] S. Pinho et *al.*, 2012, *Phys. Chem. C*, 2285-2291.

562

Comparative examination of magnetic resonance contrast agents on low and high magnetic field

L.I. Lánczi[1], E. Balázs[1], M. Béres[1], G. Tircsó[2], E.L. Berenyi[1]
[1]*Dept. of Biomedical Laboratory and Imaging Science, University of Debrecen, Debrecen/HUNGARY,* [2]*Department of Inorganic and Analytical Chemistry, University of Debrecen, Debrecen/HUNGARY*

Purpose/Introduction:
Magnetic resonance imaging (MRI) is one of the most developing and promising fields of medical imaging. Our research aim is to compare relaxometry properties of MRI contrast media and different solutions on Earth-field and on 1.5T magnetic field.
Subjects and Methods:
Experiments were performed on an Earth-field MRI device and on a 1.5T clinical MRI scanner. Different concentrations of Na, Mn and Gd containing solutions and three types of contrast media (Omniscan, Optimark, Dotarem) were investigated. T1 and T2 relaxation time measurements were performed five times in a row and five times separately as a control on the Earth-field device for each concentration. T1 and T2 mapping were performed on 1.5T. Evaluations were performed using dedicated software packages. Results were summarized into a database.
Results:
Relaxation times of paramagnetic solutions and contrast agents changed according to the concentrations. Relaxation times were correlated on 1.5T magnetic field and on the Earth's magnetic field, but shortening of relaxation times were observed even in lower concentrations on Earth-field . The concentration differences of diamagnetic solutions has no effect on relaxation times. Discrete changes of temperature had no influence on relaxation times.
Discussion/Conclusion:
Paramagnetic solutions (containing Mn and Gd) has effect on relaxation times, specific to the solution's type and concentration. EfNMR measurements were more accurate on low contrast-media concentrations comparing to experiments on 1.5T device. T1 relaxation times were significantly different ($p<0.05$) on low and on high magnetic field of paramagnetic compounds solutions we studied. The presented research can be a forerunner of developing new contrast media and biomarkers that can support new clinical applications on both low and high field MRI.
References:
Packard M, Varian R. Free nuclear induction in the Earth's magnetic field. Phys Rev 1954;93:941.
Eric J. Werner, Ankona Datta, Christoph J. Jocher, and Kenneth N. Raymond: High-Relaxivity MRI Contrast Agents: Where Coordination Chemistry Meets Medical Imaging. Angew. Chem. Int. Ed. 2008, 47, 8568 – 8580
P.T. Callaghan, A. Coy, M.W. Hunter, O.R. Mercier, and J.N. Robinson: New Zealand Developments in Earth's Field NMR. Appl. Magn. Reson. (2007) 32, 63-74
Tircso G, Webber BC, Kucera BE, Young VG, Woods M: Analysis of the conformational behavior and stability of the SAP and TSAP isomers of lanthanide(III) NB-DOTA-type chelates. Inorg Chem. 2011 Sep 5;50(17):7966-79.

563

WITHDRAWN

564

Assembly of modular blocks for molecular imaging

C. Beauvineau, **B.-T. Doan**, G. Chabot, J. Herscovici
UPCGI, UMR8151, U1022, Chimie Paristech, CNRS, Paris/FRANCE

Purpose/Introduction: Advances in personalized medicine require probes development for the early detection of pathology markers. Our goal is to design and synthesize targeted imaging probe for molecular imaging. As MRI presents high contrast but low sensitivity and natural ligands for receptors have low affinity, our proposal is to increase these features using a modular approach by composing a scaffold enabling the connection of various building blocks bearing imaging probes (MRI/scintigraphy, optics) and ligands of choice grafted on polyfunctional molecules like leaflets, dendrimers, liposomes, nanoparticles…[i].
Subjects and Methods: These blocks are constructed by functionalizing a molecular scaffold prepared by a 3-component reaction[i] intended to be grafted on a macromolecular support. A 3-component reaction between a secondary amine (to settlet complexing groups for Gd or Tc salts), an alkyne (to introduce a ligand or a chromophore (Cy5.5)) and a bifunctional aldehyde (to hang a brick on the support) is used. Two types of bricks are generated : one for targeting and one for imaging, with the possibility to graft them on a polymer. We designed and evaluated blocks for tumoral activated endothelium targeting and having two metallic salts complex for the detection (MRI or scintigraphy). We also developed a bimodal MRI and optical NIR probe. Different pools of probes (figure 1) carrying a flavonoid for antitumoral activity were evaluated by relaxometry (0,47T, 4,7T, 7T). These probes have complexed Gd^{3+} and Cu^{2+} resulting from the Huisgen cycloaddition (table1).
Results:

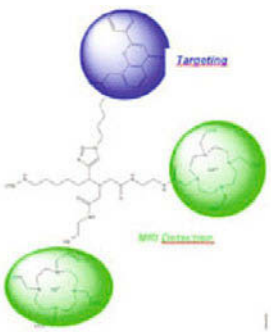

Figure 1 : *Structure of a bifunctional block (Targeting/MRI)*

N° Pool	Complex Gd-DO3A/Gd-DO3A	Complex Gd-DO3A/Cu-DO3A
Pool 1	100 %	0 %
Pool 2	66 %	33 %
Pool 3	50 %	50 %

Table 1 : % of chelated Cu^{2+}

The values of the 7T r1 relaxivity (r1=10mM-1.s-1) of the pool 1 consisted of complex Gd-DO3A/Gd-DO3A are twice bigger than the pool 3 consisted in 50 % by complex Gd-DO3A / Gd-DO3A and in 50 % by complex Gd-DO3A / Cu-DO3A (figure 2). The relaxivity is also interestingly twice the commercial Gd Complex, in agreement with the probably shorter rotational correlation time of the molecule, underlining the utility to couple two complexes of Gd salt on the skeleton to optimize MRI features.
Discussion/Conclusion: These modular blocks should allow to obtain images with better contrast than with the commercial Gd complexes, or to use lower

concentrations of CA, leading to new efficient agents for molecular imaging. Afterwards, the grafting with original ligands from our library (not shown here) will allow us to increase the affinity, the functionalization on polymeric or nanoparticles support to optimize MRI sensitivity with optical imaging features.

References:

[i] M. E. Gindt, *Expert Opin. Drug Deli.*, **2009**.
[ii] N. Gommermann, C, *Angew. Chem. Int. Ed.*, **2003**.

565

Optimisation of pulse sequences and T1/T2 mapping for the detection of a novel multimodal nanoparticle class based on Prussian Blue

N. Kovács[1], M. Babos[2], S. Hóbor[2], I. Horváth[3], K. Szigeti[3], D. Máthé[1]
[1]-, CROmed Ltd., Budapest/HUNGARY, [2]-, Mediso Ltd., Budapest/HUNGARY, [3]Department of Biophysics and Radiation Biology, Semmelweis University, Budapest/HUNGARY

Purpose/Introduction: Our group has recently patented a nanoparticulate contrast agent with bi-modal readout properties. The nanoparticles exhibit paramagnetic properties based on the special ferrous crystal structure of Prussian Blue and can be also labelled with different isotopes.
Characterizing these contrast agents needs the determination of their relaxivity which can be determined from T1 and T2 mapping. According to the determined relaxivity values sequences can be optimised for contrast enhanced imaging.
Subjects and Methods: Prussian blue particles were prepared and diluted to perform the phantom measurements. NanoScan PET/MRI (Mediso Ltd, Hungary) with 1 T permanent field magnet, 500 mT/m gradients and 250 µs rise time was used for imaging.T1 relaxation rates were calculated with two different techniques based on different sequences (snapshot gradient echo with inversion recovery and T1 weighted spin echo) and compared according to the attainable precision and time efficiency. T2 relaxation rates were determined by multiecho spin echo imaging.
Results: For T1 mapping of phantoms snapshot gradient echo was found to be the better technique because of suitability of acquisition time length. T1 relaxivity value were found to be around 1 $mM^{-1}s^{-1}$. According to the calculated relaxivities our Prussian blue based nanoparticles are suitable for contrast enhanced imaging due to their T1 shortening effect. The most appropriate T1 weighted sequence is the gradient echo sequence.
Discussion/Conclusion: The readout of image contrast with MR enables precise anatomical localization of these nanoparticles. Exhibiting T1 contrast enhancement the particles will be well suited to biological readouts. Their complementary isotopic tomography (PET/SPECT) readouts will ensure precise concentration measurements. Using the GRE sequence defined herein, further studies will explore the biological applications in brain trauma and cell tracking.

References:

Surname, Initials, Year, Abbreviated Journal Name, Pages
Máthé D. and Szigeti K., 2012, PCT/HU2012/000010 patent

599

Correlation between DCE-MRI and SPECT: a comparison of two pre-clinical tumour models

K. Bol[1, 2, 3], J.C. Haeck[1, 2, 3], W.M. Van Weerden[4], M.R. Bernsen[2, 3], M. De Jong[2, 3], **J.F. Veenland**[1, 2]
[1]Biomedical Imaging Group Rotterdam, ErasmusMC, Rotterdam/NETHERLANDS, [2]Radiology, Erasmus MC, Rotterdam/NETHERLANDS, [3]Nuclear Medicine, Erasmus MC, Rotterdam/NETHERLANDS, [4]Urology, Erasmus MC, Rotterdam/NETHERLANDS

Purpose/Introduction: This study investigates the relation between radiolabeled peptide uptake imaged with SPECT, and Dynamic Contrast-Enhanced (DCE) MRI derived perfusion parameters, for two pre-clinical tumour models: 1) pancreatic tumours overexpressing somatostatin receptors, 2) prostate tumours overexpressing gastrin-releasing peptide receptors. Both tumour models can be imaged and treated using radiolabeled somatostatin-derived (pancreas) or bombesin-derived (prostate) peptide-analogues [1,2]. Heterogeneous peptide uptake in these tumours has been observed in high-resolution SPECT images. With DCE-MRI, tumour perfusion and vessel permeability influencing this peptide distribution can be studied non-invasively.
Subjects and Methods: Four rats with pancreatic CA20948 tumours and 3 mice with human prostate PC295 carcinoma were used. Rats were injected with the somatostatin-analogue ^{111}In-DTPA-Octreotide (50 MBq), mice received the bombesin-analogue ^{111}In-DOTA-JMV (25MBq). Subsequently SPECT-CT and MRI scans were made. DCE-MRI was registered to SPECT-CT to enable direct spatial correlation. For voxel-based quantification of DCE-MRI data both semi-quantitative analysis and a quantitative analysis method applying the standard Tofts equation were used. Spearman's rank correlation coefficients (ρ) between SPECT and DCE-MRI-derived parameters were calculated over the whole tumour volume.
Results: For all tumours in the pancreatic and prostate datasets, areas with low peptide uptake also showed low values for all DCE-MRI-derived parameters. Comparing the signal-enhancement-over-time curves in DCE-MRI for both datasets, we observed a much slower contrast enhancement for the prostate data: almost no washout was visible. DCE parameters primarily associated with the exchange of contrast between blood vessels and tumour tissue showed mean ρ ranging from 0.46 to 0.56 ($p<0.05$) for the pancreatic data, and from 0.48 to 0.57 ($p<0.05$) for the prostate data (washout excepted). At the same time, DCE parameters primarily associated with the amount of contrast in the tumour showed lower mean ρ, ranging from 0.33 to 0.39 ($p<0.05$) for both datasets.
Discussion/Conclusion: In the correlation between SPECT and DCE-MRI-derived parameters some clear trends can be observed for both pancreatic and prostate data: 1) areas with low parameter values corresponded to low peptide uptake, which could hamper therapeutic efficacy, 2) 'exchange-related' parameters seemed to correlate better with peptide uptake better than 'contrast-amount-related' parameters. Consequently, fast and efficient diffusion over the vessel wall into tumour tissue is an important factor for peptide delivery. As such application of DCE-MRI opens the opportunity to study the effects of vascular characteristics on the peptide delivery and treatment efficacy of radiolabeled peptide-analogues.

References:

[1] F.Forrer, 2007, Best.Pract.Res.Clin.Endocrinol.Metab., 111-129
[2] R.P.J.Schroeder, Elsevier Methods, 2009, 200-204

EPOS™ Poster

Methods for neuroscience

566

A multimodal approach combining EEG, fMRI and DTI for mapping epileptic networks

R. Abreu[1], R.G. Nunes[2], A. Leal[3], P. Figueiredo[1]
[1]Department of Bioengineering, Institute for Systems and Robotics / Instituto Superior Tecnico, Technical University of Lisbon, Lisbon/PORTUGAL, [2]Institute of Biophysics and Biomedical Engineering, Faculty of Sciences, University of Lisbon, Lisbon/PORTUGAL, [3]Centro de Investigação e Intervenção Social (CIS-IUL) and Department of Neurophysiology, Centro Hospitalar Psiquiátrico de Lisboa, Lisboa/PORTUGAL

Purpose/Introduction: Simultaneous EEG-fMRI can be used to map the epileptic focus of patients with refractory focal epilepsy who are candidates for epilepsy surgery. Often, it would also be desirable to map eloquent cortex located in proximity to the epileptic focus, in order to better inform pre-surgical planning. Diffusion tensor imaging (DTI) may provide additional information regarding fiber tracks connecting the regions of interest, but only a few studies have combined DTI with EEG-fMRI so far [1]. Here, we present a case study where we combine DTI fiber tracking with EEG-informed fMRI.

Subjects and Methods: A 32-year old patient with a large left-frontal cortical dysplasia with refractory focal epilepsy was studied on a 3T Siemens Verio MRI scanner, using an MR-compatible 32-channel EEG system (Brain Products). Three 10min resting-state and two 5min finger-tapping motor-task fMRI runs were collected using gradient-echo EPI (TR/TE=2500/62.5 ms, Voxel=3.5×3.5×3.0mm^3). DTI data were acquired using a doubly-refocused EPI sequence (b=1000s/mm^2, 60 directions, Voxel=1.8×1.8×5.2mm^3). Structural images were collected using MPRAGE and DIR sequences.

After standard pre-processing, the EEG was decomposed using ICA in EEGLAB. The root mean square frequency (RMSF) of the ICs corresponding to the activity of interest was computed by time-frequency analysis and used as a regressor for a GLM analysis of the fMRI data using FSL [2]. Standard fMRI analysis was performed for the motor task. For DTI analysis, eddy current correction and probabilistic tractography were performed using FSL [3]. To map the pyramidal fibers pathways, seeding was performed from the primary motor cortex to a target region in the mesencephalon. Fibers crossing to the contralateral hemisphere were excluded.

Results: BOLD changes correlated with the RMSF metric extracted from the EEG were found within the area of cortical dysplasia, consistently with the location of the hypothesized epileptic focus (Fig.1). BOLD changes were found in the left primary motor cortex in association with the right-hand motor task, consistently with the location of the pre-Rolandic gyrus, and non-overlapping with the dysplasia or epileptic focus. The pyramidal tract identified by DTI was also shown not to overlap with the dysplasia (Fig. 2).

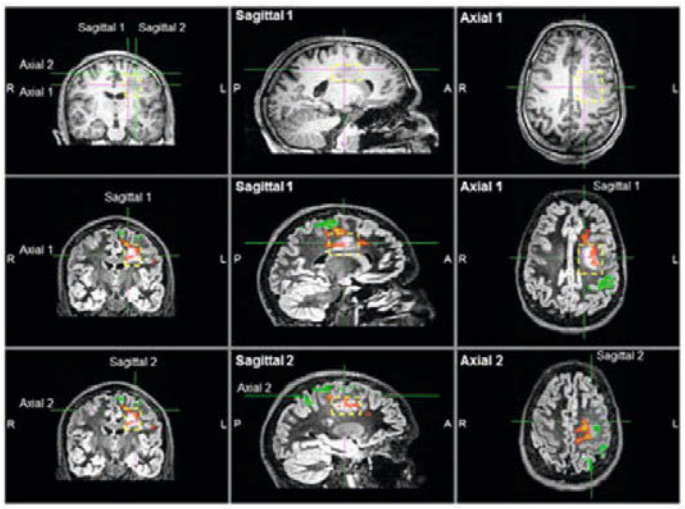

Fig.1: Epileptic focus and motor cortex mapping, in relation to dysplasia. From left to right: (Top Row) coronal, sagittal and axial images acquired using the MPRAGE sequence with the dysplasia roughly inside the yellow dashed square. (Middle Row) The same slices as in (Top Row) using the DIR sequence where the cortical dysplasia is more clearly identified. The brain regions with BOLD changes correlated to the epileptic activity (in red-yellow) and to the motor task (in green) are superimposed. (Bottom Row) The same as in (Middle Row) showing two additional sagittal and axial slices.

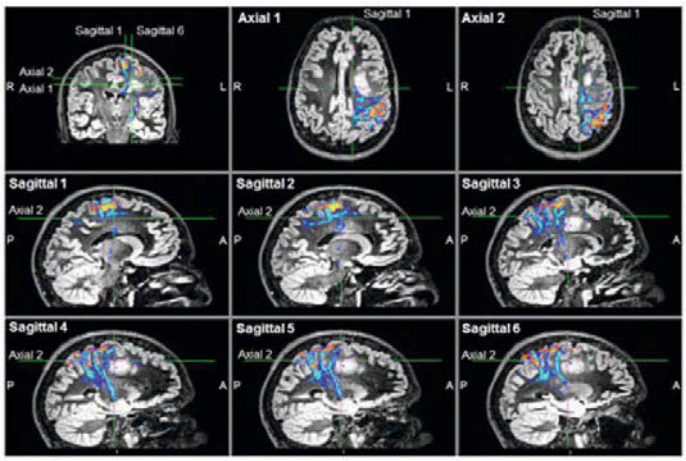

Fig. 2: fMRI motor cortex mapping and DTI pyramidal tract fiber tracking. One coronal, two axial and six sagittal images are shown. The cluster of BOLD changes correlated with the finger-tapping task (red-yellow) shows a consistent location with the pre-Rolandic gyrus, posterior to the dysplasia. The estimated pyramidal tract (blue-light blue) shows the pyramidal fibers most probable pathways, never overlapping with the dysplasia (particularly evident in images Axial 1, Sagittal 2 and Sagittal 6).

Discussion/Conclusion: The combination of EEG-fMRI with DTI allowed mapping the epileptic focus, as well as eloquent motor cortex and associated pyramidal tract, in a patient with frontal cortical dysplasia, with potential impact in pre-surgical evaluation.

References:

[1] Hamandi JNeurolNeurosurgPsychiatry 2008; 79: 594–97
[2] Leite FrontNeur 2013
[3] Behrens MagnResonMed 2003, 50(5):1077-1088.

Acknowledgements:
FCT grants PTDC/SAU-ENB/112294/2009, PEst-OE/EEI/LA0009/2011 and PEst-OE/SAU/UI0645/2011.

567

Reproducibility of the visualization of the rat somatosensory network using Independent Component Analysis in whole-brain fMRI

N. Van Den Berge[1], V. Keereman[1], P. Van Mierlo[1], B. Descamps[1], S. Gutierrez[2], R. Raedt[3], C. Vanhove[1], S. Vandenberghe[1], R. Van Holen[1]
[1]ELIS/MEDISIP-iMinds, Ghent University, Ghent/BELGIUM, [2]MEDISIP, Ghent University, Ghent/BELGIUM, [3]Ghent University Hospital, Laboratory for Clinical and Experimental Neurophysiology, Ghent/BELGIUM

Purpose/Introduction: BOLD fMRI is an imaging technique to investigate neuronal activation. It is well known that non-noxious electrical stimulation of the rat forepaw leads to neuronal activation of the somatosensory network. However, to our knowledge, no neuroimaging studies have been able to visualize the entire rodent somatosensory network, especially the subcortical regions. This is possibly due to the small field-of-view used in most BOLD fMRI studies performed in rodents[1] and a lack of power of the data analysis methods. The reproducibility of these studies has also not been quantified. In the present study a data-driven technique (Independent Component Analysis, ICA) is used to identify the somatosensory network. Our aim is to map cortical and subcortical neuronal responses using ICA in order to obtain a whole-brain BOLD fMRI based template that can be used for future fMRI studies. Therefore we also investigate its spatial within-subject reproducibility.
Subjects and Methods: Three rats (Wistar) were sedated with medetomidine. Electrical stimulation was applied to the right forepaw (amplitude 4mA, pulse duration 3ms, frequency of 9Hz) using a block-design paradigm (20s on/40s off). All MR images were acquired on a Pharmascan 7T (Bruker) using a rat brain surface coil. Each fMRI run consisted of 170 repetitions with TR=2s, TE=18ms, voxel size=0.375mm. For each rat four GE-EPI runs were acquired with 5min of rest between runs. Data were processed with ICA, using the GIFT toolbox in Matlab. Anatomically relevant components were selected based on their spatial localization and temporal profile. Within-subject reproducibility of each component was quantified by calculating the spatial overlap between significantly activated voxels in a single run and the mean (calculated using GIFT).
Results: Significant activation was detected in all components of the somatosensory network (fig.1): contralateral forelimb region of the primary somatosensory cortex, bilateral secondary somatosensory cortex, thalamus, ectorhinal cortex, cerebellum and pons. The within-subject variability of the different components was acceptable (60-80% overlap), except for thalamus and is shown in fig.2.

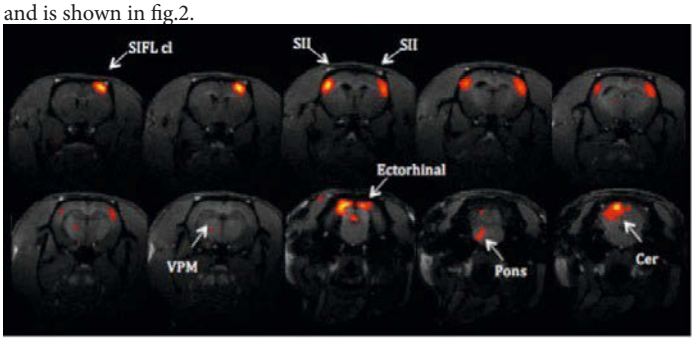

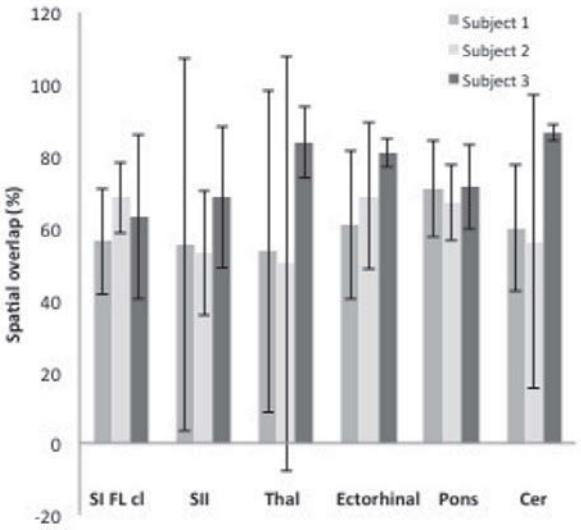

Discussion/Conclusion: To our knowledge, this is the first fMRI study visualizing the entire rat somatosensory network. This can be attributed to the use of ICA, combined with careful positioning and the use of a dedicated rat brain surface coil in order to achieve successful whole-brain coverage. In conclusion, the obtained whole-brain fMRI-based somatosensory map may serve as a template for further fMRI studies. Nonetheless, within-subject variability should be taken into account at interpretation.
References:
[1] Zhao F. et al., 2008, Neuroimage, pp.248-260.

568

A GPU accelerated temporal and spatial ICA pipeline for fMRI data analysis

R.N. Boubela[1, 2], K. Kalcher[1, 2], W. Huf[1, 2], G. Rath[1, 3], E. Moser[1, 2]
[1]MR Centre of Excellence, Medical University of Vienna, Vienna/AUSTRIA, [2]Center for Medical Physics and Biomedical Engineering, Medical University of Vienna, Wien/AUSTRIA, [3]Department of Radiodiagnostics and Nuclear Medicine, Medical University of Vienna, Vienna/AUSTRIA

Purpose/Introduction: Independent component analysis (ICA) has emerged as the tool of choice for exploratory analysis of resting-state fMRI data (Beckmann 2012). Currently spatial
ICA is more widespread than temporal ICA for two reasons. First, the low temporal resolution in a standard fMRI scan makes tICA less stable; second, its computational demands can make tICA harder to use in practice (Calhoun et al. 2001). Recent developments in MR aquistition technique (Feinberg et al. 2010)
allowing for high temporal and spatial resolution, however, enable researchers to decompose resting-state data in temporally independent ICA components (Smith
et al. 2012). Compared to standard TR (>= 2000ms) data, low TR scans are producing up to 10 times more data. To be able to handle this amount of data in group
ICA analyses efficiently there is a need for high performance ICA algorithms. This work aimed at the implementation of a scalable high-performance ICA pipeline
capable of processing large amounts of data in a short amount of time.

Subjects and Methods: The pipeline is implemented in R version 3.0.1 ('Good Sport' R 2013) and is meant to be used on already preprocessed data. The data is prewhitened and reduced
in dimensionality via principal component analysis (PCA), using the R package irlba (Baglama and Reichel 2012) for singular value decomposition (SVD). All matrix
multiplications are performed using the library phiGEMM (Spiga and Girotto 2012), which distributes computation on multiple GPUs. Finally, fastICA (Hyvarinen
1999) is used to compute temporally independent components from these data. All computations were performed on a server with Ubuntu Linux (Version 11.10
'Oneiric Ocelot'), 192GB RAM, 2 Xeon X5690 processors, 4 nvidia Tesla C2070.
Results: A parallelized ICA pipeline in R was implemented, incorporating the analysis tools mentioned above. The pipeline allows to compute temporal ICA even on very
large datasets (e.g., 20 subjects, 20000 time-points, resulting input matrix 35 GB), allowing the analysis of long scan runs as well as time-concatenated group ICA.
As an example, figure 1 shows the motor component that emerged from temporal ICA of 20 subjects along with its power spectrum.

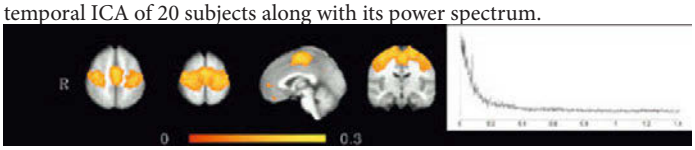

Discussion/Conclusion: The use of advanced computational statistics methods enables fMRI researchers to perform formerly time-consuming or even intractable tasks in short amounts of
time. For once, blind source separation as a goal for resting-state analysis can be undertaken more effectively, but also other tasks such as spatial ICA can profit from the enhanced computational power.

References:

Baglama,J.,Reichel,L.,2012.irlba:FastpartialSVDbyimplicitly-restartedLanczosbidiagonalization.Rpackageversion1.0.2
Beckmann,C.F.,Aug2012.Modellingwithindependentcomponents.Neuroimage62(2),891–901
Calhoun,V.D.,Adali,T.,Pearlson,G.D.,Pekar,J.J.,May2001.Spatialandtemporalindependentcomponentanalysisoffunctional MRIdatacontainingapairoftask-relatedwaveforms.HumBrainMapp13(1),43–53
Feinberg,D.A.,Moeller,S.,Smith,S.M.,Auerbach,E.,Ramanna,S.,Gunther,M.,Glasser,M.F.,Miller,K.L.,Ugurbil,K.,Yacoub,E.,2010.Multiplexedechoplanarimagingforsub-secondwholebrainfMRIandfastdiffusionimaging.PLoSOne5(12),e15710
Hyvärinen,A.,1999.Fastandrobustfixed-pointalgorithmsforindependentcomponentaanalysis.IEEETransactionsonNeuralNetworks10,626–634
RDevelopmentCoreTeam,2013.R:Alanguageandenvironmentforstatisticalcomputing.ISBN3-900051-07-0
Smith,S.M.,Miller,K.L.,Moeller,S.,Xu,J.,Auerbach,E.J.,Woolrich,M.W.,Beckmann,C.F.,Jenkinson,M.,Andersson,J.,Glasser,M.F.,Essen,D.C.V.,Fein-berg,D.A.,Yacoub,E.S.,Ugurbil,K.,Feb2012.Temporally-independentfunctionalmodesofspontaneousbrainactivity.ProcNatlAcadSciUSA109(8),3131–3136
Spiga,F.,Girotto,I.,2012.phiGEMM:aCPU-GPUlibraryforportingQuantumESPRESSOonhybridsystems.In:Parallel,DistributedandNetwork-BasedProcessing(PDP),201220thEuromicroInternationalConferenceon.IEEE,pp.368–375

569

Quantitative R2*-Response of Cortical Gray Matter to Graded Hyperoxia

C. Rossi[1], G. Gotzamanis[1], R. Kocian[2], M. Redle[1], P. Oezbay[1], S. Kollias[3], A. Boss[1], D. Nanz[1]
[1]Institute of Diagnostic and Interventional Radiology, University Hospital Zurich, Zurich/SWITZERLAND, [2]Institute of Anaesthesiology, University Hospital Zurich, Zurich/SWITZERLAND, [3]Medical Imaging, University Hospital Zurich, Zurich/SWITZERLAND

Purpose/Introduction: Mapping of the apparent transverse relaxation rate (R2*) of the MR signal allows monitoring of cerebral tissue oxygenation during hyperoxic respiratory challenge[1]. The quantification of the R2*-response to increased oxygen supply may help in the understanding of oxygen metabolism under pathological conditions[2]. The aim of this study was to quantify the R2*-response of the cortical gray matter to increasing concentrations of inspired oxygen in healthy volunteers.
Subjects and Methods: Four volunteers (mean age 24±2 years old) consented to participate in this IRB-approved prospective study. R2* was quantified by mono-exponential fitting of the MR signal measured at different echo-times, TE, and during breathing of gas mixtures containing increasing levels of oxygen (O2 (%) = 21, 50, 75, 100) with a 3D multi- gradient-echo sequence at 3 Tesla (FA = 50°, TR = 93 ms, TEs = 8, 24, 40, 56, 72, and88 ms, voxel size = 0.5x0.5x1.0 mm^3). End-tidal gas composition was monitored during the challenge using an MRI-compatible breathing system. Local R2* values were assessed in regions-of-interest drawn over the cortical gray matter at each oxygen level of the challenge.
Results: Under normoxia, a mean cortical gray-matter R2* value of 21.1±0.5 s^{-1} was found (Fig. 1). Increasing the oxygen supply resulted in a decrease of the R2* ($R2^*_{50\%}$ = 19.6±1.5s^{-1}, $R2^*_{75\%}$ = 18.4±1.3s^{-1}, $R2^*_{100\%}$ = 18.3±0.7s^{-1}). The highest relative change was obtained at the lowest hyperoxic gas concentration of 50% oxygen vs. room air (ΔR2*/R2*=7.7%). With increasing oxygen level in the breathing gas a saturation level was reached with only minimal changes between 75% and 100% oxygen. Maximum R2*-response was found during breathing of pure oxygen (ΔR2* = 2.8±0.9 s^{-1}).

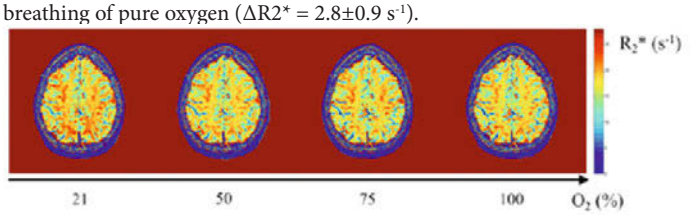

Fig. 1 R2* parametrical maps computed for one volunteer (male, 22 years old) during breathing of gas mixtures containing increasing amount of O_2. The R2*-response to the challenge reflected the graded increase of oxygen supply.
Discussion/Conclusion: These preliminary results show that R2* gradually responds to changes in oxygen supply. As the R2*-response to hyperoxia shows a saturation pattern for O2 concentrations above 75%, lower hyperoxic grade may be applied in clinical studies of tissue oxygenation.

References:

[1]NMR Biomed. 1995;8:41–47.
[2]Curr. Mol. Pharmacol. 2009;2:263–284.

570

White matter atlas for the automated tractography segmentation and its integration in clinical practice

L. Segura-Roda[1], **A. Alberich-Bayarri**[2], G. Garcia-Marti[2], L. Martí-Bonmatí[2], M. Robles[1]
[1]Biomedical Engineering, Polytechnics University of Valencia, Valencia/SPAIN, [2]Radiology, Hospital Quiron Valencia, Valencia/SPAIN

Purpose/Introduction:
Although tractography techniques are currently being implemented in most clinical workflows for the characterization of main fiber bundles by manual segmentation of the regions of interest in neurodegenerative diseases and pre-surgical planning of tumors, there are no established techniques allowing for an automated and reproducible segmentation of white matter (WM) tracts. The purpose of this work was to create a WM atlas from healthy subjects for automatic fibers segmentation and detection of changes in their microstructural properties.
Subjects and Methods:
A total of 50 healthy subjects (22 males and 27 females) were included for the atlas generation. All subjects were paired to age (28±17 vs. 30 ±20 years old, male vs. female, respectively).
MR diffusion tensor imaging (DTI)acquisitions were performed in a 3T system (Achieva TX, Philips Healthcare, The Netherlands) using a 32 channel coil and a standard SE-EPI sequence (TE=60ms; TR=6955ms; b-values: 0, 1000s/mm2) with a spatial resolution of 2x2x2mm3 and 16 gradient directions.
The images of each patient were prepared by applying eddy currents correction and a brain mask extraction using FMRIB Software Library, FSL 5 (Oxford, UK). After the preparation, the FA maps were calculated using FSL's diffusion toolbox.
In order to build the atlas, the anatomical correspondence between the set of images from the different patients was performed by a normalisation using SPM 8 (London, UK). The FA-VBS normalization toobox was applied for acquiring a mean diffusion weighted image and creating both FA and b0 customized templates.

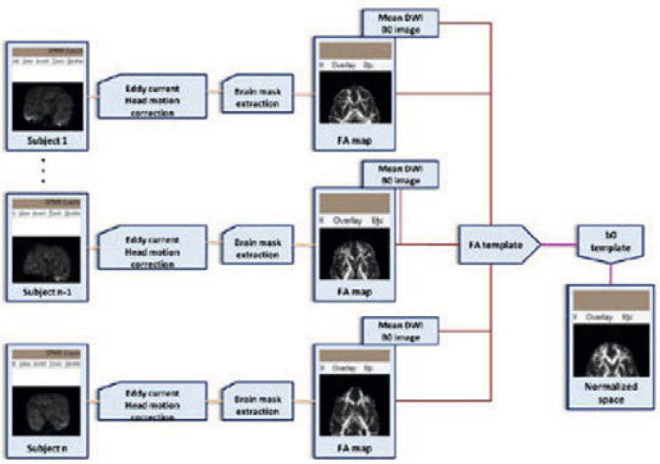

Results:
The atlas was properly created and permits the extraction of WM fibers from a new patient after the normalization of the images to the templates previously created. The preliminary evaluations show an excellent performance of the images in diffuse disease.

Discussion/Conclusion:
The process of WM segmentation in different fiber bundles has been automated by the creation of an atlas to be used in clinical routine. Further evaluations of the atlas with a wide population of patients will permit the determination of the added value if compared to current manual and semi-automatic segmentations.
References:
[1] Mohammadi S, Keller SS, Glauche V, Kugel H, Jansen A, et al. (2012) The Influence of Spatial Registration on Detection of Cerebral Asymmetries Using Voxel-Based Statistics of Fractional Anisotropy Images and TBSS. PLoS ONE 7(6): e36851. doi:10.1371/journal.pone.0036851

571

Assessment of brain connectivity changes related to age in attention task using Network Based Statistics.

P. Bertrand[1], J. Gutierrez[2], H. Gros-Dagnac[2], J.-A. Lotterie[2], I. Berry[1, 3], P. Celsis[1], A.-K. Boulanouar[1]
[1]UMRS 825, INSERM, Toulouse/FRANCE, [2]UMR 825, INSERM, Toulouse/FRANCE, [3]Service Biophysique, University Hospitals, Toulouse/FRANCE

Purpose/Introduction: We used **fMRI** to examine the **age-related functional brain connectivity** when subjects performed a task requiring **attention**. To assess the **connectivity** of all the brain regions, we used the **160 ROI's** taken from Dosenbach et al. (2) which cover all the cognitive and motor abilities. We calculate the correlation of the MRI signals of such ROI's taken 2 by 2. This poses the important issue of multiple comparisons that we solved using approach similar to the Network Based Statistics(3)
Subjects and Methods: 50 male healthy, right handed subjects aged 20 to 65 were included. Images were collected on a 3T Philips Achieva (GE- EPI, TR=2.5s, 2mm isotropic voxel, 128×128x64 voxels).
The attention task was based on visual search and was divided into 2 phases, *phase1* consisted of searching for a Q among O's which is intented to involve the **pop-out** effect(1) and *phase2* consisted of a search of an O among Q's which should be done in a **serial search** manner.
The correlation of each pair of the 160 ROI's was used a connectivity index. We correlated these coefficients to the **age** and we thresholded these correlation coefficients ($p<0.0001$). In order to test for the significance of the obtained network we used a non parametric test by a method similar to the **Network Based Statistics(3)**
Results: Two networks were identified in Pop-out (positive and negative correlations) and two in serial search task. These networks involved mainly posterior occipital areas, frontal areas, mid-insula and left angular gyrus
Discussion/Conclusion: The **Angular Gyrus** is involved in attention task with **positive correlations in 11/20 connections and also in pop-out** This region belongs to the default-mode network but is also known to contribute to the processing of auditory and visual input and in the comprehension of language. In pop-out task, we found the involvement of the **insula** (2/7 connections) but not in the serial search task . Recent work has indicated that the insula may serve in the integration of disparate functional systems involved in sensory-motor processing, the process of affect and general cognition (4). The age-related decrease of the connectivity of this area suggests that there is **a gradual age-related reduction i**n this integration ability.
References:
(1) TREISMAN, A. & GORMICAN, S. 1988. Psychol Rev, 95, 15-48.
(2) DOSENBACH, N. U., et al. 2010. I. Science, 329, 1358-61.
(3) ZALESKY, A., et al. 2010. Neuroimage, 53, 1197-207.
(4) CHANG, L. J., et al. 2013. Cerebral Cortex, 23, 739-749

EPOS™ Poster

MRI methology

572

Visualization of white matter tracts using a non-DWI method: Does intravenous gadolinium injection four hours prior to the examination affect the degree of visualization of white matter tracts?

M. Yamazaki[1], S. Naganawa[1], H. Kawai[1], M. Ikeda[2], K. Bokura[1], H. Isoda[2], T. Nakashima[3]
[1]Department of Radiology, Nagoya University Graduate School of Medicine, Nagoya/JAPAN, [2]Department of Radiological Technology, Nagoya University Graduate School of Medicine, Nagoya/JAPAN, [3]Department of Otorhinolaryngology, Nagoya University Graduate School of Medicine, Nagoya/JAPAN

Purpose/Introduction: Visualization of white matter (WM) tracts such as the corticospinal tract (CST), medial lemniscus (ML), and superior cerebellar peduncle (SCP) using heavily T2-weighted three-dimensional fluid-attenuated inversion-recovery (hT2w-3D-FLAIR) with delayed enhancement (DE) imaging four hours after intravenous gadolinium injection has recently been reported (1). In that report, all patients were clinically suspected of having Ménière's disease, because DE-hT2w-3D-FLAIR imaging of the inner ear has been reported to separately visualize perilymph and endolymph fluid and to identify the presence of endolymphatic hydrops in patients with Ménière's disease (2, 3). Therefore, previous report could not rule out the possible effect of DE. From this perspective, the purpose of this study was to evaluate the effect of DE on the degree of visualization of WM tracts on hT2w-3D-FLAIR neurography.

Subjects and Methods: The records of nine patients with suspected Ménière's disease who underwent plain (P)- and DE-hT2w-3D-FLAIR of the head at 3 T using a 32-channel head coil were retrospectively analyzed (**Fig. 1**). The exams were conducted on the same day in all patients. On axial images, the regions of interest (ROI) were set on the CST, ML, SCP, and contiguous brain parenchyma (thalamus: Th, pontine parenchyma: PP, cerebellar parenchyma: CP), respectively. In order to evaluate the signal contrast between WM tracts and contiguous brain parenchyma, the signal intensity ratios between WM tracts and contiguous brain parenchyma were calculated (CTR: CST/Th ratio, MPR: ML/PP ratio, SCR: SCP/CP ratio). These ratios were calculated for both P- and DE-hT2w-3D-FLAIR image sets, and statistical comparisons between P and DE were conducted using the paired *t*-test.

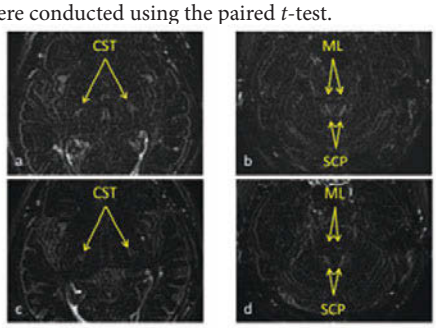

Figure 1 Axial heavily T2-weighted three-dimensional fluid-attenuated inversion-recovery (hT2w-3D-FLAIR) images at the thalamus level without gadolinium injection (a), at the trigeminal nerve level without gadolinium injection (b), at the thalamus level four hours after intravenous gadolinium injection (c), and at the trigeminal nerve level four hours after intravenous gadolinium injection (d), of a patient who was suspected to have Ménière's disease. On all of these hT2w-3D-FLAIR images, the white matter tracts (such as corticospinal tract (CST), medial lemniscus (ML) and superior cerebellar peduncle (SCP)) are visualized as high intensity areas compared to the contiguous brain parenchyma.

Results: The P-CTR was 3.75±0.67 and the DE-CTR was 3.62±0.50 (p=0.24, n=18). The P-MPR was 2.19±0.59 and the DE-MPR was 2.08±0.53 (p=0.25, n=18). The P-SCR was 4.08±0.91 and the DE-SCR was 4.04±0.96 (p=0.43, n=18). There were no significant differences between P and DE for CTR, MPR, and SCR (**Fig. 2**).

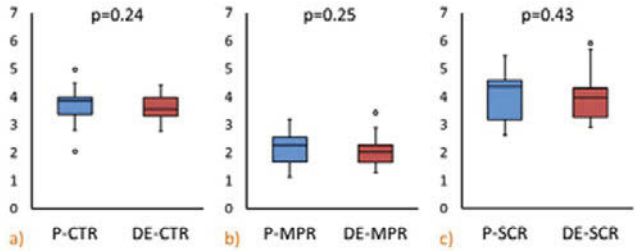

Figure 2 (a) The signal intensity ratio between the corticospinal tract and thalamus (CTR) on heavily T2-weighted three-dimensional fluid-attenuated inversion-recovery (hT2w-3D-FLAIR) images: the plain (P)-CTR was 3.75±0.67 and the delayed enhancement (DE)-CTR was 3.62±0.50 (p=0.24, n=18). (b) The signal intensity ratio between medial lemniscus and pontine parenchyma (MPR) on P-hT2w-3D-FLAIR (P-MPR) was 2.19±0.59 and the DE-MPR was 2.08±0.53 (p=0.25, n=18). (c) The signal intensity ratio between the superior cerebellar peduncle and the cerebellar parenchyma (SCR) on P-hT2w-3D-FLAIR (P-SCR) was 4.08±0.91 and the DE-SCR was 4.04±0.96 (p=0.43, n=18). There were no significant differences between P and DE for CTR, MPR, and SCR.

Discussion/Conclusion: There were no significant differences between P and DE on the degree of visualization of WM tracts on hT2w-3D-FLAIR. In conclusion, DE is unnecessary for visualization of WM tracts using hT2w-3D-FLAIR, and P-hT2w-3D-FLAIR without gadolinium may have future clinical applications as an imaging procedure.

References:

(1) Yamazaki M et al. (2013) European Congress of Radiology (ECR) 2013 DOI: 10.1594/ecr2013/C-0108
(2) Naganawa S et al. (2010) Magn Reson Med Sci 73-80
(3) Naganawa S et al. (2010) Magn Reson Med Sci 237-242

573

MR-microscopy versus µCT and high resolution ultrasound for the characterization of archaeological wet wood: A multimodal approach

A. Berg[1,2], R. Fragner[3], C. Kollmann[1], M. Töpker[3], R. Fürhacker[4], A.K. Klatz[4], M. Grabner[5]
[1]Center for Medical Physics and Biomedical Engineering, Medical University Vienna, Vienna/AUSTRIA, [2]MR Centre of Excellence, Medical University Vienna, Vienna/AUSTRIA, [3]Department of Radiology, Medical University of Vienna, Vienna/AUSTRIA, [4]GesbR, Fürhacker & Klatz, Gutenberg an der Raabklamm/AUSTRIA, [5]Institut für Holztechnologie und nachwachsende Rohstoffe, Universität für Bodenkultur Wien, Tulln/AUSTRIA

Purpose/Introduction: In archaeology X-ray-CT has shown to be very useful for the characterization of ancient Egyptian-mummies and, recently, also for the characterization of archaeological wood, regarding the annual-ring structure for dendro-chronological dating[1,2]. However CT-analysis on clinical and industrial scanners failed for wet wood due to missing contrast and limited spatial resolution for detecting the very fine annual-ring structures[1,2]. µ-CT-scanners are commercially available at small pixel-size (<20µm). Can parameter-selective MR-microscopy compete with such systems concerning spatial resolution and contrast on ancient wet-wood samples? How does high-resolution ultrasound perform with reference to these high-level micro-imaging methodologies?
The results might be relevant also for the application on other wet biological specimen including human tissue.

Subjects and Methods: MR-microscopy: prototype micro-gradient insert (G_{max}=750mT/m) in a human 7T-Siemens-Magnetom and commercial/in-house built small-sized resonators (d_i=19mm, 28mm, 72mm)[3].
µCT: commercial Micro-CT-scanner (Scanco-Medical-µCT35), E=45-70kV, FOV:12-30mm, Voxel: $(12\mu m)^3$-$(30,4\mu m)^3$.
Clinical ultrasound-system for high-resolution gynaecological imaging: GE-VOLUSON-E8: US-head: SP10-D (f=7-18MHz, 192 elements).
Resolution phantom: a micro-lithographically manufactured set of spatial grids on a silicon-wafer (smallest slit: 34µm).
Archaeological specimen: (d~1-2cm) from a middle-bronze-age (~1500 b.C.) well (Obj.764), recently discovered in Wohlsdorf/Steiermark/Austria [4,5].
Results: The µCT-scanner {Vs:$(12\mu m)^3$} is resolving the finest slits of 34µm at excellent SNR. The annual ring structure of dry beech-wood at annual-ring distance (300-600µm) is also detected. However the ancient wet wood, containing water, exhibits hardly any contrast for inner structure. MR-microscopy is capable of resolving the finest slits with an in-plane pixel-size of 25µm. With difference to µCT, the inner structure of the archaeological sample is well contrasted, even showing the size of the individual vessels of the annual rings. The ultrasound transducer is cable of resolving the 256µm slits in the phantom but no finer structures than 128µm at a nominal pixel-spacing of 39µm. The annual ring structure of the ancient wood sample is hardly to be guessed, nor quantified.

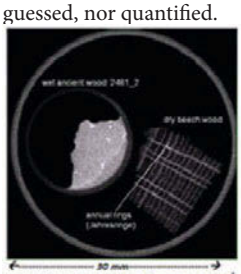

*Fig. 1 CT-microscopy (VS: 30 x 30 x 30 µm³, Mtx:1024 x 1024). **Right bottom:** the inner structure and annual rings for recent dry beech wood (d≥0mm) are well contrasted. **Left top:** archaeological wet wood. With difference, the inner structure of wet wood, similar to water containing soft tissue, cannot be contrasted and visualized.*

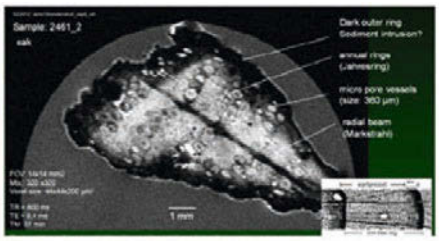

Fig. 2 T2-weighted high-resolution MR-image (VS: 44 x 44 x 200 µm³) of the archaeological wet wood sample 2461. The micro pore vessels, indicating the start of the annual growth in wet spring, can be well resolved. The black centre line (left-right) is indicative of the radial running wood rays. Note the varying distance between the annual rings due to different growth conditions in the corresponding year.

Discussion/Conclusion: Even though µCT-scanning performs best with regard to spatial-resolution, contrast in wet archaeological samples is insufficient to differentiate fibre-type texture and water, due to the low difference in electronic-density between water and carbohydrates, present in wood, similar to soft tissue contrast in humans. MR-microscopy on a prototype-insert on a high-field 7T-human scanner allows for the visualization of the inner structure in wet wood and even the quantitative determination of annual-ring width for dendrochronology (with nr. of annual-rings limited by the small FOV). The contrast is mainly based on the mobility of the 1H-nuclei (T2) and magnetic susceptibility (T2*).
References:
Literature

[1] Grabner M, Salaberger D, Okochi T. *The Need of High Resolution µ-X-ray CT in Dendrochronology and Wood Identification* (2009) in: Zinterhof P, et al. (Eds.) ISPA, Salzburg/Austria.

[2] Bill J, Daly A, Johnsen O, Dalen K. *DendroCT– Dendrochronology without damage* (2012) Dendrochronologia **30**(3) 223-230.

[3] Berg A, Potthast A, Starewicz P. *MR-Microscopy on a human 7T-Scanner (2010)* Proc. ISMRM/ESMRMB 2010,1048, Stockholm, Sweden.

[4] Fürhacker R, Klatz A K. *Der mittelbronzezeitliche Brunnen aus Wohlsdorf. Fundbergung und bisher erfolgte Maßnahmen der Konservierung und Restaurierung* (2010) *Fundberichte aus Österreich*, Ed. Bundesdenkmalamt **49**, S: 194.

[5] Berg A, Fürhacker R, Klatz AK, Grabner M. *Parameter selective MR-microimaging for non-invasive characterization of archaeological wet wood: A novel methodology for dendrochronology and a new approach in conservation science to assess wood species and condition?* (2012) ESMRMB, Lisbon/Portugal 04.-06.10.2012; MAGMA **25** 1 Suppl, oct 2012, EPOS Nr. 596

574

Visual assessment of ASL perfusion images of the brain with General Linear Modeling – a comparison of raw subtracted images and t statistic thresholding

D. Fallmar, J. Lilja, **E.-M. Larsson**
Department of Radiology, Uppsala University, Uppsala/SWEDEN

Purpose/Introduction:
MRI with arterial spin labeling (ASL-MRI) has a great potential as a clinical radiological tool for detection of regional perfusion changes. Much effort has been invested in quantification of ASL data, but several questions are currently unanswered (1). Regional differences can be qualitatively evaluated by visual assessment. ASL is sometimes hampered by inter-subject differences (2) and artefacts such as transit time effects with linear high signal in patients with slow flow in relation to the postlabel delay time (3).This problem is greater in an elderly population.
The aim of this study was to test and evaluate General Linear Model (GLM) post-processing to improve ASL maps for visual assessment.
Subjects and Methods:
17 cognitively healthy subjects, age 56-84, were included. The study was approved by the local ethics committee, and subjects gave written informed consent.
MRI was performed with a 3T scanner (Philips Achieva) including pseudocontinuous ASL. The latter had TR/TE 4100/14ms, voxel size 2,75 x 2,75mm, 20 slices, post label delay 1600ms, no vascular crushing.
ASL images were processed in two ways; standard subtraction images and "t-statistics" using GLM, in a manner commonly used in BOLD fMRI, with "label" and "control" images as contrasts. Prior to calculating t-statistics the images were smoothed using a Gaussian filter.
Results:
Figs 1 and 2 show examples of differences between subtraction images and t statistic thresholding. These t statistic images are t value thresholded at minimum 5, maximum 13.
Fig 1 shows high signal at blood vessels in the subtraction, but not in the t statistics.

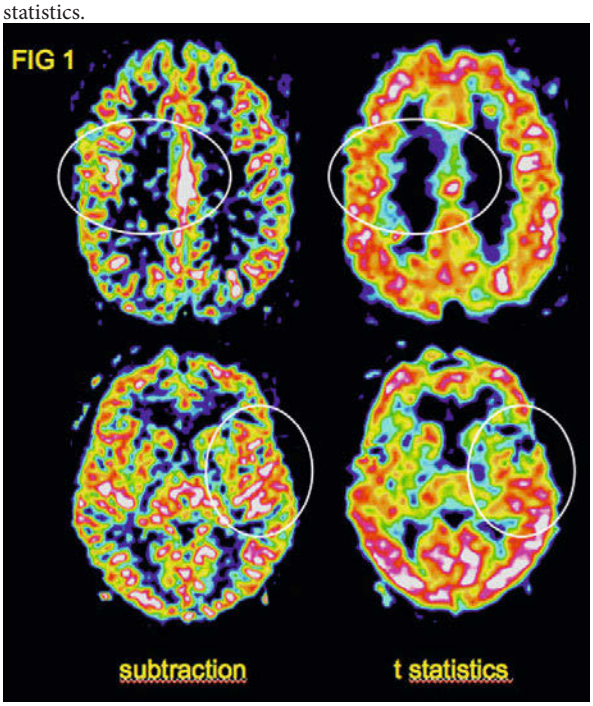

Fig 2 shows physiologic regional distribution in the occipital lobe, less pronounced with statistic thresholding.

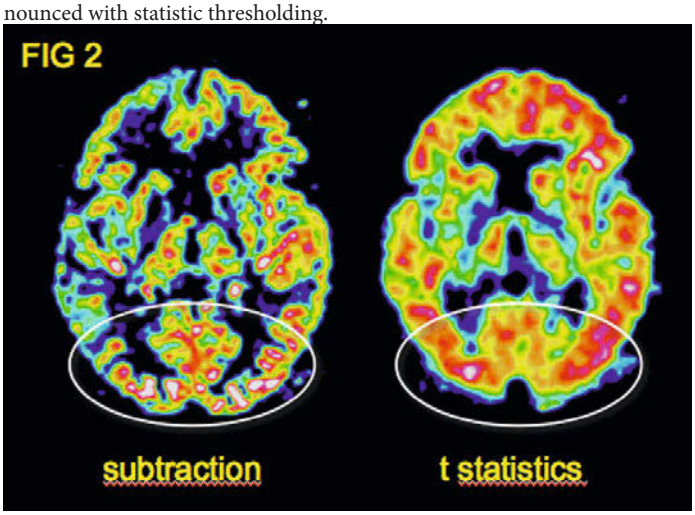

Discussion/Conclusion:
Converting the ASL perfusion maps to statistical maps of label vs. control response using GLM can provide a useful method of visual assessment of perfusion. The underlying hypothesis is that only areas that promptly respond to the labeling contrast are relevant for the assessment of perfusion. Areas with ambiguous response or poor statistical response certainty are toned down.
The t statistic thresholding seems less sensitive to some artefacts, and blood vessels with high signal are less dominating. Due to the general unit of t values, a large control group could provide a database to which patients could be compared in a diagnostic situation.
References:
1. Aslan et al. Magn Reson Med. 2010;63(3):765-71.
2. Henriksen et al. J Magn Reson Imaging. 2012;35(6):1290-9.
3. Deibler et al. AJNR Am J Neuroradiol. 2008;29(7):1228-34.

575

1.5 T Arterial Spin Labeling (ASL) regional cerebral blood flow (rCBF) mapping.

A. Pavilla[1,2], L. Ciobanu[1], A. Arrigo[2], M. Mejdoubi[2]
[1]DSV, I2BM, NeuroSpin, LRMN, CEA, Gif sur Yvette/FRANCE, [2]La Meynard, CHU PZQ, Fort-de-France/MARTINIQUE

Purpose/Introduction: Establishing normal rCBF (regional cerebral blood flow) maps is a crucial source of knowledge for accurate interpretation in neurologic pathologies such as stroke and neurodegenerative diseases including Alzheimer's dementia. This study aims to establish 1.5T PASL (Pulsed ASL) rCBF map in human brain. Only two studies proposed rCBF mapping ([1],[2]).
Subjects and Methods: Twenty healthy volunteers were studied (10 women, 10 men). Mean age was 44 ± 13. All data were acquired with a 1.5T GE MR450w (GE, Milwaukee, WI). We used a 3D Spiral PASL sequence with the following parameters: 155° flip angle, TR/TE: 4554/ 10.76 ms; Post- labeling delay=1525 ms, FOV 24 x 24 cm, matrix size 512 x 8, slice thickness 4mm (without gap). Ten equal bilaterally volumes of interest (VOIs) in cortical and subcortical grey matter (GM), white matter (WM) and cerebellum were drawn by visual inspection of anatomical MR images. Single VOIs were drawn in protuberance and vermis.
Results: No significant lateral asymmetry was observed in any region. Frontal cortical GM had the highest mean CBF: 69.6 ± 0.3 mL/100g/min. Occipital, parietal and temporal cortical GM CBF were 64.8 ± 2.4, 62.6± 0.6 and 56.7 ± 1.3 mL/100g/min, respectively. Subcortical mean CBF values were 57.6 ± 1.7, 53.0 ± 0.5 and 53.4 ± 1.5 mL/100g/min for thalamus, caudate nucleus and hippocampus, respectively. Putamen had the lowest subcortical GM CBF (44.7±0.4 mL/100g/min). Cerebellum mean CBF was 57.9±0.2 mL/100 g/min. Vermis had high perfusion value with 67.9±12.0 mL/100 g/min and protuberance mean CBF was 45±6.7 mL/100g/min. WM CBF was the lowest of all regions (23.73± 0.3 mL/100 g/min).
Discussion/Conclusion: Our results are similar with those obtained with 3T pCASL (pseudo continuous ASL) [2] except that we didn't find any lateral significant asymmetries. Our results differ significantly from those obtained throught 1.5 T CASL (Continuous ASL) study that used another approach by vascular territories and not anatomical structures for CBF assessment [1]. We also found as in [2] rCBF variability across the brain with higher values in frontal cortical GM. This finding may be explained by the role of the frontal areas in attention control and maintenance. Lowest GM perfusion was found in putamen, likely due to the close pallidum which contains a high concentration of iron shortening the local T1.
Quantitative knowledge of these normal physiological rCBF will be useful for proper neurologic physiology and pathology interpretation.
References:
[1] Floyd ,T, 2003, J.Magn.Reson.Med ,18:649–655
[2] Pfefferbaum,A,2010,Psychiat.Res-Neuroim,182 :266–273.

576

The effect of slice thickness on perfusion imaging in posterior circulation stroke

A.A. Khalil[1,3], I. Galinovic[2], P. Brunecker[2], K. Villringer[2], J.B. Fiebach[2]
[1]International Graduate Program Medical Neurosciences, Charité Universitätsmedizin Berlin, Berlin/GERMANY, [2]Centre for Stroke Research Berlin, Charité Universitätsmedizin Berlin, Berlin/GERMANY, [3]ERASMUS MONDUS Joint Master Programme in Neuroscience, Bordeaux/FRANCE

Purpose/Introduction: Perfusion MR imaging, which has been used to reveal potentially salvageable tissue after cerebral ischemia and to guide treatment strategies[1], is challenging in the infratentorial compartment. Partial volume effects and susceptibility artefacts hinder the clinical application of this technique in posterior circulation stroke[2]. This study aimed to investigate the effect of a high-resolution perfusion imaging (PI) sequence on posterior circulation stroke lesion volumes compared to the standard PI sequence using two commercially available perfusion analysis softwares.
Subjects and Methods: Thirteen patients with a clinical diagnosis of posterior circulation stroke admitted to the Charité Universitätsmedizin Berlin received a standard MRI stroke protocol on the day of admission (including diffusion weighted imaging, FLAIR, standard 5mm slice-thickness PI and an MR angiography) and a modified protocol with a 2.5mm slice-thickness PI sequence on day 2. A diffusion weighted image (DWI) done on day 6 was used to assess final infarct size. The perfusion data was analyzed using Perfusion Mismatch Analyzer (PMA) version 3.4.0.6 and StrokeTool version 2.3 to generate quantitative cerebral blood flow (CBF) maps. Arterial input functions were automatically selected, manually optimized and a threshold (20ml/100g/min) was set to generate volumes-of-interest corresponding to the perfusion deficits. Signal-to-noise ratios (SNR) were calculated for both sequences using Analyze version 11.0.
Results: The mean perfusion lesion volumes for the standard sequence were 3.43ml and 5.92ml for StrokeTool and PMA respectively. For the high-resolution sequence the lesion volumes were 3.14ml and 3.51ml for StrokeTool and PMA respectively. Agreements between the softwares (limits of agreement = 15.56ml to -18.50ml) and the slice-thicknesses (limits of agreement = 19.8ml to -17.11ml) were poor. Differences between initial perfusion lesion volumes and final DWI volumes were smaller with the high-resolution sequence (0.09ml with StrokeTool and 0.45ml with PMA) compared to the standard sequence

(0.37ml with StrokeTool and 2.86ml with PMA). The standard sequence had a significantly higher SNR (mean=89.77, SD=16.6 versus mean=55.01, SD=7.56).

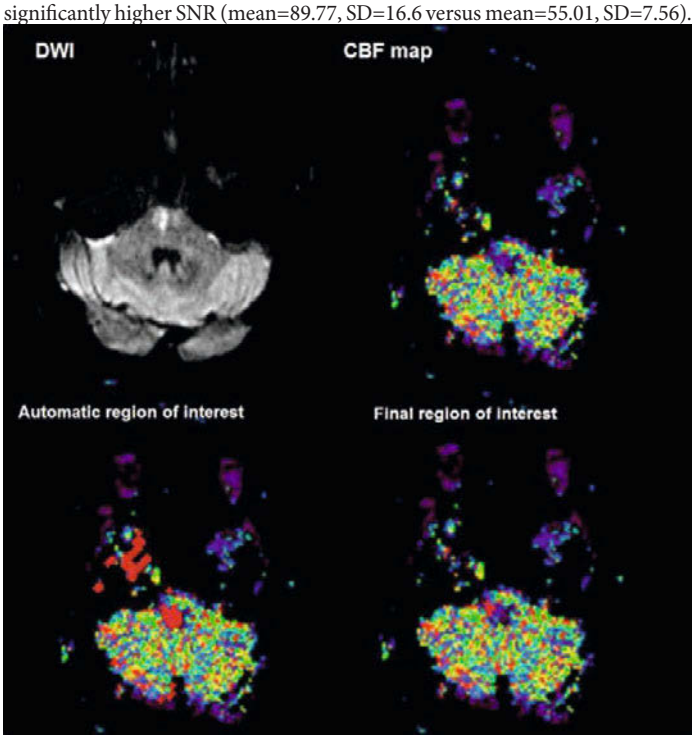

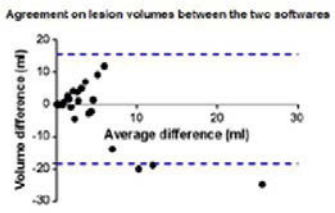

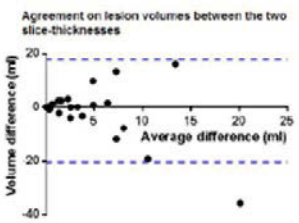

Discussion/Conclusion: There is currently little knowledge on whether noise or contrast has a greater influence on the accuracy of perfusion imaging. In this study, despite being associated with a higher level of noise, the high-resolution imaging sequence was relatively accurate in predicting final DWI outcomes in posterior circulation stroke compared to the standard sequence.

References:

- [1] Albers, G.W., et al., 2006, Ann Neurol, 508-517
- [2] Alvarez-Linera, J., 2010, Semin Ultrasound CT MR, 230-245

577

ADC measurements with an endorectal coil: an in vitro study

J.-M. Verret[1, 2], F. Pilleul[3], C. Rabrait[1], O. Beuf[2]

[1]Clinical Science Development Group, General Electric Healthcare, Buc/FRANCE, [2]CNRS UMR 5220, Inserm U630, Université de Lyon, CREATIS, Villeurbanne/FRANCE, [3]HEH, Gastroenterology, Hospices Civils de Lyon, Lyon/FRANCE

Purpose/Introduction: Diffusion Weighted Imaging (DWI) of the rectal cancer is a promising modality both for the detection of the rectal cancer and assessment of the response to chemotherapy treatment [1]. Because sensitivity of endorectal coil decreases rapidly with distance (fig 1) thus we aimed at assessing the accuracy and reproducibility of Apparent Diffusion Coefficient (ADC) measurements with distance.

Subjects and Methods: Acquisition: Experiments were performed on a GE DVMR750 3T system (General Electric Medical Systems), on bottles of tridecane (8 cm long, 3.3 cm diameter), pentadecane (9.5 cm long, 4 cm diameter) and hexadecane(15 cm long, 6.5 cm diameter) solutions whose ADC values are known (Table 1).

	Tridecane (mm^2/sec)	Pentadecane (mm^2/sec)	Hexadecane (mm^2/sec)
Luciani 2008	$6.77 \pm 0.19 \times 10^{-4}$	$4.61 \pm 0.27 \times 10^{-4}$	$3.50 \pm 0.39 \times 10^{-4}$
Brugières 2004	6.53×10^{-4}	4.39×10^{-4}	3.62×10^{-4}

Table 1: Alkane ADC values [1] [2]

ADC measurements were performed either with our double loop endorectal coil prototype (60 mm length, 6 mm width) was successively taped on each bottle (fig 1) or an 8-channel torso array coil. *Acquisition sequence:* DW-EPI with FOV = 9 cm, matrix = 64×64, 3 in 1 gradients and 6 b-values: 0, 100, 300,500,800, 1100 s/mm2.

Data Processing:For a given alkane, a ROI was defined and kept the same for all measurements (fig 2, 3,4).Inside the ROI, for each pixel, we performed a monoexponential fit with Levenberg-marquardt algorithm in order to estimate the ADC. Since the solution is homogeneous, the ADC final value was computed as the average value over the ROI we defined. The routine was developed under MATLAB (Mathworks). 10 consecutives measurements were performed (test-retest) on the same ROI. The coefficient of variation CV (ADC standard deviation / ADC mean) in the ROI was computed for reproducibility assessment.

Results:

	Tridecane ADC (mm^2/sec)	Pentadecane ADC (mm^2/sec)	Hexadecane ADC (mm^2/sec)
8-channel torso array coil	$6.6 \pm 0.4 \times 10^{-4}$	$4.57 \pm 0.35 \times 10^{-4}$	$3.29 \pm 0.39 \times 10^{-4}$
Endorectal coil	$6.41 \pm 0.33 \times 10^{-4}$	$4.28 \pm 0.4 \times 10^{-4}$	$3.61 \pm 0.38 \times 10^{-4}$

Table 2: Measured Tridecane, Pentadecane and Hexadecane solutions ADC-values

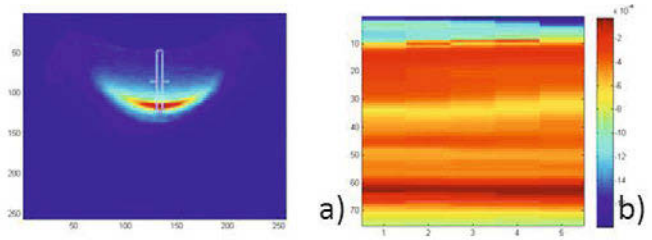

Fig 2: DW-EPI image of the pentadecane solution a) ROI orthogonal to the endorectal coil b) ADC map of the ROI

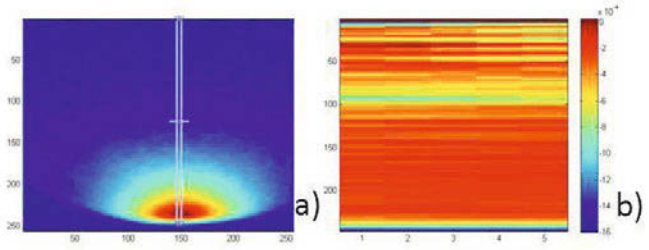

Fig 3: DW-EPI image of the hexadecane solution a) ROI orthogonal to the endorectal coil b) ADC map of the ROI

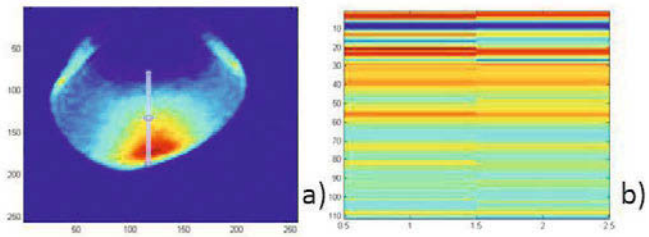

Fig 4: DW-EPI image of the tridecane solution a) ROI orthogonal to the endorectal coil b) ADC map of the ROI

ADC map acquired with the endorectal coil were relatively uniform except near the edge of the bottle due to restricted diffusion. The short term reproducibility was established at *7.8 %*.

Discussion/Conclusion: Despite its sensitivity profile, the endorectal coil provides ADC values consistent with literature, but the reproducibility was deceiving. Further careful assessment with SNR and distance from the coil has to be investigated as well as the origin of discrepancies between repeated measurements.

Acknowledgement:
This work was performed within the framework of the LABEX PRIMES (ANR-11-LABX-0063) of Université de Lyon, within the program "Investissements d'Avenir" (ANR-11-IDEX-0007) operated by the French National Research Agency (ANR).

References:
[1] T. Bäuerle et al, European Journal of Radiology, Volume 82,March 2013
[2] Luciani et al, Radiology , Volume 249, December 2008
[3] Brugières et a, AJNR Am J Neuroradiol , May 2004

578

Spillover Correction for Creatine in Muscle

E. Rerich, M. Zaiss, P. Bachert
Medical Physics in Radiology, German Cancer Research Center, Heidelberg/ GERMANY

Purpose/Introduction: In skeletal muscle endogenous chemical exchange saturation transfer (CEST) effects are influenced by direct water saturation and magnetization transfer (MT) effects. In this study we present a method which corrects the CEST data from spillover and apply it to in vivo data.

Subjects and Methods: In order to study CEST effects in skeletal muscle 3-pool model simulations were performed. The water and MT pools were described by using the data from Ref. [1]. The metabolite pool comprised only the creatine pool with k_b (pH = 6.9, T = 37°C) = 945 Hz (data from Ref. [2, 3]).

Data was evaluated with two methods MTR_{asym} [4] and the proposed spillover correction MTR_{pcm} [5, 6, 7]. The in vivo CEST imaging was performed on a 3 T whole body MRI scanner using a 8-channel Tx/Rx knee coil. Z-spectra were B_0-corrected employing a WASSR map [8].

Results: Appropriate sequence parameters were determined by numerical simulations of the Bloch-McConnell equations. The simulated signal enhancement was maximum for a 100 ms saturation pulse train comprising 10 gaussian pulses (duty cycle: 60%) and a B_1 = 1.1 µT.

MTR_{asym} increases with B_1 and decreases when spillover, induced by MT, T_2 and B_1, becomes dominant (Fig.1 (a)). After spillover correction the signal intensity elevates with increasing B_1 until a plateau is reached. In contrast to MTR_{asym} MTR_{pcm} shows less dependency on f_c and R_{2a} (Fig.1 (b, c)).

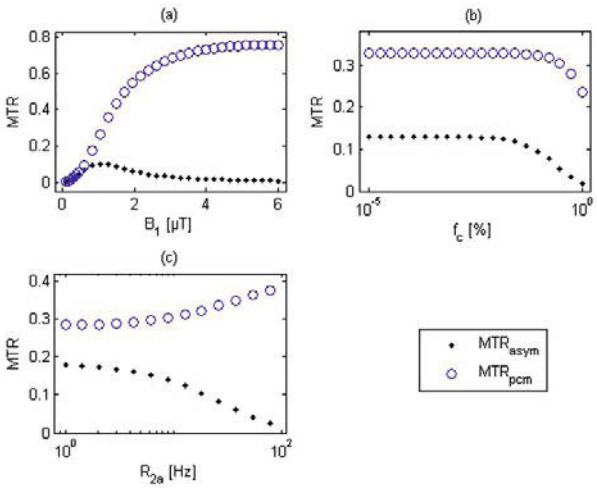

Figure 1: Comparison of magnetization transfer ratio (MTR) normalizations as a function of B_1 (a), f_c (b) and R_{2a} (c). Spillover correction of MTR_{pcm} exceeds MTR_{asym}.

After spillover correction the CEST effect is greater in the respective pixel (compare (a) and (b) in Fig. 2).

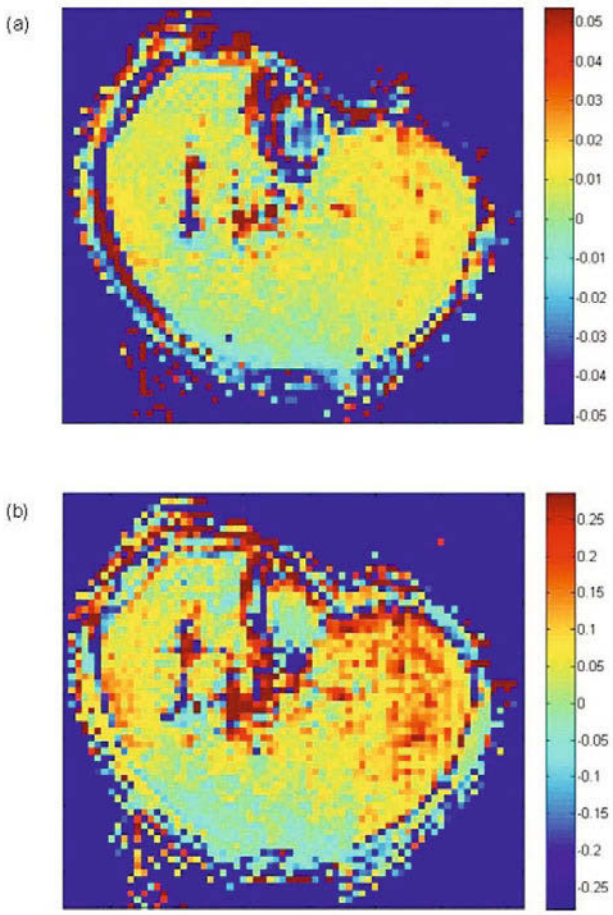

Figure 2: Transversal tomogram of a skeletal muscle of the calf: (a) MTR_{asym} map and (b) spillover corrected - MTR_{pcm} - map (please note the colormap code which shows the signal intensity at 1.8 ppm).

Discussion/Conclusion: In this study we showed that a spillover correction for creatine in muscle is feasible.

References:

[1] Stanisz et al., Magn Reson Med, 54: 507–512 (2005)
[2] Görke et al., ESMRMB or Diploma Thesis, Univ HD, 2012
[3] Haris et al., NMR Biomed., 25: 1305–1309 (2012)
[4] Zhou et al., Progress in Nuclear Magnetic Resonance Spectroscopy 48, 109–136 (2006)
[5] Zaiss et al., Journal of Magnetic Resonance 211, 149 (2011)
[6] Zaiss et al.,arXiv:1203.2067 (2012)
[7] Zaiss et al. ,NMR Biomed., 26: 507–518 (2013)
[8] Kim et al., Magn Reson Med, 61: 1441–1450 (2009)

579

dGEMRIC MR-microimaging to evaluate the Glycosaminoglycan (GAG) content in an animal model for cartilage repair

J. Friske[1], T. Lindner[2], M. Pachowsky[3], A. Berg[4], G.H. Welsch[3], K. Gelse[3], S. Trattnig[2]

[1]Department of Radiology, MR Center of Excellence - Medical University of Vienna, Vienna/AUSTRIA, [2]Department of Radiology, MR Center of Excellence - Medical Universtity of Vienna, Vienna/AUSTRIA, [3]Department of Trauma Surgery, Friedrich-Alexander University Erlangen-Nuremberg, Erlangen/GERMANY, [4]Center for Medical Physics and Biomedical Engineering, MR Center of Excellence - Medical University Vienna, Vienna/AUSTRIA

Purpose/Introduction: Quantitative MRI techniques (qMRI) have shown to characterize cartilage damage especially concerning early onset of osteoarthritis [Binks 2013]. Non-invasive assessment of tissue damage is possible in a stage where tissue repair is still achievable. Modern regenerative therapy options like microfracture-technique(MFX) and autolog-cartilage-transplantation (ACT) [Welsch 2008] need a carefully designed follow-up procedure to monitor repair stages of cartilage tissue.We use the sheep knee joint as a model similar to human size and mechanical loadings.

One of the most validated qMRI methods is relying on T1 based *dGemric* , which has shown to be directly related to the Glycosaminoglycan (GAG) content in both ex-vivo and clinical [Link2011] studies.

To further improve the resolution of qMRI in order to images and differentiate even smaller biochemical changes we used a high-field(7T) human scanner and an additional micro-imaging insert [Berg 2011].

Subjects and Methods: Two types of surgical procedures (MFX/ACT) were applied to living merino sheep. Cartilage samples were harvested 26 weeks after surgery from the sheep knee and examined in details using a microimaging system equipped with a 39mm diameter resonator on a clinical 7T scanner (Siemens).

A standard Spin Echo Inversion Recovery sequence (TE= 5.1ms;TR=12500ms+TI,TI:60,100,150,200,250,300,400,500, 750,1000,1500,2000,3500[ms]) was used to acquire 10 slices (VS: 140x140x1000 μm^3). After the first measurement each sample was submerged in 1 mmol/l Gd-DTPA (Magnevist) for 4 h. Then we performed the second measurement using the same inversion times.

An adapted Matlab routine was used to perfom a pxel-wise T1-fit to the experimental data using a fast nonlinear least square algorithm with polarity restoration NLS-PR (Barral2010). Pre- and post contrast T1-maps are used to calculate the GAG content using the dGemric formula according to [Link2011] (Tab1) with the relaxation coefficient of 3.3(l/(mmol s)) [Noebauer2010].

Results:

T1 maps of two typical samples are shown in Fig1-4 before and after application of the contrast agent.

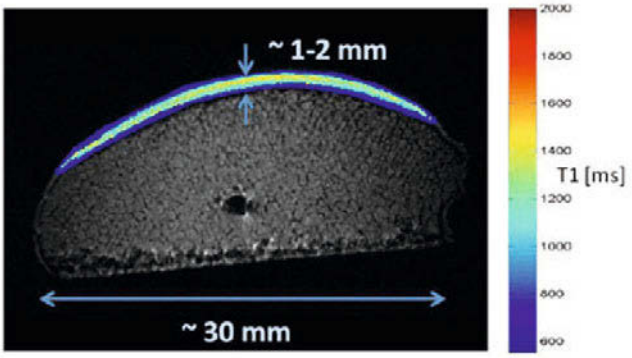

Fig 1: Calculated T1 map of a sheep condyle sample (left, lateral) without defect . Overlay to morphological SE-IR micro image with a resolution VS: 140x140x1000 μm^3 .

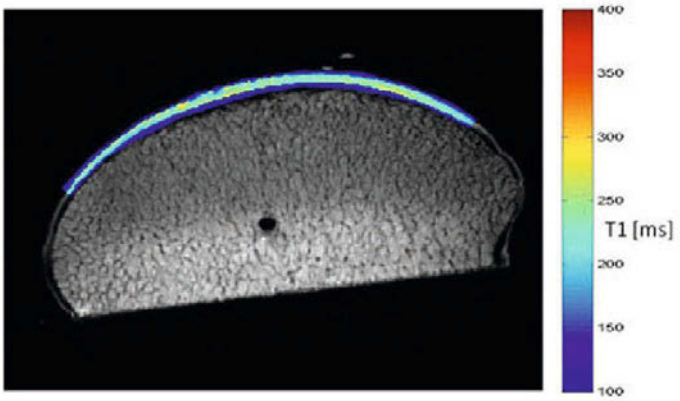

Fig 2: Same sample as Fig1 but after 4 hours application of the contrast agent Gd-DTPA

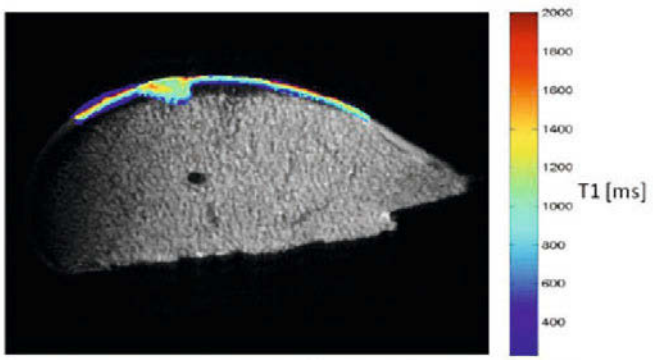

Fig 3: Calculated T1 map of a sheep condyle sample (left medial) with defect ACT and macroscopic good repair tissue 26 weeks after surgery.

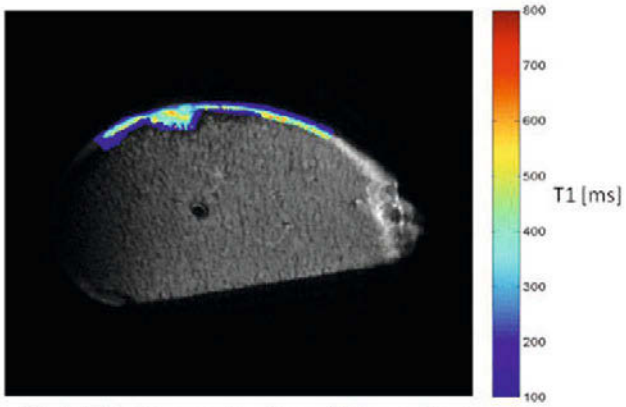

Fig 4: After the application of the contrast agent Gd-DTPA

Sample one is surgically untreated while sample two experienced an ACT surgery. Results are shown in Tab1.

Sample	Mean T1 [ms] (+/- SD) T1no-Gd	Mean T1 [ms] after contrasts agent (+/- SD) T1Gd	[Gd(DTPA)2−]tissue [mM]
Sheep condyle without defect (Fig 1,2)	1213 +/- 266	234 +/- 26	1.05
Sheep condyl including defect region (Fig 3,4)	928 +/- 250	399 +/- 261	0.43

Tab1: Whole cartilage was segmented to calculate the mean T1 values. [Gd(DTPA)2−]tissue = (1/R)[(1/T1Gd) − (1/T1no-Gd)] , R = 3.3 l/(mmol*s)

Discussion/Conclusion: The $[Gd(DTPA)^{2-}]$ values are in an expected range compared to the literature [Nissi2007]. However the concentration of the healthy tissue is comparably high .The affected region has a significant lower $[Gd(DTPA)^{2-}]$ concentration compared to the healthy sample which is attributed to non-perfect replacement and growing of the transplanted cartilage matrix. It also shows a broad variety of different T1 values (high SD) after applying the contrast agent which indicates different repair stages of the tissue .

References:

Binks et al. Br J Radiol 2013:8620120163
doi:10.1259/brj.20120163
Berg, A. et al. (2011):
http://dx.doi.org/10.1594/ecr2011/C-2029
Barral et al.(2010) doi:10.1002/mrm.22497
Link, T.M. (ed.), Cartilage Imaging, 171DOI 10.1007/978-1-4419-8438-8_14
Noebauer-Huhmann Iris M. (Invest Radiol 2010;45:554-558)
Nissi M.J. Osteoarthritis and Cartilage, Volume 15, Issue 10, October 2007 10.1016/j.joca.2007.03.018
Welsch, G. et al. (2008): *J. Magn. Reson. Imaging* 28 (4), S. 979-986

580

A new automatic apparatus to determine the induced torque for medical devices in MR scanner static fields.

S. Blanc[1], L. Hammen[2], J. Felblinger[3], C. Pasquier[3]
[1]MRI compatibility, Clinical Investigation Centre Innovative Technology of Nancy University Teaching Hospita, Nancy/FRANCE, [2]R&D, Healtis, Nancy/FRANCE, [3]CIC-IT 801, INSERM, Nancy/FRANCE

Purpose/Introduction: MRI contraindication can cause health hazards due to the interactions between medical devices and tough MRI electromagnetic environment [1]. The standard method for magnetically induced torque measurement on medical devices in MR environment is established in the ASTM-F-2213 [2]. However, visual evaluation used in this method is imprecise, causing multiple sources of measurement uncertainty. Here, we propose a novel apparatus using angle encoders to provide more accurate and robust measurements of fero-magnetic device deflection angles inside MR environment automatically.

Subjects and Methods: The apparatus is composed of a wooden structure with two angle encoders (0.07° increment, measurement frequency 70Hz), interconnected with a rotational rod. To measure the torque, it is first calibrated by creating a torque with a set of mass to determine the relation between deflection angle and known induced torque [Figure 1.a]. The measurements in MR scanner environment are then made with a stainless steel rod placed in a homogeneous field at 3T [figure 1.b].

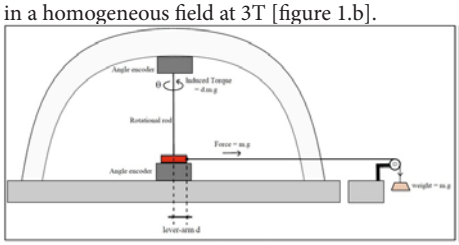

Figure 1.a: Apparatus schema for calibration

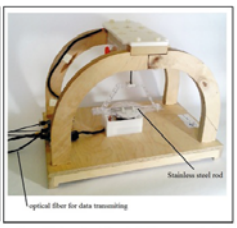

Figure 1.b: Apparatus picture for MRI measurement with the 90mm stainless steel rod.

Each deflection angle is measured at every 10° taken after 10s to suppress the oscillations. The deflection angle is calculated as the angle between the long axis of the rod and the direction of static magnetic field. The induced torque is calculated with the relation given by the calibration. The magnetic susceptibility is also measured at 3T in a magnetic susceptometer to determinate the theoretical torque [3].

Results: A linear relation is obtained with the calibration, type T=a*θ+b (with T[N.m] and θ[rad]). The evolution of the experimental induced torque is plotted as a function of the rod orientation in the magnetic field [Figure 2a], showing two peaks at 45° and 135°, a minimum at 0°, 90°and 180° and an horizontal asymmetry beside the two peaks. The same maximum and minimum values are observed in the calculated theoretical torque, but without the asymmetry [Figure 2b]. The average standard deviation of the induced torque measurement is 0.519mN.m.

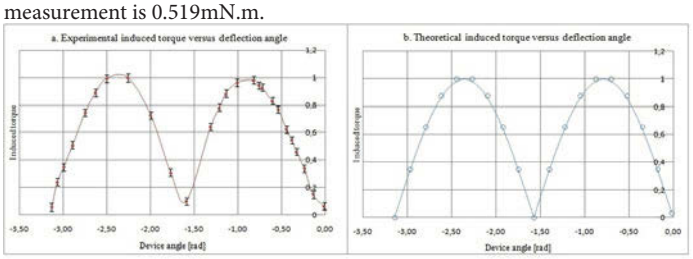

Figure 2: Experimental and theoretical induced torque as function of the rod orientation in 3T magnetic field.

Discussion/Conclusion: *We* showed that the proposed apparatus can provide torque measurements at high accuracy by both experiments and theoretical simulation. The asymmetry appeared in the experimental curve may be due to the non centering of the stainless steel rod attached point. A future amelioration will be an automated rotating rod with a magnetic compatible motor to reduce oscillations and to allow eddy-currents induced torque measurements.

References:

1-Shellock FG, 2002, Journal of Magnetic Resonance Imaging.
2-ASTM-F-2213, 2006.
3-John F. Schenck, 2000, Journal of Magnetic Resonance Imaging.

581

High field compatible thermometer

Y. Pilloud[1], R. Gruetter[2]
[1]LIFMET, CIBM-LIFMET, École Polytechnique Fédérale de Lausanne, Lausanne, SWITZERLAND, Lausanne/SWITZERLAND, [2]CIBM-LIFMET, École Polytechnique Fédérale de Lausanne, Lausanne/SWITZERLAND

Purpose/Introduction:

A thermometer compatible with high magnetic field to monitor rodent body temperature is expensive and difficult to find. Here, the temperature is converted to frequency and transmitted through an optical fiber to avoid ground loops and perturbations.

The system is made of two aluminium enclosures, one with the sensor amplifier and optical fiber transmitter and the second one with the receiver and USB interface (Fig.1).

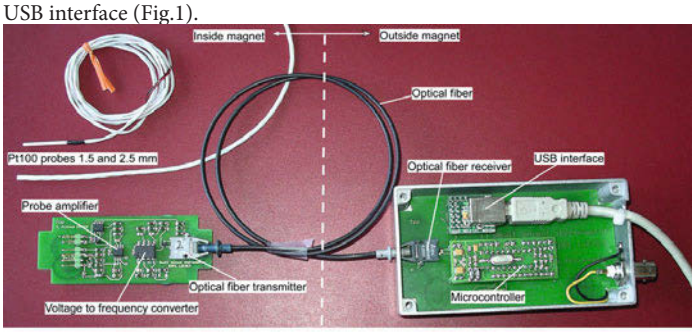

Fig.1: Whole system except battery. The optical fiber shown is for tests only, in real use the length is more than 15 meters.

Subjects and Methods:

Different temperature sensors are available but not all are usable at high fields. The sensor choosen is the Pt100 for it's availability in different sizes and the non-magnetic materials used. It's a high accuracy platinium resistor which gives 100Ω at 0°C (Equ.:1).

$$\text{Equ. 1: } R(t)=R(0)\cdot(1+A\cdot t+B\cdot t^2)$$
$$\text{with: } R(0)=100\ \text{Ohms @ } 0°C,\ A=3.908\cdot10^{-3},\ B=5.775\cdot10^{-7}$$

Total consumption is 25.5mA. The system inside the magnet is powered by a 6V/1.2Ah lead battery for an autonomy up to 40 hours.

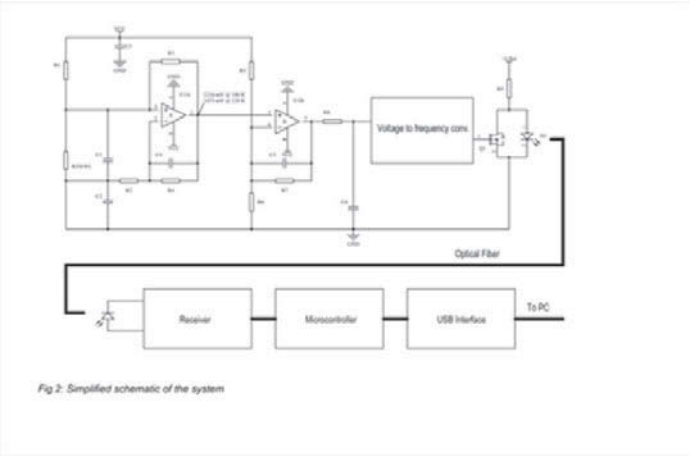

Fig 2: Simplified schematic of the system

The first operational amplifier (Fig.2) is used to bias the sensor and amplify the voltage. The positive feedback compensates the non-linearity of the temperature coefficient of the Pt100. The second is used to amplify and shift the voltage. A voltage to frequency converter is used to drive an optical fiber transmitter. A receiver and a microcontroller send the measured frequeny to a PC through a USB connection.

A Labview (National Instruments Inc.) VI manages the communications, calibration, and computes the temperature to display it (Fig.3).

All the adjustments/calibrations are done in Labview to avoid any calibration on the circuit. To achieve a good precision, the system is calibrated with a 0.1% 100Ω resistor to adjust the 0°C offset. A second resistor of 120Ω is used to adjust the gain at 51.6°C.

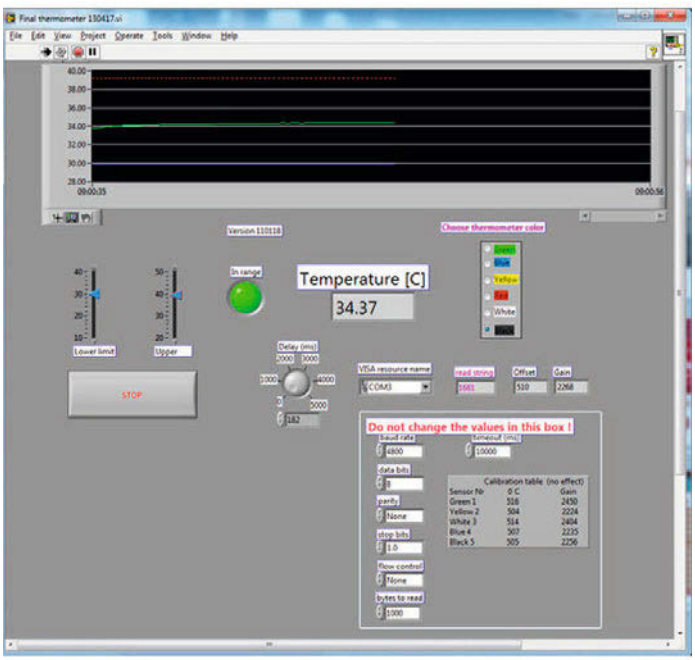

Fig.3: Labview VI with temperature display and calibration values.

Results:

Care should be taken for the construction to avoid some pertubations from the RF signal. The system is not sensitive to power supply voltage. Output frequency is between 500 and 2500 Hz to avoid wide spectrum perturbations to the RF signal.

The accuracy of ±0.15°C is determined by the quality (class) of the Pt100 probe.

Discussion/Conclusion:

A few of these thermometers are used on NMR magnets at 9.4T and 14.1T to monitor body temperature of rats and mice. Except some nickel plating on components, there is no any other magnetic materials. The cost of this system is a fraction of a commercial one and the sofware can be implemented for different applications and sensors.

References:

www.omega.com
http://pdfserv.maximintegrated.com/en/an/AN3450.pdf

Acknowledgements:

This study was supported by Centre d'Imagerie BioMédicale (CIBM) of the UNIL, UNIGE, HUG, CHUV, EPFL and the Leenaards and Jeantet Foundations.

582

Gazing at the very early stages of plant life with MRI

E. Belin[1], **D. Rousseau**[2], G. Craipeau[1], F. Chapeau-Blondeau[1], S. Ducournau[3], D. Demilly[3], C. Dürr[4], F. Franconi[5]
[1]Laboratoire d'Ingénierie des Systèmes Automatisés (LISA), Université d'Angers, Angers/FRANCE, [2]CNRS UMR5220 ; Inserm U1044 ; INSA-Lyon ; Université Lyon 1, Université de Lyon, CREATIS, Lyon/FRANCE, [3]SNES, Station Nationale Essais Semences (SNES), Beaucouzé/FRANCE, [4]UMR 1345, IRHS, INRA, Beaucouzé/FRANCE, [5]PRIMEX (CIFAB), Université d'Angers, Angers Cedex/FRANCE

Purpose/Introduction:

MRI has been shown useful at various scales and stages of plants [1], from seeds up to root growth of adult plants to provide information on water dynamics, functional imaging of the abiotic stress response or host-pathogen interaction. We report the use of MRI to observe a specific stage of plant development which is the elongation occurring after the imbibition and germination stages of the seed. During this stage, the seed is in the soil. Following a geotropism, the seedling shoot grows to reach the light and activates photosynthesis while the radicle, goes deeper and anchors in the soil. It has recently been shown that radicle and hypocotyl parts display distinct functional contrasts with thermography [2]. We question this contrast with MRI.

Subjects and Methods:

We highlight the contrast observed during the seedling elongation with various MRI sequences including RARE, T1 Map, T2 map, DTI, Spectro-RMN. The seeds are pea, sugar beet, and Medicago as a scientific reference in plant science. These seeds are sown in sand with water and maintained vertical in a homogeneous field region. Experiments were conducted with a Bruker Avance DRX300 equipped with a vertical superwide-bore magnet and a Bruker Biospec 70/20 Avance III.

Results: For illustration, Fig. 1 displays the fractional anisotropy observed in DTI on a seedling of Medicago. An hypersignal in blue in Fig. 1 corresponding to strong vertical fractional anisotropy all along the middle axis of the seedling is observed.

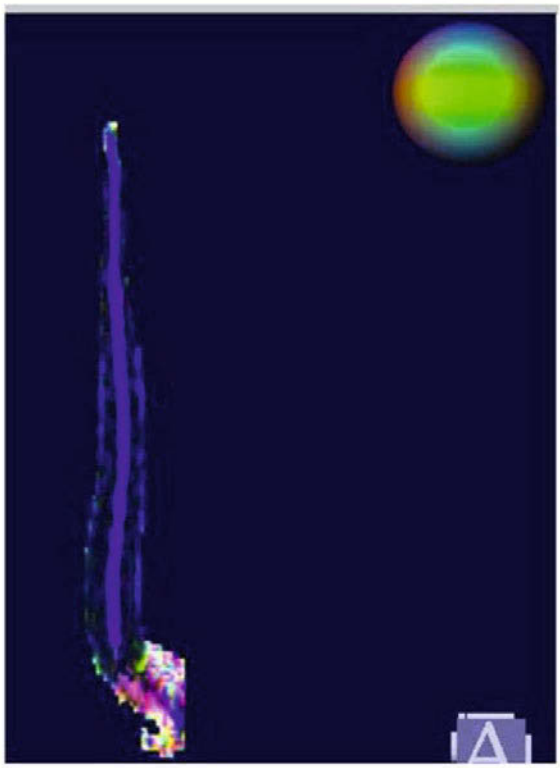

Fig. 1 A fractional anisotropy map in DTI of a seedling of Medicago.

Discussion/Conclusion:

These observations are compatible with the existence of specific cells in the seedling core, which constitutes a channel for nutrient transport as shown in Fig. 2. From the viewpoint of water diffusion our results reveal that there is no contrast between radicle and hypocotyl.

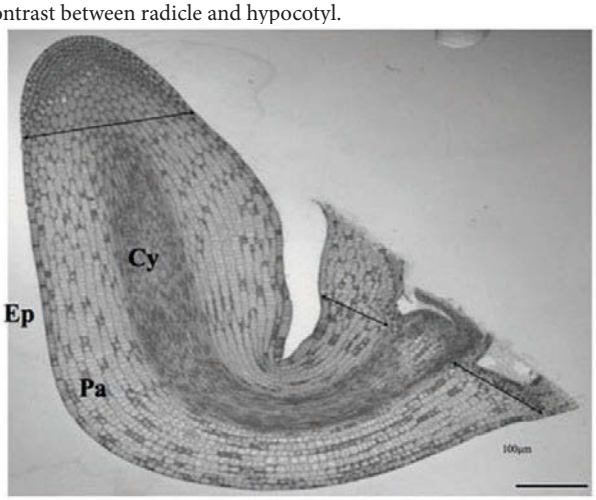

Fig. 2 Longitudinal section of hypocotyl from imbibed seeds (reproduced from [3]). Black arrows are limits for hypocotyl ; Cy central cylinder; Ep, epidermis; Pa parenchyma.

References:

[1] Borisjuk L., et al, "Surveying the plant's world by magnetic resonance imaging", The Plant Journal (2012) 70, 129–146.

[2] Belin E., et al, "Thermography as a non invasive functional imaging for monitoring seedling growth", Computers and Electronics in Agriculture (2011) 79, 236-240.

[3] Pierre J., et al. "Combined ecophysiological and transcriptomic analysis of medicago truncatula seedling growth in cold conditions." 10th *ISSS Conference*, *2011*, Brazil.

Work supported by ANR "Investissements d'Avenir" AKER program.

583

Microscopic MRI velocimetry of flowing liquids in comparison with numerical simulations

D. Edelhoff[1], F. Frank[1], M. Heil[1], L. Walczak[2], F. Weichert[2], D. Suter[1]

[1]Experimental Physics III, TU Dortmund, Dortmund/GERMANY, [2]Computer Sience VII, TU Dortmund, Dortmund/GERMANY

Purpose/Introduction: Altered blood flow is associated with various cardiovascular diseases such as arteriosclerosis. It induces abnormal wall shear stress or the formation of thrombosis. The exact knowledge of the flow behavior can provide information about treatment options, risks, or initial reasons for patient-specific diseases. [1,2] We characterize microscopic flow distributions within different model geometries with time-of-flight as well as phase-contrast MRI. These data were compared to numerical simulations [3] as well as analytical solutions in order to access the accuracy of these methods.

Subjects and Methods: We use a 14 T NMR spectrometer equipped with a 1 T/m gradient unit to acquire images with microscopic. The experimental setup generates velocities typically occurring in the human arterial system (approx. 5-50 cm/s). The used model geometries consisting of PVC tubes and glass phantoms, modeling aneurysms, stenosis or simple vessels. Phase Contrast MRI as well as time-of-flight measurements were performed to obtain a precise image of the velocity vector field with a resolution of 300 x 27 x 27 μm^3.

Results:

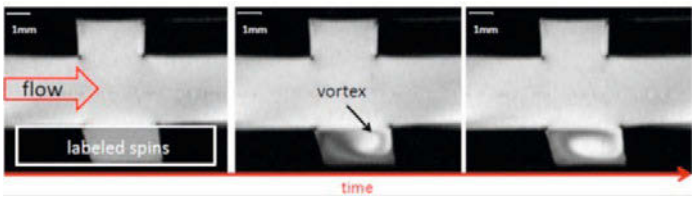

Fig. 1: Images of time of flight measurements of a simple aneurysm phantom. The first image visualizes the observed geometry and the labeled area whereas the following images show the time-dependent evolution of the labeled spins (dark) and the development of a vortex inside the aneurysm which appears bright due to the inflowing unlabeled spins.

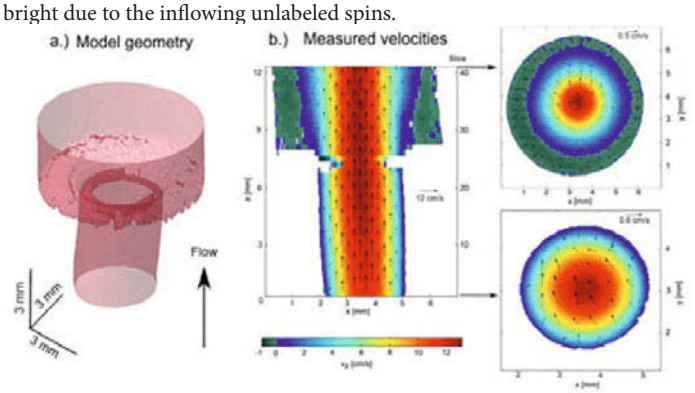

Fig. 2a. : Reconstructed stenosis geometry from a phase contrast MRI dataset. Fig. 2b : cross-sections through the measured velocity distribution. The slow recirculating flow in the outer region of the wider section arises from vortices in this area.
Compared to numerical methods we achieved very good agreements with 2 % deviation between measured and computed velocities within the shown stenosis phantom, while in further systems the deviation decreases to less than 1 %.
Discussion/Conclusion: NMR microscopy is an excellent tool for characterizing the stationary flow behavior in different model geometries with high spatial resolution and can provide experimental datasets for fluid dynamics simulations. Furthermore these methods can be used to characterize the formation of cardiovascular diseases with high spatial resolution for future applications within real arterial samples.
References:
[1] Boussel et al., Aneurysm growth occurs at region of low wall shear stress, Stroke, 39:2997-3002, 2008
[2] Hathcock, Arteriosclerosis, Thrombosis, and Vascular Biology, Journal of the American Heart Association, 26: 1729-1737, 2006
[3] Walczak et al., Exploring Therapy Options with an Interactive Simulation of Intra-Aneurysmal Blood Flow on the GPU, GI-Jahrestagung, 1745-1754, 2012

EPOS™ Poster

Primary brain tumours: Animal models and humans

584

Fitting the Two-Compartment Filtration Model in Renal DCE-MRI by Linear Inversion

D. Flouri[1,2], D. Lesnic[2], S. Sourbron[1]
[1]*Division of Medical Physics, University of Leeds, Leeds/UNITED KINGDOM,* [2]*Department of Applied Mathematics, University of Leeds, Leeds/UNITED KINGDOM*

Purpose/Introduction: Improvements in DCE-MRI data quality have led to the development of increasingly complex tissue models, such as the two-compartment renal filtration model (2CFM) [1]. A practical limitation of these models is the need for non-linear least squares fitting. This is prohibitively slow for pixel-by-pixel analysis, and is biased by the choice of initial values. The aim of this study is to develop a linear approach to fitting the 2CFM and use simulations to compare it to the non-linear method.

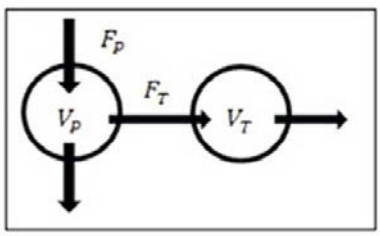

Figure 1: The 2-Compartment model

Subjects and Methods: The analytical solution of the 2CFM (Fig.1) provides a relation between the concentration-time curves in tissue C(t) and a feeding artery $C_A(t)$.

$$C(t) = \left(\frac{V_P}{T_P}e^{-t/T_P} + \frac{V_T}{T_P T_T}e^{-t/T_T} * e^{-t/T_T}\right) * C_A(t) \qquad (1)$$

The model parameters represent volumes and transit times of plasma and tubuli, * denotes convolution. Parameter values can be determined by non-linear least-squares fitting. To derive a linear inversion method, the derivatives of C(t) are combined into a second-order equation [3]:

$$\frac{-C(t)}{T_P T_T} - \left(\frac{1}{T_P}+\frac{1}{T_T}\right)\frac{dC(t)}{dt} + \frac{V_P}{T_P}\frac{dC_A(t)}{dt} + \left(\frac{V_P+V_T}{T_P T_T}\right)C_A(t) = \frac{d^2C}{dt^2}(t) \qquad (2)$$

The need for numerical differentiation is removed by integration over time [4]. With *N* time points this forms a matrix equation:

$$\underset{N\times 4}{\begin{bmatrix} A \end{bmatrix}} \quad \underset{4\times 1}{[x]} = \underset{N\times 1}{\begin{bmatrix} B \end{bmatrix}}$$

By using the linear least-squares methods, the parameters can be derived. For the simulations, C(t) was calculated at a pseudo-continuous temporal resolution (0.1s), using a literature based $C_A(t)$ [2]. C(t) and $C_A(t)$ were then downsampled at TR=1s intervals for 5 min, where the initial sampling point t_0 was randomly and uniformly distributed over the interval [0,TR]. Gaussian noise was added with zero mean and standard deviation p*max(C_A) with p=0, p=0.01 and p=0.03. All simulations were repeated 10000 times.

Results: The linear method is faster by a factor of approximately 8. In the noise-free simulations, values for the linear method are narrowly distributed around the exact values (Fig.2a); histograms for the non-linear method are bi-modal, with one peak near the initial values, and a second near the exact value. When noise is added (Fig.2b,c), the linear method becomes increasingly inaccurate, while the non-linear method is less affected (Table 1).

Discussion/Conclusion: While the linear fitting algorithm is faster and more accurate for noise-free data, the non-linear algorithm is more accurate in the presence of noise.The instability of the linear method for noisy data is currently unclear. Future studies will aim to identify the source of the problem by studying simpler models [4] and alternative time discretisations [3].

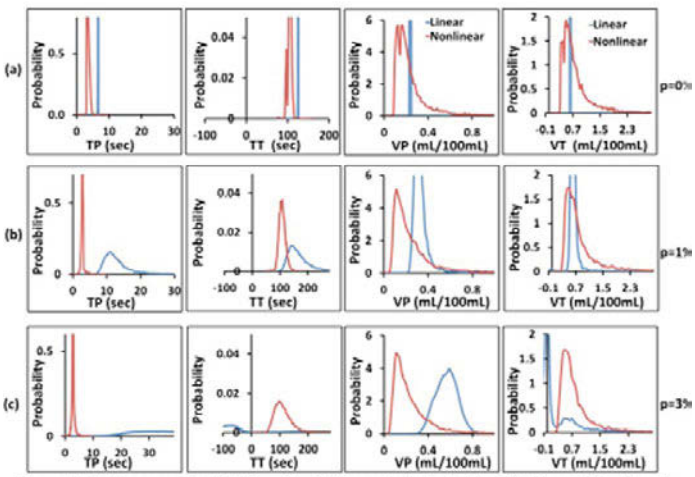

Figure 2: Histograms for T_P, T_T, V_P, V_T (from left to right) with linear (blue) and non-linear (red) methods. The histograms of T_T and V_T for $p = 3\%$ are truncated for reasons of clarity.

Parameter	Exact value	Noisy input	Linear	Non-linear
TP	6.5	p=0%	6.6 (0.02)	3.4 (1.2)
		p=1%	12.0 (13.4)	2.84 (0.67)
		p=3%	36.4 (46.6)	2.83 (1.16)
TT	125	p=0%	125 (0.1)	105 (15)
		p=1%	158.6 (183.7)	107 (38.6)
		p=3%	-105.4 (2764.1)	105.8 (98.1)
VP	0.24	p=0%	0.24 (0.00025)	0.19 (0.5)
		p=1%	0.32 (0.18)	0.19 (0.65)
		p=3%	0.57 (0.33)	0.19 (0.61)
VT	0.63	p=0%	0.62 (0.0003)	0.65 (1.6)
		p=1%	0.61 (0.2)	0.66 (1.84)
		p=3%	-0.01 (3.5)	0.66 (1.81)

Table 1: Median and 90% confidence interval of the 4 model parameters estimated using Linear Least-Squares method and the Non-linear Least-Squares method as a function of noisy input.

References:
[1]Sourbron SP et al 2008 *Invest Radiol* 43: 40-8
[2]Parker GJM et al 2005 *Magn Reson* Med 56: 993-1000.
[3]Zeng G L et al 2012 *Phys Med Biol* 57: 5809-5821.
[4]Murase K 2004 *Magn Reson* 51: 858-862.

585

High Temporal Resolution Mouse Renal Blood Flow (RBF) Imaging with pseudo-continuous ASL (pCASL) at very High Field

V. Prevost, O.M. Girard, P. Cozzone, G. Duhamel
Aix Marseille Université - CNRS 7339, CRMBM, Marseille/FRANCE

Purpose/Introduction: Non-invasive and reliable assessment of the renal perfusion is important for many diseases. Arterial Spin Labeling (ASL), which offers a simple quantification model and blood contrast specificity without any contrast agent injection is a well adapted tool for non invasive perfusion imaging. A recent study[1] demonstrated the advantage of the pseudo-continuous ASL approach in terms of sensitivity for mouse renal perfusion measurement. In the present study, we investigated more deeply pCASL in combination with fast imaging EPI, TrueFISP and RARE in order to determine the most adapted protocol in terms of sensitivity, reduced scan time, multislice acquisition and imaging orientation for mouse renal perfusion imaging.
Subjects and Methods: Experiments were performed at 11.75T on anaesthetized mice (n=7). pCASL was combined with 2shot SE-EPI, single shot RARE and TrueFisp for the acquisition of perfusion images (200x220µm^2 resolution) in the axial (single slice and multislice) and coronal planes. Data were averaged between 1 and 4 minutes.
Results:

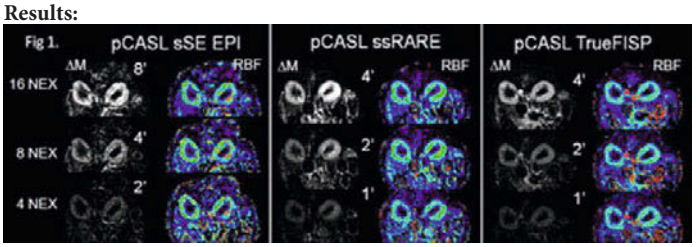

Fig.1 shows axial pCASL perfusion maps obtained with EPI, TrueFISP and RARE imaging for different total acquisition time (TA). Due to segmentation of the readout, EPI was less efficient in terms of signal per unit of time, leading to less data averaging and therefore lower ASL signal for a given acquisition time ($\Delta M^{TrueFISP} \geq \Delta M^{RARE} > \Delta M^{EPI}$). In terms of sensitivity though, higher values were obtained for pCASL EPI ($\Delta M/M_0^{EPI}$=16.1±3.6%, $\Delta M/M_0^{TrueFISP}$=13.5±1.2%, $\Delta M/M_0^{RARE}$=13.1±2.1%). These high sensitivity values allowed accurate RBF quantification for all the imaging modules (Fig1): (TA=4') RBF^{EPI}=679±149ml/100g/min, RBF^{RARE}=545±95ml/100g/min and $RBF^{TrueFISP}$=577±60ml/100g/min. The acquisition time could be decreased to 1' while keeping accurate values for TrueFISP and RARE with lower standard deviation obtained with TrueFISP (10% vs 23%).

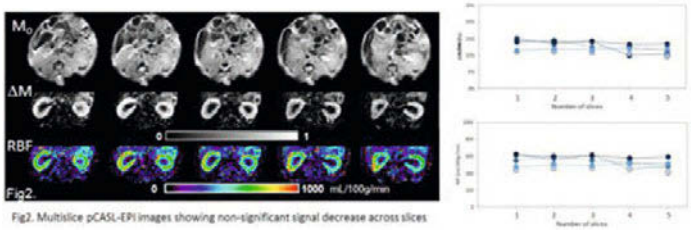

Fig2. Multislice pCASL-EPI images showing non-significant signal decrease across slices

For multislice imaging, the short acquisition train length of EPI (25ms) allowed acquiring up to 5 slices with minimal ASL signal loss and RBF underestimation for the distal slices (Fig2). Multislice perfusion imaging in a single session was not possible with long acquisition train techniques RARE (200ms) and TrueFISP (130ms).

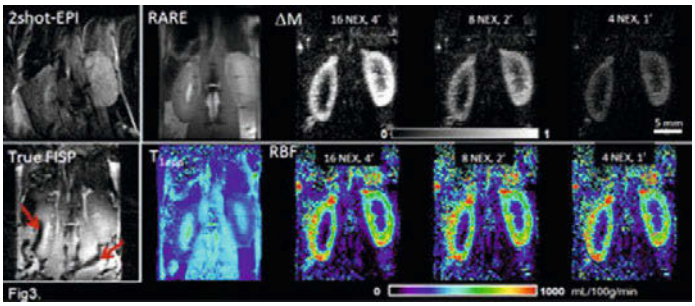

Finally, for coronal perfusion imaging, best results were obtained with pCASL RARE which provided good image quality, high contrast and a decent robustness to motion (Fig3).
Discussion/Conclusion: pCASL combined with fast imaging allowed obtaining RBF maps (200x200µm2 of spatial resolution) in less than 4 mins. TrueFISP should be preferred for single slice axial imaging (high sensitivity and low dispersion); EPI is ideal for multislice imaging (short acquisition train length) and for coronal imaging, pCASL combined with single-shot RARE appeared to be very robust.
References:
[1]Duhamel and al,MRM 2013

586

Quantification of ADC and SUV values in patients with cervical cancer or lymph node metastases using a simultaneous PET-MRI system

P. Brandmaier[1], S. Purz[2], H. Barthel[3], O. Sabri[3], T. Kahn[1], **P. Stumpp**[1]
[1]Radiology, University Hospital Leipzig, Leipzig/GERMANY, [2]Nuclear medicine, University Hospital Leipzig, Leipzig/GERMANY, [3]Nuclear Medicine, University Hospital Leipzig, Leipzig/GERMANY

Purpose/Introduction: The correlation between metabolic PET-CT data (standardized uptake value, SUV) and functional MRI data (apparent diffusion coefficient, ADC) in different tumor entities has so far been controversial (1). The purpose of this study was to evaluate whether a simultaneous PET-MRI examination provides more reliable SUV and ADC values in patients with primary and recurrent cervical cancer as well as suspicious lymph nodes.
Subjects and Methods: We included 17 patients (54 ± 14 y. o.) with cervical cancer (12 lesions) or lymph node metastases (22 lesions) who underwent simultaneous whole-body 18F-fluorodeoxyglucose (FDG) PET-MRI. MRI consisted of T2-HASTE, TIRM and EPI-DWI sequences (b= 0 and 800 mm/s^2) and also included a dedicated pelvic examination using T2-TSE, pre- and post-contrast T1-TSE (with and without fat suppression) and EPI-DWI (b= 0, 50, 400, 800 mm/s^2). One reader defined volumes of interest for ADC and SUV in suspicious cancer areas and regions of maximum FDG uptake in positive lymph nodes with short axis diameters above 5 mm. ADC-min, ADC-mean, ADC-ratio (=ADC_{min}/ADC_{mean}), SUV-min, SUV-max and SUVmean were calculated using the gluteus maximus muscle as reference non – tumor tissue tissue. Lesions were simultaneously analyzed on a dedicated workstation (*syngo.via*, Siemens Medical Solutions, Erlangen, Germany). Pearson's *r* was computed between five combinations of ADC and SUV values.
Results: Cancer lesions generally showed higher SUV-max and lower ADC-min values than lymph node metastases. Values in all lesions were significantly different from those in reference tissue. Pearson testing revealed strong (significant) inverse correlations between ADC-mean and both SUVmean (*r*=-0.613) and SUV-max (*r*=-0.605) in cancer lesions and weak correlations at best (*r*=-0.254 for ADC-mean versus SUV-mean) in lymph node metastases.
Discussion/Conclusion: Functional (ADC) and metabolic (SUV) parameters could be successfully determined in a simultaneous PET-MRI examination.

The strongest inverse correlation was observed between ADC-mean and either SUV-mean or –SUV-max in tumor lesions.

References:

(1) Functional imaging of head and neck squamous cell carcinoma with diffusion-weighted MRI and FDG PET/CT: quantitative analysis of ADC and SUV. Varoquaux A, Rager O, Lovblad KO, Masterson K, Dulguerov P, Ratib O, Becker CD, Becker M.

587

Increasing tumor grade separability by combining MR parameters

N.P.L. Sauwen[1,2], D.M. Sima[1,2], S. Van Cauter[3], J. Veraart[4], U. Himmelreich[5], S. Van Huffel[1,2]

[1]Electrical Engineering - ESAT/SCD, KU Leuven, Leuven/BELGIUM, [2]KU Leuven Future Health Department, iMinds, Leuven/BELGIUM, [3]Radiology, University Hospitals Leuven, Leuven/BELGIUM, [4]Vision Lab, University of Antwerp, Antwerp/BELGIUM, [5]Biomedical MRI unit / MoSAIC, Imaging and Pathology, KULeuven, Leuven/BELGIUM

Purpose/Introduction: MR diffusion, perfusion and spectroscopic data provide complementary information in brain tumor grading. We show that combining MR parameters of different modalities can improve diagnostic accuracy.

Subjects and Methods: MR data: MR data were acquired on a 3T Philips Achieva scanner from 5 glioma patients: 2 grade II astrocytomas, 1 grade II oligodendroglioma, 2 grade IV glioblastomas. DSC-MRI was acquired with a GE-EPI sequence: TR/TE=1350/30msec, with 60 dynamic scans during the first pass of a 0.1mmol/kg body weight bolus of Dotarem (Guerbet) injected at 4ml/sec. Cerebral Blood Volume (CBV) values were calculated using DPTools (www.fmritools.org). DKI data were acquired using an SE-EPI sequence: TR/TE=3200/90msec, δ/J=20/48.3msec, b=700,1000,2800sec/mm2. Mean Diffusion (MD) and Mean Kurtosis (MK) values were calculated as in [1]. MRSI data were acquired using PRESS volume selection, TR/TE=2000/35msec, MOIST water suppression, receiver bandwidth=2000Hz. AQSES-MRSI [2] was used for metabolite quantification. All imaging modalities were coregistered to anatomical data.

Analysis: Perfusion and diffusion maps were normalized with respect to NAWM. 5 parameters were considered: CBV, MD, MK, Lips/TCho (Lipids over total Choline) and Cre/sum (Creatine over summed metabolites). All voxels in the active tumor ROIs were included, resulting in class C1 of 1821 low-grade glioma voxels and class C2 of 873 high-grade glioma voxels (Fig.1).

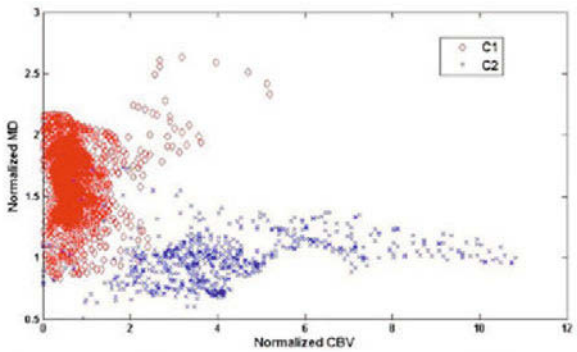

Fig.1: Scatter plot of CBV versus MD for LGG class C1 and HGG class C2

Intra-class Homogeneity and inter-class Separation were computed:

$$Hom_{C_i} = \frac{1}{N_{C_i}} \sum_k D(x_k, \mu_{C_i})$$

$$Sep_{C_i,C_j} = D(\mu_{C_i}, \mu_{Cj})$$

with N_{Ci} the number of data points in class C_i, D a distance measure, x_k the k^{th} point in class C_i and μ_{Ci} the class centroid. Mahalanobis is used as distance measure, taking into account the directional spread of the data. Based on *Hom* and *Sep*, the HS-index is calculated:

$$HS_{C_i,C_j} = Sep_{C_i,C_j} - Hom_{C_i}$$

Results: Table1 and Table2 show HS-indices of C1 with respect to C2 and vice-versa. The HS-values on the diagonal are for 1 parameter only. Green cells indicate the combinations for which the HS-index is increased with respect to both parameters' individual HS-values. The HS-value when combining all parameters is shown at the bottom of the table.

	Lips/TCho	Cre/sum	CBV	MD	MK
Lips/TCho	5,98	6,29	9,31	5,67	5,64
Cre/sum		0,59	6,30	1,09	0,71
CBV			6,64	6,80	6,45
MD				1,46	1,15
MK					0,44
All params	15,51				

Table 1: $HS_{C1,C2}$ values for combined MR parameters

	Lips/TCho	Cre/sum	CBV	MD	MK
Lips/TCho	1,01	2,04	1,22	2,66	1,40
Cre/sum		2,09	2,73	3,03	2,44
CBV			1,01	3,66	1,87
MD				2,72	2,69
MK					1,33
All params	6,67				

Table 2: $HS_{C2,C1}$ values for combined MR parameters

Discussion/Conclusion: The separability of tumor grade classes can improve by combining certain MR parameters. However, a slight decrease of the combined HS-index is found for other combinations. For all parameters combined, the HS-index is higher than for any combination of 2 parameters. Tumor grade separability can be maximized by considering the optimal combination of parameters.

References:

1. Veraart J. et al, "Comprehensive framework for accurate diffusion MRI parameter estimation", Magn. Reson. Med. 2012, Epub ahead of print
2. Croitor Sava A.R. et al, NMR Biomed. 2011 Aug;24(7):824-35.

588

Longitudinal T1 mapping for the follow-up of patients with abdominal solid tumors

M.-E. Cohen[1], F. Frouin[1], S. Raslan[1,2], M. Lefort[1], A. De Cesare[1], C. Pellot-Barakat[1], O. Lucidarme[1,2]

[1]Laboratoire d'Imagerie Fonctionnelle, UPMC/INSERM, Paris/FRANCE, [2]Radiologie générale et oncologique, AP-HP, CHU Pitié Salpêtrière, Paris/FRANCE

Purpose/Introduction: Dynamic MRI with contrast injection is generally used to characterize the micro vasculature in patients with abdominal solid tumors. Response Evaluation Criteria in Solid Tumors (RECIST) [1] are conventional morphological criteria to evaluate the tumor response to a treatment. This work proposes a new approach based on the T1 mapping to quantify the tumor response.

Subjects and Methods: Seven patients with abdominal solid tumors were examined using a dedicated MRI protocol before and during the course of

an antiangiogenic treatment (Cetuximab® and Temsirolimus® association), resulting in 18 datasets. Flip angle volumes (2°, 8°, 12°, 18° and 24°) were specifically acquired (TR= 3.79 ms, TE= 1.25 ms, voxel size= 0.8x0.8x5 mm³). To evaluate the tumor response, the relative variation of the lesion diameters (RECIST criteria) was computed. T1 maps were computed using the 5 flip angle volumes [2]. In order to reposition each post-treatment T1 volume with its corresponding pre-treatment T1 volume, a longitudinal registration is needed. Four rigid registration methods (mutual information, mutual information after thresholding, mutual information with gradients, and chamfer matching) were tested. The best registration was selected by visual inspection. Finally T1 variations were calculated in boxes surrounding the tumors. Their relative variations were compared to the RECIST measures.

Results: Figure 1 shows the T1 maps corresponding to the pre-treatment (a), and post- treatment (b) examinations as well as the color map (c) corresponding to the subtraction between the registered pre and post-treatment examinations . High variations of T1 values (red) appear on the tumor borders and low values (blue) inside the tumor. Null variations are coded in green. A correlation (r=0.49) was observed between longitudinal relative variations of RECIST measures and variations of T1 values inside tumoral regions (n=11).

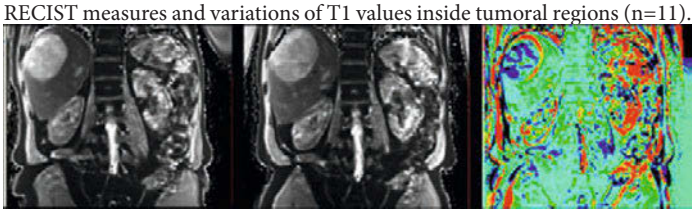

Figure 1(a,b,c)

Discussion/Conclusion: T1 mapping after longitudinal registration can be used to evaluate the tumor response to an antiangiogenic treatment. Comparison with RECIST criteria indicate a good matching for important variations (increases or decreases) of tumor diameters (n=6). Modifications of T1 with low variations of tumor diameter need to be further investigated. This new procedure could be optimized by modifying the number and values of flip angles and the registration procedure, including non rigid approaches. Although results need to be confirmed on a higher number of patients, they already reveal a potential interest of this parameter for longitudinal follow-up.

References:

[1] EA Eisenhauer et al, European Journal of Cancer 2009, 45:228–247
[2] HLM Cheng et al Magnetic Resonance in Medicine, 2006, 55:566-574

589

(b)SSFP sequences with navigator based retrospective motion correction for in vivo iron-labeled cancer cell and metastases detection in the mouse liver at 7T

E.J. Ribot, T. Duriez, A. Trotier, J.-M. Franconi, S. Miraux
CNRS/University, RMSB Center, Bordeaux/FRANCE

Purpose/Introduction:

Cellular MRI using iron-based nanoparticles allows for the detection of single cancer cells in vivo in the mouse brain [1,2]. Furthermore, brain tumors can be easily delineated due to their high contrast [3]. However, respiratory motion, susceptibility artefacts and low SNR prevent accurate detection of labeled-cells and tumor volume measurement in the abdomen, notably in the liver, and particularly at high magnetic field. Our study describes the use of navigator echo method in combination with 3D- SSFP (Fisp) and 3D-bSSFP (TrueFisp) MRI sequences to correct these artefacts.

Subjects and Methods:

Bl6/Ctrl mice were injected via the mesenteric vein with murine melanoma cells (B16F10) previously labeled with MPIO (micron- sized iron particles). Mice were imaged on a horizontal 7T small-animal scanner (Bruker) at day 1, 8 and 15.

The MRI resolution was 117x172x156µm. The flip angle was set to 20° and 10° for the TrueFisp and Fisp sequences, respectively. Four phase offsets were used to reconstruct by sum-of-scare TrueFisp images.

A navigator echo was inserted into both sequences by turning on the ADC right after a non-selective RF pulse. Retrospective image reconstruction was performed by deleting the respiration corrupted k-space lines. As 8 and 4 repetitions were set for Fisp and TrueFisp sequences respectively, missing lines in one k-space were filled by the k-space of other repetitions.

Results:

The navigator echo correction induced artefact-free MR images using both Fisp and TrueFisp sequences. Although liver SNR was higher on Fisp (34.3) than on TrueFisp images (27.1), liver-to-kidneys contrasts were lower on Fisp (2) than on TrueFisp images (21). Iron-labeled cancer cells were easily detected as voids with similar FSL (1.3) on Fisp and TrueFisp images. Liver metastases with diameters smaller than 1mm were detected due to natural T2-like contrast. Accurate measurements of metastases volumes were performed on TrueFisp images due to high CNR (25.8) compared to Fisp images (13.2).

Discussion/Conclusion:

Fisp and TrueFisp sequences performed with a retrospective method involving a navigator echo allowed for the in vivo detection of iron-labeled cancer cells and melanoma metastases in the liver of mice, by correcting breathing artefacts. These 3D images allows for in vivo cancer cell tracking in the abdomen on living mice, and will be useful tools to better understand cancer cell dissemination and evaluate cancer therapies.

References:

[1]- Heyn C et al. MRM 2006;55:23–29.
[2]- Shapiro E et al. PNAS 2004;101(30):10901–10906
[3]- Miraux S et al. JMRI 2008;28:497–503

590

Increased magnetic resonance image contrast by Synthetic PArameter-weighted images based on Relaxometry (SPARE) at 9.4T

D. Milford[1], M. Weiler[2,3], M. Fischer[1], T. Keßler[2], M. Bendszus[4], S. Heiland[1]
[1]Section Exp. Radiology, Department of Neuroradiology, University Hospital of Heidelberg, Heidelberg/GERMANY, [2]Clinical Cooperation Unit Neurooncology, German Cancer Reseach Center (DKFZ), Heidelberg/GERMANY, [3]Neurology Clinic, University Hospital of Heidelberg, Heidelberg/GERMANY, [4]Department of Neuroradiology, University Hospital of Heidelberg, Heidelberg/GERMANY

Purpose/Introduction:

High magnetic field strength offers a high signal to noise ratio (SNR) which in turn allows for higher resolution. One issue of higher field strengths is the convergence of the relaxation times which limit contrast between tissue types [1]. Furthermore, It was shown that as the field strength increases the contrast between normal tissue and contrast enhance region goes down [2]. It is for this reason that quantitative mappings (of the T1 and T2 relaxation times) are of importance, as they offer a means of gaining knowledge of a pathological region without relying on signal contrast alone. Another benefit of attaining these quantitative maps, are the parametric weighted images that can be synthesized. Synthesizing the images was first presented by Ortendahl et al.[3] in 1984 and again in 1994 by Zhu et al.[4]. Although the technique showed promise the problem for both was the limited SNR available for optimal quantitative mapping of T1 and T2 relaxation times. Here we present a program for Synthetic PArameter weighted images based on RElaxometry (SPARE) at 9.4T. It is shown that desired contrast can be obtained offline and with a higher enhancement of a contrast agent (CA).

Subjects and Methods:
With the use of MRI relaxometry (before and after CA) of mouse brains with implanted tumors, we calculate quantitative maps (Q-maps) with an in house developed program. These Q-maps are used for the synthesization of different parametric weighted images offline and compared to standard acquired images of the same weightings.
Results: With the use of the SPARE technique, contrast between tissue increases and the noise, within the image, is reduced. It is further shown that unattainable parameters at the MR scanner can be achieving though synthesis, allowing for higher enhancement and tissue differentiation. Furthermore, SPARE using T2 Q-maps alone, allows visualization of CA enhance tumors and high image contrast between the bounding tissue.
Discussion/Conclusion: Parameter-weighted images reconstructed retrospectively with SPARE offers higher tissue contrast and reduced noise for different combination of TR and TE. Using the SPARE technique thus offers a solution for overcoming the lost contrast due to the convergence of T1 at high magnetic field strengths.
References:
1. Korb, J.P. and R.G. Bryant, Magn Reson Med, 2002. **48**(1): p. 21-6.
2. Rinck, P.A. and R.N. Muller, Eur Radiol, 1999. **9**(5): p. 998-1004.
3. Ortendahl, D.A., et al., Magn Reson Med, 1984. **1**(3): p. 316-38.
4. Zhu, X.P., C.E. et al., Br J Radiol, 1994. **67**(802): p. 976-82.

591

Multimodal imaging in the characterization of a rat model of glioblastoma by using MRI and 18F-FDG PET/CT

M.C. Vieira-Leite, P. López-Larrubia
Experimental animals for human diseases, Instituto de Investigaciones Biomédicas Alberto Sols, madrid/SPAIN

Purpose/Introduction: Glioblastoma is the most frequent primary brain tumour but despite the advances achieved in the last decades in treating human malignancies, its prognosis has not experienced a great change (1). In this line, magnetic resonance imaging (MRI) is the most used and versatile tool used nowadays (2), and PET/CT has become of clinical importance as it can also offer additional metabolic information with a high sensitivity (3,4). This study aimed to characterize a rat model of glioma C6, by using multiparametric MRI and comparing results with the data provided by 18F-FDG-PET/CT.
Subjects and Methods: Male Wistar rats (N=17) were submitted to a surgical injection of 10^5 C6 cells in their right caudate-putamen. Sham animals (N=5) were used as a control group. All the individuals were studied with MRI, when tumour's volume was 10-100 mm^3, using a 7T system and the following protocol: T2, T2* and T1 weighted images to yield relaxation time maps, diffusion tension imaging (DTI) to obtain mean diffusivity (MD) and fractional anisotropy (FA) maps, and magnetization transfer (MT) to determine the MT ratio maps. Colour based maps were computed pixel-by-pixel, by fitting the signal to the appropriate equation, using a home-made software developed in Matlab. Data were analysed by selecting ROI's in the tumour, contralateral hemisphere and healthy tissue. Six animals (5 tumour-bearing and 1 control) were also submitted to an 18F-FDG-PET/CT study, analysing ROI's in the tumour, contralateral hemisphere and liver.
Results: Results are shown in figures 1-6. Tumour ROI´s compared with Sham animals, showed significantly different values of MTR, T1, T2 and T2*. The comparison between the tumour region and its contralateral hemisphere was also relevant on the MT, MD, T1, T2 and T2* measurements. By comparing the tumour and healthy tissue, there were significant differences on MT, FA, T1 and T2. PET/CT images showed tumour regions with significantly higher SUV values when compared to their contralateral, although a clear correlation between the SUV values and the MRI parameters could not be found.

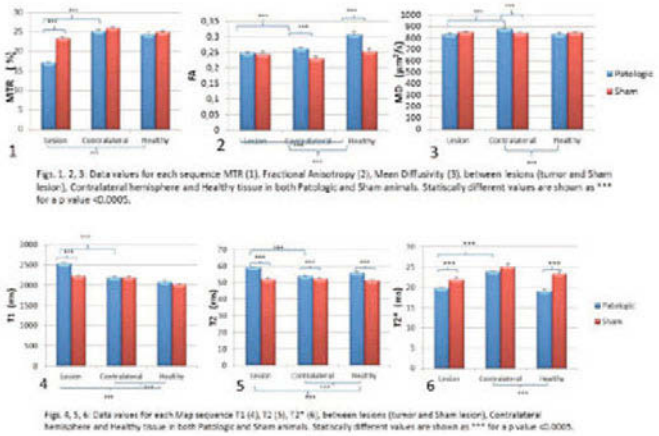

Figs. 1, 2, 3: Data values for each sequence MTR (1), Fractional Anisotropy (2), Mean Diffusivity (3), between lesions (tumor and Sham lesion), Contralateral hemisphere and Healthy tissue in both Pathologic and Sham animals. Statically different values are shown as *** for a p value <0.0005.

Figs. 4, 5, 6: Data values for each Map sequence T1 (4), T2 (5), T2* (6), between lesions (tumor and Sham lesion), Contralateral hemisphere and Healthy tissue in both Pathologic and Sham animals. Statically different values are shown as *** for a p value <0.0005.

Discussion/Conclusion: There are significant differences in MRI parameters related to inflammation, oedema and hypoxia between tumour areas and both the contralateral hemisphere and healthy. 18F-FDG-PET/CT images provided a new type of information, which can be used additionally to the MRI data. This characterization can help in the proper selection and follow-up of patients who will benefit from tailored therapies, mainly those targeting angiogenesis and inflammation.
References:
1.Cancer.J, 2012;18:89–99
2.López-Larrubia,P. et al. Cap.12, ISBN:978-953-307-284-5
3.Am.J.Roent 2008;190:W365–W369
4.Am.J.Neuroradiol 2013;34:944-950

592

Multiparametric MRI characterization of the tumoral and inflammatory microenvironmentof a glioma rat model in two growth stages.

A. Amor-López, **P. López-Larrubia**
Departamento de Modelos experimentales de enfermedades humanas, Instituto de Investigaciones Biomédicas, CSIC-UAM, Madrid/SPAIN

Purpose/Introduction: Alterations in inflammation and microvasculature underlying the most complicated brain pathologies, like cancer. A deeper characterization of the inflammatory and tumoral microenvironment would improve the diagnosis and prognosis of neoplastic process and the validation of new-targeted therapies. In this line, MRI is established as a powerful tool for obtaining structural, functional and molecular information[1,2].
Subjects and Methods: Experiments were carried out using sham adult male Wistar (n=5) and glioma bearing animals in two stages of the tumor growth (early, n=10, tumors≤50µl; late, n=10 tumors≥75µl).
MRI experiments were performed on a 7.0-T horizontal system equipped with a ^1H selective birdcage resonator. The imaging protocol was: Magnetization transfer, MT (TR/TE= 2500/9.85 ms, 50 pulses, 5.5 µT, 1500 Hz); diffusion tensor imaging, DTI (TR/TE= 3000/40 ms, Δ/δ= 20/4 ms, 7 directions, b values 300 and 1400 s/mm^2); and dynamic contrast enhanced, DCE (TR/TE= 100/6 ms, 50 repetitions)
Images were computed on a pixel-by-pixel basis using My Map Analizer (in-house software developed in Matlab) and the obtained parametric maps were analyzed in three brain regions: tumor, contralateral hemisphere and apparently healthy tissue.
Results: Figures 1-4 depict the main results. Values measured in all cases showed significant differences between the regions and groups of animals assesed. Changes in MT and MD values are linked to the tumor progression,

the concomitant inflammation and edema. MT (fig.1) decreased in tumor compared with non-tumoral regions, and increases in late stages indicating alteration in the macromolecular-bound proton pool associated with the pathology and its progression. MD (fig.2) reflected the extension of the cellular swelling due to the inflammatory process, taking place in the brain just the tumor growing. Decreases in FA (fig.3) were correlated with the structural integrity loss in the brain because of the tumor´s presence. A higher ΔSI of larger tumors in DCE studies was in accordance with the expected increase in the disruption of the microvasculature in the late stages.

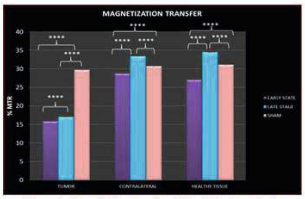

Figure 1. Magnetization transfer MRI obtained results by comparing rats with tumors in early and late stages, and Sham animals . (**** p ≤ 0.0001)

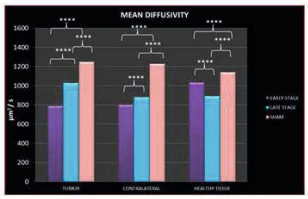

Figure 2. Mean diffusivity from diffusion tensor imaging obtained results by comparing rats with tumor in early and late stages, and Sham animals. (**** p ≤ 0.0001)

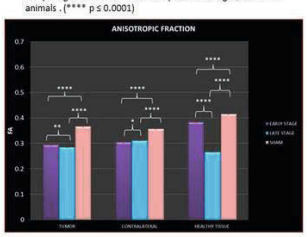

Figure 3. Anisotropic fractionfrom diffusion tensor imaging obtained results by comparing rats with tumor in early and late stages, and Sham animals. (**** p ≤ 0.0001)

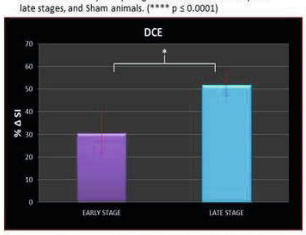

Figure 4. Changes in the signal intensity form DCE-MRI studies by comparing rats with tumors in early and late stages, and Sham animals (* p ≤ 0.05)

Discussion/Conclusion: Multiparametric MRI studies in this glioma model have allowed establishing clear and significant differences between regions in the brain, associated with the development not only of the tumor but also of the associated inflammation. MTR and MD measurements have clearly indicated that apparently healthy regions in the brain are actually affected in the late stage of the tumor development. DCE analysis indicate either an increased in the vascular permeability in large tumors compared with smaller ones.

References:

1.Lizarbe B. et.al, Neuroimage.2013, 64:448-457. 2. Lopez-Larrubia P. et.al, Cap.12, 2012, ISBN 978-953-307-284-5

593

Molecular Imaging of Tumors and Metastases using Chemical Exchange Saturation Transfer (CEST) MRI

M. Rivlin[1], J. Horev[2], I. Tsarfaty[2], G. Navon[1]
[1]School of Chemistry, Tel Aviv University, Tel Aviv/ISRAEL, [2]Sackler School of Medicine, Tel Aviv University, Tel Aviv/ISRAEL

Purpose/Introduction: The increased glycolytic rate and glucose avidity of malignant cells (Warburg effect) in comparison to normal tissue is the basis of the ability of FDG-PET imaging to accurately differentiate cancer from benign tissue regardless of morphology. The two glucose analogs 2-deoxy-D-glucose (2-DG) and 2-fluoro-2-deoxy-D-glucose (FDG) are preferentially taken up by cancer cells, undergo phosphorylation and accumulate in the cells. Both 2-DG and FDG have 4 hydroxyl residues, which are potential candidates for Chemical Exchange Saturation Transfer CEST NMR/MRI. The method enables to detect low concentrations of metabolites that contain residues with exchangeable protons such hydroxyl[1].
In the present work we take advantage of the enhanced accumulation of 2-DG and FDG in tumors to obtain large CEST values and would like to suggest either 2-DG-CEST or FDG-CEST as a potential replacement of PET/CT or PET/MRI in the clinic for the detection of tumors and metastases, distinguishing between malignant and benign tumors and monitoring tumor response to therapy.
Subjects and Methods: CEST-MRI experiments were performed on implanted xenograph mammary tumors (DA_3) of mice injected with 2-DG or FDG, scanned at 7T MRI. A series of gradient-echo images were collected from a single 1 mm axial slice after presaturation pulse, applied at several frequency offsets from the water, to produce the desired CEST effect[2].
Results: The tumor exhibited a CEST effect of about 20% for mice injected with 2gr/kg of 2-DG and about 30% for mice injected with 1gr/kg of FDG. These high values are the combined results originating from the injected glucose analogs, their phosphorylated products and from other metabolic products. The diagnostic benefit and uniqueness of this technique, is that the method is sensitive enough to detect regional differences in tumor uptake. We have shown that 2-DG CEST MRI enables to distinguish between the viable parts of tumor from the necrotic region of the tumor, unlike the conventional anatomical images.
Discussion/Conclusion: This novel imaging modality will also shed a new light on tumor basal metabolism, expression of tumor markers and the metabolic alteration induced by constitutive activation of oncogenes in tumor development. We expect that the developed novel imaging modality will enable early detection of tumors, tumor response to therapy, and tumors metabolism noninvasively by using MRI, without the need for radio-labeled isotopes.

References:

(1) Ward, K. M.; Aletras, A. H.; Balaban, R. S. **2000** *J Magn Reson*, *143*, 79.
(2) Zhou, J.; Zijl, P. C. M. v. **2006** *Progress in Nuclear Magnetic Resonance Spectroscopy*, *48*, 109.

594

Robust Coregistration of Sestamibi SPECT and MR Images in Patients with High Grade Glioma: a revisited approach

J.-M. Tacchella[1, 2], E. Roullot[1], M.-E. Cohen[2], M. Lefort[2], M. Reynal[3], J.B. Martini[3], R. Guillevin[4], J.-Y. Delattre[5], G. Petrirena[5], M.-O. Habert[2, 6], N. Yeni[2, 6], A. Kas[2, 6], **F. Frouin**[2]
[1]PRIAM, ESME SUDRIA, Ivry sur seine/FRANCE, [2]Laboratoire d'Imagerie Fonctionnelle, Inserm/UPMC, Paris/FRANCE, [3]Centre d'Acquisition et de Traitement des Images, UPMC, Paris/FRANCE, [4]Service de Radiologie, Université de Poitiers and CHU Poitiers, Poitiers/FRANCE, [5]Service de Neuro-oncologie, AP-HP, CHU Pitié-Salpêtrière, Paris/FRANCE, [6]Service de Médecine Nucléaire, AP-HP, CHU Pitié-Salpêtrière, Paris/FRANCE

Purpose/Introduction: The usefulness of the Technetium-99m labeled Sestamibi SPECT modality in addition to the MRI modality has been suggested in therapy management for patients with high grade glioma [1]. The SPECT/MRI registration that is required for further data analysis is a complex preprocessing step due to the physiological distribution of the MIBI tracer. This work aims at proposing an efficient registration of SPECT/MRI data, which is optimized for each dataset.
Subjects and Methods: The database includes 62 SPECT/MRI datasets in patients with high grade glioma. The registration strategy consists in testing different methods and selecting the best one for each dataset thanks to a quantitative uptake criterion (UC), based on the physiological behavior of Sestamibi within particular anatomical structures [2]. The criterion relies on the high uptake of the tracer in the oculomotor muscles and pituitary gland and the low uptake in the eyeballs. Global strategy proceeds in 3 steps, embedded in the Brainvisa/Anatomist package: 1) a systematic application of 16 registration methods (Mn) derived from algorithms of Brainvisa and SPM software; 2) for each dataset, ranking of the 16 methods according to decreasing values of UC and selection of the best registration method, M* ; 3) visual assessment of M* as good, intermediate, or bad registration.

Results: Figure 1 shows an example of good and bad registrations obtained on the same data set with two different methods. Global results are shown in Figure 2, indicating the percentage of cases for which each method is ranked first, and the percentage of associated good, intermediate and bad registrations.

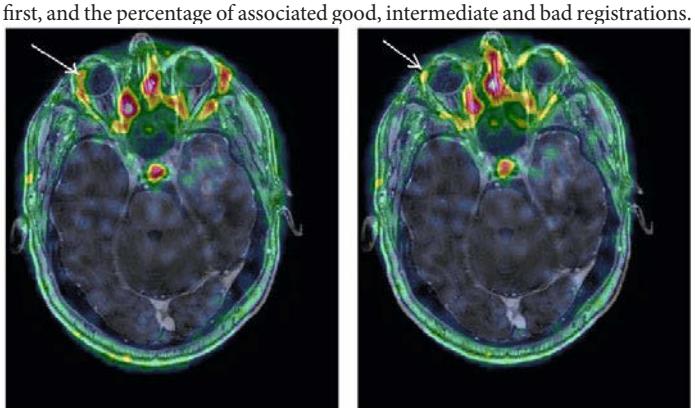

Figure 1: Examples of a bad registration (left: with an anormal uptake in the eyeball indicated by the arrow) and a good registration (right).

Methods	Rank1	good	intermediate	bad
M1	16.1	11.3	3.2	1.6
M2	0	0	0	0
M3	1.6	0	0	1.6
M4	0	0	0	0
M5	0	0	0	0
M6	9.7	8.1	1.6	0
M7	12.9	11.3	1.6	0
M8	3.2	3.2	0	0
M9	12.9	11.3	1.6	0
M10	4.9	3.2	1.7	0
M11	14.5	9.7	4.8	0
M12	0	0	0	0
M13	8.1	0	8.1	0
M14	3.2	1.6	1.6	0
M15	1.6	1.6	0	0
M16	11.3	8.1	3.2	0
total	100	69.4	27.4	3.2

Figure 2: Frequency for each method (in %) to be ranked first and associated quality of the registration.

Discussion/Conclusion: As underlined in a preliminary study using only 9 registration approaches [2], no method can achieve a good performance on all datasets. The benefit of the registration strategy in the context of Sestamibi SPECT/MRI registration was demonstrated on 62 datasets. It increases the number of good registrations (69%) compared to the 30% obtained using only the top method (M1) on the database. Some additional methods will be tested soon in order to further improve results.

References:

[1] Prigent-Le Jeune F., et al, 2004, Eur J Nucl Med Mol Imag., pp. 714-9.
[2] Tacchella J.M., et al.,2013, IEEE EMBC (in press).

595

Sex diferences in effect of intravenous Gd administration on diffusion imaging of a high-grade glioma rat model.

R. Pérez-Carro, **P. López-Larrubia**
Modelos Experimentales de Enfermedades Humanas, Instituto de Investigaciones Biomédicas, Madrid/SPAIN

Purpose/Introduction: Since its clinical introduccion,[1] Diffusion Weighted MR imaging (DW-MRI) has become a powerful tool in the assessment of brain lesions. Even more, DWI has recently proven its capacity in studying cerebral functionality in humans[2] and animal models.[3] Furthermore, sometimes it is necessary to administrate a contrast agent (CA) to improve the information afforded by the images. Although some authors maintain that signal-to-noise and contrast-to-noise ratio are not affected by the presence of Gd, more controversies exists related to the effect on diffusion parameters.[4] We analyzed the regional and sex-dependent alterations in fractional anisotropy (FA) and mean diffusivity (MD) after the injection of Gd-DTPA in a glioma rat model.
Subjects and Methods: High-grade gliomas were induced in Wistar rats by stereotaxic injection of C6 cells in the right caudate nucleus.
MR images were obtained on a 7T-system with a ^{1}H selective birdcage resonator. Experiments were carried out when tumors reached 150-200 mm3. Protocol: one before and three (6, 15 and 27 min) after 0.2 M CAi.v. injection (1mL/Kg b.w). ssDTI-EPI sequences were acquired (TR/TE=3000/40 ms, 7 directions, *b* 300 and 1400 s/mm2, Δ/δ=20/4ms, FOV= 35x35 mm, mtx=128x128; plane resolution, 273 μm/pixel).
Images were computed with a home-made software application written in MatLab (R2007a) yielding parametric maps of FA and MD. Data were analyzed in each animal with Image J by measuring four brain regions: cortex, white matter, peripheral and core tumor.
Results: MD values measured in male (Fig. left panel) and female (Fi. right panel) rats are represented in four regions at different time points after Gd-DTPA administration. Statistical analysis revealed significant differences not only between regions and before or after of injection, but also related to the sex of the animal. In males, a decrease in MD takes place in the tumor whereas an increase in the healthy brain. In females, a more marked decrease happens in all regions. Similar results are obtained in FA values (not shown).

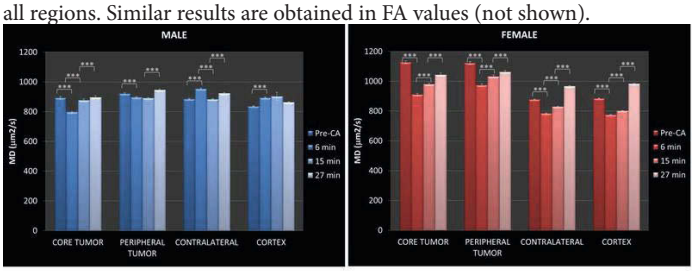

Figure. Mean diffusivity values measured in males (left panel) and females (right panel) in four brain regions (core tumor, peripheral tumor, contralateral and cortex) over the time. First measurement (Pre-CA) was performed right before injecting Gd-DTPA as contrast agent, and the others 6, 15 and 27 after gadolinium administration. (***, p<0.0001)

Discussion/Conclusion: The acquisition of diffusion images right after the CA administration, can seriously compromise the obtained results also in tumor and healthy regions. This is especially important when DWI is used in functional studies. The use of gadolium prior DTI acquisition should be considered only when it is mandatory by clinical indications.

References:

1) Le Bihan D, et al. Radiology, 1986, 161:401–407; 2) Le Bihan, D. Nat. Rev. Neurosci. 2003, 4:469–480; 3) Lizarbe B, et al. Neuroimage, 2013, 64:448-57; 4) Firat AK, et al. *Neuroradiology*. 2006, Jul; 48(7):465-70.

596

Functional magnetic resonance imaging of the brain in the studies of the process of self-regulation in the mode of real and imitation biocontrol.

M. Rezakova, **Y. Stankevich**, A. Tulupov
MRI Technologies, ITC SB RAS, Novosibirsk/RUSSIAN FEDERATION

Purpose/Introduction: Investigation neuroimaging of cognitive control of the virtual game. The study of the sequence of involvement of brain structures in the formation of new neural network in the mode of biocontrol. Visualized using fMRI of new neural networks in real and imitation biocontrol when the actual behavioral strategy is replaced by a random uncontrolled development of the game story.
Subjects and Methods: The studies were carried out on the 1.5 T Achieva Nova Dual (Philips, Netherlands). The experiment involved 16 volunteers, men (18-33 years). Playing arbitrarily ruled one of the divers, falling to the bottom, with a view to overtake an opponent, which speed is the speed of a player, that was achieved in the previous attempt; to win, a person must demonstrate to developing the skills of self-regulation is to learn how to slow down the heart rhythm during in one session (15 attempts) in the magnet. Investigator is not informed of the fact that this was imitation biocontrol. Imitation means that the registration of real duration cardio intervals during the experimental task, but in this case, the on-screen display "false" biocontrol. Imitation biocontrol conducted 2-4 weeks after the real. Using MatLab SPM8.
Results: It is shown that the starting and finishing «the territory» differ significantly from each other. The initial state («default») - is characterized by a limited number of activated voxels. The maximum growth in activity was in the second stage of the biocontrol (4-6 attempt to), there is an increase in the number and volume of activated voxels in the cortical, cerebellar and stem lesions. This is the involvement of cortical areas characterized by the highest values of voxels in the mid-temporal, occipital and frontal areas. Changes in the volume of activated voxels in the cingulate gyrus. Imitation biocontrol leads to the involvement of the maximum number of voxels.
Discussion/Conclusion: The localization of the dynamics of the areas of activity allows to make an assumption about the consistently deployed in time of the program of cognitive operations in game mode, organized adaptive feedback. Virtual game can give a person - healthy or sick - the ability to find hidden opportunities, successfully implemented in real life.
References:
Jackson G. et al. Functional MRI // Modern Magnetic Resonance, Springer, 2008.
Kaplan A.Y. et al. Unconscious operant conditioning in the paradigm of brain — computer interface based on color perception // Int. J. Neurosci. 2005. V. 115. P. 781–802.

597

A quantitative analysis of glioma response to hypoxia targeted therapy using intelligent image processing in a rat model

A. Benítez, N. Arias-Ramos, J. Pacheco-Torres, S. Cerdan, P. López-Larrubia
Department of Experimental Models of Human Disease, Instituto de Investigaciones Biomédicas Alberto Sols CSIC-UAM, Madrid/SPAIN

Purpose/Introduction: Oxygen tension (pO_2) performs a very important role in the appropriate working of tissues and organs as well as in the correct developing of an organism. It has been seen that hypoxia has a fundamental role in the evolution of different pathologies like tumors, and also a negative influence in resistance to therapies and poor patient outcome. Several treatments have been developed to modulate hypoxia in order to improve therapy success. Who patient respondes to this treatments is highly heterogeneous, because tumors are not homogeneous among patients and at intratumoral level, and it would be desiderable to discriminate them as early as possible, to tailor treatment accordingly. Here we report a multivariate analysis approach on the discriminant power of MRI to predict the irradiation therapy success in hyperoxic conditions by using a high-grade glioma (HGG) rat model.
Subjects and Methods: Animals bearing a C6 glioma were imaged in a 7T system following the tumors growing by volumetric measurements. MRI protocol consisted in T2-weighted and gadolinium enhanced T1-weighted images acquired at different times after glioma implantation. 6 animals were irradiated in hyperoxic and 6 in normoxic conditions with a biologic irradiator. Fisher's discriminant analysis [1] was applied to day-1 and day-3 after irradiation data sets in order to find the linear projection that best discriminates the pixels as belonging to "*responder*" or "*non-responder*" animals to therapy in hyperoxia.
Results: Figures 1 and 2 show the results in the treatment of the animals. Results obtained after Fisher's discriminant analysis application are illustrated in Figure 3. The Fisher's projection (Figure 3) separates the pixels of the *"responder"* (red) and *"non-responder"* (blue) classes. Then we used the mean of pixels that are most representative of each class, located at the edges of the histogram (<20% or >80%), as classification criterion. Using leave one out cross validation strategy we achieved 100% accuracy in the classification.

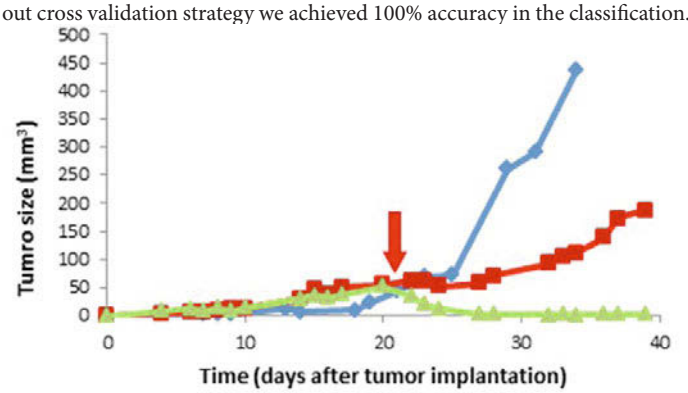

Fig 1. Evolution of tumor size after implantation. Tumors treated in normoxic conditions (blue line) stopped their growing immediately after irradiation but after 3-4 days, they grew again. Some tumors size of rats treated in hyperoxia (green) decreased. Some tumors treated in hyperoxic conditions behaved similarly to normoxic ones (red).

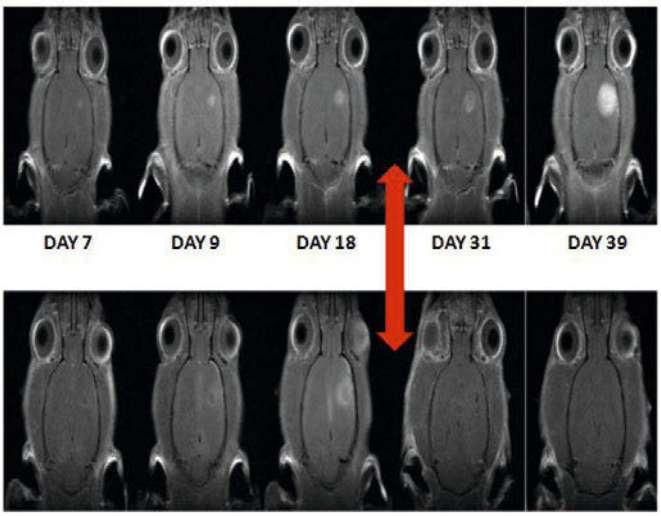

Fig 2. GdCE T1W images at different times after C6 cells intracranial injection. Red arrow indicates the day of radiation. Top row: a rat treated in normoxic conditions. Bottom row: a rat treated hyperoxic conditions that responded to the treatment.

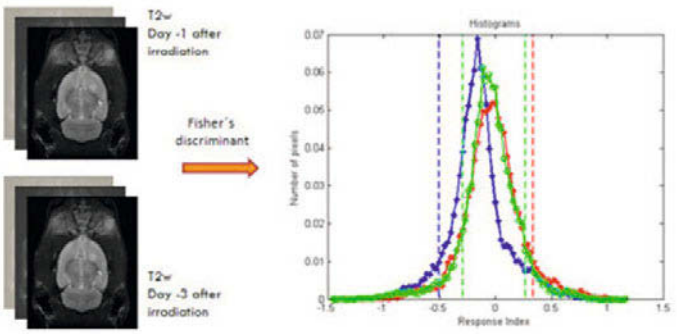

Fig 3. Histograms of the projected pixels for "responder" class (red), "non-responder" class (blue) and a example rat (green).Dashed lines represent the classification criterion, that is to say, the means of pixels most representative of each class. Note that the right mean of the example rat is closer to the "responder" class mean, therefore the result of the classification is "responder".

Discussion/Conclusion: We provide a protocol for the prediction of radiotherapy response in hyperoxic conditions in a glioma model based on an extensively used image acquisition in clinical routine (T2W-MRI images), being a direct and easily movable method to human studies. Results provide 100% successful predictions on leave one out cross validation strategy using T2w data sets; however this prediction accuracy isn't statistically significant (5% significance level) in two of the six rats.

References:

[1] Hastie, T., et al, 2001.The elements of statistical learning.Data mining, inference, and prediction. Springer Series in Statistics. NY.

598

Comparative metabolomics profiles of murine melanoma

I.P. Grudziński[1], **W. Szeszkowski**[2], P. Bogorodzki[3], A. Cieszanowski[2], M. Pisklak[1], J. Orzeł[3], M. Cywińska[1], M. Bamburowicz[1]
[1]Department of Toxicology, Medical University of Warsaw, Warsaw/POLAND, [2]II Dept. of Clinical Radiology, Medical University of Warsaw, Warsaw/POLAND, [3]Institute of RadioElectronics, Warsaw University of Technology, Warsaw/POLAND

Purpose/Introduction: Melanomas are the most aggressive skin cancers in humans, in part, due to their unique ability to rapidly invade the different tissue and organs, thus making anticancer therapy much more difficult [1]. Since ^{1}H-MRS can be helpful in analyzing metabolic profiles in cancers, we decided to distinguish between major melanoma metabolites analyzed in both tissue culture of the melanoma origin and animal melanoma models as well.
Subjects and Methods: Mouse melanoma (B16-F10) cells were injected (sc) into mice (C57BL/6) and metabolite profiles were assessed from ^{1}H using SVS PRESS (NA 512, TR 1500 ms, TE 25/136/270 ms) in animals bearing 3-week tumors at 7.0T system. The melanoma tissues collected from the mice were also extracted using methanol/water (M/W) and chloroform (Chl) solvents, and both the M/W and Chl extracts were subjected to ^{1}H-NMR analysis using a 9.4T system (Excitation impulse $\pi/2$ with time 8.63 ms, Acquisition time 3s, TR 4s). The LC-Model was applied to metabolomic analysis, and T2-weighted MR images were also performed to data using Turbo RARE (TR 4500 ms, TE 39 ms, TA 2:45 min, matrix 256 x 128) at 7.0T scanner.
Results: Alterations in metabolite profiles including taurine Tau (3,42 ppm), total choline tCho – (GPC+PCh) (3,22 ppm), total creatine tCr – (Cr+PCr) (3,03 ppm), glutamine and glutamate Glx – (Glu+Gln) (2,35 ppm, 2,12 ppm), lipids Lip13 – (Lip1.3a+Lip1.3b) (1,3 ppm), lipids Lip09 (0,9 ppm), macromolecules and lipids Mms (Mm+Lip) (1,2 ppm, 1,3 ppm, 1,4 ppm), N-acethylaspartate NAA (2,02 ppm) and inositol Ins (1,53 ppm) were identified in murine melanoma (in vivo). Studies evidence that tumors also exhibited a significant increase in lactate Lac (1.23 ppm) levels in mice. MRI/MRS-based measurements distinguished between normal and hypoxic areas in growing melanoma. In ^{1}H-NMR in vitro studies, Lac (1.23 ppm), tCho (3,22 ppm), tCr (3,03 ppm) as well as alanine (3.79 ppm) and glycine (3.43 ppm) were mainly identified in the M/W extracts. In contrast, lipid and cholesterol fractions were mainly determined in the Chl extracts from murine melanoma tissues.
Discussion/Conclusion: Both ^{1}H-MRS and ^{1}H-NMR are quite comparable in metabolomics profiling of melanoma in applied preclinical models, however, the advantage of the ^{1}H-MRS technique is due to noninvasive tissue measurements in animals.
References:

1) Evans MS et al. Current and future trials of targeted therapies in cutaneous melanoma. Adv Exp Med Biol 2013;779:223-55.

This project was supported by a grant from the National Science Centre, Poland (N N518 381737).

599

see p. 426 Contrast agents

600

WITHDRAWN

601

Metabolomics (31P) studies of metastatic-like glioma in rat models

I.P. Grudziński[1], **W. Szeszkowski**[2], A. Cieszanowski[2], P. Bogorodzki[3], M. Pisklak[1], J. Orzeł[3], M. Cywińska[1]
[1]Department of Toxicology, Medical University of Warsaw, Warsaw/POLAND, [2]II Dept. of Clinical Radiology, Medical University of Warsaw, Warsaw/POLAND, [3]Institute of RadioElectronics, Warsaw University of Technology, Warsaw/POLAND

Purpose/Introduction: Metabolomics profiling of metastatic gliomas, in particular the assessment of metabolites by phosphorous-31 magnetic resonance spectroscopy (^{31}P-MRS), is nowadays in the center of new anti-cancer drug design targeting to biochemical pathways involving phosphorous containing molecules [1,2]. Since ^{31}P-MRS can provide information regarding energy stored agents such adenosine triphosphate (ATP), it may be also used to describe tumor burden in growing metastatic gliomas (in vivo).
Subjects and Methods: In this study, rat glioma (C6) cells were intraperitoneally injected into Wistar rats, which served as preclinical transplant models [3], and cancer metabolites (beta-ATP, alpha-ATP, gamma-ATP, phosphocreatine PCr, phosphodiesters PDE, phosphomonoesters PME, and inorganic phosphor Pi) were assessed from ^{31}P-MRS using localized multivoxel CSI (TR 440 ms, TE 2.30 ms, NA 512, TA 31:52 min, voxel 40 x 13 x 13 mm) and unlocalized FID (TR 700 ms, TE 0,34 ms, NA 512, TA 6 min) methods in animals bearing 3-4 week syngeneic gliomas. Normal rats were used as controls. A 1.5T MR system (AVANTO SQ-Engine TIM [76x32]; SIEMENS) equipped with ^{31}P/^{1}H coils (12 cm x 24 cm) and RF multinuclear enhancers was applied to MRS data.
Results: The increased level of metabolites such as beta-ATP/PCr, alpha-ATP/PCr and gamma-ATP/PCr ratios was mainly observed in metastatic glioma tissues growing into the peritoneal cavity in rats. A similar pattern in global ATP/PCr ratios was also noted in rats bearing gliomas. Studies evidence that transplanted gliomas slightly increased Pi/PCr ratios in animals. No such changes were observed in PME/PCr ratios.
Discussion/Conclusion: The present results suggest that murine C6 glioma requires a large body of energy in growing out of the animal brain due to intraperitoneal injection in rats. Studies show that the ^{31}P-MRS method can be helpful in analyzing total ^{31}P-based metabolic profiles in rat bearing glioma tissues.
References:
1/ Hattingen E et al. Bevacizumab impairs oxidative energy metabolism and shows antitumoral effects in recurrent glioblastomas: a 31P/1H MRSI and quantitative magnetic resonance imaging study. Neuro Oncol. 2011;13(12):1349-63.
2/ Solivera J et al. Assessment of 31P-NMR analysis of phospholipid profiles for potential differential diagnosis of human cerebral tumors. NMR Biomed. 2009;22(6):663-74.
3/ Guevara P, Sotelo J. C6 rat glioma grown into the peritoneal cavity, a large source of tumoral cells for subcutaneous transplant of glioma. J Neuro-Oncology 1999;44:91-92.
This project was supported by a grant from the National Science Centre, Poland (N N518 381737)

EPOS™ Poster

qMRI

602

Synthesis and characterization of Cobalt-zinc ferrite magnetic nanoparticles coated with DMSA

D. Shahbazi-Gahrouei[1], S. Manochehri[2], M. Abdolahi[3], L. Ghasemian[1]
[1]Medical Physics, Isfahan University of Medical Sciences, Isfahan/IRAN, [2]Physics, Maleke-ashtar University of Technology, shahin-shahr, Iran, Shahinshahr/IRAN, [3]Physics and Radiation Technology, Bushehr University of Medical Sciences, Bushehr, Iran, Bushehr/IRAN

Purpose/Introduction: Synthesis of magnetic nanoparticles has been desperately interested because of their
unique features and potential applications such as magnetic resonance imaging, treatment of cancer, magneto-optical devices and biomedical drug delivery. Spinel ferrite nanoparticles have been extensively investigated due to their favorable
magnetic properties especially in MRI. Different types of monomers such as DMSA (dimercaptosuccinic acid) were assessed as anchors for easy attachment of polymer coatings on
magnetic nanoparticles. In the
present work, magnetic nanoparticles of cobalt-zinc ferrite (CZF-MNPs) and CZF-MNPs coated with DMSA have been investigated.
Subjects and Methods: Cobalt-zinc ferrite (CZF-MNPs) magnetic nanoparticles were prepared in air environment by conventional coprecipitation method using ferric, zinc and cobalt salts with sodium hydroxide, at 80˚C of solution temperature and were coated with biocompatible DMSA. The morphology of desired nanoparticles was investigated by TEM. The structural and crystal phase of CZF-MNPs was determined by X-ray diffraction (XRD).
Results: The XRD results confirmed the spinel ferrite phase formation. The results show that sample is single phase. The average of crystallite sizes was calculated from the broadening of the most intense peak (311), using Scherrer's formula, about 18 nm. Magnetization measurements of samples were performed up to maximum field of 9000 Oe at room temperature with a device Alternating Gradient Field Magnetometry (AGFM). Figure 1 shows a typical M-H loop of a sample coated with biocompatible DMSA. The FTIR spectra of the samples have been analyzed in the frequency range 400-4000 cm-1, which confirms the results of XRD and formation of Co-Zn ferrite phase.
Discussion/Conclusion: The maximum magnetization of coated nanoparticles was declined compared with the bare nanoparticles. Also the results show that the quantities of saturation magnetization decreased by increasing molariy of DMSA coated. These spectra showed the presence of cover on the surface of nanoparticles and also water in the samples.
References:
There are no references.

603

Semi-Active Resonant Circuit Approach for MR-Enhancement Imaging of Stent-less Aortic Valve

M. Fatahi[1], E. Immel[1], A. Melzer[1], B. Cox[1], R. Boyd[2]
[1]Imaging and Technology, IMSaT , Institute for Medical Science and Technology, Dundee/UNITED KINGDOM, [2]Imaging technology, Vueklar Cardiovascular, Edinburgh/UNITED KINGDOM

Purpose/Introduction: With the advent of MR guided minimally invasive cardiovascular procedures MR-enhancement imaging of cardiovascular implants such as prosthetic heart valves and Vena Cava filters has an important role in detailed visualization and localization of them during those procedures. In Aortic valve replacement procedures Stent-less valves are proven to perform superior to stentted and mechanical valves [1] due to bypassing problems including artifacts and heating issues. In this study MR-enhancement imaging of stent-less Biovalsalva Aortic valve conduit is achieved through the incorporation of a small wireless resonant circuit which is tuned to 63.8 MHz (Larmor frequency at 1.5T MRI).
Subjects and Methods:
The resonator which is mounted on the skirt part of the valve conduit consists of a coil made of insulated copper wire (0.40mm diameter) and a non-magnetic Surface Mounted Device (SMD) capacitor (56 PF, Vishay Inter-technology, Inc, US) which is tuned to the 63.8 MHz [2].
Scanning was performed on the GE Signa HDX, 1.5T MR Unit, with a GE 8-channel head coil .The MRI sequences used were taken from the standards for testing devices in MRI. The Stent-less valve placed in a plastic cylinder, the ends of which were connected by silicone tubing to a Heart-Lung Machine (Maquet HL-30) to create natural pulsatile and a constant flow to fully open and close the valve.The flow through the valve was set to the following parameters: Fluid: water, Temperature range: 25-35°C, Pressure 60mm-120mm ,2.96 liters/minute, Heart rate 64 beats/min.
Results:

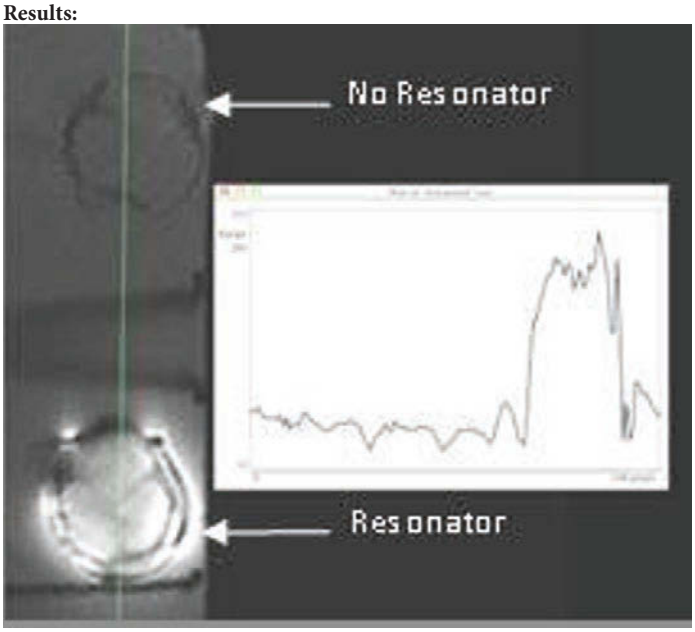

The result demonstrates that high resolution MR images of the stent-less aortic valve may be feasible when employing MR-enhancement resonators to locally enhance signal intensity. Signal intensity plot in different location of the coil was approximately symmetric which indicates that resonator can give us a homogenous enhancement. The signal intensity is approximately 4 times with MR-Enhancement than without resonant circuit.

Discussion/Conclusion:

This initial evaluation has helped to characterize the potential configurations of the resonator,but the final design of the resonator for the valve requires more testing and modeling to meet all the requirements.

The main advantages of this wireless resonant circuit is being less complicated and more cost-effective as we can bypass the need for MRI contrast agents. This could be very beneficial in terms of procedural cost, time and complexity.

References:

[1] David TE,Aortic valve replacement stentless and stented porcine valves, Thorac Cardiovasc Surg. 1998, Aug; 116 (2): 236-41

[2] Harald H. Quick, Interventional MR: Devices, Applications, Electromagnetic safety concern, 18th Int. Zurich Symposium ,2007

604

Whole brain T2 mapping at 7T with pSSFP and Extended Phase-Graph Data Fitting

P.L. De Sousa[1], A. Grigis[1], A. Amadon[2], D. Le Bihan[2], A. Vignaud[2]

[1]ICube (UMR 7357), FMTS, Université de Strasbourg, CNRS, Strasbourg/FRANCE, [2]DSV/I2BM/Neurospin, UNIRS/NeuroSpin/I2BM/DSV/CEA, Gif sur Yvette/FRANCE

Purpose/Introduction: T2 has been shown to be a sensitive biomarker of neurological pathologies [1]. We aim to use the novel partially spoiled Steady State Free Precession (T2-pSSFP) technique [2,3] for human brain T2 mapping at 7T. The analytical model used to derive T2 from pSSFP images yields accurate results only for large excitation flip angles (FA) [3,4]. At very high fields (≥7T), this working assumption does not hold due to strong B1+ inhomogeneities and SAR concerns. We propose to replace the analytical pSSFP model by a more accurate approach based on the extended phase graph (EPG) [5].

Subjects and Methods: In vivo 3D pSSFP 1.25 mm isotropic images were acquired on a 7T Siemens MRI scanner with 2-ms rectangular excitation pulses, FA= 60°, TR/TE = 12/3ms, TA= 3min/pSSFP scan. T1 was estimated according to the DESPOT1 method [6]: TR/TE= 17/3ms, α_1/α_2 =5°/20°, and B1+ was measured with a 3D AFI sequence [7].

T2 measurement was carried out voxelwise from four T2-pSSFP images (φ = [1,10,15,20]°) by NNLS fitting of the experimental data to the EPG-simulated curves. For comparison, the pSSFP data were also fitted to the analytical pSSFP equation (Eq. 1 of [4]). In both cases FA was corrected by B1+ map.

Results: The 7T T2-pSSFP maps derived from the analytical- and EPG-fittings are presented in Fig.1bc, respectively. The arrows in Fig.1b highlight regions where the analytical-fitting fails since the assumption of large RF flip angles does not hold. The proposed EPG-fitting approach achieves more consistent measurements.

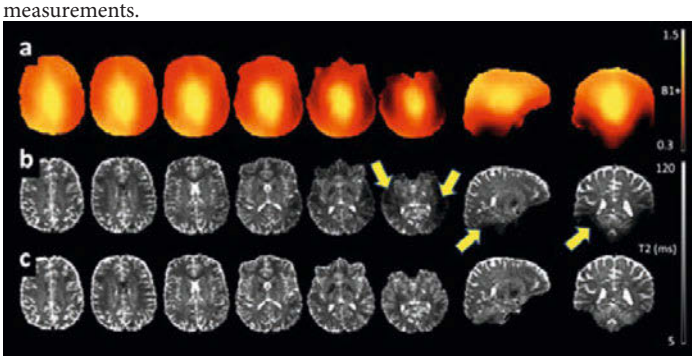

Fig.1:Axial, sagittal and coronal views from 3D **(a)** relative B1+ map, and **(b-c)** T2-pSSFP maps derived from the analytical and EPG models, respectively. Arrows highlight the regions where the analytical model assumption breaks down (FA < 20°).

Discussion/Conclusion: We show here that EPG-approach can be applied for T2-pSSFP mapping in the case of strong B1+ heterogeneities. The proposed EPG-fitting might open promising perspectives for the computation of high field T2-pSSFP mapping. This strategy enhances significantly the quality of the measurement while increasing the computation time. Future work will aim to optimize acquisition parameters and increase the spatial resolution.

References:

1. Bauer C.M., 2010, NeuroImage 52:508–514
2. Ganter C., 2006, MRM 55 :98-107
3. Bieri O et al, 2011, MRM 66:410-418
4. de Sousa P.L. et al, 2012, MRM 67:1379-1390
5. ScheffIerK., 1999, Concepts Magn.Reson. 11:291–304
6. Deoni S.C.L., et al, 2003, MRM 49 :515-526
7. Yarnykh V.L., 2007, MRM 57:192-200

605

Fractal dimension and lacunarity in liver pathology

K. Byk[1], K. Jasinski[1], K. Jablonski[2], T. Skorka[1]

[1]Department of Magnetic Resonance Imaging, Institute of Nuclear Physics PAN, Krakow/POLAND, [2]Chair of Gastroenterology, Hepatology and Infectious Diseases, Jagiellonian University Medical College, Krakow/POLAND

Purpose/Introduction: The vascular branching or pathological changes in an organism reveal a complexity of structure that can be describe as a self-similarity under proper magnification. This similarity can be investigated with geometrical structures – fractals. The purpose of this study was to assess a influence of liver hepatitis on fractal dimension (FD) and lacunarity (L), which is a measure of heterogeneity of an image [1].

Subjects and Methods: The experiment was conducted on 9.4T Bruker magnet (Ettlingen, Germany). 18 female BALB/c (weight 19.40±1.31g) mice were divided into 3 groups based on concanavalin A (ConA) dose: contr - without ConA (8 animals), 1x05 - 5mg/kg ConA dose (4 animals), and 1x10 - 10mg/kg ConA dose (6 animals) administrated 24h before experiment. Images were taken in axial projection with T2-weighted sequence with parameters: TE 5.72±0.12ms, slice thickness 1mm, FOV 22x22mm^2, spatial resolution 0.13x0.13. Animals were anesthetised with isoflurane via nose can, and their heart rate and breath were monitored.

FD and L of liver images were calculated with the use of ImageJ (NIH, USA) software. Results were compared and analyzed, ANOVA (p=0.05) test and linear fitting, in OriginPro8.6 (OriginLab Corporation, USA). The standard box counting approach was chosen [2].

Results: Multifractal analysis of MR images displayed two (at least) systems of scaling, which can stand for vascular system and pathological lesions. The FD mean value was the lowest for group 1x10 but without significant difference. Good linear correspondence can be observed between fractal dimension and lacunarity, the lower FD the higher L (Fig1) [3].

Fig.1: Linear ralation between lacunarity and fractal dimension.

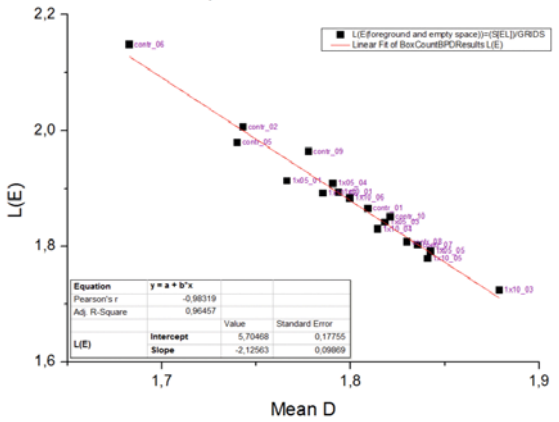

Discussion/Conclusion: The application of the fractal analysis in pathology is leaning on theoretical basis [2,4]. However, it results in a spectrum of FDs and Ls, depending on spatial resolution, SNR or the slice exact position. The FD is changing not only with image homogeneity changes but also the multifractal structure of liver has its influence on fractal dimension usually increasing it.

References:

[1] S Cross 1997. Fractals in Pathology. Journal of Pathology 182: 1-8.

[2] A Karperien 2004. FracLac Advanced User's Manual. Charles Sturt University.

[3] F Moal 2002. Fractal dimension can distinguish models and pharmacologic changes in liver fibrosis in rats. Journal of hepatology 36: 840-849.

[4] T Smith 1996. Fractals methods and results in cellular morphology – dimensions, lacunarity and multifractals. Journal of neuroscience methods 69: 123-136.

606

Liver Iron Content determined with Gradient Echo MRI: Comparing R2* to Signal Intensity Ratio analysis

A.P. Wunderlich[1], A. Wegener[1], H. Cario[2], M. Juchems[3]

[1]Dept. for Diagnostic and Interventional Radiology, Univ.-Clinic Ulm, Ulm/GERMANY, [2]Pediatry, Univ.-Clinic Ulm, Ulm/GERMANY, [3]Depr. for Diagnostic and Interventional Radiology, Univ.-Clinic Ulm, Ulm/GERMANY

Purpose/Introduction: To compare two methods for addressing liver iron content (LIC) from gradient echo (GRE) MRI scans. According to theory, liver R_2* values are expected to depend on iron concentration (LIC) as follows: $R_{2\ liver}^{*} = R_{2\ tissue}^{*} + LIC \cdot R_{Fe}$ with R_{Fe} = relaxivity of iron or ferritin, resp. This implies a linear relationship between R_2* and LIC.

Subjects and Methods: 71 patients (age 3 … 79 years, mean 28,9 y) suspected for liver iron overload were examined using gradient-echo (GRE) sequences to evaluate the amount of LIC. At 1.5 T with TR/TE/FA 120/4.8-9.5-14.3-19.1/90° we used the body coil to get homogeneous signal required for signal intensity ratio (SIR) analysis of liver and muscle. Signal was measured in manually drawn circular regions of interest (ROIs) in vessel-free parts of the liver and in the paraspinal muscles [1]. LIC was determined from the liver-to-muscle SIR values [2].

R_2* was calculated with Numaris 4 software implemented on the MR scanner (Siemens Avanto, Erlangen, Germany). Since the SIR method has a limitation above LIC of 300 mmol/kg dry tissue (16.7 mg/g), we excluded patients with higher LIC.

Coefficients of determination from linear regression were calculated on all data and in certain LIC ranges to compare results obtained with both methods and test their concordance to theory.

Results: In 58/71 patients (82%; age 3 … 68 years, mean age 25,8 y) the LIC value, determined with SIR, was below 300 mmol/kg. These were included in the analysis.

For all LIC values, the coefficient of determination between R_2* and LIC was only 0.37. R_2* values showed a ceiling effect above a LIC value of 120 mmol/kg (6.7 mg/g). Patients below that value (33/58 pts., 57%) were analyzed separately, yielding a coefficient of determination of 0.72. Also, we analyzed data of patients with LIC values between 120 and 300 mmol/kg (25/58 pts.). In this range, the coefficient of determination was 0.63, but the correlation was negative.

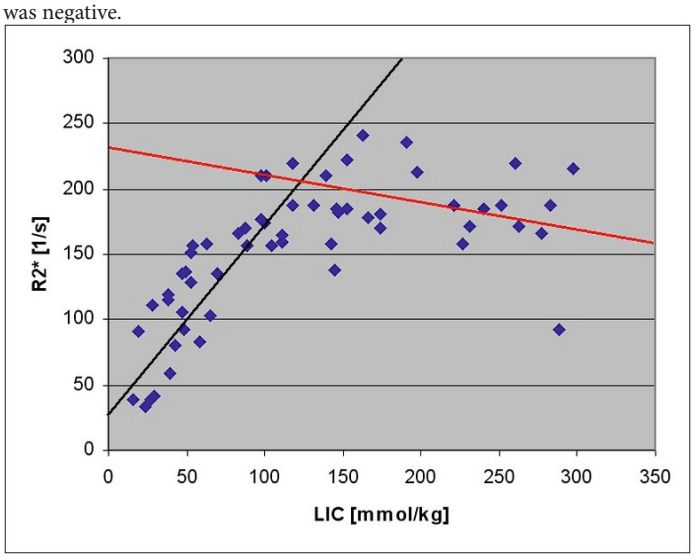

Discussion/Conclusion: In this work, we used identical GRE data to compare two approaches for determining LIC from MRI data. R_2* values determined with software implemented on the MR scanner show a linear dependence on LIC, according to theory, but only at low LIC values. We hypothesize low SNR levels, esp. for large TE, as problem for determining large R_2* values. The SIR method has been proved reliable [2].

References:

1. Gandon, Y, 2004, Lancet, 357–62

2. Wunderlich, AP, 2012, Proc. 20th ISMRM, 1293

607

Water-fat separation using low-resolution phase maps and eddy current compensation

M.D. Nickel[1], X. Zhong[2], S. Kannengiesser[1]

[1]MR Applications Development, Siemens AG, Healthcare Sector, Erlangen/GERMANY, [2]MR R&D Collaborations, Siemens Healthcare, Atlanta/UNITED STATES OF AMERICA

Purpose/Introduction: Reliable water-fat separation based on the Dixon method requires detailed modeling of the signal evolution [1,2]. In particular

when using complex data and bipolar readouts, aside from relaxation and non-trivial spectra also field inhomogeneities, eddy currents and gradient delays need to be considered [3]. This is addressed in a multi-resolution approach. The aim is twofold. First, to improve stability and numerical efficiency. Second, to show that the accuracy of the water-fat separation can be significantly improved for bipolar readout acquisitions.

Subjects and Methods: For the n-th echo at echo-time $\mathbf{TE}_n$, the signal at voxel **x** is modeled by

$$S_n(\mathbf{x}) = (W(\mathbf{x}) + c_n F(\mathbf{x}))\, e^{-R(\mathbf{x})TE_n + i\omega(\mathbf{x})TE_n + \alpha\Theta(\mathbf{x}) + i\Phi(\mathbf{x})}$$

with water signal **W(x)**, fat signal **F(x)**, fat signal evolution $\mathbf{c}_n$, relaxation rate $\mathbf{R}^*\mathbf{(x)}$, field map **ω(x)**, background phase **Φ(x),** eddy current phase **Θ(x)** and readout polarity **α**=±1. **W(x)** and **F(x)** are assumed either real- or complex-valued (then **Φ(x)**=0).

Minimizing χ^2 is addressed step-by-step. First, **W(x)**, **F(x)** and one phase are eliminated analytically. Second, the remaining variables are assumed to be of lower resolution by setting them constant over patches $P_x x P_y x P_z$.

The following procedure is proposed:

1.) Assume **W(x), F(x)** to be complex-valued and $\mathbf{R}^*\mathbf{(x)=0}$ for determining a low-resolution field map **ω(x)**.

2.) With the implicitly obtained **Θ(x)** not reliable as the complex-phases of **W(x)** and **F(x)** are not aligned, χ^2 is again minimized with knowledge of **ω(x)** assuming real valued **W(x)** and **F(x)** to obtain **Θ(x)** and **Φ(x)**.

3.) After interpolation of the low-resolution maps, **W(x)**, **F(x)** and $\mathbf{R}^*\mathbf{(x)}$ are determined.

This approach was implemented in C++. Numerical phantoms created using Matlab (Mathworks, Natick, MA, United States). Data from a healthy volunteer acquired on a 3T MRI system (MAGNETOM Skyra, Siemens, Germany) using a spoiled GRE (VIBE). Sequence parameters included TR=10ms, flip angle=5°, TE=0.79,2.04,3.29,4.54,5.79,7.04ms, voxel-size=2x2x4mm^3 for a 20sec breath-hold.

Results:

Phantom data from left to right: Image of the real-part of the first echo, field-map, eddy current phase, fat fraction and relaxation rate. Values are extracted correctly.

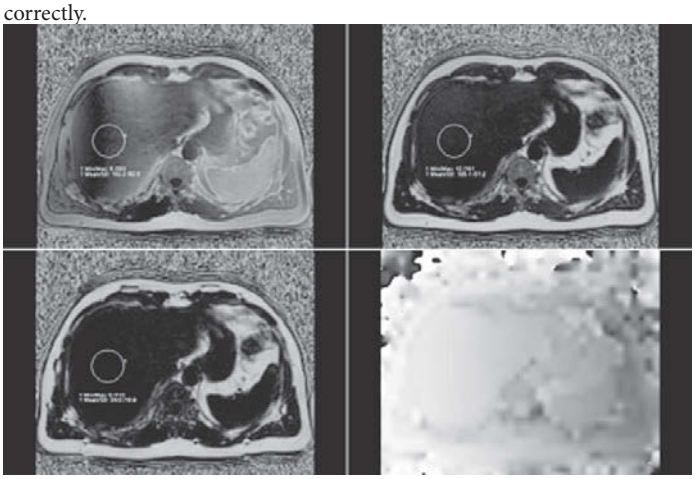

Fat fraction for a bipolar acquisition reconstructed with the proposed scheme using no eddy current phase correction (upper left), linear phase correction (upper right) and local phase correction (lower left). For the latter the eddy current phase map is shown (lower right). Within the indicated circle the fat fractions are 18.2±9.3%, 10.5±3.1 and 3.4±1.9%, respectively.

Discussion/Conclusion: Low resolution phase maps and eddy current compensation allow efficient and accurate water-fat separation also for bipolar acquisitions.

References:

[1] Yu et al. MRM 2008; 60:1122-1134.
[2] Reeder et al. JMRI 2011; 34:729–749.
[3] Lu et al. MRM 2008; 60:198-209.

608

Monoclonal Antibody-Navigated Carbon-Encapsulated Iron Nanoparticles for Murine Melanoma Cell Tracking using Molecular MRI

I.P. Grudziński[1], A. Cieszanowski[2], **W. Szeszkowski**[2], M. Bystrzejewski[3], M. Popławska[4]

[1]Department of Toxicology, Medical University of Warsaw, Warsaw/POLAND, [2]II Dept. of Clinical Radiology, Medical University of Warsaw, Warsaw/POLAND, [3]Department of Physical Chemistry, Warsaw University, Warsaw/POLAND, [4]Department of Organic Chemistry, Warsaw University of Technology, Warsaw/POLAND

Purpose/Introduction: Molecular MR imaging of cancer cells with specific multifunctional contrast nanoparticles is now recognized as a new diagnostic method for the sensitive and specific detection of molecular and/or cellular targets that characterize cancer tissues before their gross anatomical features become obvious [1,2]. In the present study, we developed carbon-encapsulated iron nanoparticles with functionalized surface containing monoclonal antibodies recognizing transmembrane integrin receptors as a novel generation of superparamagnetic nanobiocontrast agents (NanoCAs) in preclinical cancer research.

Subjects and Methods: The as-biosynthesized NanoCAs were used for direct labeling of syngeneic melanoma tumors in mice. In the first experiment, the melanoma (B16-F10) cells were labeled in vitro with NanoCAs, and the post-labeled cells were injected (s.c.) into C57BL/6 mice for cancer (B16-F10) cell tracking in growing syngeneic tumors (in vivo) using a 1.5T MR scanner. T2-weighted images were acquired using both TSE (TR/TE 3500/63 ms, voxel size (0.5×0.5×1.0 mm), flip angle 150 deg, slice thickness 1 mm, and multi-echo SE sequences with TR 2000 ms, TE (22, 44, 66, 88, 110, 132, 154, 176 ms), voxel size (0.8 x 0.6 x 2.0 mm), flip angle 180 deg, and slice thickness 2.0 mm. In the second experiment, the non-labeled B16-F10 cells were injected (s.c.) directly into C57BL/6 mice, and the animals bearing 3-week melanoma tumors were further injected (i.v.) with NanoCAs to elucidate integrin receptors on T2-images (in vivo).

Results: MRI studies demonstrate that NanoCAs targeted integrin receptors expressed on melanoma cells and/or newly formulated endothelial cells (neoangiogenesis) in murine cancer due to specific monoclonal antibodies. The measurements evidence that NanoCAs decreased T2 relaxation time on T2-images in murine melanoma tissues.

Discussion/Conclusion: This preclinical data represents an important step toward the innovative design of the theranostic (therapeutic and diagnostic) nanoplatforms that are able to navigate anti-cancer biomolecules to melanomas in translation cancer studies.

References:

1) Yu MK et al. Targeting strategies for multifunctional nanoparticles in cancer imaging and therapy. Theranostics 2012;2(1):3-44.
2) Alberti C. From molecular imaging in preclinical/clinical oncology to theranostic applications in targeted tumor therapy. Eur Rev Med Pharmacol Sci 2012;16(14):1925-33.

This project was supported by a grant from the National Science Centre, Poland (N N518 381737).

609

Characterizing scaffolds using high resolution MRI

J. Kreutner[1], D. Weber[1], S. Paul[2], P.M. Jakob[1,3], D. Haddad[1]
[1]Molecular & Cellular MRI, Research Center Magnetic-Resonance-Bavaria (MRB), Würzburg/GERMANY, [2]Polymeric Materials, PPPolymer, Stockholm/SWEDEN, [3]Experimental Physics 5, University Würzburg, Würzburg/GERMANY

Purpose/Introduction: Establishing new materials and methods to manufacture scaffolds for tissue regeneration requires well defined properties of the material and a highly reproducible process. Therefore, in the development and later in the production constant quality control assuring correct pore sizes and wall thickness is mandatory. We evaluated the possibility of characterizing a polymer scaffold using high resolution MRI.
Subjects and Methods: Two cylindrical polymer scaffolds (A&B) of 10mm diameter and with different production parameters were immersed in water and evacuated prior to imaging. Image acquisition was performed on an 11.7T system using a 3D RARE sequence with a spatial resolution of 27x27x54µm. To improve image appearance, zero filling with a factor of two in all dimensions was applied. Images were automatically segmented using Otsu's method [1] to separate water and scaffold allowing calculation of porosity of the samples. Afterwards pore size (PS) and wall thickness (WT) was calculated using the Local Thickness method [2].
Results: Representative slices for both samples are shown in Fig.1. The scaffold appears as a dark structure within the surrounding water. The images already show visually different structures but without any quantitative information. Comparing overall porosity for both samples, they appear quite similar (A:47%, B:49%). These values are in good agreement to calculations based on the relative density of scaffold and polymer (A:47%, B:46%). Looking at pore size distribution (PSD) via a histogram, allows more quantitative specification of the scaffolds. As it can be seen, both scaffolds have distinct distributions. While sample A has a maximum in its distribution at about 200µm, sample B has smaller pores of about 60µm. Furthermore wall thickness can be computed using the same algorithm but with an inverted mask. As expected sample A has thinner walls than sample B (see Fig.2), which might affect its toughness and rigidity.

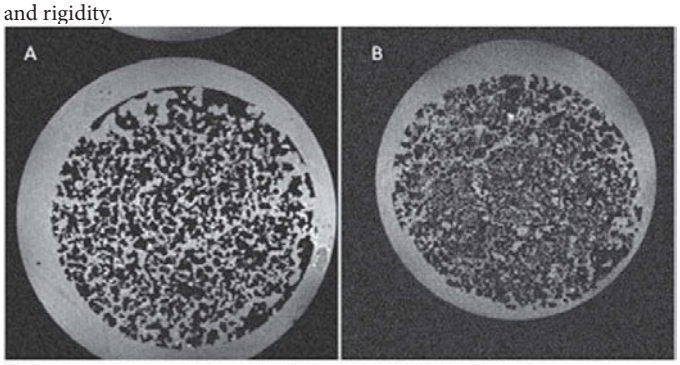

Fig. 1: Representative slices for both scaffolds (A left, B right).

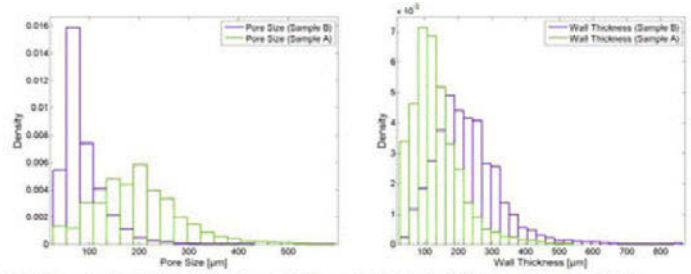

Fig. 2: Pore size distribution (left) and wall thickness distribution (right) for two different scaffolds.

Discussion/Conclusion: Our initial data show, that high resolution MRI is capable of identifying different structure characteristics in scaffolds quantitatively. Not only pores, but also material thickness can be assessed as long as they are not smaller than the acquired resolution. Therefore this technique can be used to test the influence of different production methods on the structure and also as a tool for continuous quality control. Differences can be easily identified in the histograms.
Acknowldegment:
This work received grants from the EC as part of FP7-Health project 242175 "VascuBone".
References:
[1]Otsu (1979), IEEE Trans. Sys., Man., Cyber 9 (1):62-66
[2]Hildebrand et al. (1997) J. Microscopy, 185 (1):67-75

610

T2 time prolongation after a single bout of elbow flexors concentric and eccentric exercise following two different short-term strength training protocols

J.Z. Popadic Gacesa[1], O. Barak[1], A. Klasnja[1], D. Kozic[2], R. Semnic[2]
[1]Department of Physiology, Medical School, University of Novi Sad, Novi Sad/SERBIA, [2]Centre for Imaging Diagnostics, Institute of Oncology, Sremska Kamenica, Serbia, Novi Sad/SERBIA

Purpose/Introduction: To determine T2 time prolongation changes after a single bout of elbow flexor muscles exercise (one arm concentric contractions until failure, other arm eccentric) as a result of two different short-term (2-week) upper arm strength training protocols.
Subjects and Methods: Nine healthy young men (20.8±0.3y, BMI 23.9±2.5kg/m2) were put in a two-week training protocol on isoacceleration dynamometer (5 times a week, 5 daily series with 10 maximal elbow flexions, 1 minute rest between sets) – Biceps exercising group (BE). The second group of eleven participants (20.6±0.7y, BMI 23.2±3.5kg/m2) were engaged in a different two-week training regime on isoacceleration dynamometer (5 times a week, 5 daily series with 10 maximal contractions: combination of elbow flexion and extension series alternatively, 1 minute rest between sets) – Biceps/Triceps exercising group (BTE). Transverse mid-humerus MR images were obtained on a Siemens Aera 1,5T system using a multiple spin-echo sequence (repetition time (TR) – 2500 ms, echo time (TE) – 10,20,30,40,50,60,70,80,90,100,110,120,130,140,150,160ms; total scan time 3 min 04 sec) on four occasions: before and after a single bout of elbow flexors exercise (at 80% 1RM) until failure, both baseline and following strength training. The number of repetitions, load and total exercising time for T2 map calculation after training were identical to pre-training in the same participant.
Results: In the BE group, prolongation of T2 in biceps brachii following training decreased significantly after concentric exercise: ΔT2 from 14.9±4.4ms to 12.1±4.4ms ($p<0.05$). Also, significant decrease in T2 prolongation as a result of adaptation to short-term strength training has been registered in BTE group for concentric exercise: ΔT2 from 14.9±2.7ms to 12.6±2.6ms ($p<0.05$). For eccentric exercise, ΔT2 decreased after training, but not significantly in both groups: BE: from 5.0±2.1ms to 4.5±2.1ms, BTE: from 4.9±3.9ms to 4.1±2.7ms ($p>0.05$).
Discussion/Conclusion: Short-term (two-week) strength training lead to upper arm functional muscle adaptation, with a significant decrease in concentric exercise induced T2 time prolongation, but without significant difference in T2 change comparing two different training protocols (BE group vs. BTE group).
References:
- Fisher MJ, 1990, Invest Radiol 25: 480–485.
- Jenner G, 1994, J Appl Physiol, 76: 2119–2124.
- Kinugasa R, 2006, Magn Reson Imaging, 24: 639–644.
- Prior BM, 1999, J Appl Physiol, 87: 2107–2114.

- Shellock FG, 1991, Radiology, 179: 659–664.
- Vandenborne K, 2000, Eur J Appl Physiol, 82: 76-82.
- Yue G, 1994, J Appl Physiol, 71: 84–92.

611

Automated Cell Quantification in high resolution at 4.7T

D. Balvay[1,2], J. Kolosnjaj-Tabi[1,3], G. Autret[1,2], F. Gazeau[3], A. Alfaraj[3], C. Wilhelm[3], O. Clément[1,2]

[1]LRI, PARCC HEGP UMR970, Inserm / Université Paris Descartes, Sorbonne Paris Cité, Paris/FRANCE, [2]Plateforme d'Imagerie du Petit Animal, Université Paris Descartes, Paris/FRANCE, [3]LMSC -UMR 75013, CNRS _Université Paris Diderot, Paris/FRANCE

Purpose/Introduction: With the development of cryogenic probes, high resolution MRI of magnetically labeled cells has allowed the detection of localized black spots which could correspond to individual cells. The aim of this study was to quantify the number of labeled monocytes, suspended in agarose phantoms, by the number of black spots (BS). The method was based on a statistical analysis of the neighborhood of each MR pixel. BS was correlated with the actual cell number (CN).

Subjects and Methods: Cell were labeled with anionic magnetic nanoparticles and suspended in agarose. Number of cells per mm^3 were 0, 1, 2, 5, 10 and 20, the tubes were made in triplicates. The FISP-FID 3D MRI sequence was used and the parameters were the following: TR/TE = 20/5 ms, $\alpha = 25°$, FOV 1.5x1.5x0.65 cm, spatial resolution 50x50x50 mm. The first step of the quantification procedure was the neighborhood analysis, where the distribution of the neighborhood of each pixel was evaluated. As MR noise is rician [1], it corresponds to Rayleigh noise for a negligible signal to noise ratio (cluster1), a Gaussian noise for high SNR (cluster2), and intermediate noise between these cases (cluster3). The identification of each cluster was evaluated by comparing effective quantile values of 1 and 5 % and quantile of 5% estimated from interquartile range, assuming a Gaussian distribution. Pixels in the center of Gaussian neighborhood were considered as black spots (cluster 4) if corresponding to outliers. The correlation between BS and CN was then performed.

Results: Correlation between BS and CN was high (R^2>94% taking into account an outlier result and R^2>99% otherwise). Without the outlier result, root mean square error value, indicating the precision, was 0.02 BS/mm^3. The estimated linear coefficients were BS = 0.05·CN – 0.003, indicating a moderate sensitivity of 5% and a low constant value indicating a correct specificity of the counting.

Discussion/Conclusion: Black spot detection was highly correlated with the number of cells in tubes, with a ratio of 1:20 between detected black spots and cells. This indicated both the high efficiency and the moderate sensitivity of the technique developed for following in vivo experiments, for which black structures of tissues have to be separated from black spots, which is a second major step for quantification.

References:

[1] Robust Rician noise estimation for MR images. Coupé P, Manjón JV, Gedamu E, Arnold D, Robles M, Collins DL. Med Image Anal. 2010 Aug;14(4):483-93

612

MRI measurements of 200µL intradermal gels on rabbits using dedicated surface coils at 0.2T

T. Feuillet[1,2], M.-J. Seurin[1], O. Beuf[2]

[1]Cirma, Cirma, Marcy l'Etoile/FRANCE, [2]Université de Lyon; CREATIS, CNRS UMR 5220 ; Inserm U1044 ; INSA-Lyon ; Université Lyon 1, Villeurbanne/FRANCE

Purpose/Introduction: Low-field MRI applied to veterinary imaging is provided with commercial volume or large surface coil not suitable for surface analysis. A dedicated receiving surface coil was designed to image and quantify the volume of innovative plastic surgery gels injected on intradermal sites on rabbits for a preclinical study. After a validation protocol using volume calibrated phantoms, volume (~200µL) variations of four gels were followed over time.

Subjects and Methods: MR experiments were performed on a Vet-MR 0.2T device (Esaote®). The geometry of a receiving surface coil was optimized for an examination at the skin surface(1,2). Volume quantification technique was validated on calibrated volumes of 20µL and 100µL in microtubes (precision and accuracy measured through five repeated experiments). 200µL calibrated volumes of four distinct gels were distributed over twenty intradermal injections using five rabbits. Gel #4 is a commercialized reference gel, whereas gels #1 to #3 are new gels under test in this preclinical study. The coil was then set close to every site at day-0, day-28 and day-84. The MR imaging sequence was a 3D Gradient Echo sequence (Fig.1).

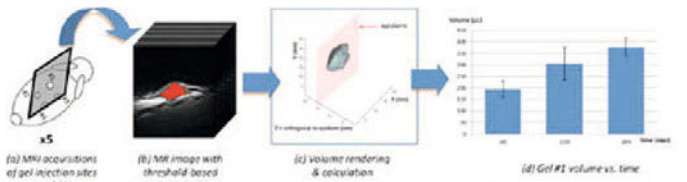

Figure 1: Acquisition and volume measurement steps. MRI of each site (a) with 3D Gradient Echo sequence (T_E=51ms, T_r=24ms, N_{ex}=1, FA=85°, matrix=256x256x52 / FOV=120x120x31.2mm³); Image segmentation (b): threshold segmentation. Volume calculation and rendering (c). Gel #1 volume follow-up (d).

Voxel size was minimized by reaching the maximum amplitude of the gradients (20mT/m), along with the smallest bandwidth available. Volume of all sites was quantified after threshold-based image segmentation. Significance of the volume variations through time was established using a Wilcoxon test.

Results: In-vitro validation results for the volume measurement technique are reported on Table1. MR images performed on the rabbits showed that SNR provided by the surface coil with the 3D sequence was suitable to measure the volume of all four injected gels (Fig.2).

Volume (µL)	Precision (%)	Accuracy (%)
20	7.0	14.0
100	5.7	0.5

Table 1 : Precision and accuracy for in-vitro volume measurement technique, for 20µL and 100µL tubes.

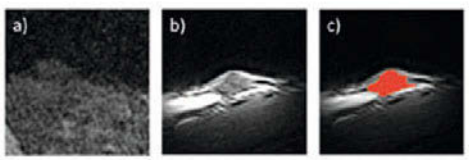

Figure 2: MR images of a site injected with gel obtained at 0.2T for: a) commercial volume coil ; b) ø20mm surface coil ; c) threshold-based segmentation to quantify gel volume.

The in-vivo volumes for the four gels all showed a significant swelling (p<0.06) from d0 to d28 and from d0 to d84 (Fig.3). Volume increase from d0 to d84 was 78%, 74%, 78% and 109% for gels #1 to #4 respectively (standard deviation of 24%, 23%, 26% and 24% respectively).

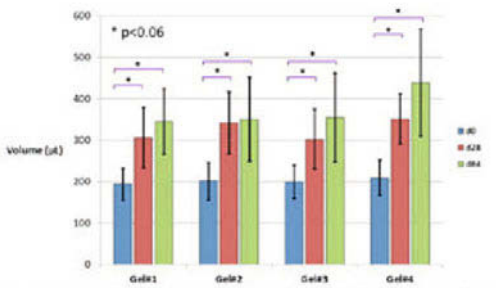

Figure 3: Mean volumes for gels #1 to #4 measured at d0, d28 and d84 (N=5 sites each). Reference: Gel #4.

Discussion/Conclusion: In this preclinical study, we demonstrated that volumes of injected gels on rabbits can be quantified and accurately followed using a dedicated surface coil associated with a high spatial resolution MR 3D sequence. No significant swelling difference between all four gels was observed. Moreover, volume rendering gave interesting information about gel shape evolution after injection.

References:

(1) DOTY - NMR Biomed.,Vol.20, 304–325 (2007).
(2) HYDE - eMagRes (2007).

613

Do Magnetic Resonance Elastography Inversion Methods Successfully Handle Bulk Waves?

E. Barnhill[1], P. Kennedy[1], C. Johnson[2], M.O. Mada[3], N. Roberts[1]
[1]Clinical Research Imaging Centre, The University of Edinburgh, Edinburgh/UNITED KINGDOM, [2]Beckman Institute for Advanced Science & Technology, University of Illinois at Urbana Champaign, Urbana/IL/UNITED STATES OF AMERICA, [3]Wolfson Brain Imaging Centre, University of Cambridge, Cambridge/UNITED KINGDOM

Purpose/Introduction: Magnetic Resonance Elastography (MRE) [1] is a non-invasive method of obtaining tissue viscoelastic parameters by encoding shear wave propagation in the MR phase image. Propagation of shear waves into the body generates compression waves as well, but they are too fast and too long to invert in MRE, and potentially confound analyses. Approaches to MRE compression waves vary, including neglect [2], removal with high-pass filter [3], and inversion of the curl field [4]. The present study is the first to compare these approaches.

Subjects and Methods: The present study uses 3D, full vector field acquisitions of:

a) agarose phantom with inclusions, vibrated 100Hz
b) brain, vibrated 100Hz

The inversion procedure was modified to handle compression waves in four ways:

i) neglect (i.e. assumption of pure shear)
ii) high-pass filter with value from the literature [3]
iii) curl field - direct method with gradient kernels[5]
iv) curl field - weighted least squares method [6]

Because many of these methods incorporate some degree of regularisation, two additional control conditions were used:

v) smoothing with unweighted 3D mean filter
vi) smoothing with sigma=1 Gaussian filter

For storage modulus, median stiffness was calculated and the images were analysed for the integrity of known physical structures.

Results: The twelve resulting images and their median storage modulus values are in the accompanying Figure.

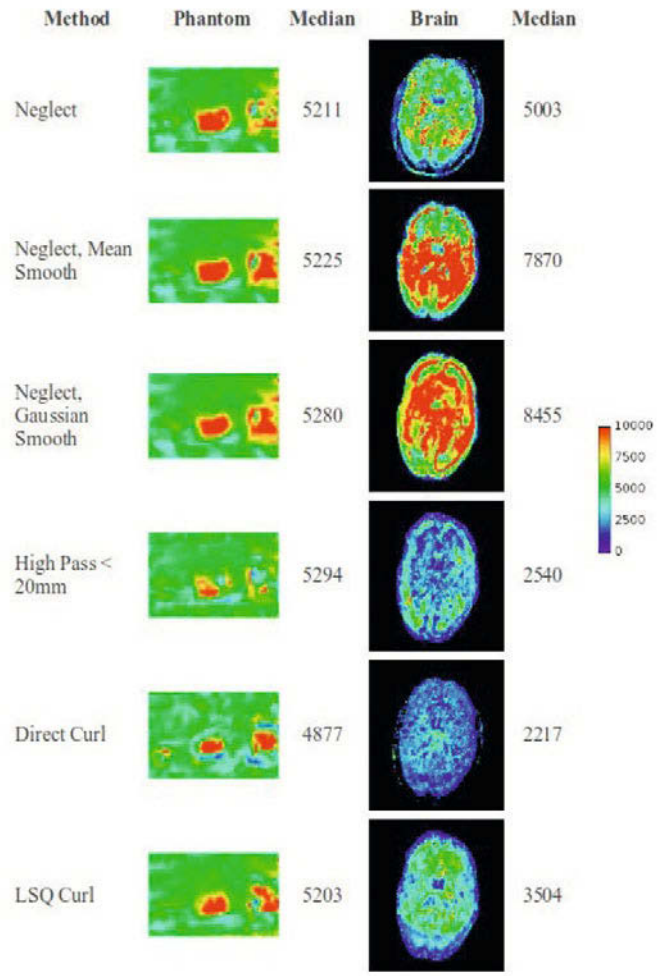

Discussion/Conclusion: Discussion

Phantom: all approaches produced similar median storage modulus (~5.2-5.3 KPa) excepting the direct curl method (~4.9 KPa). Visual inspection shows the high pass filter to be most destructive of the image features, while the direct curl provided the best detail, and was the only method to detect a small inclusion.

Brain: Methods removing bulk waves produced a lower range of values (~2.0 to 3.5 KPa) than methods neglecting the bulk wave (~5.0 to 8.5 KPa). The former also showed more uniform values across the brain, though only the LSQ curl preserved the ventricle.

Conclusion

For in vivo 3D MRE, methods to remove the bulk wave show varying sensitivity to noise and image features and can make a substantial change to the image values that is not simply a smoothing effect. Future work will apply this analysis across multiple subjects and multiple organs.

References:

[1] Muthupillai et al Science 1995:5232:1854-7
[2] Manduca et al Med Im An 2001:5:4:237-54
[3] Hamhaber et al Acta Biomater 2007:3:1:127-37
[4] Sinkus et al 2005 MRM 53:372-87
[5] Leclaire et al Comps & Fluids 2011:48:(1):98-112
[6] Bahl et al JOSA A 2012:29:11:2421-27

614

Spherulites as new MRI contrast agents for theranostic applications

B.-T. Doan[1], M. Hatem[1], H. Dhotel[1], S. Crauste-Manciet[1], C. Bourgaux[2], D. Brossard[2], L. Jugé[1,3], G. Autret[4], C.-A. Cuenod[4], D. Scherman[1], M. Bessodes[1], N. Mignet[1]
[1]UPCGI, UMR8151, U1022, Chimie Paristech, CNRS, Paris/FRANCE, [2]Faculté de Pharmarcie, Université Paris XI, Chatenay-Malabry/FRANCE, [3]NeuRA, Neuroscience Research Australia, Randwick Sydney/AUSTRALIA, [4]LRI - INSERM U.970, PARCC - HEGP, INSERM U.970 Université Paris Descartes,Sorbonne Paris Cité, Paris/FRANCE

Purpose/Introduction: Among the in vivo imaging techniques, magnetic resonance imaging (MRI) is distinguished by its high spatial resolution, its non-invasive and 3D properties. MRI is recognized as a powerful anatomical and functional imaging tool for hospital diagnosis in humans to identify diseased tissue. However, MRI lacks sensitivity and contrast agents could help visualising the different biological tissues. The development of more effective agents of MRI contrast remains the strategy of choice for reliable diagnosis and to assist in therapeutic monitoring.
Nanoparticulate contrast agents represent a strategy of choice as the local concentration of contrastophore can be considerably enhanced and multivalency can be obtained by grafting on the surface a specific ligand.
The spherulites (1) are organized structures that have multiple concentric alternating aqueous and lipidic layers. We chose to evaluate them as new MRI contrast agent.
They are also able to encapsulate with high efficiency soluble macromolecules. Constituted of FDA approved excipients, they are a priori non toxic nanoparticles. We proposed here three approaches to render spherulites paramagnetic: encapsulating a soluble contrastophor, inserting a lipidic contrastophor derivative or grafting a soluble contrastophor at the surface of the spherulites.
Subjects and Methods: Cryoelectron microscopy and small angle light scattering enabled the spherulite structure characterisation in concentric multilayers. The spherulites were obtained after shear stress of a lyotropic phase of lipids. Reference liposomes were also prepared in parallel to compare both scaffolds. The effect of the paramagnetic spherulites was studied by magnetic resonance imaging at different magnetic fields, 0,47T, 4,7T, 7T on Bruker relaxometer and spectrometers (Biospec and 300WB), by r1 and r2 relaxivities measurements. ICP MS analysis were performed to quantify the Gd concentration in spherulites.
Results: The conservation of the spherulite structure, throughout these three strategies, was shown by cryoelectron microscopy and small angle light scattering. The results showed that insertion of a contrastophor lipidic derivative into spherulite bilayers and grafting a contrastophor at the surface of the spherulites were the two strategies which led to the highest MRI contrast improvement (about 10mM-1.s-1).

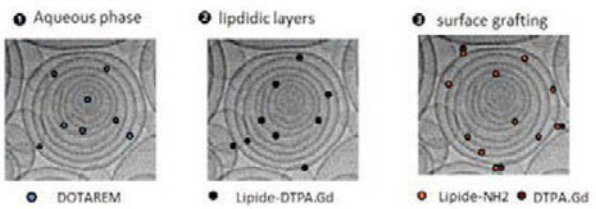

Figure 1 : Schemes of the 3 spherulites Gd loading strategies

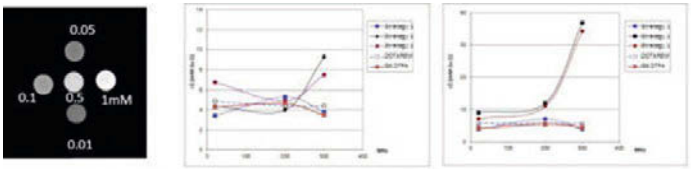

Figure 2 : Relaxometry at 0,47, 4.7 and 7T of spherulites in water

Discussion/Conclusion: To conclude, our results show that spherulites are potential interesting nanoparticles with MR imaging features as 'positive' contrast agent. It would enable the particles detection for further in vivo use as a diagnosis tool but also to vectorize active molecules for therapeutical purpose.
References:

- (1) Diat, O.; Roux, D., Preparation of monodisperse multilamellar vesicles of controlled size and high encapsulation ratio. *J. Phys. II* **1993,** 3, 9-14.

615

The potential applications of dispersion profiles method in NMR imaging

L.W. Skorski[1], B. Blicharska[1], D. Wierzuchowska[2]
[1]Radiospectroscopy Department, Jagiellonian University, Krakow/POLAND, [2]Institute of Physics, Pedagogical University, Krakow/POLAND

Purpose/Introduction: NMR relaxation measurements in vitro provide a powerful tools for investigation in vivo tissue anatomy and functional imaging. Two of NMR relaxation methods called "dispersion profiles" are currently used in research on the properties of macromolecules systems: There are a dependence of spin-lattice relaxation time $T_{1\rho}$ in rotating frame plotted as a function of low magnetic field B_1 and CPMG T2 versus ¶ pulses frequency. The advantage of this methods is an opportunity to observe the slow molecular motion and protons exchange in the range typical for water associated with proteins and bio-molecules.
Subjects and Methods: We reported the results performed using Bruker Minispect NMR spectrometer working at a proton resonance frequency 60 MHz for samples of proteins: egg white and bovine serum albumins and lysozyme – lyophilized powders and its aqueous solutions.
Results: The present communication is intended to focus attention on the connections of obtained parameters of molecular dynamics with conformation changes of proteins. The obtained dispersion profiles were analyzed using relaxation models: based on dipole–dipole interaction water protons adsorbed on protein surface.
Discussion/Conclusion: Image contrast in clinical MRI determined by the T_2 and $T_{1\rho}$ differences of water proton relaxation provide novel information about molecular dynamics in tissues (for example: in the case of brain ischemia in vivo). Presented $T_{1\rho}$ dispersion profile method of investigation is easier and faster than previous approaches involving measurements of the temperature and field dependences of spin-lattice relaxation times. We hope that the current results in vitro give a new information on protein systems and can be helpful in contrast study of tissue imaging in vivo.
References:

Y.A. Goddard, J-P. Korb, R.G. Bryant, J.Magn. Reson. 199, 68 (2009).
V.A. Jarymowycz, M.J. Stone, Chem. Rev. 106(5), 1624 (2006).
C.-L. Teng, H. Hong, S. Kiihne, R.G. Bryant, J. Magn. Reson. 148, 31 (2001).
J-P.Korb, A. Van-Quynh, R.G. Bryant, Chem. Phys. Lett. 339, 77 (2001).
G. Schauer, R. Kimmich, W. Nusser, Biophys. J. 53, 397 (1988).
E.L. Chen, R. J. Kim, PloS One 6(1), e8565, (2010).
B. Blicharska, H. Peemoeller, M. Witek, J. Magn. Reson. 207(2), 287 (2010).

EPOS™ Poster

Recongintion & simulation

616

Iterative Multi-Slice Compressed Sensing Reconstruction for Peripheral MRA

J. Hutter[1,2], R. Grimm[1], M. Ciocan[1], J. Hornegger[1,2]
[1]*Pattern recognition lab, Department of Computer Science, Universitaet Erlangen-Nuernberg, Erlangen/GERMANY,* [2]*School of Advanced Optical Technologies, Universitaet Erlangen-Nuernberg, Erlangen/GERMANY*

Purpose/Introduction: The combination of parallel MRI and Compressed Sensing (CS) [1] promises accelerated acquisition while maintaining image quality. Non-contrast-enhanced MR angiography, such as Time-Of-Flight (TOF), is an attractive application as it suffers from long acquisition times. Here, we present a multi-slice CS reconstruction for TOF in the peripheral arteries, where vascular continuity across slices can be exploited. Multi-slice reconstruction, sampling patterns and different regularization terms are evaluated.

Subjects and Methods: Volunteer data was acquired on a clinical 3T scanner (MAGNETOM Trio, Siemens Healthcare, Erlangen, Germany). A matrix of 448 x 168 was fully sampled over 448 x 168 mm and retrospectively undersampled using 29 of 168 phase-encoding steps in each slice. Further parameters include: slice thickness 2 mm, TR/TE=34.7/5 ms, flip angle 70°.

The data was partitioned into slabs of N_s slices and image volumes $\mathbf{x}$ were reconstructed from the slabs $\mathbf{y}$ by optimizing the objective function $f(\mathbf{x})$ (Eq.1), consisting of the data fidelity term (containing the sampling patterns $\mathbf{P}$, Fourier Coefficients $\mathbf{F}$ and Coil Sensitivities $\mathbf{C}$). TV-L2 as well as anisotropic and isotropic Total Variation [2] regularization was applied.

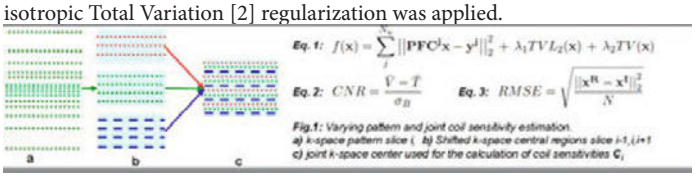

As shown in Fig.1, the sampling pattern $\mathbf{P}$ is interleaved between slices. By sharing k-space data across slices, full sampling in the center is achieved, which allows the estimation of coil sensitivity profiles without an external reference scan. The influence of the weighting terms λ_i, slab size N_s and the varying pattern was studied. Quantitative comparison against the fully sampled reference included the Contrast-To-Noise-Ratio (CNR) and the Root-Mean-Square-Error (RMSE) (Eq.2-3). In addition, Maximum-Intensity-Projections (MIPs) were calculated for visual assessment.

Results: Fig.2 shows CNR and RMSE for the TV-L2 regularization for N_s=5 (2a) and N_s=15 (2b). Increasing λ_1 leads to higher CNR and lower RMSE, but can cause staircase artifacts and artificial straightening of the vessels especially for N_s=5, as illustrated in Fig.3. Interleaving the sampling patterns significantly increases CNR, as evident in Fig.4. As shown in Fig.5, with isotropic TV a higher CNR is achieved than with anisotropic TV.

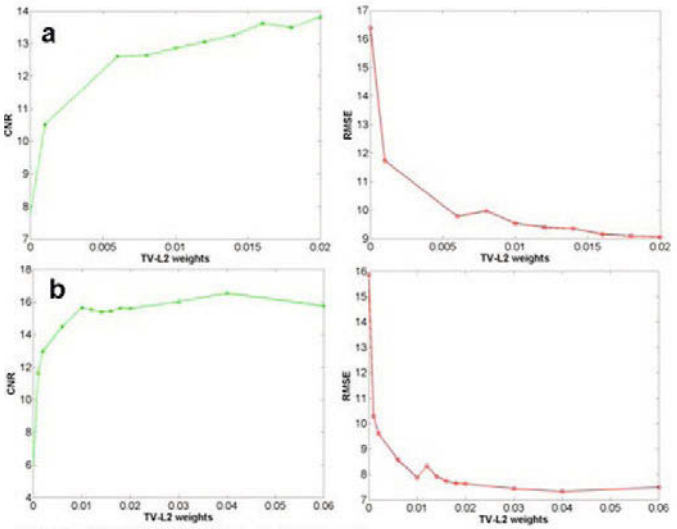

Fig.2: CNR / RMSE: a) N_s=5, b) N_s=15

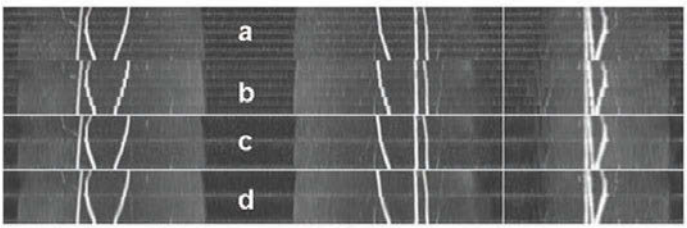

Fig.3: MIPs: a) N_s=5, λ_1=0.006 b) N_s=5, λ_1=0.06 c) N_s=15, λ_1=0.006 d) N_s=15, λ_1=0.06

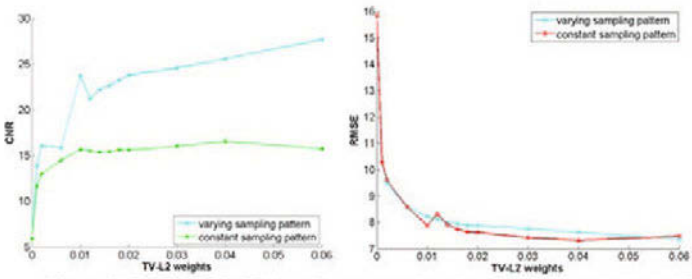

Fig.4: CNR / RMSE for TV-L_2 with constant / varying sampling pattern N_s=15

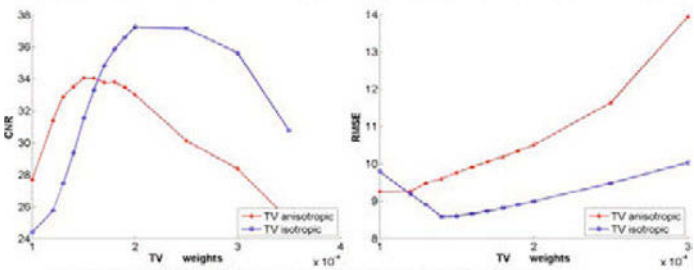

Fig.5: CNR / RMSE for anisotropic and isotropic TV, N_s=15

Discussion/Conclusion: A multi-slice CS algorithm for TOF in peripheral arteries was proposed and evaluated. The combination of a varying pattern and iterative reconstruction using isotropic TV and TV-L2 allows a significant acceleration (17% of the data, no external reference scan) while maintaining a high CNR and a low RMSE. Further studies will be carried out on patient data and include additional regularization techniques such as multi-slice Wavelet.

References:
[1] Lustig, MRM 58(6):1182-1195, 2007
[3] Block, MRM 57(6):1068-1098, 2007

617

Real-time MR simulation by combining Extended Phase Graph Diagrams and Bloch Equation Simulations

C. Cordes[1], M. Günther[1,2]
[1]*MEVIS, Fraunhofer, Bremen/GERMANY,* [2]*Faculty 01 (Physics/Electrical Engineering), University Bremen, Bremen/GERMANY*

Purpose/Introduction: The extended phase graph (EPG) algorithm [1] is commonly used to predict echo amplitudes of sequences with repeating radio frequency (RF) pulse succession. Combining a set of EPGs with Bloch equation simulation (BES) for the RF pulses allows for signal calculation with no drawback in accuracy compared to a contemporary direct BES while improving the simulation time significantly for common use cases.
Subjects and Methods: The EPG algorithm requires fixed parameter values for T1, T2, T2*, constant offset frequency, B1-inhomogeneity, B0-inhomogeneity and z-position for a sequence containing slice selective pulses. The simulation phantom data structure is chosen to be a set of parameter combinations with corresponding spatial densities.
To calculate the echo amplitudes accurately, exact BES results of the pulses are used.
The effect of a RF pulse on a spin ensemble including relaxation effects can be expressed by a 4x4 matrix resulting from the BES of four orthogonal spin ensembles, which is then reused for repeating pulse shapes to avoid computational redundancy. The BES time can be improved even further by reparameterization to reduce the degrees of freedom in parameter space for the RF pulse simulation and optimize the interpolation efficiency. The BES matrices are then transformed to EPG factors and used for signal calculation alongside with the Fourier transformed densities. A framework has been developed in MeVisLab [3] to combine the speed of C++ with advanced memory management techniques and rapid prototyping capabilities.
Results: A variation of the Shepp-Logan phantom [2] containing six different tissues has been used to simulate FLASH, TSE and 3D-GRASE [4] sequences with different spoiling schemes. Partial volume effects with an intra-slice z-resolution of 256 can be replicated accurately while maintaining real-time speed on a standard PC with arbitrary imaging resolutions.
Discussion/Conclusion: An EPG-based signal simulation is a powerful tool that should be considered as an alternative to established BES frameworks. If there is no need for simulating a large number of tissues and B1/B0-inhomogeneities at the same time, there is a great chance that EPGs outperform a pure BES approach in simulation time. The EPGs intrinsically do not suffer from inaccuracies due to insufficient spatial resolution, thus yielding generally superior signal quality when investigating stimulated echoes or T2*-decay.
References:
[1] Hennig, J., 1988, JMR 78(39):397-407
[2] Gach, H.M. et al., 2008, ICSEng '08: 521-526
[3] Ritter, F. et al., 2011, IEEE pulse, 2(6):60–70
[4] Günther, M. et al., 2005, MRM 54(2):491-498

618

Fractional Brain Segmentation using Spoiled Gradient-Recalled Echo with Multiple Flip Angles

A. Ahlgren[1], R. Wirestam[1], F. Stahlberg[1,2,3], L. Knutsson[1]
[1]*Department of Medical Radiation Physics, Lund University, Lund/SWEDEN,* [2]*Department of Diagnostic Radiology, Lund University, Lund/SWEDEN,* [3]*Lund University Bioimaging Center, Lund University, Lund/SWEDEN*

Purpose/Introduction: Data-driven segmentation by modelling of dynamic MR signal has numerous potential applications [1,2]. In this work, a spoiled gradient-recalled echo (SPGR) with multiple flip angle acquisition is proposed for fractional segmentation, and the potential of the method is demonstrated through simulations.
Subjects and Methods: The SPGR signal equation is given by:

$$S(\theta) = S_0 \sin(\theta)\frac{1-e^{-TR/T1}}{1-\cos(\theta)e^{-TR/T1}}e^{-TE/T2^*} \qquad [1]$$

where S_0 is equilibrium signal and θ is the flip angle. T1 mapping is feasible by variable flip angle (VFA) acquisition with subsequent fitting of Eq. 1 [3]. The SPGR signal is modelled as follows:

$$S(\theta) = \sin(\theta)\sum_i f_{s,i}\frac{1-e^{-TR/T1_i}}{1-\cos(\theta)e^{-TR/T1_i}} \qquad [2]$$

where $f_{s,i}$ is the fractional signal contribution and $T1_i$ is the longitudinal relaxation time (i denotes the compartment). For demonstration purposes, grey matter (GM), white matter (WM) and cerebrospinal fluid (CSF) were segmented, i.e., i={GM,WM,CSF} (transversal relaxation effects neglected). Fractional signal values may be estimated by linear least squares, if relaxation terms are known (Figure 1).

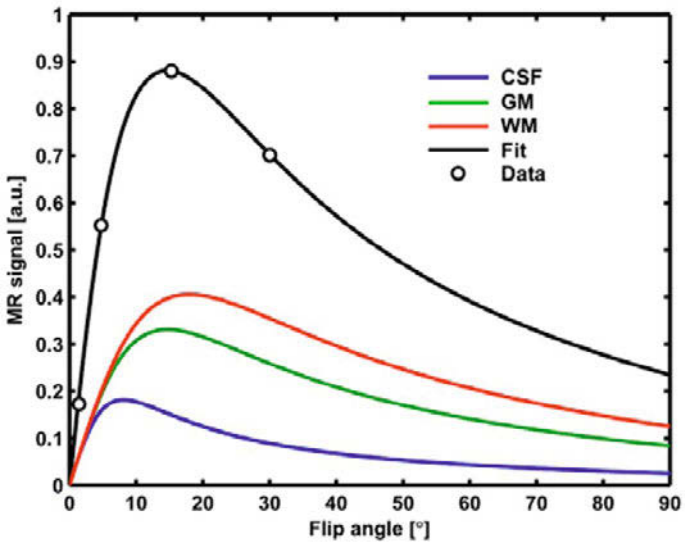

Fig 1. Schematic illustration of the model.

Fractional brain maps from an established segmentation method [2] were used as the ground truth. Data were simulated according to Eq. 2 using S_0=1, $T1_i$={1.5,1.0,5.0} s, θ={2°,5°,15°,30°}, TR=10 ms, SNR={10,25,50,100,150,200}. The performance of the segmentation was assessed by calculating the absolute difference, averaged over the entire brain, between the estimated fractional volume and the ground truth (accuracy), the root mean square error of the corresponding difference (precision), volume agreement (VA) and volume overlap

(VO), for each compartment. VA is the agreement in total volume [4], and VO is the spatial correlation of fractional volumes (cf. Dice's coefficient) [5].
Results: Segmentation results from one slice are exemplified in Figure 2. Figure 3 displays results from the assessment of performance.

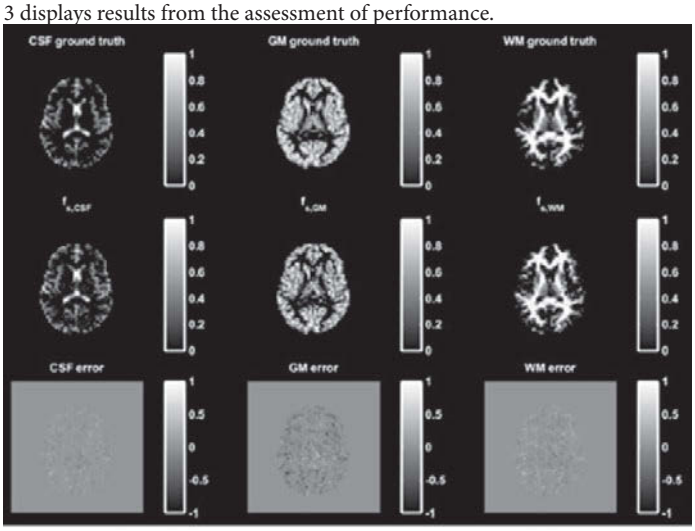

Fig 2. Segmentation results from one slice (SNR=100).

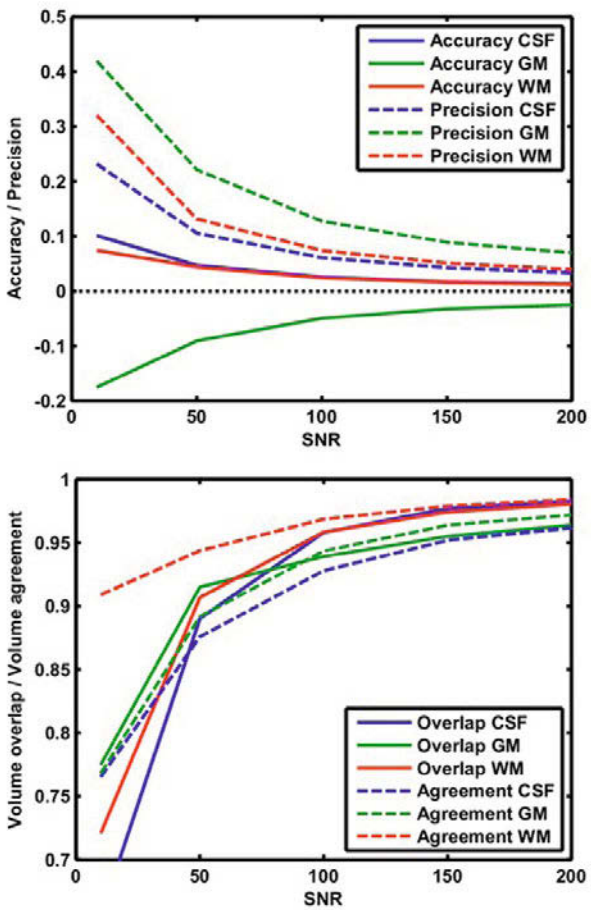

Fig 3. Performance quantities (values are absolute, i.e., not percentage of ground truth).

Discussion/Conclusion: At least three different flip angles are required to resolve the different compartments. Simulations indicated that four flip angles are sufficient for robust segmentation, which implies the possibility of rapid acquisition. Accuracy and precision were reasonable, and VA and VO suggested excellent agreement, with values consistently above 0.7 for SNR>10 [6]. The proposed approach is particularly suitable for applications in which SPGR T1-mapping is already included (e.g., DCE-MRI), thereby allowing implementation without additional scans. Future work includes in-vivo verification, protocol optimization and correction for B1-inhomogeneities.
References:
[1] Shin W et al. 2010 Neuroimage 52:1347. [2] Ahlgren A et al. Proc. ESMRMB 2011, #554. [3] Fram EK et al. 1987 MRI 5:201. [4] Liu T et al. 2006 NeuroImage 31:51. [5] Cardenas VA et al. 2001 Psychiat Res-Neuroim 106:193. [6] Zijdenbos AP et al. 1994 IEEE Trans Med Imaging 13:716.

619
Least Memory Non-Uniform FFT

K. Vahedipour[1], N.J. Shah[1, 2]
[1]*INM-4 Medical Imaging Physics, Forschungszentrum Juelich, Juelich/GERMANY,* [2]*Department of Neurology, Faculty of Medicine, JARA, RWTH Aachen University, Aachen/GERMANY*

Purpose/Introduction: Reconstruction of parallel non-Cartesian data can be very challenging, particularly when big imaging matrices, off-resonance correction and/or non-linear reconstruction strategies coincide. Random undersampling in the non-Cartesian context patticularly, gives rise to increased complexity. However, Bloch dynamics as well as Faraday's law display spatiotemporal symmetries, which can be exploited through time-reversal[1]. Although such a reverse solution of the Bloch equation is *per se* slower than non-uniform FFT solutions, the outcome tilts when off-resonances are considered. Through parallelisation, speedups of orders-of-magnitude are realisable when compared to modern multithreaded libraries. Code of this algorithm is available along with test data (codeare.org).
Subjects and Methods: Recently, we proposed the exploitation of spatiotemporal symmetries for computation of small tip-angle (STA) pulses [1] in parallel transmission. The Bloch equation, neglecting the dissipative effects of T_1 and T_2^*, which is an autonomous ODE, and the reciprocity-principle [4], the consequence of Faraday's law for MRI, display symmetries which allow one to consider signal acquisition and STA excitation [5] along the same trajectory as a Fourier pair in parallel MRI (Eq.1). The operation that transforms a shape $\mathbf{m}(\mathbf{r})$ into signals $s_n(t)$, is the acquisition or the Fourier-analysis and the inverse operation is the Fourier-synthesis or STA excitation. While the strict validity of reciprocity only applies to the stationary frame, i.e. transmit and receive sensitivities product $\sigma^*_n \sigma_m \neq \delta(n\text{-}m)$, one designs simulations where the rules are bent accordingly.

$$s_n(t) = i\gamma m_0 \sum_{m=1}^{N} \int_0^T b_m(\tau) \times \left(\int_{\mathbb{R}^3} \sigma_n(\mathbf{r})^* \sigma_m(\mathbf{r})\, e^{i(\mathbf{k}(T-t)-\mathbf{k}(\tau))} d\mathbf{r} \right) d\tau$$

Eq.1: Signal equation for n-th receive channel. The sensitivties, sigma are the actually measured receive sensitivities , which are used in simulation of the time inversion of the spin system, which gave rise to the measured signal. The k-spaces for receive and transmit are identical apart from time-reversal. Individual spins can be dealt with seperately (space integral) allowing one to parallelise the algorithm .

Results: Figure 1 shows the runtimes and memory consumption for different parallelisation schemes and data sets. Figure 2 shows a "money-shot" reconstructed using the proposed method.

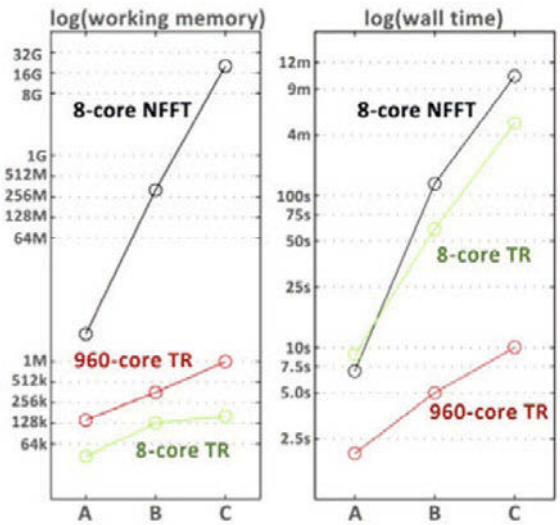

Figure 1: Comparison of runtimes and working memory consumption for 3 different datasets and according grid sizes. A: 2D 128^2, B: 3D 128^3, C: 3D 512^3. The reconstructions were performed with NFFT on 8 CPU cores (black line), with the proposed method on 8 CPU cores (green line) and on 960 GPU cores (red line).

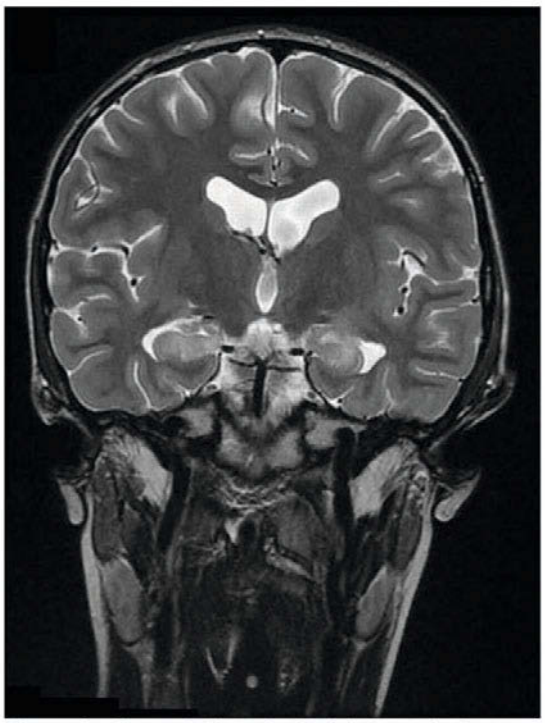

Figure 2: Coronal slice of a 2D 24-shot spiral scan 32-channel acquisition with b_0 correction (+/- 40Hz) from 3T.

Discussion/Conclusion: The MRI machine and sequence traditionally Fourier-transform a weighted magnetisation-density function as an analogue computer while the appropriate reconstruction applies the inverse transform. In contrast to reality, where the reciprocity principle is violated at any Larmor-frequency, a perfect world can be designed in simulation for reversing MRI signal formation process for image reconstruction. The proposed method is conceptually simple and opens up a range of useful instruments. It should be applied always, when multi-channel data is reconstructed including field corrections.

References:

[1] Vahedipour et al, ISMRM 2012 [2] Katscher et al. MRM 49(1):144–150 (2003) [3] Zhu et al. MRM 51(4):775–784 (2004) [4] Hoult et al, CMR 12(4):173-187 (2000) [5] Pauly et al. JMR 82(3):571-587 (1989) [6] Pruessmann et al. MRM 46(4):638–651 (2001) [7] Jaynes et al. PRL 98(4):1099-2004 (1955) [8] Stöcker et al, MRM 64(1):186-193 (2010) [10] Lustig et al, MRM 58(6):1182-1195 [9] Knopp et al. IEEE TMI 28(3):394-404 (2009)

EPOS™ Poster

RF & quality control

620

Low cost preamplifiers and T/R switches for ultra-high field NMR

E.B. Giacomini[1], G. Ferrand[2], M. Luong[2], J. Novo[2], G. Radecki[1], C. Poupon[1], D. Le Bihan[1]
[1]DSV/I2BM/Neurospin, CEA, gif sur yvette/FRANCE, [2]IRFU-SACM, CEA-Saclay, Gif-sur-Yvette/FRANCE

Purpose/Introduction: The design of a phased array RF coil for high field MRI requires highly efficient T/R-switches and preamplifiers. Common specifications are given with a minimum gain of 30 dB, a maximum noise figure of 2 dB, and a minimum isolation of 40 dB during transmission. The following design was proposed for a 12-dipole transceive coil, for 7 T proton MRI. The size of the system, and their cost have been considered.
Subjects and Methods: The device is implemented on a single PCB of FR-4, with dielectric constant of about 4.5 and dissipation factor 0.02 at 300 MHz [1]. Each preamplifier chip (Hittite HMC616) gives a gain of 15-20 dB when supplied with 3V, a 0.5 dB noise figure, in a narrow bandwidth centered at 300 MHz. Input and output are matched to 50 Ω. To obtain the 30-dB gain specification, two chips are cascaded. The T/R-switch is based on a series-shunt configuration scheme using PIN diodes and λ/4-transmission lines [2] (Fig.1). The stripline technology is used for λ/4-transformers instead of coaxial lines. They are traced directly on the PCB (Fig.2) and provide more accurate implementation et lower sensitivity to EMI. Footprint of the circuit is 10x8 cm. PCB and parts cost about 200€.

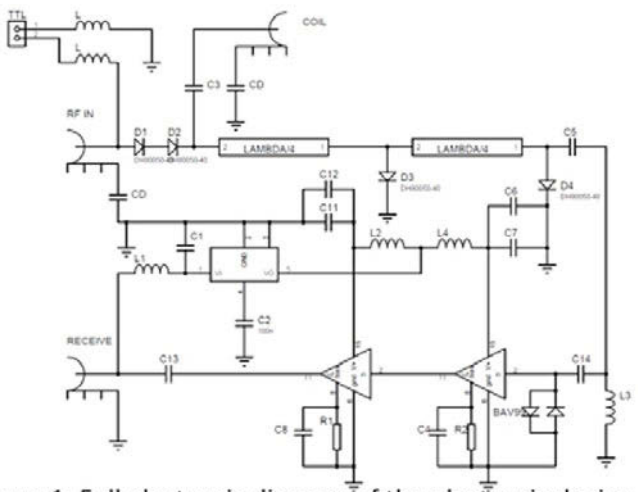

Figure 1: Full electronic diagram of the electronic device

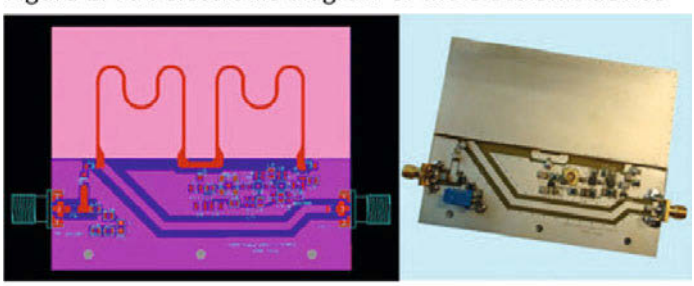

Figure 2: trace (left) and picture (right) of the TR/switch + preamplifier device

Results: Comparison between a commercial device and our design is given in Fig. 3. The new design significantly reduces the noise factor while increasing the isolation of the T/R-switch and preamplification gain. At 300 MHz outside the magnet, the signal-to-noise ratio inscreases by 10%. The same experiments were performed in the MRI scanner. Performances are even slightly better in the magnet provided that the chip surface is parallel to the field (G=32.4±0.4 dB and NF=1.38±0.1 dB). Nevertheless, performances drop drastically in another configuration (G=26.0±0.4 dB and NF=2.6±0.2 dB, when the chip surface is perpendicular to the field).

Frequency (MHz)	280	290	300	310	320
			Gain (dB)		
Commercial	24.8	26.3	23.6	19.9	18.0
New design	31.9	31.6	31.0	31.1	31.3
			Noise factor (dB)		
Commercial	2.42	1.90	2.25	3.55	2.50
New design	1.45	1.35	1.43	1.35	1.58
			Isolation (dB)		
Commercial		-21	-32	-35	
New design		-46	-46	-47	

Figure 3: Comparison between the commercial TR-Swith / preamp commercial device and our new design, without magnetic field.

Discussion/Conclusion: Efficient and flat T/R-switches can be produced for 200€ per unit. Footprint of the circuit is dominated by the quarter-wavelength transformers. Redesigning the meanders may compact further the circuit. A low loss substrate like Arlon AD450 can also contribute to a 0.4 dB reduction in the noise figure at the expense of a slightly higher cost. Extension of the current design to higher field/frequency is very straightforward.
References:
[1]Industrial Laminating Thermosetting Products, *NEMA Standards Publication N°LI1-1998.* [2]An SPDT PIN Diode T/R-Switch for PCN Applications, *Agilent Application Note 1067.*

621

Design and characterization of a four channel surface receiver coil array dedicated to fMRI in rat brain.

A.-L. Perrier[1], D. Grenier[1], N. Ravel[2], P. Litaudon[2], O. Beuf[1]
[1]Creatis, CNRS UMR 5220, Inserm U1044, Insa-Lyon, Université Lyon1, Villeurbanne/FRANCE, [2]Centre de Recherche en Neurosciences de Lyon, CNRS UMR 5292, Inserm U1028, Université Lyon1, Lyon/FRANCE

Purpose/Introduction: One of the multiple techniques to decouple neighbour elements of multi-channel coil array is based on the loop junction [1]. This technique is usually used to conceive two-channel coil array; decoupling between channels is realised with a capacitor in series with the common conductor. The design and decoupling for two-channel coil array was recently formalized using impedance transformation approach [2]. The same approach and common conductor technique was used to conceive a four-channel coil array for high resolution imaging of both rat knees [3]. Based on these two precedent works, a four-channel receiver coil array, dedicated to rat head at 7T for fMRI, is presented and characterized in this paper.
Subjects and Methods: The specific four-channel coil array, shown in Fig. 1, was built to fit the animal morphology. Coil array was first characterized with a four port VNA. Imaging performances of the array were performed on a

Bruker 7T Biospec MR system: SNR profiles were measured on images of a cylindrical phantom (30 mm diameter) filled with doped saline water solution (NiSO4 1.25 g/L and NaCl 5 g/L); BOLD signals were detected on rat brain by fMRI with an olfactory stimulation of the animal. The experimental protocol was approved by the Animal Ethics Committee of our institution. *In vitro* images were acquired with a FLASH 3D sequence (TR/TE=15/6ms, FA=15°, FOV=7x4x4cm^3, 256x146x146 pixels). *In vivo* images were acquired with an EPI sequence (TR/TE=1000/19ms, FOV=2.5x2.5cm^2, 128x128 pixels). In both acquisitions, a vertical orientation of B_1 was necessary to obtain a uniform signal with the array.

Results: $|S|$ measured parameters of the array are presented in Fig. 2: $|S_{ii}|$ and $|S_{ij}|$ parameters inferior to -20 dB shown the good matching of each channel and sufficient decoupling between elements, respectively. The array geometry, covering almost entirely the cylindrical phantom, allows having signal from deep region of the sample (Fig 3 a)). Maximum SNR is about 280 in extern region and about 100 in the phantom centre (Fig 3 b)). The sensitivity of the array in rat brain region allowed the detection of activations in the olfactory bulb and in the olfactory cortex (Fig. 4). The detection in the deep region of brain could be improved.

Fig. 1 *Photograph of the four channel coil array built for rat head.*

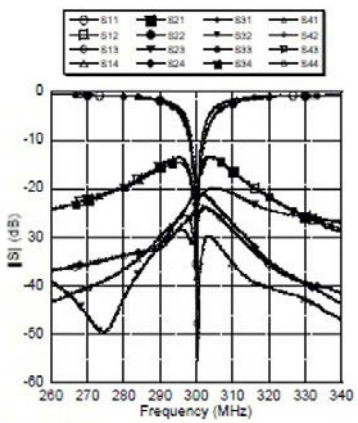

Fig. 2 *|S| parameters measurements of the four-channel coil array.*

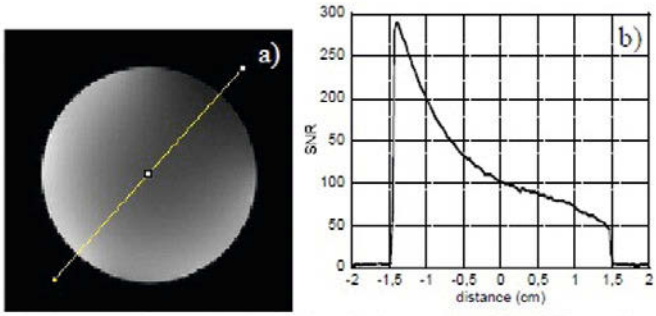

Fig. 3 a) *Axial image of cylindrical phantom and b) SNR profile.*

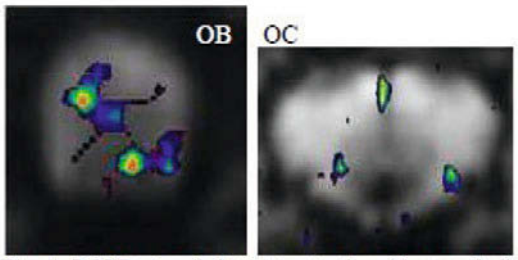

Fig. 4 *BOLD signal detection in the olfactory bulb (OB) and in the olfactory cortex (OC); blue to red for down to high level.*

Discussion/Conclusion: Although performances of the receiver were demonstrated on in vivo acquisitions, the B_1 alteration cause by the array has to be studied.

References:

[1] J. Wang. ISMRM-1996.
[2] A.-L. Perrier *et al.* IEEE-Sensors-Journal-2012.
[3] A.-L. Perrier *et al.* IEEE-Sensors-Journal, in press.

622

Investigation of shielded volume coil performance using dielectric cylinders with variable diameter at 7 Tesla

A.I. Osorio[1], S.E. Solis-Najera[2], R. Martin[2], F. Vazquez[2], A.O. Rodriguez[3]
[1]Dep Ciencias Basicas e Ingenierias, UAM Azcapotzalco, Mexico DF/MEXICO, [2]Facultad de Ciencias, Departamento de Fisica, Universidad Nacional Autonoma de Mexico, DF/MEXICO, [3]Dep. Ingenieria Electrica, UAM Iztapalapa, Mexico DF/MEXICO

Purpose/Introduction:
Shielded volume RF coils have proved to be reliable and good performance devices to generate high quality images. The use of dielectric material with resonator coils for RF inhomogeneties was first investigated by Foo and collaborators [1]. The advantages of the dielectric materials in MRI have been already reported [2,3]. The position and diameter of the dielectric material for optimal coil performance still remains to be investigated. We numerically computed the coil performance for various dielectric cylinders with different diameters and positions.

Subjects and Methods:
Coil performance and SAR at 300 MHz were computed via the return loss simulations of a copper- shielded 16-rug birdcage coil (10cm long/5cm diameter) and a dielectric cylinder (10cm long/5.15cm diameter) between the coil and the shield (position 3 in Fig. 2.b). We used the dielectric constants (DC): 0.3, 0.5, 0.85, 1, 5, 20, 35, and 110 and computed SAR100 mg of tissue using a rat's simulated brain phantom and eq. (1) [4]. We then calculated the coil performance at different locations of the dielectric cylinder as shown in Fig.

2.b), using DC=110. The FIM method implemented in CST (CST Microwave Studio, Darmstadt, Germany) was used for all simulations.

Results:

Plots of performance-vs.-dielectric constant and Maximum-deposited-power-fraction-vs.-dielectric constant are shown in Fig. 1. As already known, shielded volume coils have better performance with associated high SAR levels. Coil performance and SAR increase as the DC values grow, but both values are not greater than the reference values of SAR and performance for the shielded coil.

Discussion/Conclusion:

A DC>100 is needed to produce a better performance, with the disadvantage of generating high SAR levels. A lower DC is better in terms of the SAR, but with low coil performance. These simulations indicate that lower SAR levels come with lower coil performance and vice versa. The coil performance as a function of the dielectric cylinder diameter is shown in Fig. 2.a). The performance seems to be fairly the same regardless the dimensions and the locations of the dielectric cylinders. In the vicinity of the RF shield, the performance values are pretty close to that of the shielded coil only. Dielectric with higher constants may solve this limitation.

Acknowledgments. We thank CONACYT Mexico for research grant 112092. S.E.S. thanks DGAPA-UNAM for a postdoc stipend. email: arog@xanum.uam.mx.

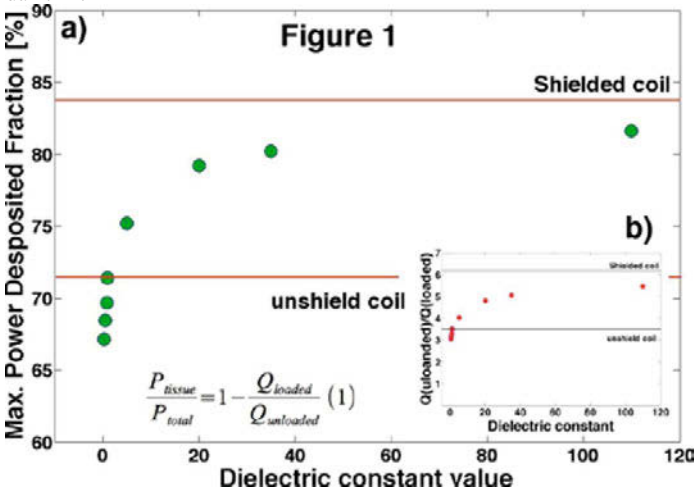

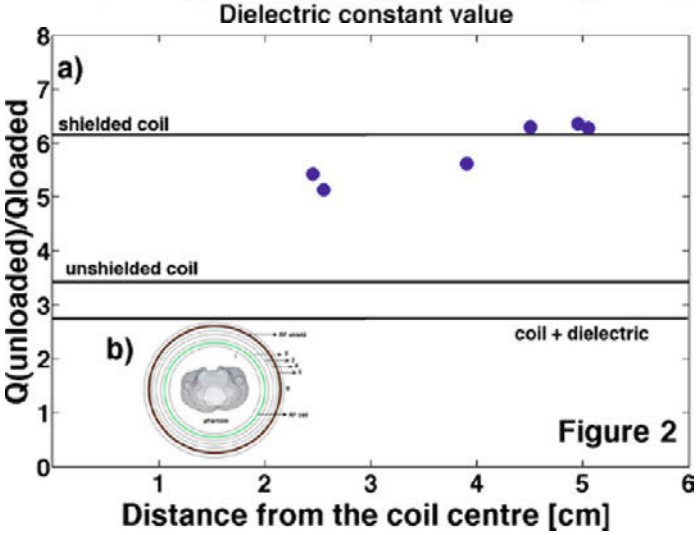

References:

1. Foo et.al. Magn Reson Med 23,287,1992. 2-. Snaar et.al. NMR Biomedicine, 24,873,2010. 3. Webb. Conc Magn Reson 38A,148,2011. 4. Prock et.al. Phys Med Biol 47,1805,2002.

623

Assessment of Ultem as a susceptibility matching material: a comparative study

J.-M. Verret[1, 2], F. Pilleul[3], C. Rabrait[2], O. Beuf[1]

[1]CNRS UMR 5220; Inserm U630, Université de Lyon, CREATIS, GEHC, Villeurbanne/FRANCE, [2]Clinical Science Development Group, General Electric Healthcare, Buc/FRANCE, [3]Gastroenterology, Hospices Civils de Lyon, Lyon/FRANCE

Purpose/Introduction: A double loop endorectal coil was developed to observe the rectal wall but it suffered from artifacts due to the magnetic susceptibility gradient between air (inside the coil) and water (outside the coil). Thus, we investigated Ultem™ (i.e Polyetherimide: $C_{37}H_{24}O_6N_2$) as a susceptibility matching material and compared it with barium sulfate, already used in the literature [1] [2].

Subjects and Methods:

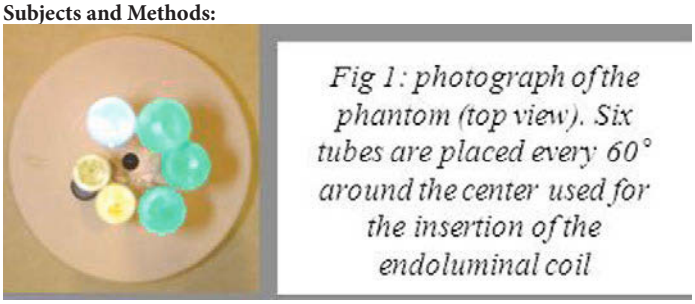

The difference of susceptibility between two media results in artifacts in shape and signal intensity due to pixels shift in readout direction. The experiments were set to maximize this susceptibility effect on images. For a given susceptibility difference between two media and a given shape (cylindrical or other), artifact amplitudes will depend on the orientation regarding the magnetic field B0. For a cylinder, it is maximal when the cylindrical axis is orthogonal to B0. Because of the frequency dispersion on images, the artifact is larger for a narrow receiver pixel bandwidth. The slice thickness was set to 2 mm to limit slice deformation during selection process in presence of inhomogeneities. *Phantom* : water-filled cylinder with holes allowing insertion either of high resolution NMR tubes (empty or filled with barium sulfate) or ultem cylinder (fig 1).The shim values were kept the same to observe differences coming only from the susceptibility modifications.

	TE/TR (ms)	Slice Thickness (mm)		Pixel Bandwidth (Hz/ px)	Matrix	FOV (mm^2)
FSE-XL	29.1 / 1500	2	Echo Train = 10	27.1	320×256	70×70
GRE	15.8 / 300	2	Flip Angle = 30 °	46.5	512×384	80×80

Table1 : Parameters for the acquisition of axial slices of the cylindrical phantom.

Results:

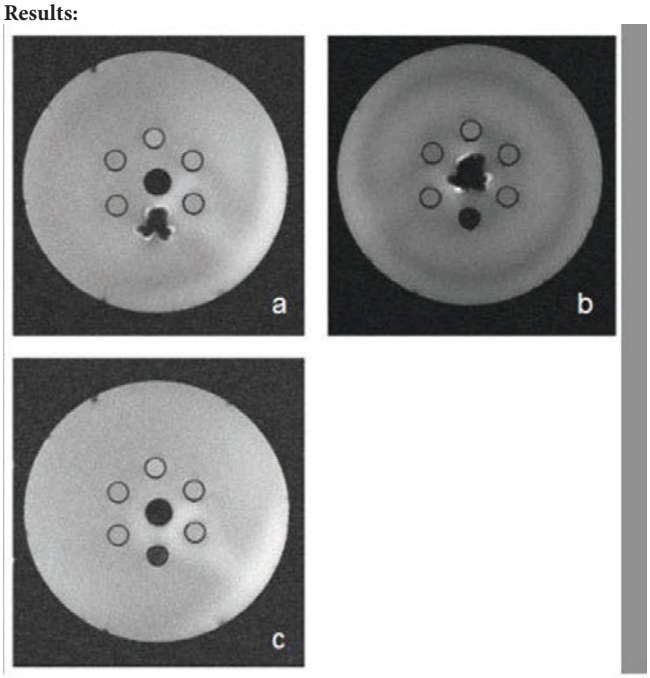

Fig 3: GE of the phantom a) central hole = ultem and bottom hole = air b) central hole = air and bottom hole =barium sulfate c) central hole = ultem and bottom hole = barium sulfate

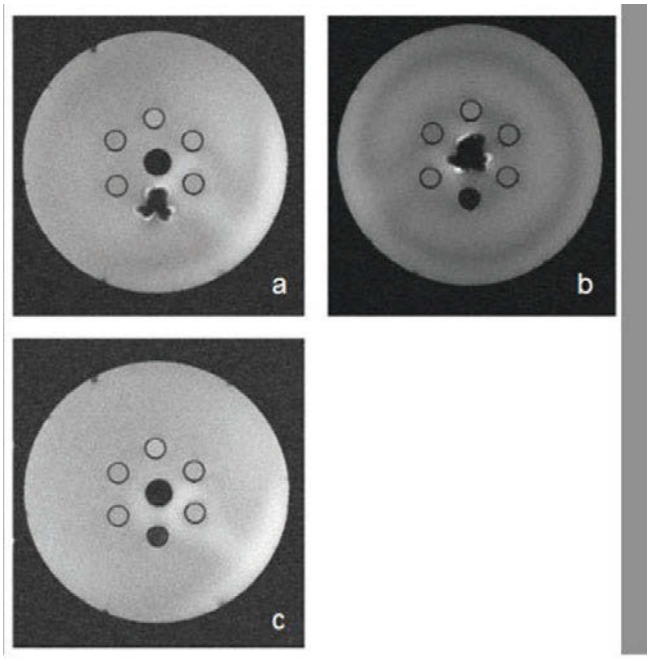

Fig 3: GE of the phantom a) central hole = ultem and bottom hole = air b) central hole = air and bottom hole =barium sulfate c) central hole = ultem and bottom hole = barium sulfate

Both materials greatly decrease the susceptibility artifact. Ultem is better than barium sulfate which produces a water drop shape: the diamagnetic susceptibility of barium sulfate at 100% w/v is inferior to water susceptibility. Another advantage of ultem is the total lack of signal intensity.

Discussion/Conclusion: Ultem was slightly better than barium sulfate for suppressing image artifacts. Furthermore its solid state enables an easier integration as a solid support for the endorectal coil. Thus, we believe ultem to be a promising susceptibility matching material for the acquisition of images devoid of susceptibility artifacts with an endorectal coil.

References:

[1] Rosen et al, Magn Res Med, Volume 57, Number 5, May 2007
[2] Choi et al, AJR Am J Roentgenol, Volume 190, Number 4, April 2008

624

Motion correction of multi-contrast images applied to T1 and T2 quantification in cardiac MRI

A. Menini[1], G. Slavin[2], J. Stainsby[3], P. Ferry[1, 4], J. Felblinger[1, 4], F. Odille[1, 4]
[1]IADI, Université de Lorraine, Nancy/FRANCE, [2]GE Healthcare, GE, Bethesda/UNITED STATES OF AMERICA, [3]GE Healthcare, GE, Toronto/CANADA, [4]INSERM, U947, Nancy/FRANCE

Purpose/Introduction: The ability to manipulate image contrast and thus to obtain complementary information is one of the main advantages of MRI [1]. Motion consistency within the whole dataset is a key point in the context of multi contrast imaging. In cardiac and abdominal MRI, the acquisition strategy uses multiple breath-holds, and often relies on acceleration methods that inherently suffer from a signal-to-noise ratio loss. The aim of this work is to propose a free-breathing multi-contrast acquisition and reconstruction workflow to improve image quality and the subsequent data analysis.

Subjects and Methods: We extended a previously proposed motion compensated image reconstruction method (GRICS) [2] for multi-contrast (MC) imaging. In the novel method proposed here (MC-GRICS), shared information throughout the imaging protocol is exploited by the image reconstruction in the form of an additional constraint based on image gradient sparsity [3]. This constraint helps minimizing the amount of data needed for efficient non-rigid motion correction. T_1 and T_2 weighted images were reconstructed from free-breathing acquisitions in 4 healthy volunteers and in a phantom. The impact of multi-contrast motion correction was evaluated in terms of precision and accuracy of T_1 and T_2 quantification. We studied the trade-off between acquisition time, i.e. number of repetitions N_{rep}, and image quality.

Results: In the phantom, the proposed method achieved an accuracy of 94.3% on the quantified parameters against 88.0% before motion correction (Fig. 1). In volunteers, images reconstructed with our method from free-breathing acquisitions with $N_{rep} \geq 2$ showed a better image quality than breath-held images (Fig. 2). Thus, T_1 and T_2 quantification was obtained with 10 minutes of free-breathing acquisition.

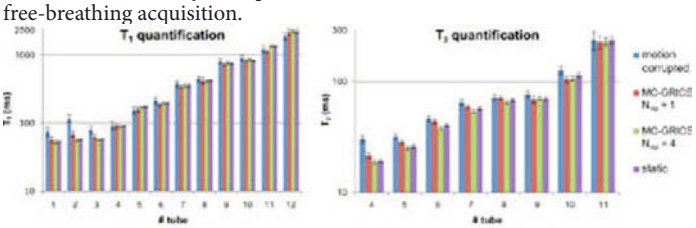

Fig. 1 T_1 (left) and T_2 (right) quantification on the phantom scanned while moving. Measurements are compared before (motion-corrupted), after motion correction with MC-GRICS (with 1 and 4 repetitions) and without motion (static). Error bars represent 95% confidence intervals.

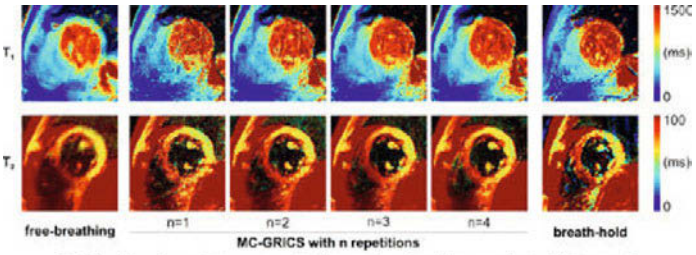

Fig. 2 Evolution of quantitative maps against the number of repetitions on volunteer #1 (top row: T_1 maps, bottom row: T_2 maps)

Discussion/Conclusion: We proposed an efficient multi-contrast imaging method in free-breathing with no prior assumption about contrast and thus applicable to a wide range of examinations. To our knowledge, the proposed method is the first that can correct for motion in multi-contrast imaging.

References:

[1] Kellman et al.(2005) Magn Reson Med., [2] Odille et al. (2008) Magn Reson Med., [3] Haldar et al. (2012) Magn Reson Med.

625

Gradient artifact reduction on ECG signal using an LMS algorithm: Optimization of adaptive algorithm

A.P. Guillou[1, 2], S. Menetre[1], G. Petitmangin[1], L. Zhang[2, 3], J. Felblinger[2, 4, 5, 6], L. Bonnemains[2, 5, 7]

[1]R&D, Schiller SAS, Wissembourg/FRANCE, [2]U947, Inserm, Vandœuvre-lès-Nancy/FRANCE, [3]Cardiologie, CHU Brabois, Vandœuvre-lès-Nancy/FRANCE, [4]CIT801 (CIC-IT Nancy), INSERM, Vandœuvre-lès-Nancy/FRANCE, [5]IADI, Université de Lorraine, Nancy/FRANCE, [6]Brabois, CHU de Nancy, Nancy/FRANCE, [7]Department of Cardiology, CHU Nancy, Nancy/FRANCE

Purpose/Introduction: During cardiac MRI, switching of magnetic gradients and magneto-hydrodynamic effects alter the ECG and impair its use, both for triggering and monitoring. Least Mean Square (LMS) algorithm is a simple and efficient adaptive filter frequently used to denoise ECG. It uses a parameter called step size (μ) which influences directly the quality of artifact reduction. The parameter μ has a large range of possible values (from 10^{-5} to 10^{-1}) and therefore is difficult to choose. According to the linear time-invariant system (LTI) theory, the optimal μ should depend on the variance of the Gradient signal. We verified this assumption in MRI context on classical clinical cardiac sequences.

Subjects and Methods:

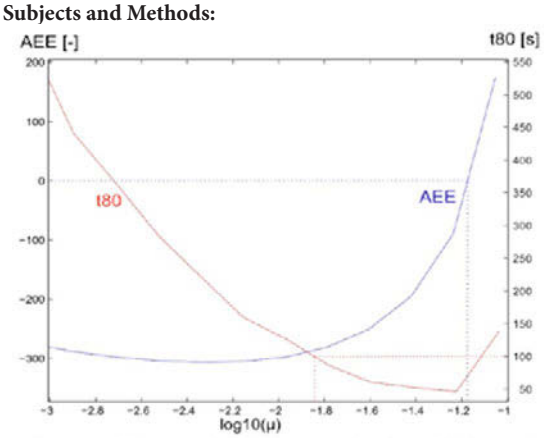

Figure 1 : AEE and t80 for different values of μ for one ECG acquisition during a SSFP. AEE beeing a logarithm of the quotient energies, AEE>0 implies a noise energy enhancement, and is unacceptable. Optimal μ for this patient is $10^{-1.84}$ =0.015

Three minutes of ECG were recorded for 16 volunteers (8 normal, 8 presenting arrhythmias, total of 15,000 QRS complexes) at 1.5T with 2 MRI sequences (Steady State Free Precession, Fast Spin Echo). Each ECG was denoised with LMS algorithm using 40 values of μ logarithmically distributed within the range of possible μ.

LMS efficiency was assessed with two factors:

1/Artifact Energy Evolution (AEE): logarithm of the quotient of the annotated artifacts energies (Square sums of amplitudes) after and before LMS denoising.

2/ Convergence time (t80): time to reach an 80% reduction of the local variance of the estimated solution (which gives information about the LMS speed of adaptation to a non-constant optimal impulse response solution).

The optimal μ was defined as the minimizer of AEE under the constraint of t80<100ms, to enable quick convergence between QRS complexes (Fig.1). AEE should always be positive, to ensure denoising was effective.

Results: An optimal μ, different for both sequences, was found (Tab.1). Moreover, these optimal values of mu were close to the theoretical limit values, without ever exceeding it. Fig.2 presents two examples of LMS artifact reduction with a default and the empirical optimal values of μ for a SSFP sequence.

	Theoretical limit mu	Empirical optimal mu	
		Mean	Standard deviation
SSFP	$3.5e^{-2}$	$1.5e^{-2}$	$2.7e^{-3}$
FSE	$2.5e^{-1}$	$1.9e^{-1}$	$1.5e^{-2}$

Table1: Empirical and theoretical values of optimal μ.

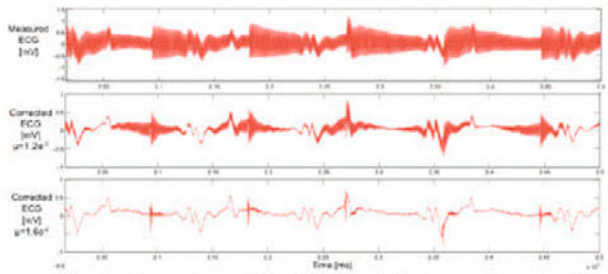

Figure 2 : LMS correction of an ECG acquired during a SSFP sequence, with two values of μ

Discussion/Conclusion: The optimal value of mu depends on the sequence, and can be predicted using LTI theory. This value can be used to parameter real-time LMS algorithms for ECG denoising in cardiac MRI for better triggering or monitoring. Such results can be extended to other clinical sequences, such as Myocardial Delayed Enhancement (MDE).

References:

R. Abächerli et al., "Suppression of MR gradient artefacts on electrophysiological signals based on an adaptive real-time filter with LMS coefficient updates", Magnetic Resonance Material in Physics, Biology and Medecine (2005)

B. Widraw and S.D.Stearns, "Adaptative Signal Processing". New Jersey: Prentice-Hall, 1985

626

A novel diffusion phantom imitating white matter for both DWI and DTI MR Imaging.

I. Filipiak[1], C. Destrieux[1], J.-P. Cottier[1, 2], L. Barantin[1, 2]

[1]Equipe 5 Imagerie et Ultrason, INSERM U930 - Universite Francois Rabelais, TOURS/FRANCE, [2]Service de Neuroradiologie, Groupement Imagerie Médicale, Hopital Bretonneau, CHRU Tours, Tours/FRANCE

Purpose/Introduction: To investigate brain microarchitecture and white fibers organization, Diffusion Weighted Imaging (DWI) and Diffusion Tensor Imaging (DTI) [1], are applied as non-invasive MR techniques based on water diffusion mobility. Quantitative information can be extracted like Apparent Diffusion Coefficient (ADC), fractional anisotropy (FA), or mean diffusivity

(MD). An indirect visualization of the white fiber organization is possible using tractography algorithms [2]. The lack of available phantom reproducing the three dimension orientation, anatomical structure, and different diffusion properties, make that the validation is not optimal.
In this study, we developed a homemade phantom to imitate white matter tracts organization to improve the accuracy of diffusion measure.
Subjects and Methods:
The 3D skeleton as 6 slices reproducing isotropic and anisotropic anatomy properties. Slice1 is composed of 3 compartments of sucrose solutions with various concentrations; one of hydro-alcoholic gel and another of pure water. The Slice 2 is composed of 5 longitudinal bundles. Different U-shape bundles were placed in slice 3. The slice 4 imitates different angular bundles. The slice 5 makes 2 crossing bundles and 1 S-shape. Finally, slice 6 permits the position of fan shape with a specific device. Dyneema and nylon fibers were used. This test object was validated with a 3T MR scanner using the same parameters used for clinical practice.
Post-processing consisted to investigate the number, value and the combination of b-value points needed to accurate ADC measurement.The diffusion tensor data was calculated for each voxel. Then tracts were reconstructed using deterministic algorithms (Interpolated Streamline, FACT, tensorline) to evaluate position error and tractography shifts.
Results:
Analysis revealed under-estimation about -7% in the mean of ADC between the clinical acquisition protocols (as b1=0 s/mm^2) and reference (11 b-values). In comparison with b1>0 s/mm^2, the relative difference was less than 1.5%. In fiber bundles, FA, MD, did not significantly differ with fiber shape ($p>0.05$) and imaging session. Tractography algorithms used were all able to reconstruct all fiber bundles.
Discussion/Conclusion:
We suggest using b1=50 to guaranty accuracy of ADC. FA, MD, values were similar across imaging sessions and the different fiber shapes were representative of the human white fibers anatomy. Tractography was doable on the phantom and length of detected fibers varied depending of the used material and algorithm.
This new phantom significantly expands the potential of quality control in diffusion imaging to improve the accuracy of diffusion data and tractography in clinical practice.
References:
[1] Basser et al., 1994
[2] Fillard et al. 2011

627

Orthodontic appliances and quality of cleft and speech MRI.

M. Wylezinska-Arridge[1], M. Pinkstone[2], N. Hey[3], M. Birch[1], M.E. Miquel[4]
[1]Clinical Physics, St. Bartholomew's Hospital, London/UNITED KINGDOM, [2]Speech and Language Therapy, Great Ormond Street Hospital for Children, London/UNITED KINGDOM, [3]Dental and Maxillfacial Department, Great Ormond Street Hospital for Children, London/UNITED KINGDOM, [4]Barts and the London Cardiovascular Biomedical Research Unit and Clinical Physics, Barts and the London NHS Trust, London/UNITED KINGDOM

Purpose/Introduction: MRI is a promising tool for the assessment of cleft palate anatomy and the evaluation of velopharyngeal function during speech [1,2]. Stainless steel and other metals used in prosthetic dentures and orthodontic braces are known to create artefacts around facial area [3]. In general implants do not present safety concern at field less than 3T [4] and are of little concern for image quality in brain imaging [3]. However, due to their proximity, they are likely to interfere with palate imaging. The purpose of this work is to investigate in more detail the effects that different appliances commonly used in braces may have on MR image quality.

Subjects and Methods: Measurements were performed on 1.5T Philips Achieva (Best, the Nertherlands).
Examined appliances included archwires and push-coils (both titanium alloy and stainless steel), stainless steel molar bands and brackets (3D, USA).
These were mounted on a plastic mouth guard immersed in a copper(II) sulfate solution.
MRI sequences included: spin echo (TE=10 ms; TR=800ms), bSFFP (TE=1.6 ms, TR=2.9 ms used for real time acquisition [1]) and 3D T2 weighted sequences for anatomical imaging. From in vivo images an average ROI was defined as the region that encloses the soft palate (rectangular volume as shown in Fig 1); image quality was assessed within ROI (artefact size and a linewidth).
Results: The most prominent effect was local signal loss around metallic parts. Titanium elements (arch wire with push-coil) had minimal effect (Fig 2); and linewith from ROI water signal was < 20 Hz. The area affected by individual molar bands and stainless steel archwires was large and signal loss reached the ROI (Fig3) with a linewith > 200Hz.

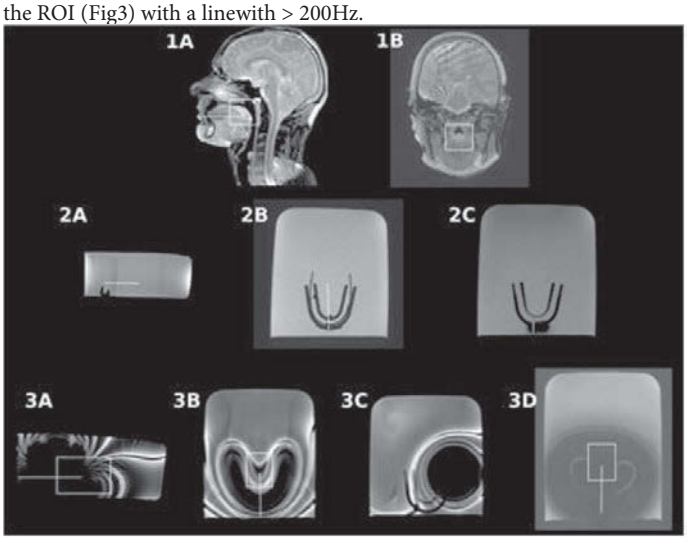

Discussion/Conclusion: Metallic orthodontic appliances have different effects on image quality. They are of little concern when made from titanium alloys. However, stainless steel arch wires and stainless steel molar bands create extensive distortion which can produce artefacts in the palate region. The extent of artefacts caused by metallic brackets when mounted on the front teeth is limited and does not extend to the ROI, but may become problematic when placed on the back teeth. Type of patient's orthodontic devices should be included in the screening process, and it might be necessary to remove them before imaging.
References:
1. Bae et al *Cleft Palate Craniofac J* 2011;48:695-707.
2. Scott et al *Brit J Radiol* 2012;85:e1083-92.
3. Sadowsky et al *Angle Orthodont* 1988;Jan:9-19.
4. Shellock *Reference Manual MRI Safety, Implants and Devices* 2011.

EPOS™ Poster

Spectroscopy

628

Influence of breathing to myocardium lipids determination

M. Drobny, P. Sedivy, M. Dezortova, M. Hajek
Department of Diagnostic and Interventional Radiology, Institute for Clinical and Experimental Medicine, MR Spectroscopy, MR Unit, Prague/CZECH REPUBLIC

Purpose/Introduction: Examination of the heart using 1H MR spectroscopy is technically difficult due to the artifacts caused by heartbeat and breathing. The aim of the study was to compare the results of the measurement of the lipid contents in myocardium by three different techniques of breathing together with ECG triggering. Examination protocols were tested on two groups of volunteers.
Subjects and Methods: Two groups of healthy subjects were examined. The group A consisted of 9 subjects without any special training (14m/2f, mean age 30±11 years); group B consisted of free divers who were able to hold their breath up to several minutes (13m/1f, mean age 37±8 years). All examined subjects were informed about the examination protocol, and their written consent was obtained according to the local Ethical Committee rules.
The examination was performed in supine position on MR system Siemens Trio 3T equipped with surface array coil. Localized 1H MR spectroscopy with PRESS sequence in the area of myocardium (intraventricular septum) was used with and without water suppression (see Table 1). The homogeneity of the static magnetic field was set by GREshim shimming method (WIP sequence provided by Siemens). Group A was examined during free breathing with ECG. Group B was examined in breath-holding with ECG and with using respiratory navigator and ECG.
Spectra were evaluated using jMRUI in the form of summation of individual integrals after one acquisition in the range of 0.52 ppm for total lipid quantification, as well as from the total signal amplitudes in absolute spectra.
Standard tests (F-test, t-test, ANOVA) were used.
Results: The results of measurements are shown as ratios of lipid signals to the water signal (see Table 1).
The ratios of lipid signals to the signal of water do not statistically differ between protocols and groups of volunteers. One subject was examined repeatedly. The reproducibility measured from one subject was found 13 %.

Table 1: Lipids to water ratios obtained by various breathing techniques

Group	Examination protocol	Lipids/water ratio [%] (real spectra)	Lipids/water ratio [%] (absolute spectra)
A	*Free breathing	0.6±0.4	0.9±0.6
B	**Breath hold	0.6±0.5	1.0±0.7
B	***Respiratory navigator	0.7±0.3	1.1±0.7

*free breathing -128 acquisitions, TE=30 ms; **breath hold - 64 acquisitions, TE=35 ms; ***respiratory navigator - 64 acquisitions, TE=35 ms

Discussion/Conclusion: Our results show no difference between both groups of volunteers and the content of lipids is similar as was described for healthy subjects in literature [1,2]. We also found, that there is not significant difference among used protocols and that the application of long breath hold or breath navigator does not improve results of simple measurement of lipid content in myocardium.

References:
[1] van der Meer R.W., et al.: *RadioI* 245(1):251-257,2007.
[2] Belen R., et al.: *Magn Reson Med* 66:619–624,2011.
Study was supported by projects IGA MZ CR: NT11275-6 and Institutional support 00023001IKEM, Czech Republic.

629

First semi-localized in vivo spectroscopy (Slice Localized Spectroscopy, SLS) and CSI of drosophila by HRMAS NMR.

N. Joudiou[1], F. Louat[1], S. Même[1], M. Decoville[1], J.-C. Beloeil[1], V. Sarou-Kanian[2]
[1]CBM, CNRS, Orleans/FRANCE, [2]CEMHTI, CNRS, Orléans/FRANCE

Purpose/Introduction: Animal models are commonly used to study biological processes and human diseases. Among them the *Drosophila melanogaster* is a model of choice. Indeed, over 75% of the genes known to be involved in human diseases have a counterpart in drosophila. In spite of its very small size, NMR spectra of the whole drosophila have already been obtained [1]. The NMR of live drosophila absolutely needs the fly to be in air. At high magnetic field, this situation induces magnetic susceptibility problems. The aim of this study was 1) to use HRMAS technique to overcome this problem [1] and 2) to perform localized spectroscopy on drosophila with the use of three magnetic field gradients. The obtained localization is perpendicular to the rotation axis to select the metabolic information selectively from the head, the thorax and the abdomen.
Here we present the first *in vivo* SLS by NMR HRMAS for studies of drosophila metabolism.
Subjects and Methods: Material:
- WB 750 MHz *Bruker Avance III.*
- HRMAS
- Drosophila were placed in an HRMAS rotor (3.2 mm inner diameter) and spun up to 2.6 kHz.
- Anesthesia was provided by decreasing the temperature around 3°C.
MRS acquisition:
- 1D and 2D ^{1}H HRMAS
- ^{1}H SLS HRMAS NMR spectroscopy (selectively: head/thorax/abdomen)
- CSI (2D: Rotation and gradient axis, chemical shift axis)
Drosophila:
We used two groups, *up*^{101} mutant and wild type (wt). The *up* mutant cannot take flight and shows a wings-up phenotype because of indirect flight muscles (IFM) degeneration.
Results: We identified numerous metabolites (with 1D and 2D global spectroscopy) and their localization (with the SLS and the CSI acquisition). For example, we observed that ß-alanine (which is present in muscle at high concentration) was decreased in the *up*^{101} mutant compared to wt. With SLS acquisition we find that the difference comes from the thorax. Several metabolites were different in male and female abdomen (for example male specific galactoside [2]).
Discussion/Conclusion: The efficiency of the semi-localized acquisition of ^{1}H HRMAS spectra has been proved on two examples that open numerous possibilities of study of metabolism in genetically modified drosophila. The semi-localization (head/thorax/abdomen) gives a much more precise information on the observed metabolism. CSI brings up information on the spatial relations of metabolites

References:
[1] Righi V, Int J Mol Med, 2010, 26(2): 175-84
[2] Chen PS., Biochemistry, 1977, 16(18): 4080-5.

630

MRSI data denoising to improve metabolite quantification

A. Laruelo[1], L. Chaari[2], B. Rowland[1], S. Ken[1], H. Batatia[2], R. Ferrand[1], J.-Y. Tourneret[2], A. Laprie[1, 3, 4]

[1]*Department of Radiation Oncology, Institut Claudius Regaud F-31052, Toulouse/FRANCE,* [2]*IRIT - INP-ENSEEIHT, Univ. of Toulouse, Toulouse/FRANCE,* [3]*Imagerie Cérébrale et Handicaps Neurologiques UMR 825, INSERM, TOULOUSE/FRANCE,* [4]*Paul Sabatier, Université Toulouse III, Toulouse/FRANCE*

Purpose/Introduction: The analysis of MRSI data is hampered by the inherently low signal-to-noise ratio (SNR) and spatial variability of the signals as shown in Figure1. We show that quantification accuracy can be substantially improved by reducing the noise present in MRSI data.

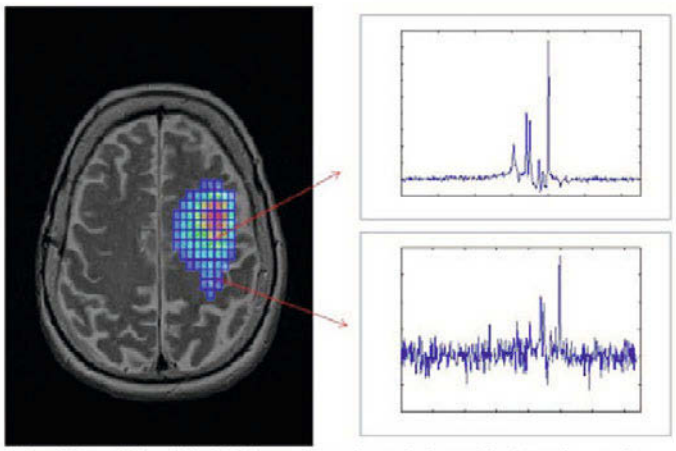

Figure 1: Data variability within a MRSI data set. Spectra from voxels close to the border contain more noise than spectra from central voxels.

Subjects and Methods: Synthetic brain MRSI data with different levels of noise were generated based on values commonly reported in the literature [1]. *In vivo* data were also acquired from a healthy volunteer and 12 patients with gliobastoma multiforme included in a prospective clinical trial (1.5T, TE/TR=135ms/1.5s) [2].

Data were processed using three different approaches: 1)Quantification, 2) Quantification with previous denoising [3], 3)Quantification using a novel method that performs quantification and denoising simultaneously (Figure2). This method is based on a metabolite database and takes advantage of the spectral-spatial nature of MRSI data. It incorporates sparsity promoting priors using wavelet transforms and relies on an efficient optimization algorithm not subject to local optima. For 1) and 2) data were quantified using the model in Figure2.6 [4].

The processing pipeline used for this work has been developed for clinical application in the radiotherapy context as part of the SUMMER (Software for the Use of Multi-Modality images in External Radiotherapy) project [5].

$$z = Bu + n \tag{1}$$

$$\mathcal{J}(S) = \mathcal{D}(z, Bu) + \lambda g(Bu) + \beta h(Bu) \tag{2}$$

$$\mathcal{D}(z, Bu) = \|z - Bu\|^2_{\Sigma^{-1}} \tag{3}$$

$$g(u) = \sum_{f}^{N} (R^{spat}(T(Bu)_f)) \tag{4}$$

$$h(u) = \sum_{r} (R^{spec}(F(Bu)_r)) \tag{5}$$

$$S(t) = \sum_{k=1}^{K} a_k e^{j\phi_k} e^{(-d_k + i f_k)t} v_k \tag{6}$$

Figure 2
(1) Observation Model
(2) Optimization criterium
(3) Data fidelity
(4) Spectral regularization
(5) Spatial regularization
(1)-(5) z: Observed signal; B: Metabolite basis matrix; u: Coefficients vector; n: Gaussian noise; Σ Noise covariance matrix, R^{spat} Spatial regularization term, R^{spec} Spectral regularization term, F 1D wavelet operator, T 2D wavelet operator, f frequency, r spatial position
(6) Quantitation model a_k: amplitude, ϕ_k phase shift, $-d_k$ damping correction, f_k frequency shift, v_k metabolite profile

Results: The presence of noise hampers the fitting of MRSI signals by the quantification model (Figure 3). As a consequence, the accuracy of the quantification decreases.

The reduction of noise allows an improved fit between the quantification model and the data. This is visible as more accurate quantification for cases 2 and 3 compared to 1 (Figure4).

Approach 2 provided the most accurate quantification. This is because 3 does not account for individual metabolite profile distortion as 2 does.

Differences between real and estimated metabolite concentrations decrease in both cases between 5% and 20% depending on the level of noise and the metabolite analyzed (Figure5).

Values estimated from previously denoised *in vivo* signals are more in accordance with values in literature [1] (Figure6).

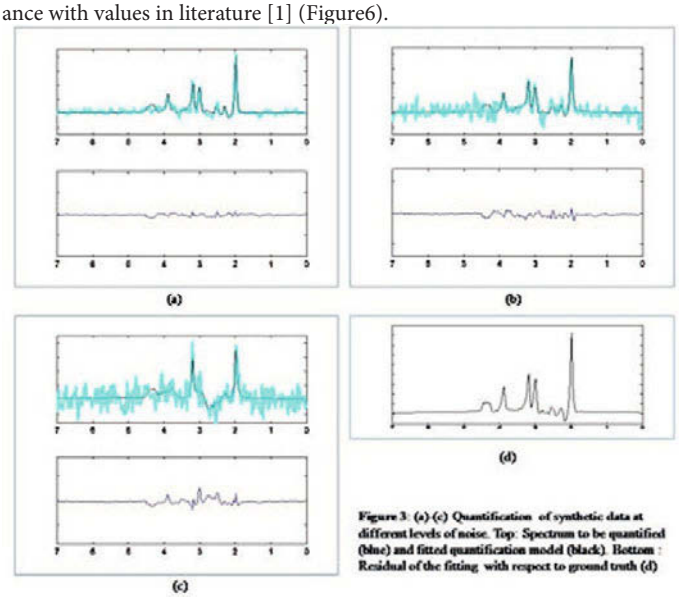

Figure 3: (a)-(c) Quantification of synthetic data at different levels of noise. Top: Spectrum to be quantified (blue) and fitted quantification model (black). Bottom : Residual of the fitting with respect to ground truth (d)

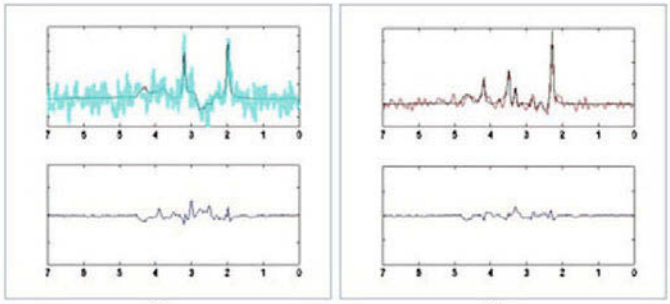

Figure 4:
(a) Quantification without previous denoising. Top: Noisy spectrum (blue) and fitted quantification model (black). Bottom: Residual of the fitting with respect to the ground truth (Fig. 3d).
(b) Quantification of spectrum in (a) after previous denoising. Top: Denoised spectrum (red) and fitted quantification model (black). Bottom: Residual of the fitting with respect to the ground truth (Fig. 3d).

Level of noise	low		medium		high	
	d_{noisy}	$d_{denoised}$	d_{noisy}	$d_{denoised}$	d_{noisy}	$d_{denoised}$
NAA	1.54	1.44	3.32	2.95	4.51	3.71
Cho	2.88	2.41	4.30	3.02	7.42	6.01
Cr	3.39	3.03	6.39	5.41	9.65	7.36

$$d = 100\left|\frac{a_{real} - a_{estimated}}{a_{real}}\right|$$

Figure 5: Average differences between real and estimated concentrations.

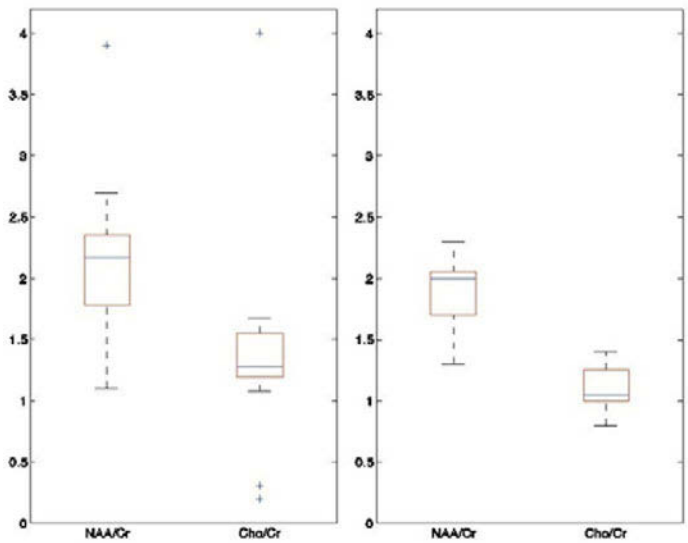

Figure 6: Boxplots showing the distribution of relative concentrations, NAA/Cr and Cho/Cr, in healthy appearing tissue estimated by: (a) quantification only (b) denoising and quantification.

Discussion/Conclusion: Quantification accuracy can be significantly improved by reducing the noise in MRSI data. We have shown that this can be done efficiently by two different approaches, but other different quantification methods may be incorporated.

References:

[1] Safriel et al. AJNR 2005
[2] Ken et al. Radiation Oncology 2013
[3] Laruelo et al. EMBC 2013
[4] Poullet et al. NMR Biomed. 2007
[5] Massoptier et al. Int Symp Biomed Imag 2012

631

Reproducibility of 1H MR Spectroscopy of Human Lumbar Vertebrae at 3 Tesla

B. Neumayer[1], A. Petrovic[1], T. Widek[1], C. Boesch[2], E. Scheurer[1]
[1]*Clinical Forensic Imaging, Ludwig Boltzmann Institute, Graz/AUSTRIA,*
[2]*AMSM (DKF - DIPR), University & Inselspital Bern, Bern/SWITZERLAND*

Purpose/Introduction: ^{1}H MR spectroscopy (MRS) is used to measure the composition of bone marrow, mainly based on the water and fat signal, for investigating pathological processes. It was shown that the fat content of vertebral bone marrow is significantly lower in females and increases with age for both, women and men [1,2].
Thus, with a sufficient degree of reproducibility, the fat content could inversely be used to determine retirement age in people without birth certificates. Therefore, the aim of this study was to assess the reproducibility of fat content measurements of lumbar vertebral bone marrow by using ^{1}H-MRS at 3T.
Subjects and Methods: Six healthy volunteers (3f [age:25,32,43y], 3m [age:30,32,34y]) underwent ^{1}H-MRS of L2 and L3 on a clinical 3T MR scanner. Measurements were repeated 3 times for each volunteer; the volunteers were removed from the scanner and repositioned after finishing the measurement protocol. The measurements were repeated for 3 (2f,1m) of the 6 volunteers after one week.
After the acquisition of imaging sequences in sagittal, coronal and transversal planes for the positioning of the voxel (20x20x20mm^3, but reduced if necessary), ^{1}H-MRS was performed using STEAM with TR/TE=5000ms/20,40,60,80,100ms and TR/TE=600,1000,2000,3000,10000/20ms, BW=2000Hz, NEX=10.
All spectra were quantified using jMRUI[4] (AMARES algorithm[5]). For fat content determination water and fat results were corrected for T_1 and T_2. Reproducibility was determined using SPSS18 (GLM, repeated measures) with vertebral body and gender as variables, age as covariance.
Results: Fig.1 shows the postitioning of the voxel (L3) and Fig.2 an exemplary spectrum for TE/TR=20/5000ms. The results regarding the reproducibility are shown in Tab.1.
For a linear interpolation of the fat fraction from literature (0.0063/year [1,3]), the error due to the measurement transforms to an error in age of 1.4y (SD) and an overall error of 15.4y (SD).

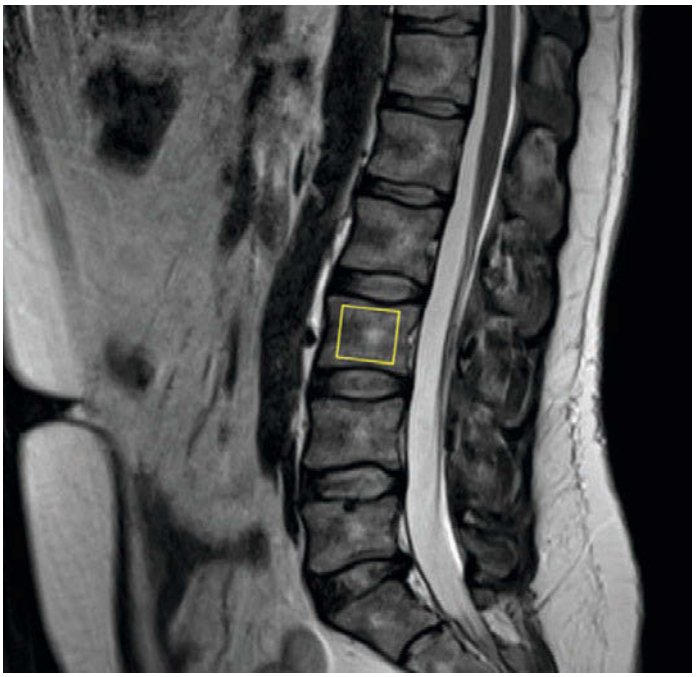

Fig.1:Voxel position

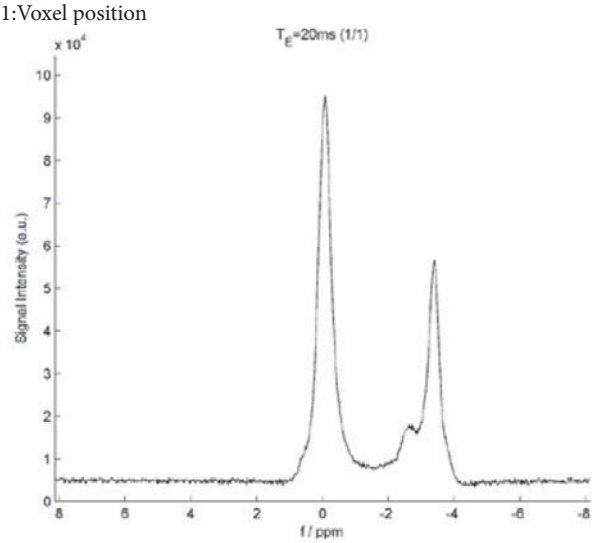

Fig.2: Spectrum

Tab.1:Results for reproducibility

	AVG	SD overall	SD repeat	vertebrae	gender	age
Fat Fraction	0.349	0.097	0.009	0.989	<0.001	0.005
T1(water)	1064	94.07	27.40	0.929	<0.001	0.413
T2(water)	22.65	2.652	0.832	0.242	<0.001	0.033
T1(fat)	345.2	23.66	14.28	0.298	<0.001	0.001
T2(fat)	61.76	1.750	1.010	0.897	<0.001	<0.001

Discussion/Conclusion: Our results show a good reproducibility of the measurements. However, physiological variability between subjects and the rough approximation for the fat content's age-dependent variation decrease the method's accuracy for an application in age determination. Considering additional physiological parameters and determining the age-dependent variation of the fat content are expected to enhance accuracy.

References:

[1]Kugel H;2001;JMRI;13:263–268
[2]Schellinger D;2000;Radiology;215:910–916
[3]Jung C;2000;Radiologe;40:694–699
[4]Naressi A;2001;MAGMA;12:141–152
[5]Vanhamme L;1997;JMR;129:35–43.

632

Improved off-resonance phase behaviour using a phase-inverted adiabatic half passage pulse for 13C NMR spectroscopy in humans at 7T.

E. Serés Roig[1], L. Xin[1, 2], D. Gallichan[1], V. Mlynarik[1], R. Gruetter[1, 2, 3]
[1]Laboratory for Functional and Metabolic Imaging, Ecole Polytechnique Fédérale de Lausanne, Lausanne/SWITZERLAND, [2]Department of Radiology, University of Lausanne, Lausanne/SWITZERLAND, [3]Department of Radiology, University of Geneva, Geneva/SWITZERLAND

Purpose/Introduction: In-vivo ^{13}C-MRS is currently performed using surface coils in combination with adiabatic pulses for excitation. Adiabatic pulses [1] are advantageous since they can generate a uniform nutation angle independent of the RF amplitude once adiabatic condition is reached. Nevertheless, the excitation bandwidth of adiabatic-half-passage (AHP) pulses is asymmetric relative to the carrier frequency, which could lead to asymmetric excitation of spectral lines relative to the center of the spectrum. Therefore, the aim of this study was to implement a pulse-acquire sequence for adiabatic ^{13}C excitation with a symmetric bandwidth, utilizing a combination of two AHP pulses with inverted phases in alternate scans, and then to test its feasibility for in vitro and in vivo ^{13}C-MRS at 7T.

Subjects and Methods: All experiments were performed on a 7T human MR-scanner (Siemens Erlangen/Germany). A ^{13}C-^{1}H RF surface coil was built, consisting of a ^{1}H-quadrature coil and a ^{13}C-linear coil [2]. Two pulse-acquire sequences with AHP excitation (2050μs) were implemented together with Waltz-16 ^{1}H-decoupling [3]: one using an AHP pulse for excitation, and the other using an AHP and a phase-inverted reverse-AHP (RAHP) in alternate scans. Bloch simulations, in-vitro and in-vivo experiments were performed for each sequence (AHP and AHP+RAHP). In-vitro experiments were performed on a small sphere (7mm diameter) containing 99% ^{13}C-enriched formic acid, placed in the centre of the ^{13}C-coil. The bandwidth of each sequence was measured by exciting formic acid at frequency offsets in a range of 2kHz in 50Hz steps. In-vivo glycogen experiments were performed on human calf using Waltz-16 (21ms decoupling duration), vector size=2048, BW=20 kHz, TR=1s and 256 averages.

Results: Bloch simulations show a proof-of-concept of the symmetric saturation of the longitudinal magnetization obtained with pulse-acquire when aternating AHP and RAHP.In-vitro measurements on formic acid demonstrated a symmetrically excited bandwidth over 2kHz using pulse-acquire when alternating, in agreement with Bloch simulations using the required γ*B1=122Hz for the excitation of formic acid (Figure 1). Natural abundance of glycogen-C1 was detected in human muscle, as well as glycerol and fatty lipid peaks (Figure 2). In particular, intensities of the lipids peaks are close to those theoretically predicted when using AHP+RAHP sequence, compared to those obtained with the AHP sequence.

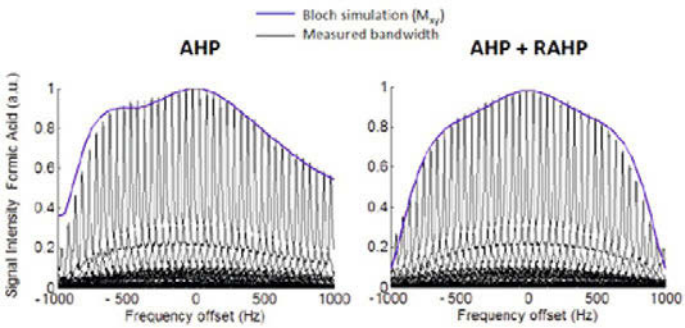

Figure 1: Bloch simulation (M_{xy}) and ^{13}C-MRS excited bandwidth measured in vitro on formic acid 99% ^{13}C-enriched (γ*B_1=122Hz), using an adiabatic-half-passage **(AHP)** pulse-acquire (left), and a adiabatic-half-passage (AHP) combined with a phase-inverted reverse-AHP **(RAHP)** in alternate scans (right), together with Waltz16 ^{1}H-decoupling. Parameter settings: pulse duration 2ms, vector size 2048, TR 10s, 1 average (AHP) and 2 averages (AHP + RAHP).

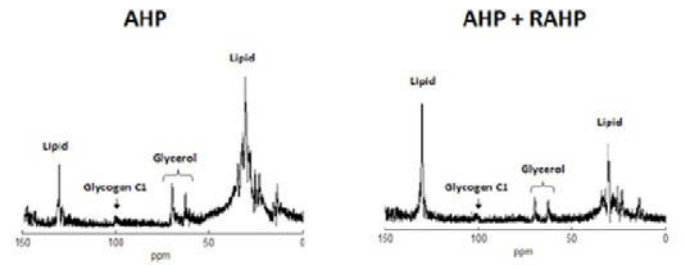

Figure 2: ^{13}C NMR spectra showing detection of the calf muscle glycogen (100.5ppm), Glycerol (62 and 69ppm), and fatty lipids (30 and 130ppm) from a male subject, using a ^{13}C-^{1}H surface coil and FID sequence with an adiabatic-half-passage (AHP) pulse-acquire (left), and an adiabatic-half-passage (AHP) combined with a phase-inverted reverse-AHP (RAHP) in alternate scans (right), together with Waltz16 ^{1}H-decoupling (20ms), TR = 1s, BW=20kHz, 256 scans, Vector size=2048, Zero filling=2048. Both spectra are shown with the same vertical scale.

Discussion/Conclusion: We conclude that it is feasible to apply two phase-inverted adiabatic-half-passage pulses for ^{13}C excitation to achieve a flatter-phase-response to off-resonance, and this will allow further extension of this technique for ^{13}C-MRS measurements such as in human brain.

References:

[1]A.Tannús,NMRBiomed(1997)
[2]G.Adriany,MagnReson(1997)
[3]A.J.Shaka,MagnReson(1983)

Acknowledgements
CIBM/UNIL/UNIGE/HUG/CHUV/EPFL/LeenaardsJeantetFoundations.

633

Hierarchical non-negative matrix factorization applied to in vivo 3T MRSI prostate data for automatic detection and visualization of tumours

T. Laudadio[1], A.R. Croitor Sava[2], D.M. Sima[3], A. Wright[4], A. Heerschap[5], S. Van Huffel[2, 3]
[1]Istituto Applicazioni Calcolo, National Research Council, Bari/ITALY, [2]Dept. of Electrical Engineering(ESAT-SCD) - Biomed, Katholieke Universiteit Leuven, Leuven/BELGIUM, [3]Electrical Engineering - ESAT/SCD, KU Leuven, Leuven/BELGIUM, [4]Department of Radiology, Radboud University Nijmegen Medical Center, Nijmegen/NETHERLANDS, [5]Radiology (430), University Medical Center Nijmegen, Nijmegen/NETHERLANDS

Purpose/Introduction: Non-negative matrix factorization (NMF) [1] is hierarchically applied to *in vivo* three-dimensional 3T MRSI prostate data to automatically extract characteristic patterns for tumour and benign tissue, and to visualize their spatial distribution.

Subjects and Methods: NMF is a blind source separation technique imposing non-negative constraints on the extracted sources and corresponding weights. Specifically, given a non-negative matrix $X \in R^{mxn}$, and an integer k ($0<k<min(m,n)$), two non-negative matrices $W \in R^{mxk}$ and $H \in R^{kxn}$, minimizing the functional $f(W,H)=0.5(\|X-WH\|_F)^2$, are estimated. Here, NMF is embedded into a hierarchical scheme (HNMF) by setting k=2 at each step:
Step1) NMF is applied to the dataset X, containing spectra as columns: two patterns (W columns) and corresponding weights (H rows) are obtained. Signals are divided into two new datasets based on the maximum weight value.
Step2) NMF is applied to each dataset obtained in Step1 and, as above, signals are divided into four datasets. Similarly, one more NMF step is performed, thereby providing eight patterns. The two most correlated patterns with given theoretical models for tumour and benign tissue are selected.
Step3) non-negative least squares (NNLS) [2] is applied to X by using the final patterns of Step2. Two coefficient vectors are obtained which, reshaped and encoded as color channels in an RGB image, provide a visualization of the pathological area.

Results: HNMF is applied to an *in vivo* 3T 16x16x16 MRSI dataset measured by a Siemens Magnetom Trio scanner (TE=145ms, TR=790ms, voxel size: 6mmx6mmx6mm, signal length: 512 data points). Based on histopathology, the tumor is located on the left-hand side of the prostate (Fig.1).

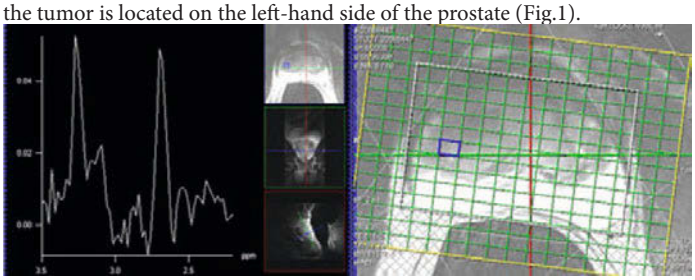

Fig.2

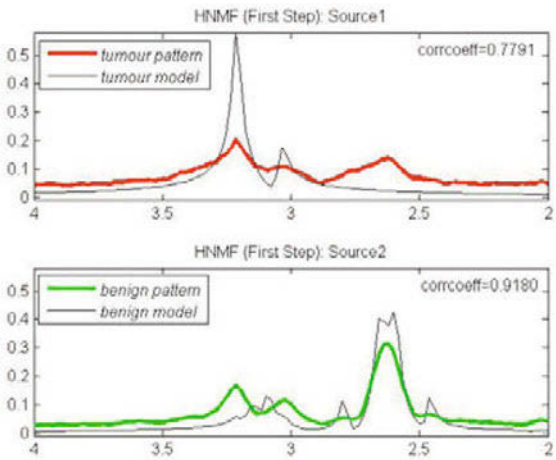

and Fig.3

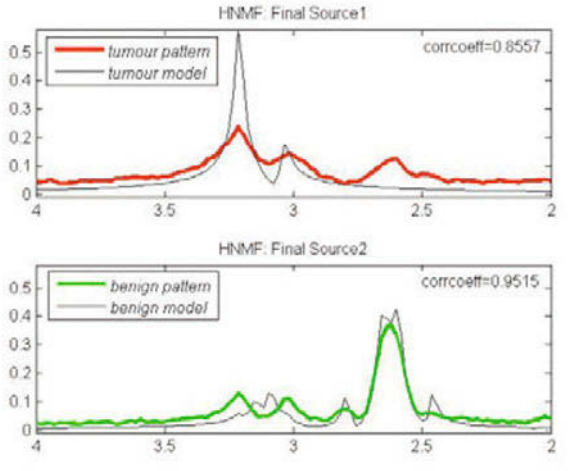

show the tumor and benign patterns provided by Step1 and Step2, respectively, along with their correlation coefficients with the theoretical models. Such values show that Step2 provides the most correlated patterns with the given models. Fig.4

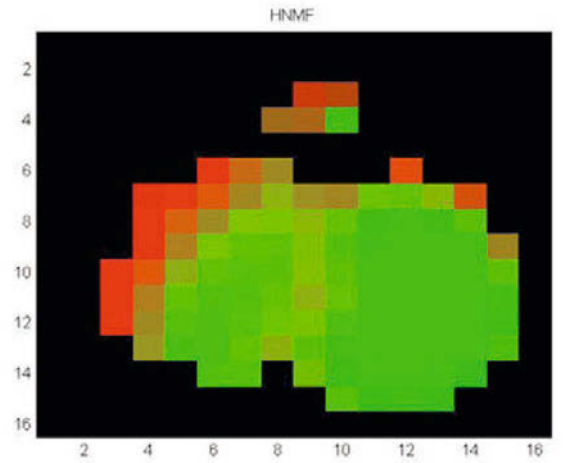

and Fig.5

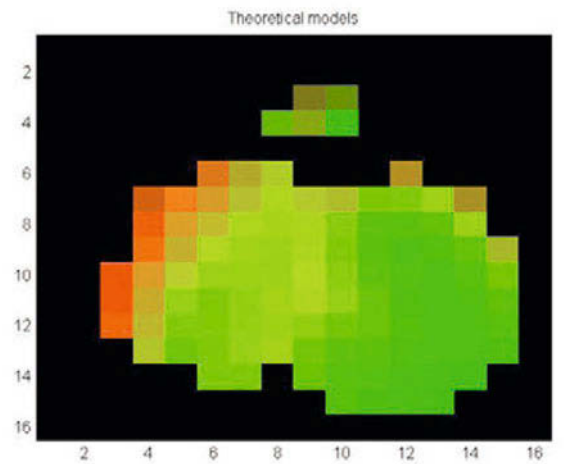

show the results of Step3 for one slice by exploiting the HNMF patterns and the theoretical models, respectively. In Fig.4 the pathological region is more enhanced than in Fig.5. The required HNMF computational time is 2.1*s*.

Discussion/Conclusion: HNMF is applied to *in vivo* MRSI data to detect prostate tumours. Our study shows that, potentially, HNMF is efficient and accurate, and provides higher quality results than applying NNLS directly with theoretical models. Indeed, HNMF is able to adapt the given models to the specific patient dataset and, therefore, to describe its spectral content more appropriately.

References:

[1] Lee, D.D., 1999, Nature, 401:788-791.
[2] Lawson, C.L., 1974, Solving Least-Squares Problems, 23:161.

634

Impact of salbutamol on muscle metabolism assessed by 31P NMR spectroscopy

N. Decorte[1, 2, 3], L. Lamalle[4, 5, 6, 7], M. Guinot[1, 2, 3, 8], P. Lévy[1, 2, 3], S. Vergès[1, 2, 3], B. Wuyam[1, 2, 3]

[1]HP2 Laboratory, Grenoble Alpes University, Grenoble/FRANCE, [2]U1042, INSERM, GRENOBLE/FRANCE, [3]Sleep & Exercise Physiology Clinics, CHU Grenoble, GRENOBLE/FRANCE, [4]IRMaGe, CHU Grenoble, Grenoble/FRANCE, [5]IRMaGe, Université Grenoble Alpes, Grenoble/FRANCE, [6]US 017, INSERM, Grenoble/FRANCE, [7]UMS 3552, CNRS, Grenoble/FRANCE, [8]Rhône-Alpes doping Prevention Agency, UM Sports & Pathologies, CHU Grenoble, GRENOBLE/FRANCE

Purpose/Introduction: The potential ergogenic effect of oral administration of salbutamol on exercise performance has been demonstrated for decades (1) but the underlying mechanisms are not completely elucidated (2). We hypothesized that an acute oral dose of salbutamol may improve muscle metabolism and increase endurance during a localized exercise in moderately trained subjects.

Subjects and Methods: Twelve healthy, non-asthmatic, physically active, male subjects were recruited to compare in a double-blinded crossover randomized study an oral dose of salbutamol (4mg) and a placebo intake before a calf fatigue test. Subjects were requested to perform plantar flexions against a progressively increasing resistance at a frequency of 0.5 Hz (maintained with the aid of a visual feedback and a rhythmic soundtrack) until exhaustion in the magnet. A continuous ^{31}P NMRS assessment was performed for 2 min at baseline before the exercise, during the exercise and during the recovery period.

Results: No significant difference was detected in metabolites concentration (PCr, Pi/PCr, ADP and ATP) at baseline, during exercise and during the recovery period ($p>0.05$). The oxidative potential indicated by the PCr resynthesis after the end of the exercise was not modified (tPCr: 38 ±8 and 39 ±9 s for salbutamol and placebo respectively; $p=0.80$). However, while the intracellular pH (pH_i) was not significantly different at rest with salbutamol compared to placebo ($p=0.43$), the decrease in pH_i values was significantly lower with salbutamol than placebo during the incremental test ($delta_{pHi}$: -0.09 vs. -0.19 for salbutamol and placebo respectively; $p=0.018$). Moreover, the P_{max} (28 ±7 W vs. 23 ±7 W for salbutamol and placebo, respectively; $p < 0.001$) and the total work performed (1702 ±442 J vs. 1381 ±432 J respectively; $p < 0.001$) during the incremental test were significantly increased with salbutamol compared to placebo.

Discussion/Conclusion:

Oral administration of salbutamol induced significant improvement in calf muscle endurance with similar metabolic responses in moderately trained sportsmen, except small changes in pHi. These results suggest that mechanisms beyond the muscle (e.g. at the CNS level) may account for the increase exercise performance with oral salbutamol intake.

References:
1. Sanchez AM, Collomp K, Carra J et al. Effect of acute and short-term oral salbutamol treatments on maximal power output in non-asthmatic athletes. European journal of applied physiology 2012;112:3251-8.
2. Collomp K, Candau R, Lasne F, Labsy Z, Prefaut C, De Ceaurriz J. Effects of short-term oral salbutamol administration on exercise endurance and metabolism. Journal of applied physiology (Bethesda, Md : 1985) 2000;89:430-6.

635

GABA detection in primary auditory cortex by magnetic resonance spectroscopy without spectral editing

D.H.Y. Tse[1], C. Wyss[2], J. Arrubla[1], W. Kawohl[2], I. Neuner[1, 3, 4], N.J. Shah[1, 4, 5]
[1]Institut für Neurowissenschaften und Medizin, Forschungszentrum Jülich GmbH, Jülich/GERMANY, [2]Department of Psychiatry, Psychotherapy and Psychosomatics, Zürich University Hospital for Psychiatry, Zürich/SWITZERLAND, [3]Department of Psychiatry, Psychotherapy and Psychosomatics, RWTH Aachen University, Aachen/GERMANY, [4]JARA-BRAIN-Translational Medicine, RWTH Aachen University, Aachen/GERMANY, [5]Department of Neurology, RWTH Aachen University, Aachen/GERMANY

Purpose/Introduction: Gamma-aminobutyric acid (GABA) is an important neurotransmitter, which is detectable by magnetic resonance spectroscopy at 3T. However, its resonance peaks overlap with other larger metabolite peaks, making its detection error-prone. Recently, Napolitano et al. [1] proposed a method which uses point resolved spectroscopy (PRESS) with a set of optimised echo time parameters to detect GABA in the anterior cingulate cortex and the precuneus region. In this study, we investigate the feasibility of using this method to detect GABA in the primary auditory cortex (PAC).
Subjects and Methods: Single voxel spectra at left and right PAC were recorded from 12 male healthy volunteers (mean age 27.7, sd 2.2) at a 3T scanner (Tim Trio, Siemens, Erlargen, Germany) with PRESS (TE_1=14ms, TE=105ms, TR=2.5s, NA=128, 25x25x25 mm^3 voxel size). The spectra were analysed with LCModel [2] using a GAMMA [3] simulated 18-metabolites basis set.
Results:

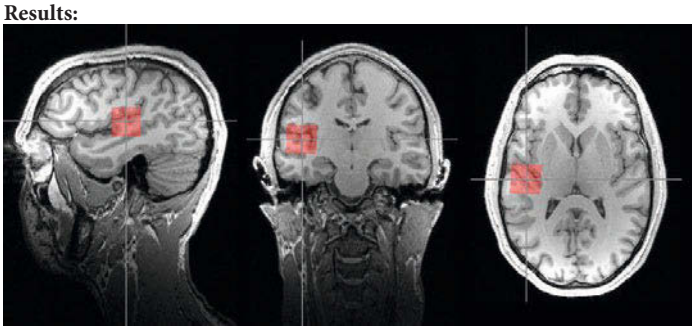

Fig. 1 shows an example of a coregistered spectroscopic volume at the right PAC on a T1-weighted image. The mean grey matter partial volume in the spectroscopic volume was 50%.

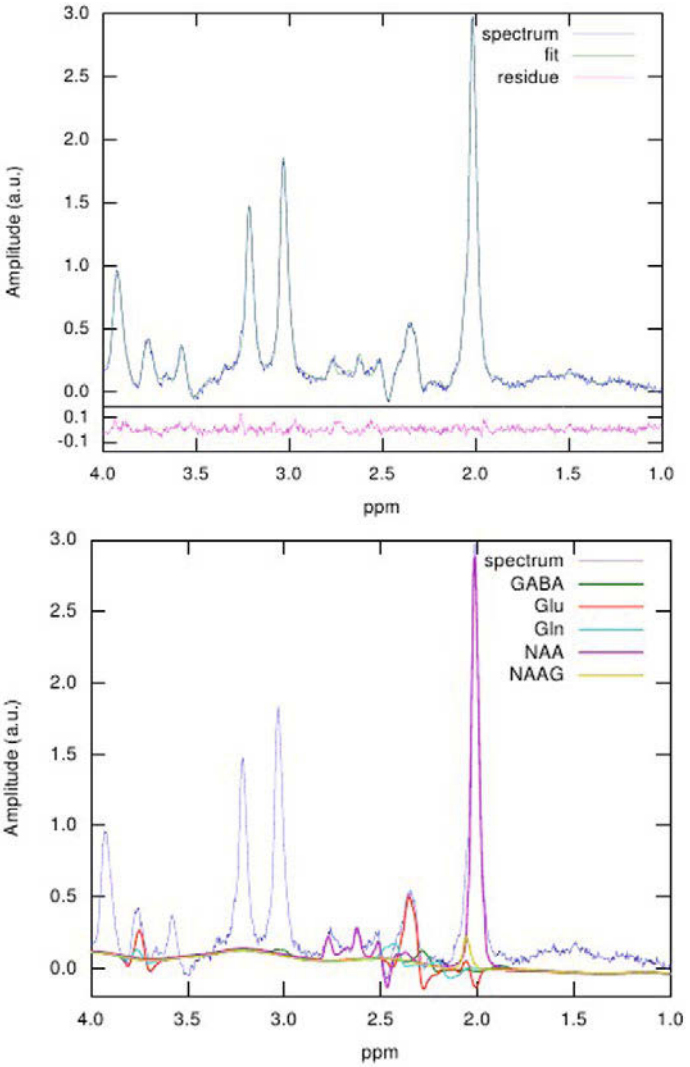

Fig. 2 shows an example of a fitted spectrum with residue and fig. 3 is the same spectrum with the individual fits of GABA, Glu, Gln, NAA and NAAG. The water peak FWHM in all 24 spectra were below 0.05 ppm and all the spectra had a SNR over 43. In all spectra, 9 metabolites were detected with Cramer-Rao lower bound (CRLB) below 20%. These metabolites were creatine (Cr), GABA, glutamate (Glu), glutamine (Gln), glutathione (GSH), myo-inositol (mI), n-acetyl aspartate (NAA), phosphocreatine (PCr) and total choline (GPC+PCh). From the 12 volunteers, the average concentration of GABA in the left and right PAC were 1.4 mM (sd 0.2 mM) and 1.5 mM (sd 0.3 mM), respectively. The corresponding CRLB from the 24 spectra were all below 18%, averaging at 14%. The intersubject variability was 18% for both left and right PAC.
Discussion/Conclusion: In conclusion, we have successfully detected GABA, as well as Glu and Gln separately, in PAC with CRLB well below 20%. The high partial volume of GM and the ease of B_0 shimming in PAC, together with the optimised PRESS echo time parameters have all helped the detections of these neurotransmitters.
References:
1. Napolitano A. et al. 2012, Magn Reson Med 69, 1528–1533. 2. Provencher S.W. 2001, NMR Biomed 14, 260-264. 3. Smith S.A. et al. 1994, J Magn Reson Ser A 106, 75-105.

636

Increase in hepatic branched-chain amino acids leucine and isoleucine by the ketogenic diet: a study by 1H HRMAS spectroscopy in the rat liver.

M.-C. Beauvieux[1], J. Naulin[1], D. El Hamrani[1], M. Roy[2], A.-K. Bouzier-Sore[1], J.-L. Gallis[1], S. Cunnane[2]
[1]*UMR5536 RMSB, CNRS Université Victor Segalen, Bordeaux/FRANCE,* [2]*Research Center on Aging, University of Sherbrooke, Sherbrooke/CANADA*

Purpose/Introduction: Ketone bodies are produced in the liver, mainly from the oxidation of fatty acids (FA), and then exported to peripheral tissues for use as an energy source, mainly in brain. The very low-carbohydrate and high-fat "ketogenic" diet (KD) is a treatment for intractable childhood epilepsy (Kossoff2009); the mechanism of action remain under active investigation (Roy2012). Hepatic metabolism is likely to play an important part in the adaptation and metabolic responses to KD inducing a unique pattern of liver gene expression (Kennedy2007). A 12wks-KD induced steatosis in mice (Garbow2011) whereas 7wks-KD prevents steatosis in juvenile ob/ob mice (Okuda2012) or in humans after 6monthes supply (Tendler2007). We investigated for the first time the metabolic hepatic profile in rats submitted to only 1wk-KD.
Subjects and Methods: Male Sprague-Dawley rats (160g at T0) were divided in 2 groups: 1/ control "Ct"; lipids:carbohydrates+proteins 1:12.6 (n=16) or 2/ "KD" undergoing 48hrs fasting before diet (lipids:carbohydrates+proteins 3.7:1) (n=16). Both diets (SAFE France) were given during 7days at 10g/d,100g body weight (BW). Some blood was withdrawn before rat euthanasia with brain focalized microwaves (5kW, 1sec, 2.45GHz, Sacron8000 France). Livers (stored -80°C) were analyzed by ^{1}H-HRMAS (Bruker AVANCE500 11.7T; 6min acquisition; CPMG echo sequence: n=16, TE=1ms; fumarate as external reference).
Results: BW was lower in 7dys-KD *vs* 7dys-Ct (240.6±13.7g *vs* 270.5±21.0g, respectively, p<0.0001). KD induced an increase in total blood βOHbutyrate (0.8±0.2mM *vs* 0.2±0.0mM, p=0.0087 in Ct). Insulinemia was lower in KD (61.3±10.4mUI/L) *vs* Ct (103.4±13.7mUI/L) (p<0.05). KD did not change FA content but increased insaturation degree (p<0.0001); KD decreased Choline/Pcholine (0.64±0.05) *vs* Ct (0.87±0.05; p=0.004). Whereas leucine+isoleucine resonance was never observed in Ct, KD induced its systematic presence ($p=6.10^{-5}$).
Discussion/Conclusion: KD induced hepatic appearance of leucine and isoleucine, ketogenics branched-chain amino acids (BCAA). KD diet preceded by 48hrs-fasting could be assimilated to a starvation leading to a net release of liver BCAA (Holecek2001). BCAA, transported rapidly in the central nervous system, are a major source of glutamate (Daikhin2000). Glutamate is a precursor of GABA whose decrease is identified in intractable epilepsy (Wang2003). Ketosis may favor the release from brain of glutamine, which transporters at the blood-brain barrier exchange for blood leucine (Yudkoff2004). Moreover, administration of ^{15}N labeled leucine in KD-mice increased labeled GABA (Yudkoff2001).The liver adaptations in KD may be highly involved in mediating the brain effects of the diet.
References:
GarbowJR, AmJPhysiol2011;300:G956
HolecekM, PhysiolRes2001;50:25
KennedyAR, AmJPhysiol2007;292:E1724
KossoffEH, Epilepsia2009;50:304
RoyM, BrainRes2012;1488:14
TendlerT, DigDisSci2007;52:589
YudkoffM, JNeurosciRes2011;66:272
YudkoffM, ProstaglandinsLeukotEssentFattyAcids2004;70:277
WangZJ, MagnResMed2003;49:615

637

The sensitivity for 19F MRI: a theoretical approach to quantitative fluorine imaging

A.J. Taylor[1], J. Granwehr[2], C. Lesbats[3], J. Krupa[4], J.S. Six[3], G.E. Pavlovskaya[3], T. Meersmann[3], D.P. Auer[1], N.R. Thomas[4], H. Faas[1]
[1]*Division of Radiological and Imaging Sciences, Clinical Sciences, University of Nottingham, Nottingham/UNITED KINGDOM,* [2]*School of Physics and Astronomy, Sir Peter Mansfield Magnetic Resonance Centre, University of Nottingham, Nottingham/UNITED KINGDOM,* [3]*School of Clinical Sciences, Sir Peter Mansfield Magnetic Resonance Centre, University of Nottingham, Nottingham/UNITED KINGDOM,* [4]*Centre for Biomolecular Sciences, Department of Organic and Biological Chemistry, School of Chemistry, University of Nottingham, Nottingham/UNITED KINGDOM*

Purpose/Introduction: Fluorine (^{19}F) MRI is increasingly popular due to the lack of biologically endogenous fluorine and the potential for cell tracking [1]. Only small concentrations of fluorinated compounds can be administered *in vivo*, hence sensitivity is crucial for applications of ^{19}F MRI. It is currently impossible to theoretically predict the minimum fluorine concentration needed given a target signal to noise ratio (SNR). Particularly the theoretical detection limit for perfluorcarbon nanoemulsions used in cell labelling and visualisation is not known [2]. We show that for fluorine nuclei a theoretical SNR model [3] can be used to predict the minimum sensitivity achievable for any fluorinated compound *in vitro*.
Subjects and Methods: On a Bruker 9.4T imager, single pulse ^{19}F NMR spectra were acquired ($\alpha = 90^{o}$; TR = 120s; NA = 10). SNR values, Ψ, were measured for three 100 mM fluorinated compounds containing 3, 6 or 9 fluorine atoms per molecule, n_e, and for varying concentrations of trifluoroacetic acid (TFA). Using equation 1, a theoretical SNR was calculated. A scanner factor (SF) was used to account for the specific coil set-up.

$$\Psi = \frac{N_A n_e V_s \gamma^2 h^2 B_0 c}{64} \sqrt{\frac{\mu_0 Q \omega_0 T_2^*}{\pi^3 k_B^3 T^3 V_c}} \quad (1)$$

Results:
The ratio of experimental and theoretical SNR values was measured for $n_e = 3$ and 6, establishing SF = 2.74. Applied to the theoretical model this predicts the SNR of TFA (Figure 1B). To determine ^{19}F sensitivity, TFA concentrations for a minimum target SNR of 3.5 were determined by extrapolation of the model.

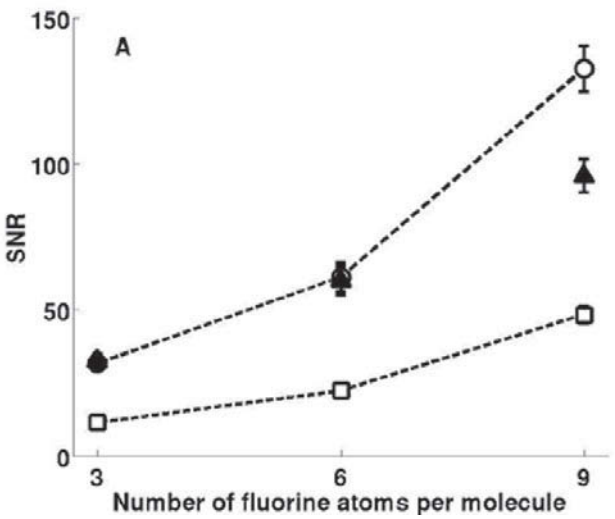

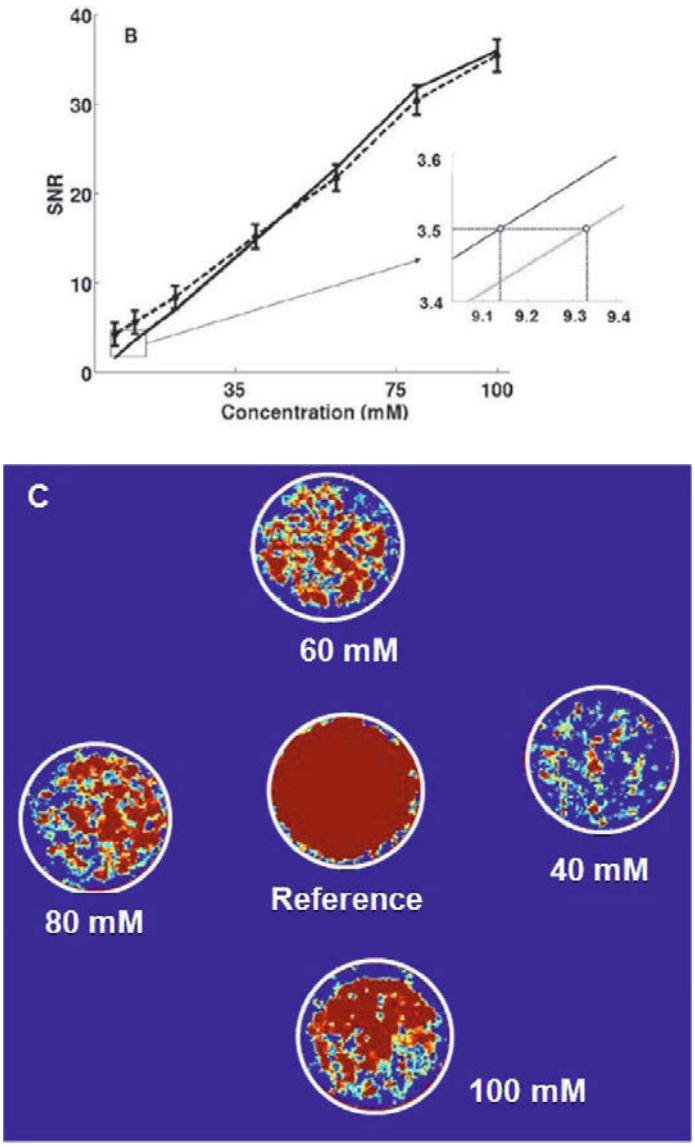

Figure 1: (**A**) SNR vs. number of fluorine atoms per molecule (n_e); the ratio between experimental data (⊠), and theoretical values from eq. 1 (-⊠-) was used to determine the SNR model with scanner factor correction (-o-). (**B**) Experimental (--) and model (—) data for TFA; model extrapolation is used to obtain minimum detectable concentrations. (**C**) MR image of ^{19}F TFA.

Discussion/Conclusion: The model allowed to estimate the sensitivity for TFA, but is applicable to other fluorine compounds. The discrepancy at $n_e = 9$ (Figure 1A) is likely due to the presence of sodium in the fluorine salt. Combining this work with optimised ^{19}F MR imaging sequences [4] would provide a better understanding of the detection limits for ^{19}F *in vivo* biomarkers.

A. Taylor is funded by the MRC and Schools of Clinical Sciences and Chemistry, UoN.

References:

1. Boehm-Sturm. P *et al.* (2011), PLoS One, e29040, **6(12)**
2. Srinivas. M *et al.* (2007), MRM, p725-734**(58)**
3. Hoult.D *et al.* (1976), JMR, p71-85**(24)**
4. Schmid.F *et al.* (2013), MRM, p1056-1062**(69)**

638

Optimizing the B0-Shimming for Single Voxel Spectroscopy in the Myocardium at 3T

A. Fillmer[1], D. Cameron[2], M. Frenneaux[2], D. Dawson[2], A. Henning[1,3]
[1]Institute for Biomedical Engineering, University and ETH Zurich, Zurich/SWITZERLAND, [2]Aberdeen Biomedical Imaging Centre, University of Aberdeen, Aberdeen/UNITED KINGDOM, [3]Institute for Biological Cybernetics, Max Planck, Tübingen/GERMANY

Purpose/Introduction: MR Spectroscopy is a useful tool for investigating heart disease[1,2], which benefits from increasing spectral resolution and SNR at higher B_0-field strengths. The complexity of B_0-field inhomogeneities, however, increases as well. By comparing spectral quality of projection-based[3,4] and image-based[5,6] B_0-shimmed measurements in the interventricular septum, an optimal approach to B_0-shimming of the myocardium for spectroscopy applications was determined.

Subjects and Methods: Measurements were performed in eight volunteers(25y–37y) on an Achieva whole-body 3T system equipped with 2nd-order spherical-harmonic shim coils and a six-channel cardiac receive coil (Philips Healthcare,Best,NL). To compensate for cardiac and respiratory motion ECG-triggering and a breathing-belt were employed during calibration, B_0-shimming and acquisition.

Cine images of the myocardium were acquired to position the spectroscopy voxel and estimate the ECG-trigger delay. A non-shimmed B_0-map (10slices,3x3x3mm^3,ΔTE=1ms) was acquired for image-based B_0-shim calculation.

Nine non-water-suppressed, PRESS-localized spectra (8averages,TE/TR=60 ms/2000ms,voxel≈8.5x57x44mm^3) were obtained per volunteer; one without B_0-shimming and eight with different 1st- and 2nd-order B_0-shim settings applied. Two B_0-shim sets were determined by a FASTESTMAP-related (**FM**) projection-based B_0-shim algorithm[3] and the remaining six, using different shim geometries(fig.1), by an image-based algorithm[5,6], which assigns different weightings to the region of interest (**ROI**) and a region of less interest (**ROLI**) during the B_0-shim calculation.

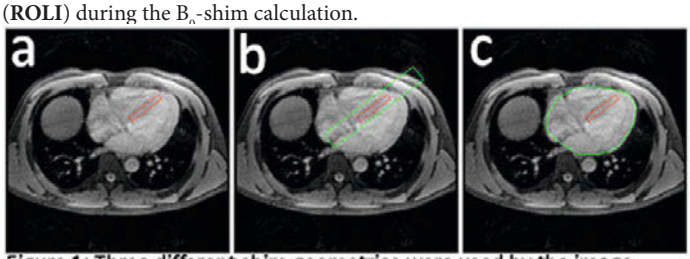

Figure 1: Three different shim geometries were used by the image-based B0-shim algorithm for B0-shim term calculation. ROI (red) and ROLIs (green) are overlaid an anatomical image. The ROI is equal to the spectroscopy voxel. (a) ROI only; (b) rectangular ROLI (c) ROLI that covers the whole heart (WH ROLI)

An ideal Voigt-line was fitted to the water peak and the FWHM was extracted. To quantify line shape distortions the spectra were normalized to their peak value. The Voigt-line fit was scaled accordingly and subtracted from the data. The area between x-axis and the difference-curve measures the deviation of the actual line shape from an ideal Voigt-line.

Results: The influence of different B_0-shim settings on line shape and width of the acquired non-water-suppressed spectra is clearly visible(fig.(2)).

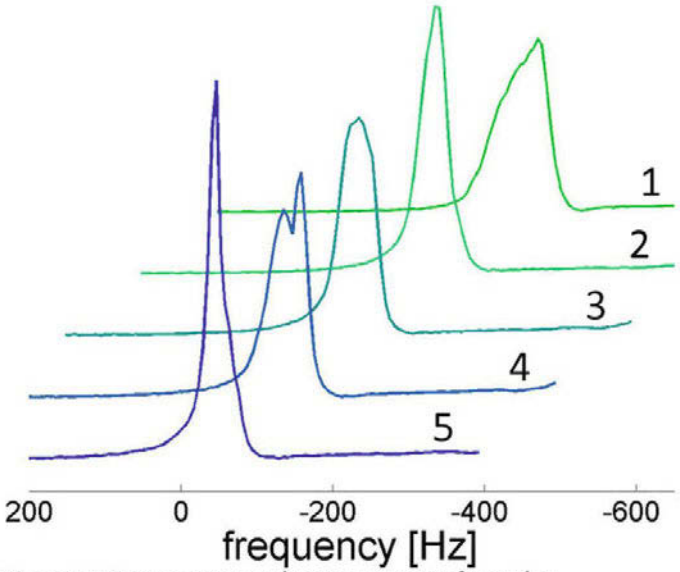

Figure 2: Non-suppressed water spectra from the interventricular septum of a volunteer's heart acquired with different linear B0-shim but otherwise identical settings. 1: no shim, 2: FM shim, 3: ST shim ROI only, 4: ST shim ROI and rect. ROLI, 5: ST shim ROI and WH ROLI. The influence on line shape and width of the differen B0-shim settings is clearly visible.

A comparison of FWHM values(fig.(3)) and deviations from a Voigt-line(fig.(4)) of the differently B_0-shimmed spectra over all volunteers shows that best results can usually be achieved, when the ROI and a WH ROLI are considered for image-based B_0-shimming.

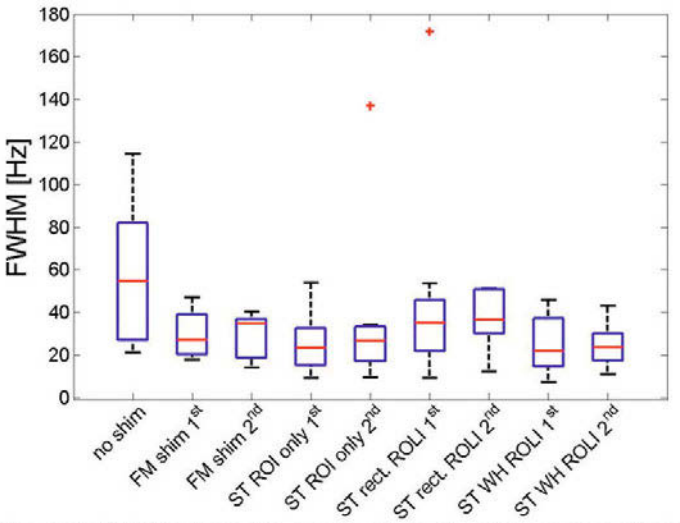

Figure 3: FWHMs from the spectra from all volunteers acquired without any shim, and with 1st and 2nd order FM shim, ST shim ROI only, ST shim ROI and rect. ROLI and ST shim ROI and WH ROLI respectively.

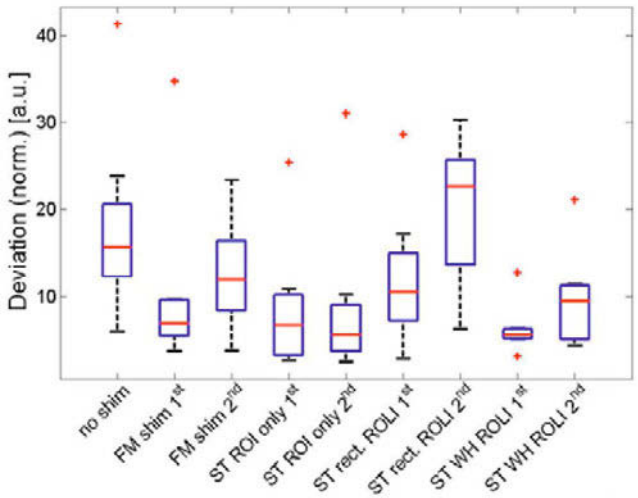

Figure 4: Deviations of the normalized spectra from a fitted Voigt line for different B0-shim settings

However, the use of a non-anatomically-conforming (rectangular) ROLI may lead to significantly reduced B_0-shim quality(fig.(3,4)).
Furthermore, B_0-inhomogeneity correction limited to linear shim terms often gives better results than a 2nd-order correction probably due to imperfect motion correction within the translationally variable 2nd-order fields[7].
Discussion/Conclusion: By employing respiratory-gated and ECG-triggered image-based B_0-shimming, including an anatomically conforming ROLI, the potential for improving the B_0-shim quality for SV spectroscopy in the myocardium at 3T is demonstrated.
References:
[1]J.A.den Hollander et.al.,MRM32,175-180(1994)
[2]P.A.Bottomley et.al.,Lancet351,714-718(1998)
[3]A.Hock et.al.,NMR.Biomed,DOI:10.1002/nbm.2852(2012)
[4]R.Gruetter,MRM29,804-811(1993)
[5]M.Schär et.al.,Proc.Intl.Mag.Reson.Med.10,1735(2002)
[6]A.Fillmer et.al.,Proc.Intl.Mag.Reson.Med.20,2065(2012)
[7]M.R.Kubach et.al.,Phys.Med.Biol.54,N467-N478(2009)

639

Proton exchange in the carnosine–water system studied in vitro by WEX and CEST experiments

O. Ivchenko[1], S. Goerke[1], M. Zaiss[1], N. Behl[1], V. Roeloffs[2], P. Bachert[1]
[1]Medical Physics in Radiology, German cancer research center, Heidelberg/GERMANY, [2]Biomedizinische NMR Forschungs GmbH, Max–Planck–Institut für biophysikalische Chemie, Göttingen/GERMANY

Purpose/Introduction:
The dipeptide carnosine occurs in mammalian skeletal muscle at 20 mM concentration[1]. Also, it has an amide group (–NH) in the peptide bond (NHCPD), which can exchange protons with water and therefore produces a CEST contrast. We explore the properties of NHCPD by determining the corresponding chemical exchange rates k_{sw} by means of WEX and CEST. These can give us insights to the amide proton transfer (APT)[2] processes in protein–water systems.
Subjects and Methods: WEX: Twelve carnosine phantoms were mixed (50 mM) at different pH (6.05 to 8.3) using the WEX spectroscopy sequence on a 3-T magnetic resonance scanner (Magnetom Trio; Siemens). The WEX pulse sequence only resolves magnetization, which is transferred from water to protons from a specific functional group during the mixing period T_m[3].

CEST: Eight phantoms (50 mM) were mixed at different pH (7.19 to 9.3) using our CEST pulse sequence implemented on the 3–T scanner with spin-lock pulses. Z–spectra were B_0–corrected employing a WASSR map[4]. By performing CEST measurement at different B_1 fit, similar to QUESP[5], we have access to the exchange rates.

Results:

WEX: The dependence of the chemical exchange rate on temperature and pH of NHCPD were determined. It was accomplished by 3D fit of k_{sw}(pH,T) data with the formula from [3]. The resulting fit constants are: activation energy E_a=(33.62±9.39)kJ/mol, collision frequency k_b=(2.92±0.43)*10^7Hz, longitudinal solute relaxation rate R_{1s}=(11.99±2.56)Hz. With those constants, one can calculate k_{sw} at any pH and temperature.

CEST: The dependence of NHCPD on pH was determined using the B_1 fit[5] of the chemical exchange rate using CEST measurements. The chemical exchange rates of carnosine from CEST data are slightly overestimated in comparison to the rates from WEX.

Discussion/Conclusion:

We studied the process of chemical exchange between the NH group of the carnosine peptide bond and water. We envisioned two approaches to determine the chemical exchange rate of the amide proton. For the first time for carnosine, experiments yielded k_{sw}(pH, T) by the WEX method and k_{sw}(pH) by CEST. The corresponding rates of the two methods are in good agreement.

References:

[1] Renner, C., et al., Mol Cancer, 2010. **9**: p. 2.
[2] Zhou, J., et al., Magn Reson Med, 2003. **50**(6): p. 1120-6.
[3] S. Goerke, Abstract 394, ESMRMB, 2012
[4] Kim, M., et al., 2009. **61**(6): p. 1441-1450.
[5] McMahon., et al., Magnetic Resonance in Medicine, 2006. **55**(4): p. 836-847.

640

Multivoxel proton magnetic resonance spectroscopy in patients with multiple sclerosis treated with stem cells

P. Gelezhe, S. Morozov
Radiology, PMGMU, Moscow/RUSSIAN FEDERATION

Purpose/Introduction:

To study the dynamics of changes in the levels of some brain metabolites (N-acetylaspartate (NAA), myoinositol (mI), N-acetylaspartate/creatine (NAA/Cr) and N-acetylaspartate/choline (NAA/Ch) ratios) with multivoxel proton magnetic resonance spectroscopy (^{1}H-MRS) in patients with primary progressive form of multiple sclerosis (PPMS). To estimate the efficiency of umbilical cord blood stem cells treatment for PPMS.

Subjects and Methods:

Ten patients with PPMS (expanded disability status scores (EDSS) 6.0-7.0) were included in the study. Written informed consents of all patients and the consent of Ethics Committee were obtained. Assessment of metabolites levels with the use of ^{1}H-MRS was carried out twice: before the introduction of cord blood cells and 6 months after the introduction. Umbilical cord blood cells were injected twice with a single dose of 2,5x10^8 cells given with a 14 day interval. Concentration levels of NAA, mI and relative values of NAA/Cr and NAA/Ch were determined. The study was conducted on the unit GE Signa HDx 3,0T (repetition time (TR)=1000,0 ms, echo time (TE)=144,0 ms, field of view (FOV)=24x24 cm^2).

Results:

There was no statistically significant difference between the values of brain metabolite concentrations measured before the administration and at 6 months after stem cells therapy. Mean NAA concentrations before and after treatment were 133053,6±8049,8 and 139276,7±6008,5, NAA/Cr - 1,65±0,07 and 1,69±0,07, mI - 12127,5±1121,3 and 11982±1272.4, NAA/Ch - 1,74±0,15 and 1,79±0,1, respectively (P> 0,05).

Discussion/Conclusion:

This study demonstrated no evidence of the efficiency of umbilical cord blood stem cells treatment for PPMS. Multivoxel ^{1}H-MRS is an appropriate method for the assessment of brain metabolites concentration, that can be used for estimation of multiple sclerosis treatment efficiency.

References:

1) Patani R., Chandran S. Experimental and Therapeutic Opportunities for Stem Cells in Multiple Sclerosis. Int J Mol Sci. 2012 Nov 8;13(11):14470-91
2) Caramanos Z., Narayanan S., Arnold D. 1H-MRS quantification of tNA and tCr in patients with multiple sclerosis: a meta-analytic review. Brain 128(11): 2483–2506.
3) Balasrinivasa R. Sajja, Wolinsky J. S., Narayana P. A. Proton Magnetic Resonance Spectroscopy in Multiple Sclerosis. Neuroimaging Clin N Am. 2009 February; 19(1): 45–58.
4) Auletta J. J., Amelia M. B., Maziarz R. T., Deans R. J., Miller R. H., Lazarus H. M., Cohen J. A. The potential of mesenchymal stromal cells as a novel cellular therapy for multiple sclerosis. Immunotherapy(2012) 4(5), 529–547.

641

Metabolic characterization and classification of Saccharomyces yeasts using high resolution NMR spectroscopy

A.R. Croitor Sava[1,2], H.-M. Daniel[3], U. Himmelreich[2], S. Van Huffel[1]
[1]Dept. of Electrical Engineering(ESAT-SCD) - Biomed, Katholieke Universiteit Leuven, Leuven/BELGIUM, [2]Biomedical MRI unit, Katholieke Universiteit Leuven, Leuven/BELGIUM, [3]Earth and Life Institut, Mycology, Université Catholique de Louvain, Louvain-la-Neuve/BELGIUM

Purpose/Introduction:

Yeasts are important in traditional food and numerous industrial fermentations. The provision of specific *Saccharomyces cerevisiae* strains as dietary supplements in viable form is claimed to improve the intestinal microbial balance (i.e. probiotic). Increasing attention to their fast and accurate identification and characterization is warranted by the ability of many yeast species, including *S. cerevisiae*, to grow under physiological conditions, bearing the risk of becoming pathogens in individuals with impaired immune response [1]. Yeasts of the genus *Saccharomyces* continue to present classification problems even when using molecular biological approaches [2]. The current study investigated strains that have been typed by molecular biological and a chemical method that reflects a very large number of cell compounds and metabolic products. The aim was to evaluate potential correlations of metabolomic with genomic data.

Subjects and Methods:

High resolution ^{1}H NMR spectroscopy using an Avance 400 MHz NMR spectrometer (Bruker Biospin, Rheinstetten, Germany) was performed to 160 yeast strains, identified by PCR-fingerprinting as *S. pastorianus*, *S. cerevisiae* type B, *S. cerevisiae* type C and *S. bayanus*. The resulting spectra were frequency aligned, normalized and a feature selection step was performed based on a T-test with pooled variance approach [3]. Binary clustering analysis, for differentiating between all pairwise groups were developed using as input features the most relevant metabolic regions.

Results:

Different spectral regions showed to help in differentiating between the pairwise groups, see Fig.1. Those regions mainly correspond to polyols, carbohydrates and amino acid residues. Cluster analyses reports that the metabolic profile of *S. cerevisiae* type B is most distinct between all the other groups, see Figure 2. *S. pastorianus* and *S. cerevisiae* type B are clearly differentiating. *S. cerevisiae* type B and *S. cerevisiae* type C are also separable. Members of *S. bayanus* show high within-the-group variability. This finding correlates with molecular biological data showing the hybrid-character of most *S. bayanus* strains [2].

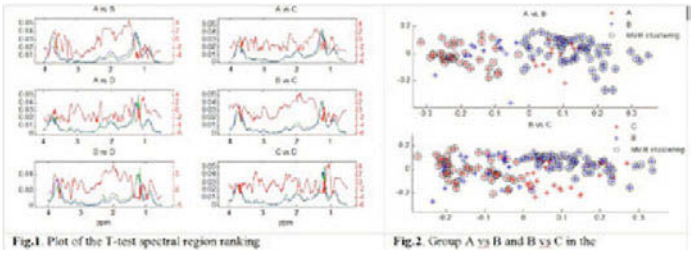

Fig.1. Plot of the T-test spectral region ranking

Fig.2. Group A vs B and B vs C in the

Discussion/Conclusion:
This study shows a good correlation between the PCR-fingerprinting and NMR spectroscopy of yeasts at species level and it proves the potential of NMR spectroscopy to become an useful tool for simple, robust and fast metabolic characterization and classification of yeasts.
References:
[1] Enache-Angoulvant and Hennequin (2005), Clin Inf Dis. [2] Libkind et al (2011), PNAS. [3] Mazhindu and Scott (2005), London UK.

642

Phospholipids composition of human milk determined by 31P NMR and relationship to intestinal maturity in premature neonates

C. Garcia[1], V. Brévaut-Malaty[2], V. Millet[3], R.D. Duan[4], C. Gire[2], U. Simeoni[3], J. Gaudart[5], M. Bernard[1], **M. Armand**[1]
[1]CNRS 7339, CRMBM, AMU, Faculté de Médecine Timone, Marseille/FRANCE, [2]Néonatologie, Hôpital Nord, AP-HM, Marseille/FRANCE, [3]Néonatologie, Hôpital de la Conception, AP-HM, Marseille/FRANCE, [4]Gastroenterology and Nutrition Lab, Lund University, Clinical Sciences, Lund/SWEDEN, [5]UF Biostatistiques, UMR 912 SESSTIM, AP-HM, Marseille cedex/FRANCE

Purpose/Introduction:
Human milk should program an optimal development of neonates by providing bioactive molecules, among them phospholipids. Dietary phospholipids exert cardio, hepato, brain protective, or anti-oxidant effects[1], or favor intestinal maturity (sphingomyelin, SM)[2]. We aimed to quantitate their real intakes in very-low-birth-weight premature neonates in an early postnatal critical window of development.
Subjects and Methods:
Forty neonates (1224±242 g ; 29.6±0.8 weeks) fed native mother's milk (n=13) or pasteurized donors milk (n=27) were followed-up from the start of minimal enteral feeding to 4 weeks. Samples of each feeding were analyzed by ^{31}P NMR for phospholipid classes identification and quantitation (Avance 400 Bruker NMR spectrometer 9.4T)[3]. Acid SMase activity was measured using radiolabelled SM[4]. Intestinal maturity was defined as the number of days for reaching total enteral feeding. Statistics were performed using SPSS ($p < 0.05$). Data are means ± SD or mean ranges over 4 weeks.
Results:
Native milk contained higher levels (µg/ml) of phosphatidylethanolamine (PE: 35.8 ±10.5 vs 29.2 ± 7.7), SM (66.5 ± 14.8 vs 55.2 ± 12.8), and exhibited a higher Smase activity (308 ± 77 vs 201 ± 78 pmol/h/ml) compared to pasteurized donors milk. SM intakes were lower (17-166 mg/week) than amounts reported to be optimal for intestinal development (60-150 mg/d)[3]. Intakes (mg/week) of PE-Plasmalogens (7.3-29 vs 4-20.2), PE (13.6-44.2 vs 9.9-42.9) and SM (23.3-100.3 vs 17.1-69.8) were significantly higher, or tended to be, for the neonates fed mother's milk. Negative correlations were found between the amounts of PE-Plasmalogens, PE, SM, phosphatidylserine, phosphatidylcholine, and Smase consumed and the time necessary to reach intestinal maturity.
Discussion/Conclusion: Phospholipids are important nutrients for neonatal gut development. Early postnatal nutrition should be improved by selecting donor milk high in SM levels, and developing formulas containing adequate amount and composition of phospholipids.
References:
1. Garcia C. et al., 2011, J. Pediatr Gastroenterol Nutr, 53 :206-212.
2. Motouri M. et al., 2003, J. Pediatr Gastroenterol Nutr, 36 :241-247.
3. Garcia C. et al., 2012, Food Chemistry, 135:1777-1783.

643

Minipig model of Huntington's disease: 1H MR spectroscopy of the brain

M. Jozefovicova[1, 2], V. Herynek[1], S. Juhas[3], J. Juhasova[3], M. Dezortova[1], F. Jiru[1], M. Hajek[1], J. Motlik[3]
[1]MR Unit, Department of Diagnostic and Interventional Radiology, Institute for Clinical and Experimental Medicine, Prague/CZECH REPUBLIC, [2]Department of NMR Spectroscopy and Mass Spectroscopy, Slovak University of Technology, Faculty of Chemical and Food Technology, Bratislava/SLOVAK REPUBLIC, [3]Institute of Animal Physiology and Genetics, Academy of Sciences, Libechov/CZECH REPUBLIC

Purpose/Introduction: Huntington's disease (HD) is a neurodegenerative genetic disorder affecting predominantly the brain. It is characterized by uncoordinated movements and a decline in mental abilities. Our aim was to determine changes in the brain of minipigs with Huntington´s disease using ^{1}H MR spectroscopy.
Subjects and Methods: Subjects: HD transgenic minipigs model according to (1) before HD onset (N=7, 2 years old), control minipigs (N=6, same age). Measurements were performed on a 3T MR scanner using a Tx/Rx head coil. PRESS-SVS sequence (TR/TE=5000/30ms, VOI=25x20x5mm, NA=96) was used for spectra acquisition in the white matter (WM). 2D-PRESS-CSI sequence (TR/TE=1510/30ms, FOV=90x90x5mm, VOI=30x30x5mm, matrix=16x16, voxel size 5.6x5.6x5.0mm, NA=32; in 1 animal measurement failed) was used for measurement in the basal ganglia, hippocampus, thalamus (Fig.1).
Spectra were analyzed using a program jSIPRO (2) with implemented LC-Model. We quantified signals of N-acetylaspartate+ N-acetylaspartylglutamate (tNAA), (phospho)creatine (tCr), choline compounds (tCho), glutamate+ glutamine (Glx), and myo-inositol (Ins). Unsuppressed water signal was used as an internal reference for the metabolite quantification. However, missing tissue segmentation may systematically shift absolute concentration values.

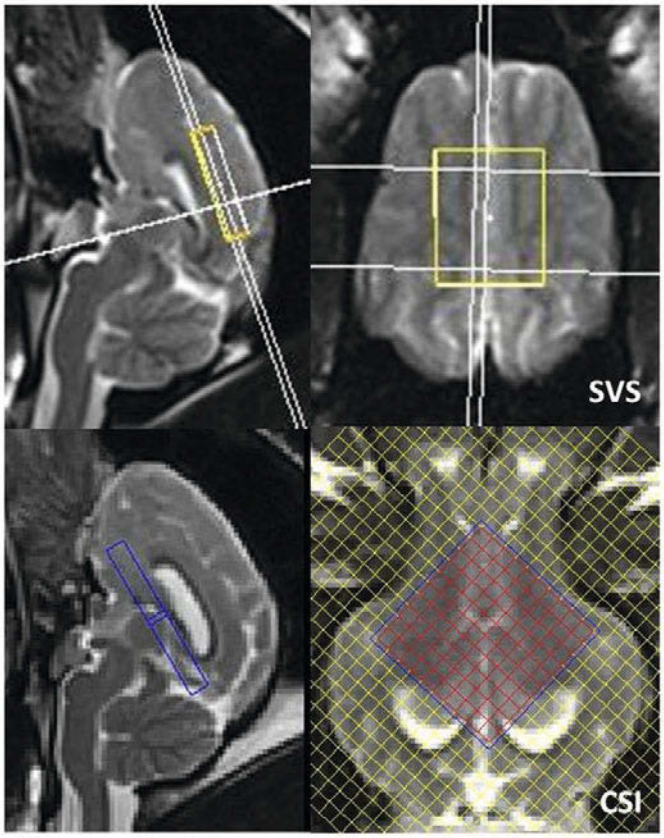

Figure 1: The position of the voxels in the white matter (SVS), and in the basal ganglia, thalamus and hippocampus (2D CSI)

Results: Relative and absolute metabolite concentrations in WM are summarized in Table 1, values from the basal ganglia, thalamus and hippocampus are in Table 2.

No significant differences were observed in the absolute concentrations in WM. An increase of tCho/tCr was found in the white matter, basal ganglia, thalamus and hippocampus.

A significant decrease of the absolute concentration of tCr was found in the thalamus and hippocampus. Ins/tCr also increased in the hippocampus of HD group.

white matter	tNAA [mM]	tCr [mM]	tCho [mM]	Glx [mM]	Ins [mM]	tNAA/tCr	tCho/tCr	Glx/tCr	Ins/tCr
controls	5.5±0.4	4.1±0.6	1.4±0.2	9.2±2.2	4.4±1.0	1.4±0.1	0.35±0.04	2.3±0.8	1.1±0.3
HD	5.3±1.0	3.6±0.8	1.5±0.3	9.1±0.8	4.4±1.2	1.5±0.2	0.44±0.09*	2.5±0.4	1.3±0.4

Table 1: Absolute concentrations of metabolites and ratios of metabolite concentrations to tCr in the white matter. Significance level *p<0.05

metabolites	tNAA [mM]	tCr [mM]	tCho [mM]	Glx [mM]	Ins [mM]	tNAA/tCr	tCho/tCr	Glx/tCr	Ins/tCr
	basal ganglia								
controls	5.3±0.4	5.4±0.6	2.2±0.2	11.5±1.1	5.3±0.7	1.00±0.10	0.41±0.04	2.2±0.4	0.99±0.15
HD	5.1±0.5	4.8±0.8	2.2±0.3	10.3±1.7	5.0±0.5	1.08±0.10	0.46±0.02*	2.2±0.4	1.06±0.09
	thalamus								
controls	5.5±0.5	4.8±0.3	1.9±0.1	9.9±1.1	4.6±0.7	1.16±0.14	0.39±0.03	2.1±0.3	0.95±0.17
HD	5.1±0.5	4.2±0.4**	1.8±0.2	9.3±1.2	4.5±0.6	1.25±0.12	0.44±0.03*	2.3±0.2	1.10±0.11
	hippocampus								
controls	5.2±0.9	4.7±0.6	1.78±0.12	10.0±1.8	4.9±0.9	1.12±0.17	0.38±0.03	2.2±0.4	1.04±0.10
HD	4.9±0.2	4.0±0.2*	1.82±0.05	9.9±1.0	5.1±0.4	1.22±0.07	0.45±0.02**	2.5±0.2	1.28±0.10**

Table 2: Absolute concentrations of metabolites and ratios of metabolite concentrations to tCr in the basal ganglia, thalamus and hippocampus. Significance level *p<0.05, **p<0.01

Discussion/Conclusion: Creatine is an important marker for brain energy metabolism. Lower creatine levels were reported in HD patients suggesting impaired energy metabolism (3) and correspond to our findings in the thalamus and hippocampus. Changes in the choline concentrations are generally associated with alterations of membrane composition. An increased choline signal was found in neurodegenerative diseases. However, we hypothesize that increased tCho/tCr is rather caused by subtle changes in energy metabolism (decrease of tCr similar to the hippocampus and thalamus) than by changes in membrane or glia composition. An increase of Ins/tCr in the hippocampus can also be caused by tCr decrease.

To conclude, Huntington's disease in transgenic minipigs is accompanied by decreased concentration of tCr associated with changes of energy metabolism.

Acknowledgement

Supported by the MH CZ-DRO („Institute for Clinical and Experimental Medicine–IKEM, IN 00023001"), CHDI Foundation (A-5378 and A-5379), TA01011466, CZ.1.05./2.1.00/03.0124, and RVO:67985904

References:

1.Baxa M,2013,JHD;2:47-68

2.https://www.sites.google.com/site/jsiprotool/

3.Van den Bogaard SJA,2011,J Neurol;258:2230-2239

644

Accurate Quantification of Metabolites' Ratios in Glial Brain Tumors Employing 1H-MRSI at 3T

A. Madadi[1], M. Mohseni[2], A. Fathi Kazerooni[3, 4], S. Karimi Alavijeh[3, 4], **H. Saligheh Rad**[3, 4]

[1]Department of nuclear engineering, Islamic Azad university,Science and Research branch, Tehran/IRAN, [2]Neurosurgery Ward, Tehran University of Medical Sciences, Imam Khomeini Hospital, Tehran/IRAN, [3]Quantitative MR Imaging and Spectroscopy Group (QMISG), Institute for Advanced Medical Technologies (IAMT), Research Center for Cellular and Molecular Imaging, Tehran/IRAN, [4]School of Medicine,Medical Physics and Biomedical Engineering Department, Tehran University of Medical Sciences, Tehran/IRAN

Purpose/Introduction: Proton magnetic resonance spectroscopy imaging (^{1}H-MRSI) has been recently debated as a fundamental tool to assess the grading of glial brain tumor, revealing the biochemical compounds of the tissue and monitor the response of the tumors to therapy **[1]**. The purpose of this study is to accurately quantify important brain metabolites to assess chemical compounds of the tumorous brain tissue, including Choline (Cho), N-acetyl-aspartate (NAA) and Creatine (Cr) to prognosticate the tumor grade.

Subjects and Methods: Experiments were performed on 15 patients with glial brain tumors (eight patients with grade 4 and seven patients with grade 2) on a 3T MAGNETOM Siemens Scanner, employing PRESS technique **[1]** in different TEs (TE1/TE2/TR = 30/140/1500msec and TE3/TR = 270/1700msec) with flip angle = 90°, sampling interval = 0.833msec, number of data points

= 1024 and bandwidth = 1200Hz, with an extra Single Voxel Spectroscopy (SVS) acquired from the normal part of the brain for further eddy current correction (ECC).

Preprocessing stage consisted of: SNR-enhancement, ECC, and residual water removal. Quantification procedure was performed in time-domain employing subtract-QUEST algorithm **[2]**. Quantification results for each metabolite were analyzed in the associated optimal TE, where the metabolite of interest has the minimum contamination or distortion from macromolecules and other neighboring metabolites **[2]**.

Results: Fig. 1 shows the analysis results of Choline/Creatine, Choline/NAA and NAA/Creatine ratio quantification for grades 2 and 4 in glial brain tumors versus corresponding normal appearing brain tissue in 3 TEs, illustrating an increase in Cho/Cr and Cho/NAA ratios, and decrease in NAA/Cr ratio (with an exception of TE=30, showing an increase in NAA/Cr, due to existence of the baseline signals) in high grade in contrast to low grade tumors and for both grades in comparison with the normal tissues **(Fig. 2)**.

We performed reproducibility test on 5 normal subjects and computed correlation coefficients (R) for 8 metabolites **(Table 1)**.

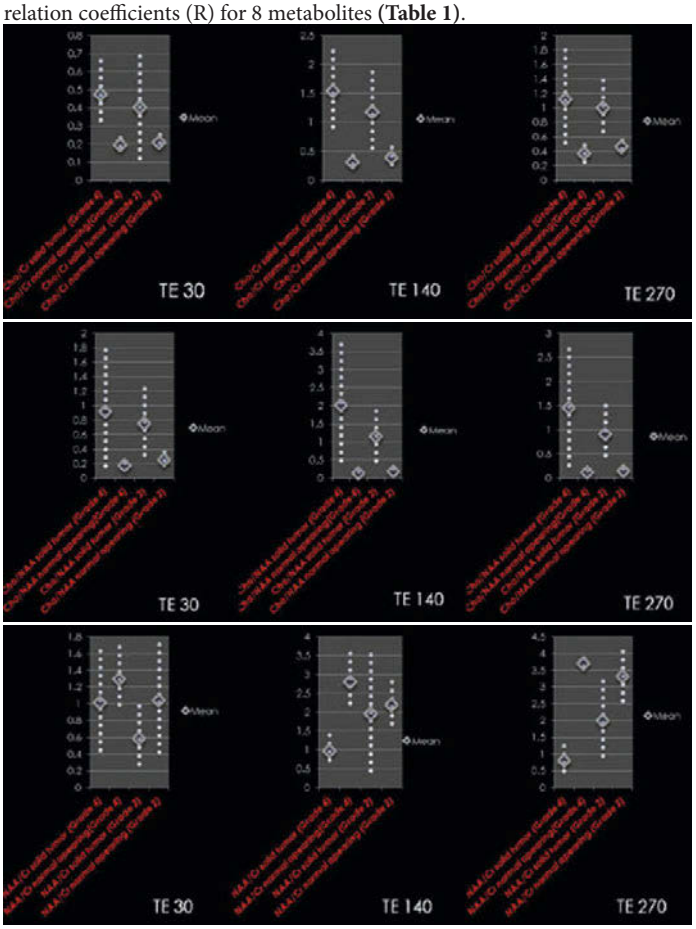

Fig. 1: the analysis results of Choline/Creatine, Choline/NAA and NAA/Creatine ratio quantification for grades 2 and 4 in tumorous brain tissue versus corresponding normal appearing brain tissue in 3 TEs.

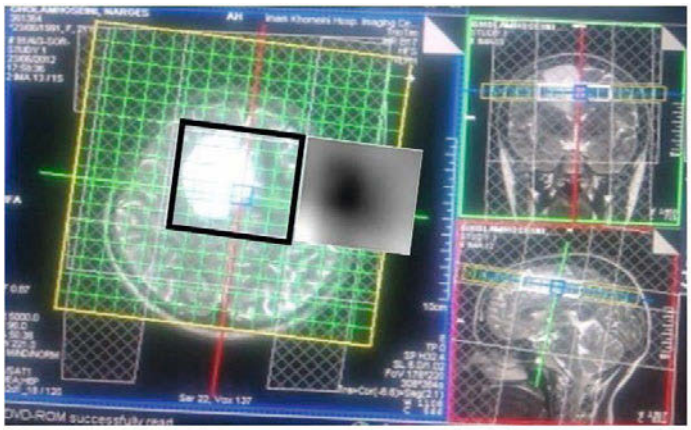

Fig. 2: Map of NAA/Creatine in one patient with glial tumor (IV-grade), showing significant decrease of NAA/Creatine in the tumorous tissue.

Table 1. Reproducibility results as correlation coefficient R computed for 8 metabolites on 5 normal subjects

Metabolites	Ala	Cho	Cr	NAA	ml	Glx	Gly	Lipids
Average *R*	0.92	0.74	0.79	0.78	0.75	0.62	0.70	0.78

Discussion/Conclusion: In this work, the database for subtract-QUEST-MRSI was optimized for the quantification of glial brain tumors. The reliability of metabolites' estimations was examined based on average Cramer-Rao bound (CRB) **[2]**, to be beyond 93%, implying trustworthy computations, observing significant differences in Choline/Creatine, Choline/NAA and NAA/Creatine ratios in different grades of glial tumors with respect to the control group, meaning our technique could distinguish tumorous from normal tissue, to be reliably used to predict the tumor grade.

References:

[1] Barker P et al. Clinical MR spectroscopy (2010).
[2] Ratiney H et al. NMR Biomed 18 (1) (2005).

645

Accurate Quantification of In-Vivo 1H-MRSI for Multiple Sclerosis at 3T; A Reproducibility Study

H. Vafaeyan[1, 2], N. Rahimian[3], A. Madadi[1, 4], M.H. Harirchian[3], **H. Saligheh Rad**[1, 5]

[1]Quantitative MR Imaging and Spectroscopy Group (QMISG), Institute for Advanced Medical Technologies (IAMT), Research Center for Cellular and Molecular Imaging, Tehran/IRAN, [2]School of Para-medicine, Shahid Beheshti University of Medical Sciences, Tehran/IRAN, [3]Department of Neurology, Imam Khomeini Hospital, Iranian Center of Neurological Research, Tehran University of Medical Science, Tehran/IRAN, [4]Department of nuclear engineering, Islamic Azad university,Science and Research branch, Tehran/IRAN, [5]School of Medicine,Medical Physics and Biomedical Engineering Department, Tehran University of Medical Sciences, Tehran/IRAN

Purpose/Introduction: Multiple Sclerosis (MS) is an inflammatory demyelinating disease. Proton magnetic resonance spectroscopy (^{1}H-MRSI) enables quantification of metabolites' concentration ratios of the brain **[1]**. The quantification ratios computed by the software on clinical scanners are usually associated with substantial errors, leading to misinterpretation of the spectral data. The purpose of this work is to accurately characterize NAA/Cho, NAA/Cr, as well as estimating its reproducibility in MS Patients.

Subjects and Methods: The ^{1}H-MRSI experiments on 10 patients and 5 healthy volunteers were performed on a3T scanner (Siemens Tim-Trio), employing PRESS pulse sequence with TR/TE=2500/30ms at the volume of interest (VOI) in the Para-ventricles. CHESS and outer volume suppression (OVS) were performed for water and lipid suppression **[4]**. A single-voxel acquisition on an external water phantom was performed for Eddy current correction (ECC). Signal pre-processing was optimized in this way: ECC, SNR improvement, phase correction and water-removal **[2]**. Time-domain quantification was performed using subtract-QUEST technique and based on an optimal metabolite database **[3]**. The simulated database was created in NMR-SCOPE. The correlation coefficients of the reproducibility were calculated in 4 normal subjects.
Results: After enough number of iterations, an optimal database was formed for the quantification the MRSI data, comprising of Choline (Cho), Creatine (Cr) ,N-acetyle aspartate(NAA) ,Lactate, Lipids, Myo- inositol, Glutamine and Glutamate. **Fig. 1** presents the ratios compared between MS patients and control groups. All voxels with more than 50% MS lesion were considered in the white matter (WM) of the patients, while similar regions of normal appearing white matter (NAWM) were considered in the controls, resulting in significant decrease of NAA in MS lesions of patients' white matter(WM) compared to normal' NAWM. Reliability of the quantification results was evaluated employing Cramer-Rao Bound (CRB) **[2]** to be about 95% for all subjects.
Table1 shows correlation coefficient (R) for 3 metabolites examined in this study.

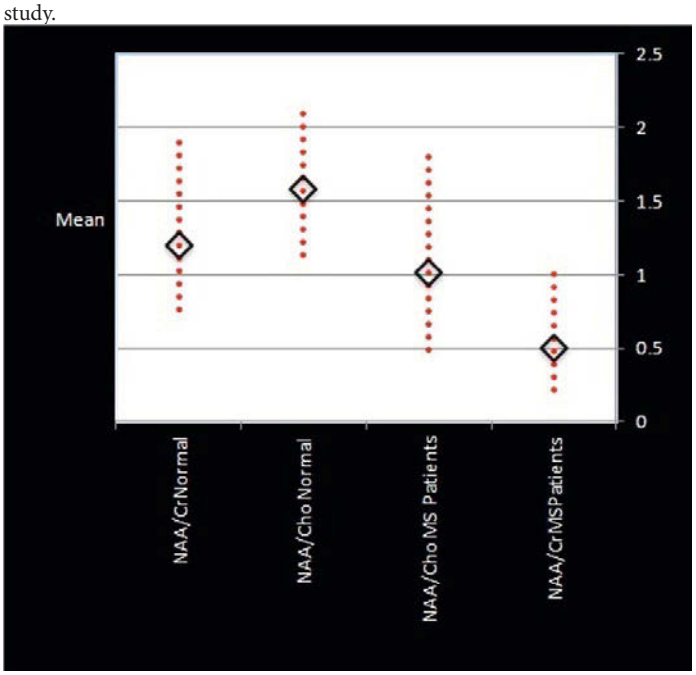

Fig1: NAA/Cr and NAA/Cho ratios for the normal group NAWM and WM lesion in patient with MS.
Table1. Correlation Coefficient of reproducibility for 4 normal subjects.

Metabolites	NAA	Creatine	Choline
Average Correlation coefficient	0.8515	0.7941	0.8792

Discussion/Conclusion: We optimally employed an accurate time-domain quantification algorithm for estimation of metabolites' ratios in MS patients. The results show significant differences between the values for NAA/Cr and NAA/Cho ratios in MS patients and normal people.

References:
[1] Aboul-Enein F et al. PLoS One 5 (7) e11625 (2010). **[2]** Jacobus FA *et al. Radiology* 240, 318 (2006). **[3]** Poullet J *et al. . JMRI* 195 (2) (2008). **[4]** Duarte J et *al. NeuroImage* 61, 342 (2011).

646

1H MRS of rat brain in the model of chronic renal failure.

R. Tuskova[1], L. Baciak[2], I. Just Kukurová[3], K. Šebeková[4], S. Kašparová[2]
[1]Department of Biochemistry and Microbiology, Slovak University of Technology,Faculty of Chemical and Food Technology, Bratislava/SLOVAK REPUBLIC, [2]Department of NMR Spectroscopy and Mass Spectroscopy, Slovak University of Technology Faculty of Chemical and Food Technology, Bratislava/SLOVAK REPUBLIC, [3]MR Center—High Field MR, Department of Radiology, Medical University of Vienna/Vienna General Hospital, Vienna/AUSTRIA, [4]Institute of Molecular biomedicine, Comenius University in Bratislava, Faculty of Medicine, Bratislava/SLOVAK REPUBLIC

Purpose/Introduction: Chronic renal failure (CRF) is a slow and progressive decline of kidney function. More than 19 million adults are living with some type of CRF worldwide. Recently has been proposed that patients with CRF suffer from cognitive impairment (1,2). Experimental model of 5/6 nephrectomy (5/6Nx) represents one of the most used rat models of CRF (3). Changes in brain metabolism are presuppose. The aim of these experiments was to obtain changes in brain metabolism after induced renal insufficiency by 1H MRS.
Subjects and Methods: 30 Wistar rats males were divided to 2 groups: 15 sham and 15 5/6 Nx. 5/6 Nx was performed by unilateral nephrectomy and either partial infarction or amputation of the poles of the remaining kidney (3). 8 rats (4 sham and 4 5/6 Nx) were used for MRS analysis 12 months after operation. 1H MRS measurements were performed on 4.7T horizontal scanner (Agilent, Yarton, UK) equipped with 400mT/m gradient and DDR console. Quadrature transmit/receive birdcage volume coil was used in combination with dual channel surface receiver. SPECIAL pulse sequence (4) with following parameters was used: TR/TE 3000ms/2.8ms and averages array 8x64 (512), voxel size of 3 x 4.5 x 3mm placed in hippocampus. Selected metabolites- NAA, PCr+ Cr, Cho+ PC+ GPC, LAC, m-INS, TMA were evaluated. The animals were anesthetized by isoflurane and the ambient temperature was maintained at 37 °C by warm air (SA instruments).
Results: No significant changes were found in control group versus nephrectomy group. Quantification of in vivo MRS signals were performed by jMRUI version 5.0 software. For data analysis independent t-test (Origin 7.0) was used. Data are presented as means with standard error (SE).

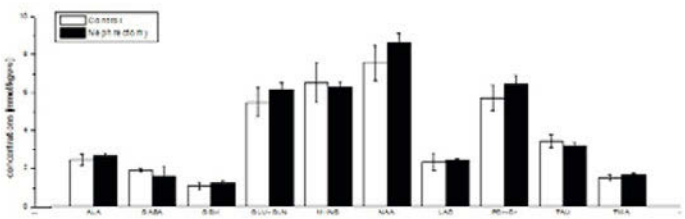

Discussion/Conclusion: Decreased kidney function is often associated with decreased cognitive functions; however, it has not yet been thoroughly ascertained. Analysis revealed no significant changes in metabolite concentrations between control and nephrectomy groups. These facts could associate from too small animal group (N=4) or aging effect that could overlap the changes in concentration caused by nephrectomy. Behavioral test or sooner measurements may help to resolve this question but the relationship between our selected metabolites and the cognitive function remain still unclear.

References:
1. Anne M Murray. 2008. Chronic Kidney Disease in Special Populations.
2. Miklós Palkovits et al. 2012. Int J Physiol Pathophysiol Pharmacol.
3. Agata L Gava et al. 2012. Int J Physiol Pathophysiol Pharmacol.
4. Mlynarik V et al. 2008. Journal of Magnetic Resonance.

647

31P MR spectroscopy of the testes of transgenic minipigs with Huntington´s disease

M. Jozefovicova[1,2], V. Herynek[1], J. Juhasova[3], S. Juhas[3], F. Jiru[1], M. Dezortova[1], M. Hajek[1], J. Motlik[3]
[1]MR Unit, Department of Diagnostic and Interventional Radiology, Institute for Clinical and Experimental Medicine, Prague/CZECH REPUBLIC, [2]Department of NMR Spectroscopy and Mass Spectroscopy, Slovak University of Technology, Faculty of Chemical and Food Technology, Bratislava/SLOVAK REPUBLIC, [3]Institute of Animal Physiology and Genetics, Academy of Sciences, Libechov/CZECH REPUBLIC

Purpose/Introduction: Huntington's disease (HD) is a neurodegenerative genetic disorder that affects the brain, but also causes testicular degeneration and decreased spermatogenesis. It has been shown that ^{31}P MR spectroscopy of the human testes can be applied to differentiate between normal testes, primary testicular failure and testes with a chronic tubular obstruction. The aim of this study was to determine changes in testes of the minipigs with Huntington´s disease related to testicular degeneration by using ^{31}P MR spectroscopy.
Subjects and Methods: Subjects: HD transgenic minipigs (N=5) model according to (1), control minipigs (N=6).
Measurements were performed on a 3T MR scanner using a dual tuned ^{1}H/^{31}P surface coil, 2DCSI sequence (TR=4000ms, TE=2ms, FOV=240x240x25mm, matrix size 8x8x1, voxel size 30x30x25mm, NA=8). The coil was placed beneath the animal in a prone position.
Spectra obtained from each testis were processed in a program MestReNova. Quantification of the metabolites was achieved by integrating peaks of phosphomonoesters (PME), phosphodiesters (PDE), inorganic phosphate (Pi) and α,β,γ-adenosine triphosphate (ATP) (Fig. 1). The relative metabolite concentrations were related to the total adenosine triphosphate (tATP) concentration (which may include also a signal from adenosine diphosphate). PCr in the spectrum arises from the muscle contamination, as it is not present in the testicle. Therefore the ratios were corrected for the amount of muscle ATP based on percentage amount PCr and ATP (30%), which was obtained from the voxels in the muscle.

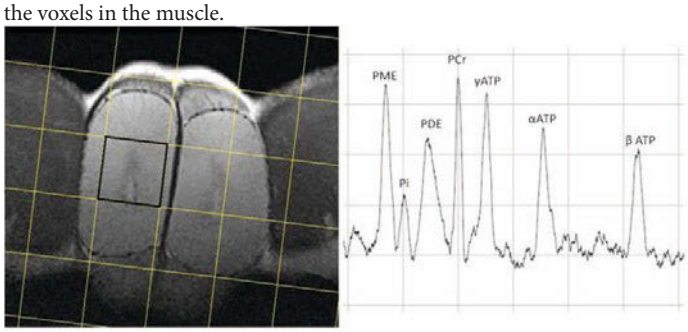

Figure 1: ^{31}P MR spectrum of the testis of a control minipig (right) from the selected voxel (left)

Results: Relative metabolite concentrations are summarized in Fig. 2. Significant decrease of PME/tATP and PDE/tATP ratios was found in transgenic minipigs compared to controls. No change was found in Pi/tATP.

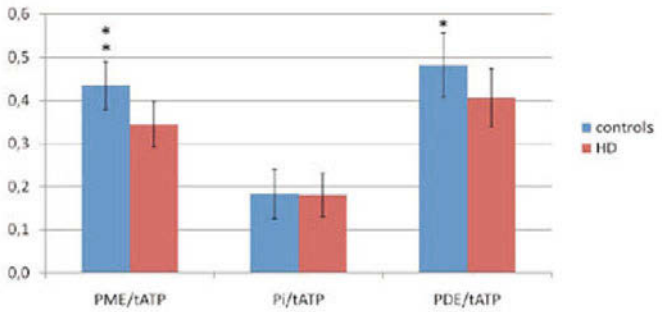

ratios	PME/tATP	Pi/tATP	PDE/tATP
controls	0.43±0.06	0.18±0.06	0.48±0.07
HD	0.34±0.05	0.18±0.05	0.41±0.07

Figure 2: Data represent mean±SD, n=6 (controls) and n=5 (HD). Statistically significant differences were found in ratios PME/tATP **p<0.002 and PDE/tATP*p<0.03

Discussion/Conclusion: Degenerative changes in the testical tissue have been already described in HD patients (lower spermatogenesis, thickening of the seminiferous tubule wall etc. (2)). The decrease of PME signal probably corresponds to lower spermatogenesis, i.e. decrease of cell proliferation and differentiation (3). Decrease of PDE/tATP ratio is probably associated with changes in cell membranes as PDE is considered to be a catabolic product of phospholipids, however, its relation to tissue degeneration on a molecular level remains unclear.

Acknowledgement
Supported by the MH CZ-DRO („Institute for Clinical and Experimental Medicine–IKEM, IN 00023001"), CHDI Foundation (A-5378 and A-5379), TA01011466, CZ.1.05./2.1.00/03.0124 and RVO: 67985904

References:
1. Baxa M et al. 2013, JHD 2:47-68.
2. Van Raamsdonk JM et al. 2007, Neurobiol Dis 26:512–20.
3. Van der Grond J et al. 1991, Fertil Steril 56:1136–42.

648

GA-QDA Based Feature Selection Classifier for Diagnosis of Brain Gliomas

K. Ghasemi[1,2], A. Fathi Kazerooni[2,3], M. Mohseni[4], A. Madadi[2,5], **H. Saligheh Rad**[2,3]
[1]Chemistry Department, Faculty of Science, Imam Khomeini International University, Qazvin/IRAN, [2]Quantitative MR Imaging and Spectroscopy Group (QMISG), Institute for Advanced Medical Technologies (IAMT), Research Center for Cellular and Molecular Imaging, Tehran/IRAN, [3]School of Medicine,Medical Physics and Biomedical Engineering Department, Tehran University of Medical Sciences, Tehran/IRAN, [4]Neurosurgery Ward, Tehran University of Medical Sciences, Imam Khomeini Hospital, Tehran/IRAN, [5]Department of Nuclear Engineering, Science and Research Branch, Islamic Azad university, Tehran, Iran., Tehran/IRAN

Purpose/Introduction: ^{1}H-Magnetic Resonance Spectroscopy (^{1}H-MRS) spectrum of normal brain demonstrates a high NAA peak, high tCr peak and low peaks of tCho, Glx, Gly and Myo-Inositol, as compared to the spectrum of abnormal tumorous tissue **[1-3]**, which can be used for grading of glioma brain tumors employing multivariate classification algorithms. The aim of this study was to develop a practical post-processing statistical tool for ^{1}H-MRS data analysis to create an effective non-invasive tool for brain tumour classification.
Subjects and Methods: The ^{1}H-MRS samples were acquired on a 3T scanner from 25 patients with glioma brain tumor and 3 healthy volunteers using

PRESS pulse sequence with TE=30msec and signal dimension of 16×16×1 (containing 256 separated signals). Then, all acquired MRS spectra were digitalized by JMRUI.V5 **[4]** and transferred to MATLAB V.7.12. In addition, spectra were preprocessed by SNR improvement, Eddy Current Correction (ECC), Water referencing, phase correction, normalization and baseline correction by SPID **[5]**.

Totally 105 spectra were selected from whole patients and 55 spectra separated for building training and the rest were taken as the test set. Two different feature selection procedures were applied to the ^{1}H-MRS data: Successive Projection Algorithm (SPA) and Genetic Algorithm (GA). Then, the outputs were introduced to Quadratic Discriminate Analysis (QDA) model as a powerful nonlinear classifier and related figures of merit were calculated.

Results: Fig.1 illustrates the probability plots of GA-QDA and SPA-QDA models, as an indication of their performance for test set. When a sample with specific class member is close to 1, it belongs to the specified class with high probability. The vicinity to 0 shows out-of-class membership.

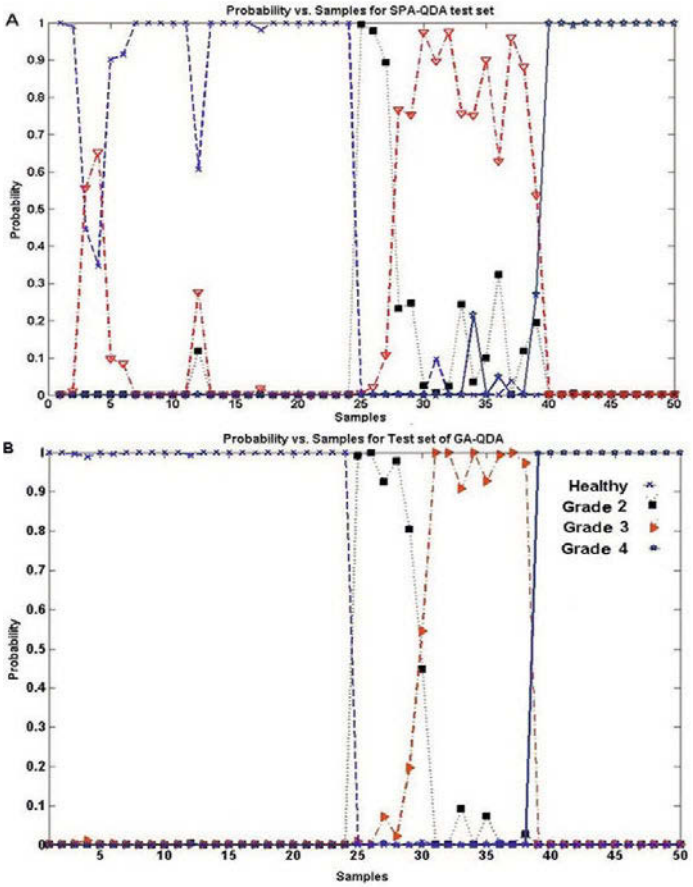

Fig.1. Probability plot for test set. SPA-QDA (A) and GA-QDA results (B).

Discussion/Conclusion: We showed that both of the variable-selection approaches improved sample classification performances. However, the 100% correctly classified samples in GA-QDA model, as a feature selection-based classifier, showed that it is an optimized tactic. It is obvious that the performance of GA-QDA model is superior to SPA-QDA, as it has a more sufficient predictive ability, and returns better results; 98% vs. 93%, respectively, for the separation of problem cases in the test set, especially in grades 2 and 3, suggesting that GA-QDA is more stable than SPA-QDA in prediction of the test set with higher confidence limit in prediction.

References:

[1] Byrd S *et al*, J. Natl. Med. Assoc. 88(11)(1996)

[2] Ross B *et al*, Magn. Reson. Q,10(4)(1994)

[3] Tong Z *et al*, JMRI,22(5)(2004)

[4] http://www.mrui.uab.es/mrui

[5] http://homes.esat.kuleuven.be/~biomed/software.php

649

Accurate Quantification of Cho/Cr in Osteosarcoma Employing Clinical 1H-MRSI at 3T; A Comparison Study with Normal Tissue

S. Karimi Alavijeh[1, 2], A. Madadi[1, 3], M. Oghabian[2, 4], M. Malek[4], **H. Saligheh Rad**[1, 2]

[1]Quantitative MR Imaging and Spectroscopy Group (QMISG), Institute for Advanced Medical Technologies (IAMT), Research Center for Cellular and Molecular Imaging, Tehran/IRAN, [2]School of Medicine,Medical Physics and Biomedical Engineering Department, Tehran University of Medical Sciences, Tehran/IRAN, [3]Department of Nuclear Engineering, Science and Research branch, Islamic Azad university, Tehran, Iran., Tehran/IRAN, [4]Advanced Diagnostic and Interventional Radiology Research Center (ADIR), Medical Imaging Center, Imam Khomeini Hospital, Tehran University of Medical Sciences, Tehran/IRAN

Purpose/Introduction: Proton magnetic resonance spectroscopy imaging (^{1}H-MRSI) has recently attracted attentions in musculoskeletal applications in general, and in Osteosarcoma in particular **[1, 2]**. Acquired spectra in the MRSI procedure are usually corrupted due to low signal-to-noise ratio (SNR), as well as baseline and residual water contaminations, leading to quantification errors and; therefore, misinterpretation of ratios calculated by the clinical scanners' software. The aim of this study is accurate quantification of Choline-to-Creatine (Cho/Cr) ratio elevating in Osteosarcoma **[3]**.

Subjects and Methods: Cho/Cr were obtained in 10 patients and 10 healthy volunteers at 3T (Siemens Tim-Trio) by MRSI (PRESS, TR/TE: 2500/135ms) using a phase-array coil with water-suppression. An extra single voxel spectroscopy (SVS) without water-suppression was acquired to provide phase information for further Eddy-current correction (ECC). Multi-stage preprocessing **[4]** was applied as follows: ECC, SNR-enhancement and water-removal. Subtract-QUEST-MRSI as a time-domain technique was employed to accurately quantify the metabolites' ratios and to estimate the baseline **[5]**. An optimal database for subtract-QUEST was achieved based on multiple trials evaluated by acceptable peak fitting and Cramer-Rao-Bound (CRB) **[6]** including Alanine, Cho, Cr, Lactate, Lipid and water. Lipids at frequencies 0.94 and 1.33ppm were combined to increase accuracy of the Lipid estimation.

Results: Table 1 presents results of Cho/Cr for 10 patients and 10 volunteers, with average values of 0.448±0.055 and 0.324±0.030, respectively, and the meaningful change of 27 % ($p<0.0001$) (**Fig1**) between the two groups. Reliability of the quantification results were estimated employing CRB that was about 93.6% for the 10 volunteers.

Patients	Cho/Cr (Mean, STD)	Volunteers	Cho/Cr (Mean, STD)
Patient1	0.42±0.01	Volunteer1	0.30±0.04
Patient2	0.43±0.04	Volunteer2	0.32±0.03
Patient3	0.46±0.05	Volunteer3	0.33±0.02
Patient4	0.41±0.04	Volunteer4	0.30±0.04
Patient5	0.54±0.15	Volunteer5	0.32±0.03
Patient6	0.48±0.08	Volunteer6	0.36±0.05
Patient7	0.44±0.07	Volunteer7	0.34±0.02
Patient8	0.42±0.03	Volunteer8	0.34±0.01
Patient9	0.45±0.06	Volunteer9	0.31±0.01
Patient10	0.45±0.047	Volunteer10	0.032±0.02

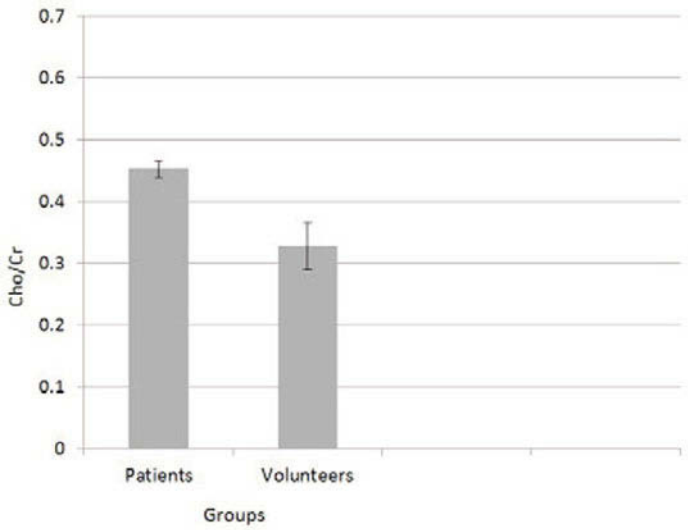

Fig1. Shows the difference between the two groups is significant.

Discussion/Conclusion: In this study, we managed to observe meaningful changes in Cho/Cr ratio in Osteosarcoma lesions versus the control group employing ^{1}H-MRSI. The best database for subtract-QUEST-MRSI was optimized in Osteosarcoma. Reliability of the quantification results was about 93.6% for the 10 volunteers.

References:

[1] Fayad L *et al., AJR* 23 (1), 23 (2006).
[2] Doganay S *et al.,Eur J Radiol* 79(2) 33 (2011).
[3] Geller DS *et al., Clinical Advances in Hematology & Oncology* 8(10), 705 (2010).
[4] Drost D j *et al., Med. Phys*. 29 (9), 2177 (2002).
[5] Ratiney H *et al., NMR in Biomedicine* 18(1), 13 (2005)
[6] Mandal P, *EJR* 81(4) 653 (2012).

650

In Vivo muscle T2 spectra measurement with an ISIS-CPMG sequence: Preliminary Findings in the Calf of Volunteers.

E.C.A. Araujo[1, 2], A. Vignaud[3], P. Carlier[3, 4]
[1]Resonance Magnetique Nucleaire, Institut de Myologie, PARIS/FRANCE, [2]Physics, UPS - Université Paris SUD, ORSAY/FRANCE, [3]RMN, CEA - Commissariat à l'énergie atomique et aux énergies alternatives, Paris/FRANCE, [4]Resonance Magnetique Nucleaire, Institut de Myologie, Paris/FRANCE

Purpose/Introduction: Mono-exponential muscle T2 obtained from qNMRI is sensitive but non-specific indicator of disease activity[1]. Multi-exponential T2 behaviour is understood as reflecting chemical and/or structural tissue compartmentation and might be sensitive to more specific tissue alterations[2]. An optimized ISIS-CPMG sequence was implemented for this purpose allowing localization with optimum parameters including short TE, high SNR and number of samples. In this work, preliminary results show T2 spectra sensitivity to exercise and vascular pre-conditioning state on normal volunteers.

Subjects and Methods: ISIS was implemented with a specially designed 10kHz bandwidth adiabatic quadratic phase pulse. CPMG was applied 2ms after each of the 8 ISIS acquisitions. ETL, TE and TR were 1000, 1ms and 18.75s respectively. Total acquisition took 5min. Only even echoes were used. T2-deconvolution was performed by regularized NNLS. NMR system was a 3T whole-body scanner (Tim Trio, Siemens Healthcare). RF-pulse transmission and detection was performed with a birdcage transceiver coil. VOIs were placed within the Gastrocnemius Medial and the Soleus (GMS), and within the Tibialis anterior (TA) of 3 male (age 38±15) and 2 female (age 31±6) volunteers, excluding blood vessels and subcutaneous fat. Data was acquired from the GMS of a male subject (age 29) before and after 15min intense local exercise, and for 3 different vascular pre-conditioning states (standard, venous-filling, and venous-draining).

Results: The T2 values and fractional areas of the T2 compartments observed in the spectra from within the GMS and TA of each volunteer are presented in Table 1. Table 2 resumes the resulting T2 spectra observed from within the GMS of a 2 years old male volunteer for different vascular filling muscle functional activity states.

Table 1: T2 values and fractional areas observed in the spectra obtained from within the GMS and TA of each volunteer

Sex	Age (years)	Tibialis Anterior		Gastrocnemius Medial and Soleus	
		T2 values (ms)	Fractional Areas %	T2 values (ms)	Fractional Areas %
M	56	33±1; 172±2	95; 5	35±1; 234±2	89; 11
M	31	32±1; 206±3	97; 3	36±1; 194±3	91; 9
M	29	30±1; 286±2	99; 1	30±1; 79±1; 335±3	92; 6; 2
F	35	3±1; 53±1; 276±3	80; 16; 4	30±1; 41±1; 220±3	55; 34; 11
F	28	33±1; 172±2	95; 5	31±1; 51±1; 225±3	54; 35; 11

Table 2: Characteristics of T2 spectra observed in the GMS of a 29 years old male volunteer for different muscle preconditioning states: vascular filling preparations and functional activity.

Vascular filling preparation	Nb of compartments	T2 values (ms)	Fractional Areas %
Normal	3	30±1; 62±1; 275±3	91; 5; 4
Venous Draining	2	30±1; 129±3	95; 5
Venous filling	3	31±1; 95±1; 368±2	88; 10; 2
Functional preparation	**Nb of compartments**	**T2 values (ms)**	**Fractional Areas %**
Before Exercise	3	30±1; 65±1; 220±3	86; 11; 3
After Exercise	3	30±1; 61±1; 234±4	76; 19; 5

Discussion/Conclusion: The Vascular filling studies support an anatomical compartmentation hypothesis and show that the technique is sensitive to changes in intra/extra-cellular spaces. The observed effects of exercise, the systematic differences between T2-spectra of TA and GMS and between male and female subjects suggest some sensitivity to glycogen concentration in cells. Results demonstrate the feasibility of the method in a clinical environment using a standard clinical system. Further investigations will be done to verify the possibility of monitoring glycogen consumption.

References:

1 Schenck JF, Zimmerman EA. High-field Magnetic Resonance Imaging of brain iron: birth of a biomarker? NMR Biomed 2004;17:433-445.

2 Saab G, Thompson RT, Marsh GD. Multicomponent T2 relaxation of in vivo skeletal muscle. Magnetic Resonance Imaging 1999; 42:150-157.

Paper Poster

Clinical neuro MRI

651
Post Partum Convulsions a Mystery to Solve: Value of Brain MRI Study

N.F. El Ameen, H.S. Abdel Ghany, A. Kotb
Radiology, El Minia univeristy, El Minia/EGYPT

Purpose/Introduction: In order to evaluate the role of MRI of the brain in women with post partum convulsion and correlate them with clinical data.
Subjects and Methods: In a prospective study, a total of 48 patients with post partum convulsions and suspected to had CNS complications were collected. The patients were delivered between January 2011 and March 2012. Obstetric surgeons from El-Minia University Hospital referred all patients to radiology department. They underwent MRI of the brain. All patients were included after meting the inclusion criteria which depends on the clinical and laboratory data. MRI findings were collected and classified according to final diagnosis.
Results: MRI examination of the brain was positive in 27 (56.3%) out of 48 patients who presented with post partum convulsions. Dural sinus thrombosis was the most frequently *encountered* finding representing 12/27 (44.4%). Intra cerebral hemorrhage was encountered in 6/27 (22.2%). Posterior reversible encephalopathy and subarachnoid hemorrhage were encountered in 5/ 27 (18.5%) and 3/27 (11.1%) patients respectively. Only one patient had pituitary apoplexy 1/27 (3.7%). The remaining 21 (43.7%) patients had negative MRI.
Discussion/Conclusion: Post partum convulsion is a serious condition and may be caused by delayed eclampsia or other neurological condition. MRI can solve this mystery and differentiate between its variable causes. So MRI of the brain must be done for these women without delay.
References:

- Matthys LA, Coppage KH, Lambers DS, et al. Delayed postpartum preeclampsia: an experience of 151 cases. *Am J Obstet Gynecol*2004;190:1464-6.
- Chames MC, Livingston JC, Ivester TS, et al. Late postpartum eclampsia: A preventable disease? Am J Obstet Gynecol2002;186:1174-7.
- Martin J, Sidman R.Late postpartum eclampsia: a common presentation of an uncommon diagnosis. J Emerg Med. 2003 Nov;25(4):387-90.
- Karumanchi SA, et al. Late postpartum eclampsia: examples and review. *Obstet Gynecol Surv*2006;61:471-80.
- Munjuluri N, Lipman M, Valentine A, et al. Postpartum eclampsia of late onset. *BMJ*2005;331:1070-1.
- Dutta A, Tonkin T and Gelman W. Postpartum convulsions—a diagnostic enigma JR Soc Med. 2006; 99(4): 203–204.
- Graeber B, Vanderwa l T, Stiller RJ, Werdmann M J. Late postpartum eclampsia as an obstetrics complication seen in the ED. Am J Emerg Med. 2005;2: 168-70.
- Ginzburg VE and Wolff B. Headache and seizure on postpartum day 5: late postpartum eclampsia. CMAJ 2009;180: 425-428
- Small KR, Cannava M, Casey S and Jacques J. Tonic-Clonic Seizures in a Postpartum Patient: Case Report. *Am J Crit Care* 2010; 19 : 307-305

652
Automated 3D Brain Tumor Edema Segmentation in FLAIR MRI

P. Dvořák[1, 2], K. Bartušek[1]
[1]Institute of Scientific Instruments, Academy of Science of the Czech Republic, Brno/CZECH REPUBLIC, [2]Dept. of Telecommunications, Faculty of Electrical Engineering and Communication, Brno University of Technology, Brno/CZECH REPUBLIC

Purpose/Introduction: This paper focuses on the fully automatic 3D brain tumor edema segmentation in FLAIR images using symmetry analysis and thresholding with automatic level determination. FLAIR was selected because of the visibility and manifestation of tumor edema in this image type. The main reason for the brain tumor edema segmentation is the tumor classification, which will be carried out using perfusion MR images. Since perfusion images are of a very low contrast, the pathological tissues has to be detected and segmented in another type of MR images.
Subjects and Methods: Since in axial plane of healthy brain, the approximate left-right symmetry exists, it is often used as a prior knowledge for searching of the approximate tumor location, e.g. in [1]. It is assumed that the tumor is not located symmetricaly in both hemispheres, which is met in most cases. For the detection, the multi-resolution approach is used, where the asymmetry map is computed using Bhattacharryya coefficient [2] for several different window sizes. The overall asymmetry map is computed as a product of the paricular maps. Since the edema manifests as a hyperintense area in FLAIR images, it is extracted using thresholding. The global threshold is determined automatically using the Otsu's algorithm [3] from the most asymmetric slice from both-sided mask of the most asymmetric areas. The edema in this slice is segmented and the resulting dilated mask is used as a prior mask for segmentation in other slices. The dilation is performed, because the edema can be a little bit larger or shifted in the neighbor slice. In these slices, the edema is again segmented by thresholding, but only inside the prior mask. The result is again used as the prior mask for the next slice.
Results: The method was tested on datasets with edema present, acquired in The University Hospital Brno. Several results of different slices in one dataset are shown in Fig. 1.

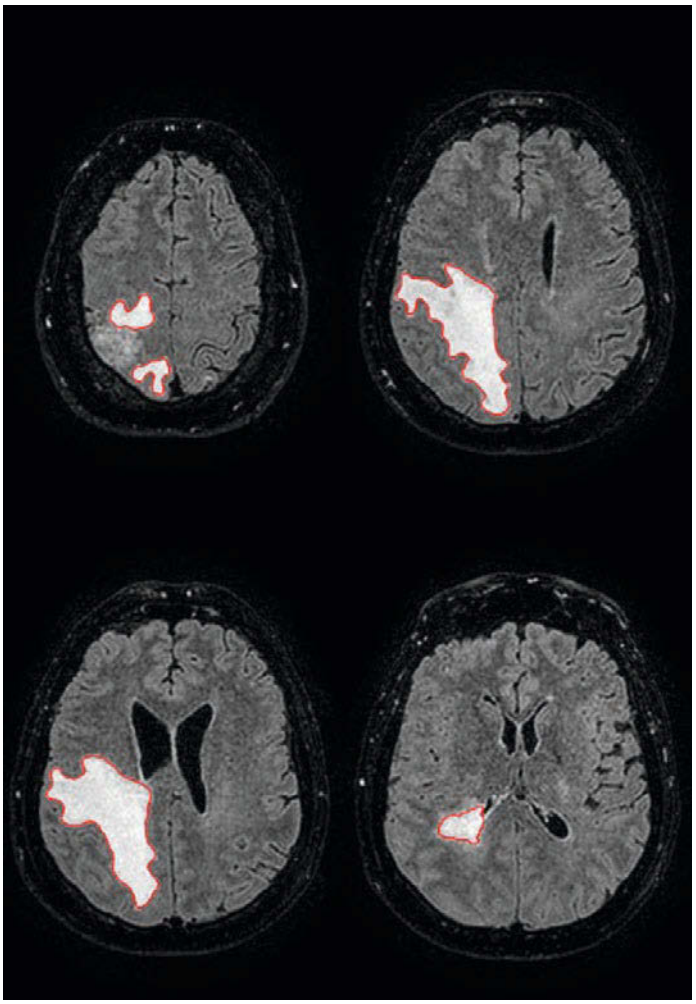

Fig. 1.

Discussion/Conclusion: This method reached promising results in segmentation of an edema, which is pathological area present with particular types of tumors. This area is very interesting from the medical point of view, because the tumor type can be determined from this area using perusion images.

References:

[1] Pedoia V. et al. Medical Imaging, 2012.

[2] Bhattacharyya A. Bulletin of the Calcutta Mathematical Society, 99–110, 1943.

[3] Otsu, N. IEEE Transactions on Systems, Man, and Cybernetics, 62–66, 1979.

Acknowledgement:

The described research is funded by projects SIX CZ.1.05/2.1.00/03.0072, GACR 102/12/1104, and CZ.1.05/2.1.00/01.0017

653

Diffusion Tensor Imaging of the Intraparotid Facial Nerve

A. Attye[1, 2], **I. Tropres**[3, 4, 5, 6], A. Karkas[7], G. Bettega[8], C. Righini[7], A. Krainik[2, 9]

[1]CLUNI, CHU Grenoble, Grenoble/FRANCE, [2]Médecine, Université Grenoble Alpes, Grenoble/FRANCE, [3]IRMaGe, CHU Grenoble, Grenoble/FRANCE, [4]IRMaGe, Université Grenoble Alpes, Grenoble/FRANCE, [5]US 017, INSERM, Grenoble/FRANCE, [6]UMS 3552, CNRS, Grenoble/FRANCE, [7]Clinique universitaire d'ORL, CHU Grenoble, Grenoble/FRANCE, [8]Clinique universitaire de chirurgie maxillo-faciale, CHU Grenoble, Grenoble/FRANCE, [9]CLUNI, CHU Grenoble, GRENOBLE/FRANCE

Purpose/Introduction: Identification of the facial nerve after the stylomastoïd foramen is of importance for patients with benign parotid tumours. Indeed, the knowledge of its position may help the surgeon in the choice of the parotid surgery way. However, facial nerve visualization remains a challenge even by modern imaging techniques. Diffusion tensor imaging (DTI) allows the identification of the cranial nerves in healthy subjects (1) or the tracking of the intracranial facial nerve among patients with cerebellopontine angle tumors (2). In this study, we attempted to visualize the facial nerve in its retroglandular and parotid parts up the cervical and temporofacial division in a patients' population admitted for benign parotid tumours. Then this method is correlated to the monitoring of the facial nerve done by the surgeon during the resection of the tumour.

Subjects and Methods: DTI was acquired in 10 patients with benign parotid tumours on a 3T Philips Achieva® scanner. The DTI sequence was performed in addition to the standard protocol including T1-, T2-weighted imaging and T1 perfusion study. The DTI parameters were: 2x2x2 mm voxel size, b=1000 mm^2/s, 32 diffusion directions.

We used the Fibertrack® Philips software to obtain facial nerve fiber tracking with the single Region of Interest method. The fraction of anisotropy was set to 0.05 and the maximal angle change to 80°.

During the surgical tumor resection, the DTI location of the facial nerve division (FND) in relation to the tumor was checked by a visual analysis and correlated with the direct stimulation of the facial nerve (Avalanche® device).

Results: Fibers corresponding to the anatomical location and course of the facial nerve from the stylomastoid foramen to the FND were identified with the fiber tracking technique in all patients. The visualization of the FND allows us to define two parts of the parotid gland (figure), superficial and deep, and to locate the tumor into one of these two parts. Among the 10 patients, only one patient suffered from partial facial paralysis one month after surgery.

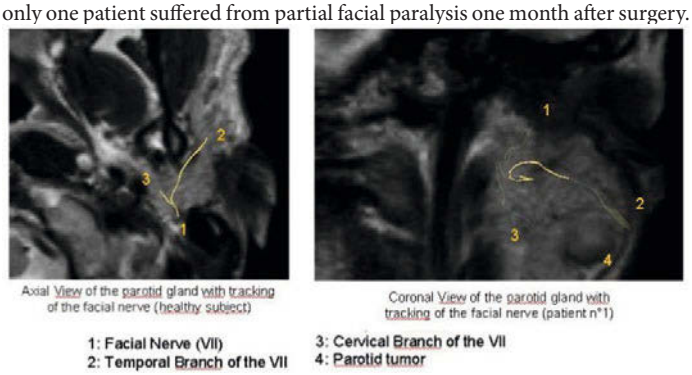

Axial View of the parotid gland with tracking of the facial nerve (healthy subject)

Coronal View of the parotid gland with tracking of the facial nerve (patient n°1)

1: Facial Nerve (VII)
2: Temporal Branch of the VII
3: Cervical Branch of the VII
4: Parotid tumor

Discussion/Conclusion: In comparison with the surgeon findings, we successfully located the facial nerve in its way through the parotid up the FND in all patients. Detection of the facial nerve in tumor vicinity by DTI MRI is therefore possible and may help for guiding the surgeon to the tumor site.

References:

(1) Hodaie et al., Neurosurgery 2010

(2) Roundy et al., J Neurosurg 2012

Paper Poster

Clinical neuro MRI

654

Magnetic resonance imaging in patients with vasculitis of internal carotid, vertebral and basilar arteries

E. Seliverstova[1], L. Dobrynina[2], M. Krotenkova[1], L. Kalashnikova[2]
[1]Department of Radiology, Research Center of Neurology, Russian Academy of Medical Sciences, Moscow/RUSSIAN FEDERATION, [2]Department of Neurology no. 3, Research Center of Neurology, Russian Academy of Medical Sciences, Moscow/RUSSIAN FEDERATION

Purpose/Introduction: Refining of magnetic resonance imaging (MRI) study protocol using 1.5-T scanner in patients with clinical suspicion of vasculitis of internal carotid and/or vertebral arteries, and/or basilar artery.
Subjects and Methods: We studied eight patients (mean age 34.5±10.2 years) with clinical suspicion of vasculitis of internal carotid and/or vertebral arteries, and/or basilar artery. MRI was performed using a 1.5-T scanner (Avanto, Siemens, Erlangen, Germany). Vascular patency and abnormalities of vessels' wall were studied using 3D time-of-flight magnetic resonance angiography (3D TOF MRA) with assessing vessels from an aortic arch to Willis' Circle. In order to evaluate arterial wall T1fat sat, T1dark blood, T2FLAIR images in axial, coronal and perpendicular to vessel's section views were obtained in all patients before and after intravenous 0.5 M gadolinium enhancement. Thickened vessel's wall with lumen narrowing or arterial occlusion and/or distribution of gadolinium enhancement in thickened vessel's wall were defined as signs of inflammation in vessel's wall. We assessed localization, length, and severity of revealed abnormalities comparing with the same segments of contralateral arteries.
Results: Inflammation signs in internal carotid arteries were revealed in six patients (75%); vertebral and basilar arteries were affected in two patients (25%). The most appropriate MRI sequences for revealing inflammation in the vessel's wall were T1fat sat and T1dark blood.
Discussion/Conclusion: Evaluating the zone from an aortic arch to Willis' Circle while performing 3D TOF MRA facilitates searching for abnormal segment of an artery. Inclusion of T1 fat sat and T1dark blood sequences while performing the MRI study on 1.5-T scanner with gadolinium enhancement improves visualization of probable inflammatory signs in internal carotid, vertebral and basilar arteries' wall in case of clinical suspicion of vasculitis.
References:
1. Birnbaum J, Hellmann DB. Primary angiitis of the central nervous system. Arch Neurol. 2009;66:704 –709.
2. Wynne PJ, Younger DS, Khandji A, Silver AJ. Radiographic features of central nervous system vasculitis. Neurol Clin 1997;15: 779–804.

655

3T multimodal quantitative longitudinal MRI study in metachromatic leukodystrophy : preliminary study

S. Kulikova[1], J. Dubois[2], C. Sevin[3], C. Chiron[4], C. Bellesme[3], N. Chemaly[4], D. Leunen[4], F. Boumezbeur[5], C. Poupon[5], P. Aubourg[3], L. Hertz-Pannier[1]
[1]Neurospin/UNIACT/UMR663, CEA-Saclay, Gif-sur-Yvette/FRANCE, [2]Neurospin/UNICOG, CEA-Saclay, Gif-sur-Yvette/FRANCE, [3]INSERM U986, Service de neuropédiatrie, Hopital du Kremlin Bicêtre, Paris/FRANCE, [4]Hopital Necker/enfants malades, UMR663, Université Paris Descartes, Paris/FRANCE, [5]Neurospin/UNIRS, CEA-Saclay, Gif-sur-Yvette/FRANCE

Purpose/Introduction: Metachromatic leukodystrophy (MLD) is a rare devastating disease with no available treatment [1-3]. 1.5T MRI poorly predicts disease progression. This study aims at finding sensitive and quantitative neuroimaging biomarkers to establish relevant criteria and endpoints for a pending gene therapy trial, by taking benefit of 3T SNR, and of new quantitative assessment offered by DTI and relaxometry. In this preliminary presentation, we aimed at developing innovative methodologies that we tested on the corticospinal tract (CST).
Subjects and Methods: Three children with late infantile MLD (29 to 66 months of age, two scans 4 months apart) were compared to ten children with focal epilepsy (18 to 60 months), from which we considered only the unaffected hemisphere. 3T MRI data were acquired under sedation (55 EPI axial slices with 2mm isotropic resolution; T2 mapping (qT2): 8 echo times TE=35->280ms; T1 mapping (qT1): 8 inversion times TI=250->1500ms + TI=2000, 2500ms; DTI: 60 orientations, b=1500 $s.mm^{-2}$; spectroscopy (CSI-SE): TE/TR = 30/1600ms, 6 OVS).
Tractography in highly demyelinated brain required alternative and dedicated approaches to avoid tract underestimation. The CST was reconstructed with regularized streamline algorithm using Connectomist software [4] and regions of interest (ROIs). DTI indices, qT1 and qT2 were measured along the tract. For spectroscopy, concentrations in NAA, Choline, Glutamate, MyoInositol and Lactate were measured in ROIs encompassing the CST in centrum semiovale (Creatine peak as a reference). Parameters were compared between the two groups (t-tests).
Results: Parametric maps (Figure 1) suggested asynchrony in the demyelination process. Quantification along the CST showed massive changes of all parameters in MLD children compared with controls, especially in the internal capsule, with a significant decrease of anisotropy (-68% on average), and increase of transverse diffusivity (up to 60%) and of qT1and qT2 (up to 67 and 57%, respectively). These changes, which were strongly correlated along the fascicle, ought to reflect the demyelination process. Spectroscopy confirmed neuronal loss (NAA and Glutamate decrease), demyelination and astrogliosis (increased Choline and MyoInositol) and metabolic stress (Lactate) (Figure 3).

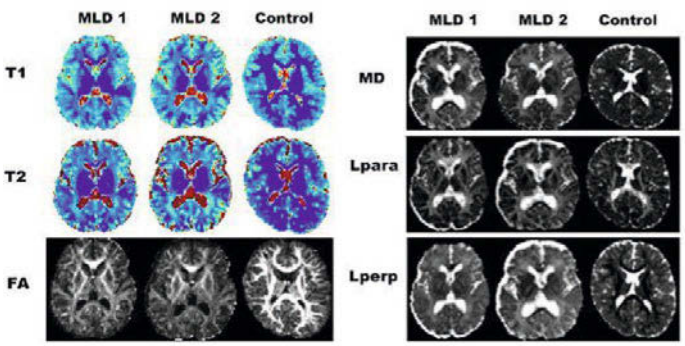

Fig 1 : Parametric map for a typical MLD child (29 months and 5 months later) et and a age-matched control child

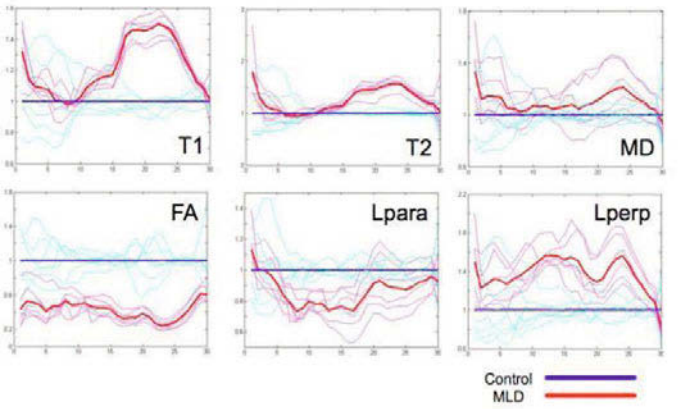

Fig 2: Values of the parameters along the CST (peduncles on the left, vertex on the right), in the MLD children (red), normalized by the control values (blue)

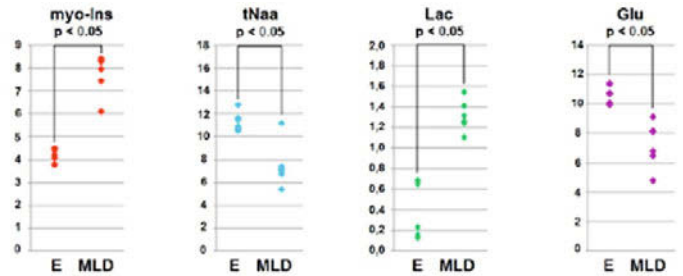

Fig3: Concentrations in metabolites compared between controls (E) and MLD children (t-tests p<0.05) Myoinositol (myo-Ins), NAA, Lactate (Lac), Glutamate (Glu).

Discussion/Conclusion: These approaches combined with ongoing recruitment and longitudinal assessment are promising to better understand the dynamics of demyelination in metachromatic leukodystrophy and will provide sensitive biomarkers to test new therapies.

References:

[1]: Martin et al, AJNR 33:1731-1739.
[2]: Groeschel et al, Neurology 2012, 79:1662-1670.
[3]: Groeschel et al, J Inherit Metab Dis 2011, 34:1095-1102.
[4]: Duclap et al, ESMRMB 2012, #842.

* The work was supported by ELA Foundation

656

Semi-automated method for ADC quantification of brain lesions

M. Alkubeyyer, I. Alorainy
Radiology, King Khalid Univeristy Hospital, King Saud Univeristy, Riyadh/ SAUDI ARABIA

Purpose/Introduction: Accuracy of apparent diffusion coefficient (ADC) measurements of brain lesions by tracing the whole lesion rather than placing oval-shaped region of interest is a tedious task. We present a method that semiautomatically trace brain lesions in comparison to manual segmentation using a home written software.

Subjects and Methods: 20 brain lesions of variable presentation were imaged utilizing echoplanar diffusion weight images with b value of (0 , 1000 sec/mm2). Two readers IA(Neuroradiologist consultant) and MK(General consultant) blinded to each other's result have segmented lesions manually and semi-automattically in two session with one week interval. Manual area tracing and measurement of the viable brain lesions excluding necrosis and cystic changes utilizing open source software ImageJ. Semi-automated measurement has been done by drawing a region of interest around the lesion, then the program would automatically segment the viable brain lesion by applying Haung thresholding method followed by morphological image processing. Time estimation of the manual and semi-automatic method were also obtained.

Results: Bland-Altman analysis showed good reproducibility of brain lesions area segmentation using the semi-automated method compared to manual method with bias, standard deviation, 95 % limits of agreement of -0.31 , 2.21 , [-4,73,4.19].

Mean time estimation for the manual method compared to the semiautomatic method was 15 minutes for the manual method compared to 5 minutes for the semi-automatic method

Discussion/Conclusion: The semi-automatic method is time saving and provides good reproducibility in compariosn to the manual method.

References:

1) J Neurosurg. 2010 Dec;113 Suppl:97-104.
2) Radiology. 2005 Jun;235(3):985-91.
3) Huang, L-K & Wang, M-J J (1995), "Image thresholding by minimizing the measure of fuzziness", Pattern Recognition 28(1): 41-51, <http://www.ktl.elf.stuba.sk/study/vacso/Zadania-Cvicenia/Cvicenie_3/TimA2/Huang_E016529624.pdf>

Paper Poster

Methods for neuroscience

657

Development of long stimulation paradigms with BOLD fMRI in the rat brain for metabolic coupling investigation

S. Sonnay[1], J.M.N. Duarte[1,2], R. Gruetter[1,2,3], N. Just[1,2]
[1]LIFMET, Ecole Polytechnique Fédérale de Lausanne, Lausanne/SWITZERLAND, [2]Department of Radiology, University of Lausanne, Lausanne/SWITZERLAND, [3]Department of Radiology, University of Geneva, Geneva/SWITZERLAND

Purpose/Introduction: Metabolic coupling between neurons and astrocytes is an important component of the BOLD response and remains to be fully understood. Neurometabolism underlying the hemodynamic response can be studied *in vivo* by ^{13}C-MRS requiring long experimental protocols and therefore sustained brain stimulation. The aim of this study was to develop long fMRI paradigms to provide prolonged brain activation for future ^{13}C-MRS experiments.

Subjects and Methods: fMRI was performed in adult rats (SD,350±20g) under light α-chloralose anesthesia on 9.4T and 14.1T magnets with ^{1}H quadrature T/R RF surface coils. First and second order shims were automatically adjusted using FAST(EST)MAP reaching water linewidths of 17–22Hz at 9.4T and 20-26Hz at 14.1T in a 270µl volume. Electrical stimulations were performed with stainless steel electrodes (cathode/anode) inserted into the limb(s) of interest. Square pulses (0.5ms width) were delivered at constant current and different frequencies. Physiological conditions were maintained during the entire experiment. The BOLD signal was measured using single shot gradient echo planar imaging (GE-EPI). Data were processed with routines implemented in MATLAB. Motion correction and data analysis were performed in SPM and STIMULATE, respectively. Activation t-value maps were computed on a pixel by pixel basis from the acquired fMRI data and the applied paradigm schemes. An average time-course from the activated region was then extracted and the relative BOLD response was calculated.

Results: At first two different paradigms including long interleaved periods (60sec OFF–60sec ON-60sec-OFF and 30sec OFF–30sec ON–30sec OFF repeated for 1hour) were tested in the left forepaw and resulted in a sustained BOLD response in contralateral primary S1 somatosensory cortex and sometimes M1, M2 (Table). Then a paradigm with shorter interleaved periods (10sec OFF–30sec ON–10sec OFF) at constant and alternative frequencies were unilaterally applied and also resulted in a sustained BOLD response in contralateral cortex (Figure 1 and Table). Reduction of activated brain area after 1.5-2 hours of stimulation was improved by varying the frequency (7-17% *vs.* 67%). Finally this protocol was bilaterally repeated for 2 hours at variable frequencies in forepaws and hindpaws, and unilaterally in trigerminal nerve and resulted also in sustained cortical BOLD responses (Table).

paradigms	*frequency / current*	*limb(s) of interest*	*sustained cortical BOLD response(hours)*	*# animals*
60sec OFF - 60 sec ON - 60 sec OFF	constant (3Hz / 3mA)	unilateral forepaw	1.0	n = 1
30sec OFF - 30 sec ON - 30 sec OFF	constant (3Hz / 3mA)	unilateral forepaw	1.0	n = 1
5sec OFF - 30 sec ON - 5 sec OFF	constant (2Hz / 3mA)	unilateral forepaw	1.5	n = 1
10sec OFF - 30 sec ON - 10 sec OFF	constant (3Hz / 3mA)	unilateral forepaw	1.0	n = 1
10sec OFF - 30 sec ON - 10 sec OFF	variable (2-3Hz / 3mA)	unilateral forepaw	1.0	n = 1
10sec OFF - 30 sec ON - 10 sec OFF	variable (2-3Hz / 2.5mA)	unilateral forepaw	1.5	n = 2
10sec OFF - 30 sec ON - 10 sec OFF	constant (2Hz / 3mA)	unilateral forepaw	2.0	n = 1
10sec OFF - 30 sec ON - 10 sec OFF	variable (2-3Hz / 2.5mA)	unilateral forepaw	2.0	n = 2
10sec OFF - 30 sec ON - 10 sec OFF	variable (2-3Hz / 3mA)	bilateral forepaws	2.0	n = 1
10sec OFF - 30 sec ON - 10 sec OFF	constant (2Hz / 2mA)	bilateral forepaws	2.0	n = 1
10sec OFF - 30 sec ON - 10 sec OFF	variable (2-3Hz / 3mA)	bilateral hindpaws	2.0	n = 1
10sec OFF - 30 sec ON - 10 sec OFF	variable (2-3Hz / 2mA)	unilateral trigerminal nerve	2.0	n = 1

Table : Paradigms for sustained cortical BOLD response

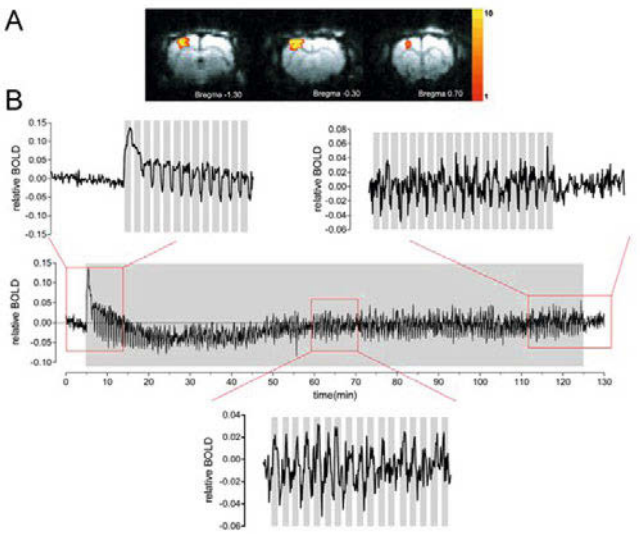

Figure 1 : Unilateral forepaw stimulation
(A) T-test activation map showing positive activation in contralateral S1 overlaid on a GE-EPI image (TR/TE=2500/25ms at 9.4T ; TR/TE=2500/17ms at 14.1T ; FOV=30×30mm ; data matrix=64×64; slice thickness=1mm ; bandwidth=300-350kHz). Only clusters including at least 3 pixels were considered as significant ($p < 0.01$). (B) Relative BOLD response after 2 hours stimulation with the paradigm [30sec ON - 10sec OFF - 30sec ON] at variable frequencies (2-3Hz).

Discussion/Conclusion: Prolonged and simultaneous stimulation of rat limbs provides a sustained and large cortical activation, which will allow to perform ^{13}C-MRS in a large voxel of interest reaching higher signal-to-noise ratio. This will also provide new tools for plasticity investigation.

References:

Duarte JM,Lanz B,Gruetter R, 2011, Front Neuroenerg. 3
Just N,Xin L,Frenkel H Gruetter R, 2013, Neuroimage. 74, 343

658

Difference in brain activation stimulating self-reference network in first episode schizophrenia: a fMRI study

J. Rydlo[1], F. Spaniel[2], I. Ibrahim[1], J. Tintera[1]
[1]MR-Unit, Dept. Diagnostic and Interventional Radiology, Institute for Clinical and Experimental Medicine, Prague/CZECH REPUBLIC, [2]Psychiatry, Prague Psychiatric Center, Prague/CZECH REPUBLIC

Purpose/Introduction: Experiencing oneself as the cause of an action or experiencing another person as being the cause of that action is mediated in healthy subjects particularly by the anterior cingulate cortex and frontomedial cortex (1).

Schizophrenia is characterized by an impaired ability to correctly attribute an action to its origin. Common symptoms include auditory hallucinations, paranoid or bizarre delusions, disorganized speech and thinking.

Our study deals with differences in activation of self-reference patterns between patients with first episode schizophrenia (FES) and controls. A paradigm to activate self-reference pattern is developed. This paradigm allows manipulating the experience of movement control by visual feedback.

Subjects and Methods: The study enrolled 29 healthy subjects and 23 FES patients.

The activation paradigm with either modified or true cursor trajectory was performed by home-built MR-compatible joystick with optical data transmission. This trajectory was displayed to subject using developed software allowing also recording of coordinates from the joystick. During the fMRI experiment 20s blocks were alternating: (A) with movement deviated artificially by in-

troducing an angle deviation and (B) with precise trajectory of the joystick movement. Subjects were instructed to recognize movements influenced by "somebody else" (A) and own movements (B). Recorded cursor position was used for later statistical evaluation.
All fMRI measurements were performed on Siemens Trio 3T scanner using GRE- EPI sequence (FOV=192x192mm, voxel 3x3x3mm, TR/TE=2000/30ms, 30 slices). Total of 240 dynamical scans was acquired and measurement lasted 8 min.
Statistical analysis was done in SPM8 using GLM. Cursor trajectory was used for definition of time periods of "owning" the cursor and "stolen" periods. Statistical group maps (p=0.05 FWE) and difference between volunteers and patients were calculated.
Results: Success rates of recognition oneself from "somebody else" differed between patients and controls. In blocks without movement distortion controls attributed correctly the movement themselves in 90% and patients in 70% of the block duration.
Controls showed increased activation compared to FES patients during B period in the following areas (fig.1a,b): anterior cingulate, mediofrontal cortex, precuneus. Increased activation in insula L/R in controls during period A was also detected (fig.1c,d).

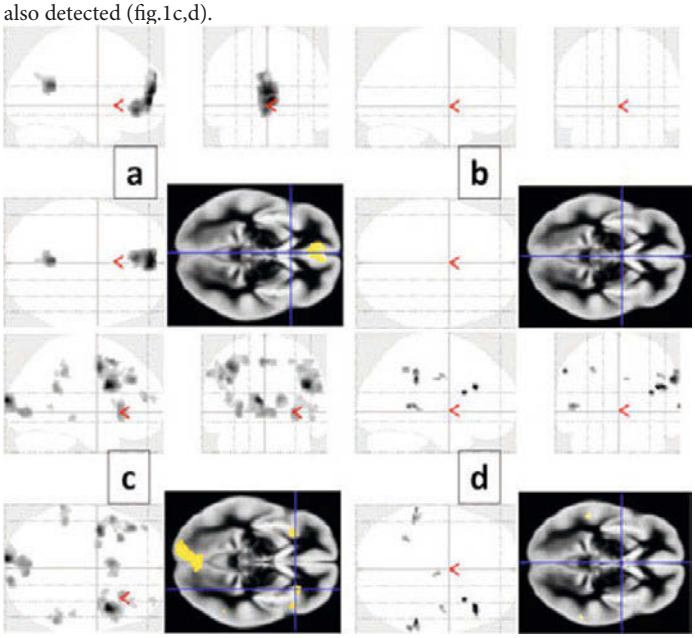

Fig1: Activation in controls (a,c) and patients (b,d) when B>A (a,b) and A>B (c,d).
Discussion/Conclusion: Patients with FES did not activate midline cortical structures during the self-reference experiment. The functional disturbance of this area may be the pathophysiological basis of the schizophrenia.
Supported by MH CZ - DRO („Institute for Clinical and Experimental Medicine – IKEM, IN 00023001") and IGA-MZCR-NT14291.
References:
(1) van der Meer L, 2010, Neurosci Biobehav Rev;34(6):935-46.

659
Spectral analysis of gyrification (SPANGY) in the developing brain

H. Angleys[1], D. Germanaud[2], F. Leroy[1], L. Hertz-Pannier[2], J.-F. Mangin[3], F. Lazeyras[4], P.S. Hüppi[5], J. Lefèvre[6], **J. Dubois**[1]
[1]Cognitive Neuroimaging Unit, INSERM-CEA, Gif-sur-Yvette/FRANCE, [2]Laboratory of Clinical Research, CEA, Gif-sur-Yvette/FRANCE, [3]Neurocomputing Laboratory, CEA, Gif-sur-Yvette/FRANCE, [4]CIBM, Geneva University Hospitals, Geneva/SWITZERLAND, [5]Department of Pediatrics, Geneva University Hospitals, Geneva/SWITZERLAND, [6]LSIS, University of Aix-Marseille, Marseille/FRANCE

Purpose/Introduction: In the developing human brain, the formation of cortical sulci is a complex process relying on the successive appearance of primary (from 14 weeks of gestational age GA), secondary (from 32w) and tertiary folds (from 39w) [1]. Recently, this progression has been finely described in preterm newborns using MRI [2]. Although folding indices have enabled to quantify the global gyrification intensity, there is still no quantitative and fully objective assessment of the timing of folds appearance along the developmental sequence in a single newborn.
In this context, we evaluated the potential of an original methodology of spectral analysis of gyrification (SPANGY) [3], which aims at quantifying the spatial frequency structure of the cortical folding pattern (CFP). In the adult brain, the CFP was transformed into a seven-frequency-band spectrum (B0-6), and the sulci were further segmented according to their frequency compound, the elements of sulci associated with B4, B5 and B6 matching with primary, secondary and tertiary folds. Here this methodology was tested over a developmental range crucial for folding.
Subjects and Methods: We studied 27 healthy preterm newborns (GA 26.7-35.7w) and 10 newborns at term (GA 37.8-40.5w). T2-weighted images were acquired with high spatial resolution at 1.5T and 3T MRI respectively. The interface between cortex and white matter was segmented using dedicated procedures [2, 4], and SPANGY analysis was performed on the mesh curvature using a dedicated Fourier-like analysis [3].
Results: The total spectral power increased with brain size (Figure 1a), and power distribution among bands differed between the two groups (Figure 1b): preterms showed immature spectrums compared with term newborns and adults [3] (higher relative powers for B4, lower relative powers for B6). CFP segmentation further provided a reproducible delineation of the folding regions across newborns (Figure 2): B4 elements were present in all newborns, with similar spatial localization in main and earliest folds, whereas B5 then B6 elements were increasing with age as branches and dimples. These preliminary results supported the hypothesis that spectrally-defined elements of sulci can be used as descriptors of the developmentally-defined folds.

Figure 1

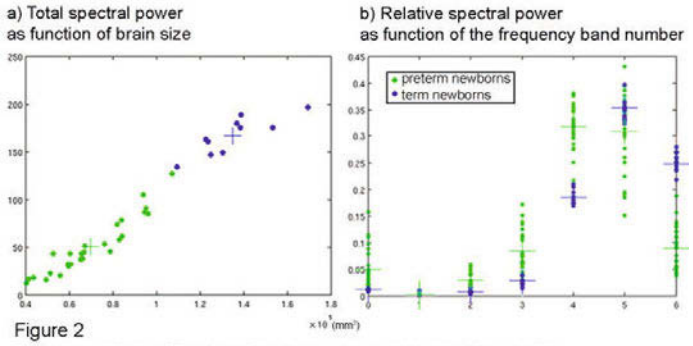

Figure 2

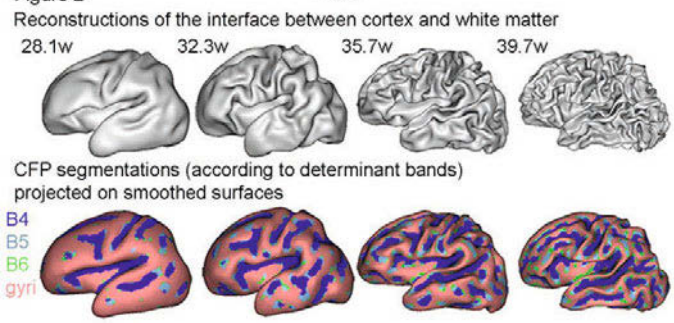

Discussion/Conclusion: SPANGY seems promising to characterize the developing folding pattern and quantify its progression. However further testing is required for full validation in newborns and during early development, for instance through longitudinal data of preterms.

References:

[1]: Chi et al. Ann Neurol 1977, 1:86-93.
[2]: Dubois et al. Cerebral Cortex 2008, 18:1444-1454.
[3]: Germanaud et al. NeuroImage 2012, 63:12571272.
[4]: Leroy et al. Plos One, 2011. 6(11): e27128.

660

Comparison of quantitative MRI parameters in the developing white matter bundles

S. Kulikova[1], L. Hertz-Pannier[1], G. Dehaene-Lambertz[2], C. Poupon[3], J. Dubois[2]
[1]Neurospin/UNIACT/UMR663, CEA-Saclay, Gif-sur-Yvette/FRANCE, [2]Neurospin/UNICOG, CEA-Saclay, Gif-sur-Yvette/FRANCE, [3]Neurospin/UNIRS, CEA-Saclay, Gif-sur-Yvette/FRANCE

Purpose/Introduction: Maturation of the white matter is a complex process, which includes several stages: fiber organization into bundles, proliferation of cells and organites, and "true" axonal myelination. These maturational processes have different impacts on quantitative MRI parameters, which are thus expected to show different dynamics according to developmental stages [1,2]. At the same time, post-mortem studies have shown that maturation is an asynchronous process [3,4], which occurs over different time periods and at different rates across different bundles. Here we describe this variability across bundles in terms of correlations between six MRI parameters: relaxation times (qT1, qT2); fractional anisotropy (FA), mean (<D>), longitudinal and perpendicular diffusivities (λ//, λ⊥), computed from diffusion tensor imaging (DTI).

Subjects and Methods: MRI data was acquired in 17 healthy infants (3-21 weeks) and 7 adults (used as a reference, mean age: 22.4±1.6 years) on a 3T MRI system (EPI, 1.8mm isotropic spatial resolution; for DTI: b=700s.mm^{-2}, 30 directions) [5]. 13 white matter bundles were reconstructed 13 white matter bundles were reconstructed using the regularized streamline tractography of Connectomist [6,7]. MRI parameters were computed (see maps Fig.1), averaged over each bundle and normalized by the corresponding mean adult values.

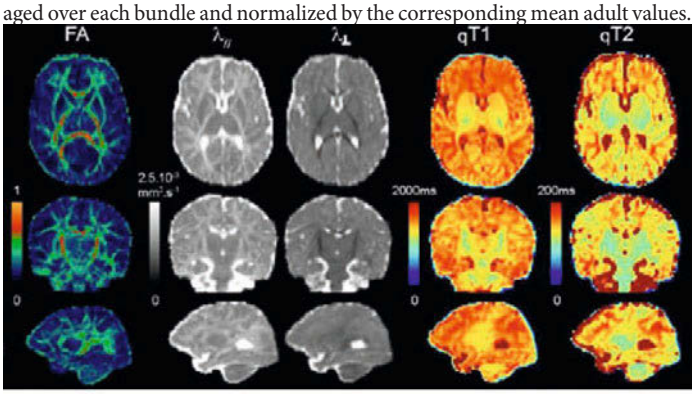

Fig.1 Quantitative maps of the MRI parameters in a 6-week-old infant

After eliminating age effects by linear regressions, correlations between parameters were computed for each bundle over the infant group and the resulting coefficients were used for bundle clustering.

Results: As expected, FA increased with age contrasting with a decrease in the other parameters across all bundles; however, the rate of these changes and the correlations between the parameters were different across the bundles. Clustering analysis showed that bundles could be separated into several groups (Fig.2).

Fig.2 Groups of bundles revealed by the clustering analysis based on the correlation between the MRI parameters

Abbreviations: CST(inf, mid, sup) - inferior, middle and superior parts of the cortico-spinal tract, STT - spino-thalamic tract, OR - optic radiations, ALIC - anterior limb of the internal capsule, EC – external capsule, AF - arcuate fasciculus, SLF and ILF - superior and inferior longitudinal fascicles, UF - uncinate fasciculus, FOF - fronto-occipital fasciculus, FX - fornix, CG(inf, sup) - inferior and superior parts of the cingulum, CC(g,b,s) – genu, body and splenium of the corpus callosum.

Certain correlations were shared by all clusters (<D>-λ⊥ and <D>-qT2), certain were bundle-specific (e.g. qT1-qT2 for the 2nd cluster) and others were not consistent in any of the clusters (e.g. <D>-qT1) (Tab.1). These variations may be related to both differences in the maturational stages and in the macrostructrural bundle organization.

cluster number	1	2	3	4
<D>-λ⊥, <D>-qT2	v	v	v	v
<D>-λ//	v	v	v	
λ⊥-qT2		v	v	v
FA-λ⊥	v			v
FA-λ//				v
λ// -λ⊥, λ// -qT2, qT1-qT2		v		
FA-<D>	v			
qT1 - λ//, qT1 - λ⊥, qT1 - <D>, qT1 - FA, qT2 - FA				

Tab.1 Consistent positive (v) and negative (v) correlations between parameters for each bundle group.

Discussion/Conclusion: Correlations of the MRI parameters can be used to describe complex and asynchronous maturational processes in the white matter, evaluate and group bundles according to their maturational stages. Similar evaluation over adult bundles is required to characterize the variability related to macrostructure.

References:

1. Dubois et al. (2008)
2. Deoni et al. (2005)
3. Dubois et al. (ISMRM, 2010)
4. Yakovlev, Lecours (1967)
5. Flechsig (1920)
6. Kulikova et al. (ESMRMB, 2013)
7. Duclap et al. (ESMRMB, 2012)

* This work was supported by ELA Foundation

661

The relation between EPI sequence parameters and electroencephalographic data during simultaneous EEG-fMRI registration: an initial report.

M. Rusiniak, T. Wolak, M. Lewandowska, K. Cieśla, H. Skarżyński
Bioimaging Research Center, World Hearing Center of The Institute of Physiology and Pathology of Hearing, Warsaw/POLAND

Purpose/Introduction: Simultaneous EEG-fMRI registration has been performed around the globe for over 15 years[1]. Numerous methods have been proposed for MRI gradient artifact correction (cf. [2], [3]). Additionally, some authors have shown that even simple modifications, such as moving the subject a few cm down in the scanner (shifting the magnetic isocentre) can improve data quality [4]. At the same time, there is still lack of knowledge about how the parameters of the fMRI sequence affect the properties of the artifact and how it is affected by filtration methods. Such an investigation is the focus of this work.

Subjects and Methods: The study was conducted at the Bioimaging Research Center of the World Hearing Center, using a Siemens 3T Magnetom Trio Tim MR scanner and a 64-electrode EEG Neuroscan system. A phantom with ensured electrical signal propagation was placed in the scanner. Electrodes selected from the 64-channel EEG cap for the experiment were: AFZ(ground), CPZ(reference), CZ and T8.

The EPI sequence was continuous scanning with following parameters: TR=2.5/2.7/3.0s, TE=23,30,40ms, number of slices=37,42,47, bandwidth=1086,1532,2368Hz/px, matrix size=54x54,72x72,96x96 voxels.

EEG data was registered with 10kHz sampling in DC-1kHz band. Twenty epochs of artifact occurrence have been averaged for FFT analysis.

Results: The main artifact frequency and harmonic frequencies were visible in the waveform spectrum. Further analysis was limited to F0 and two harmonic components, since these typically cover full EEG band (i.e. DC-50Hz). A combination of parameters and its influence have been shown in figure 1. It can be noticed that the number of slices and TR affect the frequency of the artifact waveform to the highest extent. Moreover, the interaction effect of the two factors can be described in an equation: fx=(x+1)*NS/TR, where fx is the harmonic frequency, x is the harmonic number, NS represents the number of slices, and TR stands for–Time of Repetition.

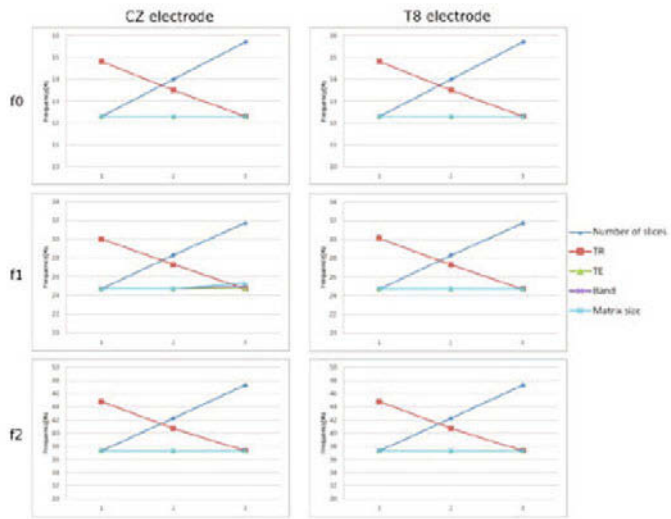

Discussion/Conclusion: In the presented study it has been shown that some parameters significantly affect the waveform of the gradient artifact induced by the MRI scanner. A specific number of slices and TR according to the given equation can be set, so that the frequencies of the artifact stay in the outrange of particular EEG signal frequency. Further work will be performed to investigate how this relates to typical artifact reduction methods and to electrode spatial location.

Supported by NSC grant no.UMO-2011/01/N/NZ4/04985

References:

[1]Laufs H.,2012,Neuroimage,pp.1056-1067
[2]Ritter P.,2007,*Magn.Reson.Imaging*,pp.923–932
[3]Yan W.X.,2009,*NeuroImage*,pp.459–471
[4]Rice J.K.,2013,*NeuroImage*,pp.476–484.

Clinical Review Poster

Clinical body, MSK and cardiac MRI

662

Repeatability and variability of ADC measurements in breast fibroglandular tissue in healthy volunteers

M.L. Nogueira[1], S. Brandão[2], E. Matos[3], R.G. Nunes[4], H.A. Ferreira[4], J. Loureiro[2], I. Ramos[2]
[1]Radiology, School of Health Technology of Porto/Polytechnic Institute of Porto, Vila Nova de Gaia/PORTUGAL, [2]Radiology, Hospital São João, Porto/PORTUGAL, [3]Department of Health Community, Institute of Biomedical Sciences Abel Salazar (ICBAS), University of Porto, Porto/PORTUGAL, [4]IBEB, Faculty of Sciences, University of Lisbon, Lisboa/PORTUGAL

Introduction: Diffusion weighted imaging (DWI) is increasingly in use in breast oncologic imaging (1). To be clinically effective, particularly when consecutive magnetic resonance (MR) examinations are performed, Apparent Diffusion Coefficient (ADC) measurements must be reliable and precise (2). To understand the magnitude of change that can be detected between examinations, it is important to know the measurement precision (3). Also, it may be relevant to assess if there are differences in repeatability between two of the most used fat suppression techniques: Short Tau Inversion Recovery (STIR) and Spectrally Attenuated Inversion Recovery (SPAIR).
Cases: Thirty-six healthy volunteers with no history of breast disease were recruited. They performed MRI at 3T, including T2w-FSE-STIR and DWI single-shot spin-echo eco planar imaging (SS-SE-EPI) with two fat suppression techniques (DWI-STIR and DWI-SPAIR) using b-values 50 and 1000 s/mm^2. These pulse sequences were performed twice in the same week to test repeatability of the ADC values. Circular regions-of-interest (ROI) with 10 mm^2 were drawn in the normal fibroglandular tissue.
For DWI- SPAIR, there were significant differences in the mean ADC values between the two measurements (p=0.03). Comparison between DWI techniques showed that, for the two measurements, the mean ADC in DWI-STIR was significantly higher than that of DWI-SPAIR (1.791×10^{-3} mm^2/s and 1.708×10^{-3} mm^2/s, respectively; (p=0.012) for the first; and 1.782×10^{-3} mm^2/s and 1.700×10^{-3} mm^2/s, respectively; (p=0.008) for the second one). Intraclass Correlation Coefficients between the measurements were 0.995 for DWI-STIR and 0.998 for DWI-SPAIR, and between techniques 0.867 and 0.878 for the first and second measurements, respectively.
Discussion: The repeatability of the ADC measurements was good for both techniques, which means that both seem to be accurate for repeated measurements in case of follow-up when monitoring the effect of neoadjuvant chemotherapy.
References:
(1) Padhani A, Koh DM. (2011) Magn Reson Imaging Clin N AM, 19:181-209
(2) O'Flynn E, Morgan V, Giles S, Souza N. (2012) Eur Radiol, 22:1512-1518
(3) Braithwaite A, Dale B, Boll D, Merkle E. (2009) Radiology, 250, 2:459-465

663

Added value of sacral coronal sequences in routine MRI of the lumbar spine

T. Bartalena[1], M.F. Rinaldi[2], E. Pravatà[3], A. Cianfoni[3], E. Rimondi[4], G. Rossi[5], L. Bartalena[6], D. Bartalena[1]
[1]Radiologia, Poliambulatorio Privato Zappi Bartalena, Imola/ITALY, [2]Radiologia, Policlinico S.Orsola-Malpighi, Bologna/ITALY, [3]Neuroradiology, Neurocenter of Italian Switzerland, Lugano/SWITZERLAND, [4]Radiologia Diagnostica e Interventistica, Istituto Ortopedico Rizzoli, Bologna/ITALY, [5]Radiologia Interventistica Angiografica, Istituto Ortopedico Rizzoli, Bologna/ITALY, [6]Facoltà di Medicina e Chirurgia, Università degli Studi di Bologna, Bologna/ITALY

Introduction:
In many imaging centers, lumbar spine MR protocols are frequently limited to sagittal and axial scan of the spine and intervertebral disk spaces with no dedicated imaging of the sacrum and of the sacroiliac joints. In our institution, dedicated coronal oblique series of the sacrum consisting of STIR, TSE T1 and VIBE T1 sequences are integral part of any routine L-spine MR examination. Optimization of technical parameters and use of parallel imaging makes possible to acquire all 3 sequence in less than 2 minutes.
Cases: We present a selection of cases showing that a wide spectrum of sacral pathologies may be disclosed by sacral coronal oblique sequences. We encountered insufficiency fractures in the elderly, stress fractures in athletes, arthritic disorders such as ankylosing spondylitis and osteoarthritis, sacral bone malformations and nerve roots tumors whose symptoms mimicked low back pain which could not be explained by findings in the lumbar spine. Most of these findings were not completely visible on sagittal images of the lumbar spine and some of those were depicted on dedicated sacral images only.
Discussion:
Optimized coronal oblique sequences can be used to image the sacrum with limited impact on overall imaging time. The additional informations that can be obtained are important in several patients and may disclose the real cause of low back pain in otherwise negative lumbar spine examinations.
References:
Diel J, Ortiz O, Losada RA, Price DB, Hayt MW, Katz DS.
Radiographics. 2001;21:83-104.
Gleeson TG, O'Connell MJ, Duke D, Ryan M, Ennis R, Eustace SJ.
Emerg Radiol. 2005;12:38-43.
Peh WC, Koh WL, Kwek JW, Htoo MM, Tan PH.
Australas Radiol. 2007;51:507-515.
Lyders EM, Whitlow CT, Baker MD, Morris PP.
AJNR Am J Neuroradiol. 2010;31:201-110.

664

Pelvic floor evaluation: what does imaging bring to computational models in urogynecology research?

S. Brandão[1], T. Roza[2], I. Ramos[1], T. Mascarenhas[3], R. Natal Jorge[2]
[1]Radiology, CHSJ-EPE, Oporto/PORTUGAL, [2]IDMEC, FEUP, Oporto/PORTUGAL, [3]Gynecology|Obstetrics, CHSJ-EPE, Oporto/PORTUGAL

Introduction: Computational and biomechanical studies help to better explain the overall model of pelvic floor dysfunction, often associated to muscle, nerve and connective tissue damage, which affect pelvic organ support[1].
Computational models based on imaging tecniques, namely MRI and US, have brought important insights about the pelvic functional anatomy[2].
The purpose of this work was to perform a review of the main inputs of the imaging techniques to the understanding of pelvic floor dysfunction, through biomechanical models.

Cases: Medline search was conducted for citations using mesh terms, including "pelvic floor imaging", "computational models pelvic floor", "biomechanical models pelvic floor", "pelvic floor modeling", "levator ani modeling", "pelvic model MRI", "pelvic model US", "pelvic floor biomechanics". Relevant publications were selected. One hundred and sixty articles were retrieved, from which 62 were excluded because they were redundant, not adjusted, or the fulltext wasn´t available. Ninety-eight papers were evaluated.
Discussion: Besides their clinical application, MRI and US are also useful for pelvic modeling. They allow a more exact understanding of the pelvic cavity physiology by performing biomechanical simulations of (individual) image datasets. Static images have been used as inputs to these models, as they allow assessing muscle and ligament positioning, alignment and thickness. Pelvic floor muscles subdivisions can be seen and segmented on the multiplanar images to perform computational simulations that simulate active and passive contraction forces and their impact to pressure distribution in the pelvic cavity. Dynamic acquisitions enable to measure the positioning and width of these structures when subjected to increased pressure to be compared with the results from biomechanical simulations. 3D and 4D US are important tools to perform this evaluation with a cheaper and easy-to-use technique.
Subtle anatomy of normal or ruptured ligament or muscle are often seen when high-resolution images are used. But there is still the ambition of more detailed description of the anatomy and interaction between the fascia and its bony, muscle or ligamentous insertions. In fact, this is a very relevant issue for the numerical simulations, since the boundary conditions often do not consider all the insertion points.
Finally, Diffusion Tensor Imaging with fiber tractography post-processing has brought a new level of anatomical detail due to its ability to depict muscle fiber direction.
In conclusion, the imaging techniques offer important data to improve the computational methodologies for pelvic cavity biomechanical modeling.
References:
[1]Ann N Y Acad Sci. 2007;1101:266-296
[2]Best Pract Res Clin Gastroenterol. 2009;23(4):487-503.

665

Klippel-Feil Syndrome and Sprengel Deformity: Clinical aspects and a MRI pictorial review

D.R.J.D. Nascimento[1, 2], M.R. Matos[2], R. Jogo[2], A.P. Petinga[2], J. Furtado[2], P.P. Mendes[2], A. Nunes[2], E. Soares[2]
[1]Serviço de Radiologia, Serviço de Saúde da Região Autónoma da Madeira, Funchal/PORTUGAL, [2]Serviço de Radiologia- Hospital Dona Estefânia, Centro Hospitalar de Lisboa Central, Lisboa/PORTUGAL

Introduction: Klippel-Feil syndrome (KF) is a complex heterogenous entity resulting in congenital cervical vertebral fusion.
It can be associated with a wide range of multisystemic anomalies. A particular one is the Sprengel deformity.
We intend to review the etiology, manifestations (with particular focus on MRI), management and prognosis of these disorders.
Cases: The most prominent, important and diagnostic feactures (such as fusion of vertebral bodies and high riding scapula) and other findings, (such as scholiosis and abnormal orientation of the scapula) will be demonstrated using MRI.
Discussion: KF is a complex heterogenous entity that results in congenital cervical vertebral fusion.
It is believed to result from faulty segmentation along the embryo's developing axis. Mutations of genes coding proteins involved in regulating growth and maturation of bone and cartilage are involved.
Numerous associated abnormalities may be present: vertebral malformations, Sprengel's deformity, torticollis, pterygium colli, genitourinary, pulmonary system and cardiovascular malformations.
Sprengel's deformity is also a complex congenital skeletal abnormality. One or both shoulder blades sit higher on the back than normally (most commonly on the left). This is the result of failure of descent of the scapula during gestation. It is also usually associated to changes in axial rotation, shape, and size of scapula and involves regional muscle hypoplasia/atrophy, which limit shoulder movement.
Sometimes an omovertebral bone connecting the elevated scapula and one of the cervical vertebrae can be present.
KF's treatment is symptomatic and includes physical therapy. Surgery may be needed to relieve cervical or craniocervical instability and constriction of the spinal cord and to correct scoliosis. If Sprengel's deformity is associated, the high scapula may be surgically restored to its normal position.
The prognosis for most KF individuals is good if treated early. If not, it can even be fatal.
References:
- Mahiroğullari M,et al: Klippel-Feil syndrome and associated congenital abnormalities: Evaluation of 23 cases. Acta Orthop Traumatol Turc. 40:234–9, 2006
- Ye M. et al Mutation of the bone morphogenetic protein GDF3 causes ocular and skeletal anomalies. Hum Mol Genet. 19(2):287-98, 2009
- Kerckhoven M.F., Fabry G.: The Klippel-Feil syndrome: a constellation of deformities. Acta Orthop Belg. 55(2):107-18
- Cavendish, L. (1972) Congenital Elevation of the scapula. J Bone Joint Surg Br vol. 54-B no. 3 395-408, 1989
- Cavendish, M.E.; Patwardhan (2009) Anomalies of Shoulder. Textbook of Orthopaedics and Trauma Volume 3; 2553
- Kadavkolan, A.S. et al (2011) Sprengel's deformity of the shoulder: Current perspectives in management. Int J Shoulder Surg. Jan-Mar; 5(1): 1–8

666

Clinical aspects and a MRI pictorial review of Proteus syndrome

D.R.J.D. Nascimento[1, 2], P.P. Mendes[2], R. Jogo[2], M.R. Matos[2], A.P. Petinga[2], E. Soares[2]
[1]Serviço de Radiologia, Serviço de Saúde da Região Autónoma da Madeira, Funchal/PORTUGAL, [2]Serviço de Radiologia- Hospital Dona Estefânia, Centro Hospitalar de Lisboa Central, Lisboa/PORTUGAL

Introduction: Proteus syndrome (PS) is a rare congenital and multisystemic condition. It has a wide spectrum of manifestations, such as skin overgrowth and atypical bone development. Its name is related to its unpredictable asymmetric gigantism/hemi-hypertrophy.
We intend to present diagnostic criteria, discuss the clinical and MRI aspects, management and prognosis of this disorder.
Cases: Imaging features are unspecific. However, PS is mentioned when there is hemimegalencephaly, extensive lymphangitic or vascular malformations and asymmetric hemi-hypertrophy.These will be demonstrated using MRI iconography.
Discussion: PS is suspected to be a genetic condition.
It primarily manifests as postnatal overgrowth, wich is irregular, almost always asymetric and rapidly progressive.
Most patients are born without significant asymmetry. The asymmetric overgrowth starts in 6–18 months of age. Its rate is such that affected body parts rapidly become disproportionate. This can involve limbs, vertebrae and calvarial bones. Progression usually stops after adolescence.
All patients with PS manifest the phenotype in a patchy pattern. The location of the manifestations varies remarkably among the patients.

Although bone, connective tissue and fat of the extremities are the most commonly involved tissues, there can be overgrowth of the central nervous system, spleen, thymus, colon and other tissues.
Radiographic features are unspecific. However, characteristically, Proteus syndrome is mentionned when there is hemimegalencephaly, extensive lymphangitic or vascular malformations and asymmetric hemi-hypertrophy.
Differential diagnosis is mostly done in a clinical basis, since most of the manifestations are not specific. It includes Klippel-Trénaunay syndrome, Type 1 Neurofibromatosis, Epidermal naevus syndrome, Encephalocraniocutaneous lipomatosis and Maffucci syndrome/Ollier disease.
The management of patients with PS is challenging. Treatment involves multiple orthopedic procedures over years to decades to control the assymetric growth. In spite of aggressive treatment, patients can suffer severe functional and physical consequences.
A common cause of death in PS is deep venous thrombosis and pulmonary embolism, even in young children. All patients should be considered for anticoagulant prophylaxis perioperatively. This, however, can be difficult to implement because patients with PS may have vascular anomalies.
References:
- Jamis-dow CA, Turner J, Biesecker LG et-al. Radiologic manifestations of Proteus syndrome. Radiographics. 24 (4): 1051-68.
- Kaduthodil MJ, Prasad DS, Lowe AS et-al. Imaging manifestations in Proteus syndrome: an unusual multisystem developmental disorder. 2012 Br Jr Rad
- Elsayes KM, Menias CO, Dillman JR et-al. Vascular malformation and hemangiomatosis syndromes: spectrum of imaging manifestations. AJR Am J Roentgenol. 2008;190
- Demir MK. Case 131: Proteus syndrome. Radiology. 2008;246 (3): 974-9.

667
Clinical and MRI features of Hemophilic Knee Arthropathy

D.R.J.D. Nascimento[1, 2], A. Ferreira[2], R. Jogo[2], M.R. Matos[2], J. Furtado[2], A.P. Petinga[2], E. Soares[2]
[1]Serviço de Radiologia, Serviço de Saúde da Região Autónoma da Madeira, Funchal/PORTUGAL, [2]Serviço de Radiologia- Hospital Dona Estefânia, Centro Hospitalar de Lisboa Central, Lisboa/PORTUGAL

Introduction: Haemophilia is an inherited X-linked recessive bleeding disorder.
70% of patients have the severe form of the disease, characterized by spontaneous haemorrhage (or following minor trauma). The most typical manifestation of hemophilia is hemarthrosis. Arthropathy almost always insues in large joints. We review the etiology and manifestations of the hemophilic arthopathy of the knee (the most commonly affected joint) and the importance of MRI and its findings. Management and prognosis are also considered.
Cases: Using Haemophilic patients' iconography, we intend to show MRI's ability for detection of early disease and showing relevant findings such as synovitis (synovial hypertrophy with increased contrast enhancement), joint effusion (with heterogeneous intra-articular content), cartilage loss, bony erosions with articular surface irregularities, widening and erosion of intercondylar notch, enlargement of distal femoral epiphysis, flattening of distal femoral condyles and subchondral sclerosis.
Symptoms such as swelling, soft tissue mass and marked local inflammation of the knee are frequent.
Discussion: With frequent hemarthrosis, synovial tissue may be unable to reabsorb the blood. To compensate, synovium will hypertrophy, resulting in chronic hemophilic synovitis (50%). This ultimately leads to sloughing of the hyaline cartlilage and secondary osteoarthritis.
Patients develop chronic joint deformities. There is marked synovial membrane hyperplasia, destruction of articular cartilage, and erosions of subchondral bone.
An abnormally increased vascularity around the epiphysis also occurs. This can cause growth disturbance with premature elongation of the bone. Overgrowth of the femoral condyles and of the patella leads to widening of the intercondylar notch, and appearance of squaring of patella's inferior pole.
Recurrent inflammation ultimately leads to premature closure of the physeal plates. This means that, once the patient reaches adulthood, an affected leg may be shorter. If the epiphyses close unevenly, joints may also develop deformities. Thus, it is important not only to avoid hemarthrosis, but also to manage it efficiently, in order to avoid the development of synovitis.
Hematological prophylactic treatment is the best way to avoid articular bleeds. In cases of well established arthropathy, sinovectomy is often necessary.
References:
- Rodriguez-Merchan EC. (1996) Effects of hemophilia on articulations of children and adults. Clin Orthop 328: 7-13.
- Greenspan, A. (2011) Orthopedic Imaging - A Practical Aproach. pg. 539,540
- Rodríguez-Merchán EC. (1997) Pathogenesis, early diagnosis, and prophylaxis for chronic hemophilic synovitis. Clin Orthop Relat Res. (343):6-11
- Kitonyi, G. W.; Kitonyi, J. M. (2009) Radiation Synovectomy: Treatment option for Haemophilia Patients with Chronic Haemarthrosis: A Review. East African Medical Journal Volume 86: S75-S79

668
Clinical and MRI features of Hepatoblastoma

D.R.J.D. Nascimento[1, 2], R. Jogo[1], E. Soares[1], A. Ferreira[1], A.P. Petinga[1], A. Nunes[1]
[1]Serviço de Radiologia- Hospital Dona Estefânia, Centro Hospitalar de Lisboa Central, Lisboa/PORTUGAL, [2]Serviço de Radiologia, Serviço de Saúde da Região Autónoma da Madeira, Funchal/PORTUGAL

Introduction: Hepatoblastoma is a rare neoplasm. Nevertheless, it is the most common primary malignant liver tumour in children under 4 years of age. The age distribution of disease in childhood is notable, with 68% of cases occurring in the first 2 years of life and 90% seen in patients younger than 5 years. It has an embryonic origin and can be composed of tissue resembling fetal liver cells, mature liver cells or bile duct cells.
This review discusses the clinical and MRI manifestations of these tumours. Management and prognosis are also considered.
Cases: Most children present with abdominal distension or an asymptomatic palpable abdominal mass. Other presenting symptoms include abdominal pain, anorexia, vomiting and jaundice.
Iconography and clinical data from cases of pathologically proven Hepatoblastomas show the importance and ability of MRI not only in providing superior definition of tumour margins but also in determining vessel involvement and adenopathies.
MRI also revealed well defined T1 hypointense lesions that can show heterogeneous enhancement. In T2 they are generally hyperintense. Usually seen as a heterogeneous mass, hepatoblastoma frequently has areas of necrosis and haemorrhage. Calcifications may be seen.
Discussion: Hepatoblastoma is an uncommon malignant liver neoplasm occurring in infants and children.
There are few know risk factors (genetic mutations and low birth weight).
Histological classification of hepatoblastoma is complicated, with multiple subtypes identified: epithelial (most common), undifferentiated small cell (worst prognosis) and mixed type.
The MRI appearance varies with the histologic nature. Epithelial type has a homogeneous appearance and is hypointense on T1 and hyperintense on T2. The mixed type is more heterogeneous, depending on the presence of necrosis, hemorrhage, fibrosis, calcification and fibrotic septae.

An important method for evaluation in hepatoblastoma is the determination of blood levels of Alpha-fetoprotein (AFP).
Infantile hemangioendothelioma, embryonal sarcoma, mesenchymal hamartoma and hepatocelular carcinoma are important differential diagnosis.
The overall survival rate is 65%–70%. Its major determinants are histology, local extension, vascular invasion and metastases. The AFP level parallels the course of the disease.
Surgical resection with neoadjuvant chemotherapy or liver transplantation can offer long term disease-free survival if complete ressection and absence of metastases.

References:

- Boechat MI, Kangarloo H, Ortega J. Primary liver tumors in children: comparison of CT and MR imaging. Radiology. Dec 1988;169(3):727-32
-Helmberger TK, Ros PR, Mergo PJ. Pediatric liver neoplasms: a radiologic-pathologic correlation. *Eur Radiol*. 1999;9(7):1339-47.
-Powers C, Ros PR, Stoupis C. Primary liver neoplasms: MR imaging with pathologic correlation. *Radiographics*. May 1994;14(3):459-82

669

Diffusion-weighted imaging in the characterization of superficial lymph nodes: effect of b-value

E. Cucci[1], S. Costanzo[2], L. Aquilani[1], S. Storti[3], G. Giordano[3], G. Sallustio[1]
[1]Radiology, Catholic University of Sacred Heart, Campobasso/ITALY, [2]Laboratory of Genetic and Environmental Epidemiology, Research Laboratories, Catholic University of Sacred Heart, Campobasso/ITALY, [3]Oncohaematology Unit, Catholic University of Sacred Heart, Campobasso/ITALY

Introduction: Technological advances have recently made it possible to obtain high-quality DW images also in extracranial compartments [1-3]. A 2012 meta-analysis documented that DW imaging is more sensitive than conventional MRI in detecting lymph nodes in patients with head and neck cancer [4]. However, there is still no single established b-value for DWI of lymph nodes. This study was undertaken to investigate the ability of DWI to differentiate malignant from benign lymph nodes using two different b-values, 600 s/mm^2 vs 1000 s/mm^2.
Cases: Purpose of our study was to evaluate the influence of b-value on apparent diffusion coefficient (ADC) - based differentiation of malignant from benign superficial lymph nodes.
From January to September 2011 were enrolled 21 subjects with enlarged superficial lymph nodes who underwent magnetic resonance imaging (MRI). MRI was performed with a 1.5 T unit with 33 mT/m gradient intensity. In all patients we acquired: short-tau inversion recovery (STIR) axial sequence; diffusion-weighted imaging (DWI) axial sequence with b-value of 0, 600 and 1,000 s/mm^2. Wilcoxon test was used for statistical analysis.
The mean ADC value of malignant was significantly lower than benign lymph nodes ($p<0.05$) for b-value 600 and 1,000 s/mm^2.
The best threshold value for differentiating malignant from benign lymph nodes was 0,917x10^{-3} mm^2/s with b-value 600 s/mm^2 and 0.93x10^{-3} mm^2/s with b-value 1,000 s/mm^2, obtaining a sensitivity and specificity of 80%. The area under the curve of ADC value was 0.800x10^{-3} mm^2/s with b-value 600 s/mm^2 and 0.823x10^{-3} mm^2/s with b-value 1000 s/mm^2. This difference was no significative.
Discussion:
Despite limitations due to sample size, these findings confirm the ability of DW-MRI to differentiate benign from malignant superficial lymph nodes and document that b-values of 600 s/mm^2 and 1000 s/mm^2 do not involve significant differences. However the non-optimal SE and SP values and the broad SD range associated with the mean ADC values of benign and malignant lymph nodes prevent the adoption of DW-MRI to replace pathological examination in clinical practice.

References:

1. Sumi M, Sakihama N, Sumi T et al (2003) AJNR Am J Neuroradiol 24:1627-1634
2. Sumi M, Van Cauteren M, Nakamura T (2006) AJR Am J Roentgenol 186:749-757
3. Abdel Razek AA, Soliman NY, Elkhamary S et al (2006) Eur Radiol 16:1468-1477
4. Wu LM, Liu MJ, Zhang XF et al (2012) Acad Radiol 19:331-340

670

Value of VIBE T1-weighted sequences with fat suppression for the diagnosis of lumbar spondylolysis.

T. Bartalena[1], M.F. Rinaldi[2], E. Pravatà[3], A. Cianfoni[3], E. Rimondi[4], G. Rossi[5], L. Bartalena[6], D. Bartalena[1]
[1]Radiologia, Poliambulatorio Privato Zappi Bartalena, Imola/ITALY, [2]Radiologia, Policlinico S.Orsola-Malpighi, Bologna/ITALY, [3]Neuroradiology, Neurocenter of Italian Switzerland, Lugano/SWITZERLAND, [4]Radiologia Diagnostica e Interventistica, Istituto Ortopedico Rizzoli, Bologna/ITALY, [5]Radiologia Interventistica Angiografica, Istituto Ortopedico Rizzoli, Bologna/ITALY, [6]Facoltà di Medicina e Chirurgia, Università degli Studi di Bologna, Bologna/ITALY

Introduction:
Spondylolysis represents a stress fracture of the pars interarticularis, encountered most frequently in adolescents at the L5 level with variable clinical manifestation, ranging from asymptomatic to spine instability, back pain, and radiculopathy. Imaging workup is usually performed with conventional radiography and multislice-CT, the latter being considered the gold standard diagnostic technique. MR is thought to be less sensitive than CT because of several pitfalls that may limit the visualization of the pars defect using traditional sequences. VIBE (volume interpolated breath-hold examination) is a T1-weighted sequence frequently used in liver imaging. We present a potential application of this sequence in lumbar spondylolysis MR imaging.
Cases:
A selection of cases of lumbar spondylolisthesis with and without spondylolysis studied with fat suppressed VIBE T1-weighted sequences is presented. Two different techniques can be used: 2D sagittal oblique (3 mm thickness) oriented parallel to each vertebral lamina and 3D isotropic sagittal (1 mm thickness) with further post-processing with multiplanar reconstructions. Fat suppression is obtained with water excitation (WE) in the 2D sequence and with spectral adiabatic inversion recover (SPAIR) in the 3D sequence. Acquisition time is 1 minute and 28 seconds for the 2D VIBE T1 WE sequence and 1 minute and 40 seconds for the 3D VIBE T1 SPAIR sequence during free breathing on a 1.5T magnet
Discussion:
VIBE T1-weighted sequences with fat suppression may be used to evaluate the pars interarticularis in cases of suspected spondylolysis in a limited amount of time. Conspicuity of pars defects is higher than traditional TSE or STIR sequences and a confident diagnosis of spondylolysis can be made on MRI similarly to CT but without using ionizing radiations. This is important because of this pathology frequently affect young patients.

References:

Leone A, Cianfoni A, Cerase A, Magarelli N, Bonomo L.
Skeletal Radiol. 2011 ;400:683-700.
Kobayashi A, Kobayashi T, Kato K, Higuchi H, Takagishi K.
Am J Sports Med. 2013 ;41:169-176.
Beck NA, Miller R, Baldwin K, Zhu X, Spiegel D, Drummond D, Sankar WN, Flynn JM.

J Bone Joint Surg Am. 2013 15;95:e651-657.
Miller R, Beck NA, Sampson NR, Zhu X, Flynn JM, Drummond D.
J Pediatr Orthop. 2013 ;33:282-2888.

671

MR-guided prostate intervention with a transperineal approach

B.M. Greenwood[1], J.J. Fütterer[2], A. Winkel[3]
[1]Clinical Product Management, Invivo, Pewaukee/UNITED STATES OF AMERICA, [2]Radiology, Radboud University Nijmegen Medical Centre, Nijmegen/NETHERLANDS, [3]Research and Development, Invivo-Germany, Schwerin/GERMANY

Introduction: Prostate MRI is an established method for targeting the prostate for intervention. Here we discuss the use of an MRI-compatible, flexible arm with a perineal plate for transperineal access.
The system consists of three components: a table fixture, an articulated arm and plug-in connection to snap the perineal plate onto the distal end of the arm. It is CT- and MR-compatible up to three Tesla. The articulated arm has three joints allowing flexible placement of the support arm in a desired position. A central knob allows all joints to be fixed and released quickly. The plug-in connection of the support arm allows it to hold different positioning systems for medical instrument insertion; here we use the perineal plate. The arm can be covered with a sterile drape and the plate is reusable and can be autoclaved.
Cases: Four patients with biopsy proven locally recurrent prostate cancer without evidence for distant metastases were treated under general anesthesia in a 3 Tesla MR system. The transperineal plate, attached to a flexible arm (Fig. A, Fig. B) was placed against the perineum of the patient.

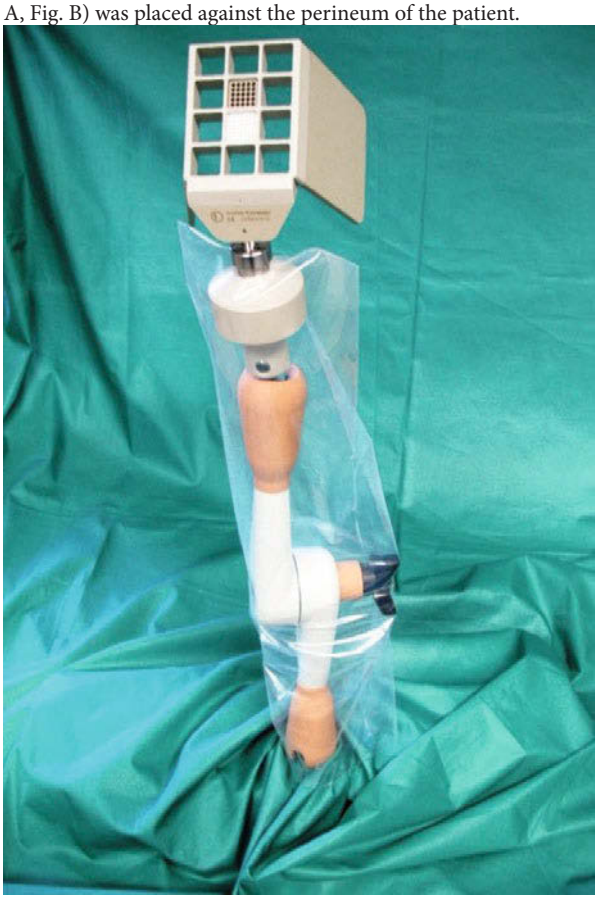

Fig. A

Fig. B
A Foley catheter was inserted in the urethra. Cryoneedles (IceSeed, Galil Medical, Yokneam, Israel) were inserted with real-time MR imaging. The bladder catheter was changed by a urethral warmer and a rectal warmer was inserted in the rectum. Both were continuously flushed with warm water (43 degrees Celsius) to protect the urethra and the rectum from freezing. Iceball growth was continuously monitored under real-time MR image guidance. Two freeze- and thaw cycles were performed. One day after the procedure a multi-parametric MRI was acquired to evaluate treatment. The patients with locally recurrent prostate cancer were successfully focally treated with MR-guided cryoablation. No complications were recorded during or after the procedure. The rectal wall was intact and patients reported no bleeding out of the urethra of rectum.
Discussion: This method is well tolerated by patients and provides an alternative approach in patients unable to undergo a transrectally delivered, MRI-guided procedure such as biopsy or focal therapy delivery.
References:
Shinohara K, Gulati M, Koppie TM, et al. Transperineal prostate biopsy after abdominoperineal resection. J Urol 2003;169:141-144.
Schwab SA, Kuefner MA, Adamietz B, et al. MRI-guided biopsy of the prostate in the supine position - introduction of a simplified technique using a large-bore magnet system. Eur Radiol 2013;23:1415-1419.
Yacoub JH, Verma S, Moulton JS, et al. Imaging-guided prostate biopsy: conventional and emerging techniques. RadioGraphics 2012;32:819-837.

672

USPIO vs. stealh magnetic liposomes (sML) enhanced atherosclerotic plaque MRI

P. Opriessnig[1], G. Almer[2], C. Vonach[3], R. Prassl[3], H. Mangge[2], R. Stollberger[1]
[1]Institute of Medical Engineering, Graz University of Technology, Graz/AUSTRIA, [2]Clinical Institute for Medical and Chemical Laboratory Diagnosis, Medical University of Graz, Graz/AUSTRIA, [3]Institute of Biophysics, Medical University of Graz, Graz/AUSTRIA

Introduction: One class of MR contrast agents are iron oxide probes. Successful performed *in vivo* measurements of activated macrophages particular mark USPIOs as surrogate marker for plaque inflammation [1]. To overcome limitations of passive targeting these probes can be functionalized for biomarker targeted imaging (VCAM-1 [2]). Another strategy is the coating of USPIOs by a PEGylated lipid bilayer to evade the reticuloendothelial system [3]. These stealth magnetic liposomes (sML) enable higher payloads of iron oxide cores,

the attachment of various functional groups for targeting molecules and the substitution of the imaging core by a drug for therapeutic purposes [4]. The aim of this preliminary investigation was to evaluate the temporal dependence of signal changes at post USPIO/sML infusion times in the aortic wall of western diet (WD) or normal chow fed NZWs.

Cases: Rabbits underwent baseline- and 24/48/144h or 56/144h post-contrast measurements of the thoracic aorta on a human 3Tesla platform. Doses of 25-35µmolFe/kg body weight (n=2) were administered intravenously. A power function [5] ($s(t)=C*t^{\alpha}*e^{-\beta*t}$) was used to fit quantitative T_2* relaxation time changes (rT_2*) of rabbit vessel walls at post-CA infusion times (*Fig.1 blue line*). The time of maximal signal change (t_{max}) was 23/17/10/28h for A1/A2/B1/B2 respectively (*Fig.1*). To get further information on the CA clearance in the circulation an exponential function ($s(t) =C*e^{-\beta*t}$) was used to fit changes of relative signal intensities (rSI_{change}) in the lumen of the thoracic aorta at post-CA infusion times (*Fig.1 green line*). The elimination half-life ($t_{1/2}$) was 30/55/23/43h for A1/A2/B1/B2 respectively (*Fig.1*). Figure 2 shows the CA mediated wall signal change over time on pre- and post-infusion images and the obvious blood pool behavior of both nanoconstructs in the lumen.

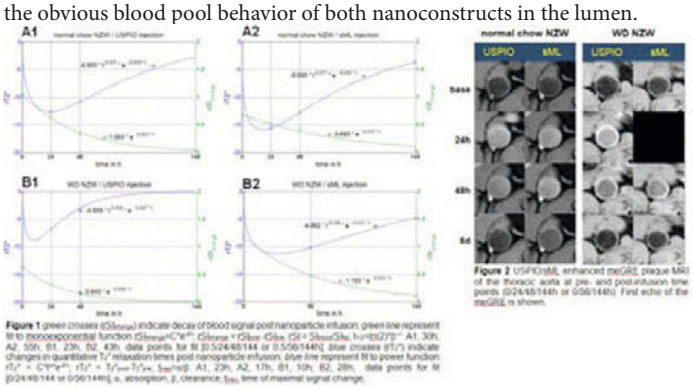

Figure 1 green crosses (rSI_{change}) indicate decay of blood signal post nanoparticle infusion, green line represent fit to monoexponential function ($rSI_{change}=C*e^{-\beta*t}$; $rSI_{change} = rSI_{max} * rSI_{max}*SI_{pre}$, $t_{1/2}=ln(2)/\beta$; A1, 30h; A2, 55h, 61, 23h, 52, 43h; data points for fit [0:24/48/144 or 0:56/144h]; blue crosses (rT_2^*) indicate changes in quantitative T_2^* relaxation times post nanoparticle infusion, blue line represent fit to power function $rT_2^* = C*e^{\alpha*t}$; $rT_2^* = T_2^*_{post}-T_2^*_{pre}$, $t_{max}=ln(\alpha)$; A1, 23h; A2, 17h, 81, 10h; 82, 28h; data points for fit [0:24/48/144 or 0:56/144h]; α, absorption; β, clearance; t_{max} time of maximal signal change.

Figure 2 USPIO/sML enhanced meGRE plaque MRI of the thoracic aorta at pre- and post-infusion time points (0:24/48/144h or 0:56/144h). First echo of the meGRE is shown.

Discussion: The $t_{1/2}$ analysis reveals blood pool behavior for both constructs, but this effect is much more pronounced for the sML's. The t_{max} analysis indicates the time of maximum wall signal drop and gives information on the appropriate imaging window. This time window coincides with the high particle concentration in the circulation and therefore a contribution of particles circulating in the *vasa vasorum* on the wall signal change cannot be excluded. For analyzing the uptake of particles in the wall it is mandatory to have no residual agent left in the circulation. Nevertheless, the prolonged time in the circulation makes the sML suitable for biomarker targeted imaging.

References: [1] Patterson AJ,2011,NMR Biomed,89-95; [2] Kelly KA,2005,Circ Res,327-336; [3] Frascione D,2012,Int J Nanomedicine,2349-59; [4] Soenen S,2009,Nanomedicine,177-91; [5] Tang TY,2009,Neuroradiology,457-65

673

Role of cardiac magnetic resonance in imaging non-ischemic cardiomyopathies of the left ventricle

R.G. Saru, M. Ouhlous, A. Moelker
Radiology, Erasmus MC, Rotterdam/NETHERLANDS

Introduction: The clinical presentation of non-ischemic cardiomyopathies of left ventricle may overlap.
With cardiac magnetic resonance (CMR) the various types of non-ischemic cardiomyopathy can be differentiated accurately, which may potentially obviate invasive testing and help to guide clinical treatment.
Cine-imaging of the heart, delayed-enhancement and T2*-weighted sequences are useful for analysing the CMR images.
This exhibit will provide tips and examples in order to make differential diagnosis between different types of non-ischemic cardiomyopathies.

Cases: Content organisation:
1. Imaging characterization of non-ischemic cardiomyopathies with CMR:
- classification
- image analysis methods
- diagnostic pitfalls

2. Clinical cases:
- Show examples of different types of non-ischemic cardiomyopathies of left ventricle visualised with CMR

Discussion:
The purpose of this educational poster is to describe imaging characteristics of various types of non-ischemic cardiomyopathies:
-genetic: hypertrophic cardiomyopathy, arritmogenic right ventricular cardiomyopathy, non-compaction cardiomyopathy;
-mixed: dilated cardiomyopathy;
-acquired: inflammatory cardiomyopathy (myocarditis), stress-provoked cardiomyopathy ("tako-tsubo").

References:
1. Barry J. et al, 2006, Circulation,113:1807-1816
2. D. Bluemke et al, Am J Roentgenol. 2010, 195(4): 935–940
3. M. H. Al-Mallah et al, Heart Fail Rev (2011) 16:369–380

674

Isotropic T2-weighted imaging of the spine with SPACE sequences: a pictorial review and post-processing tutorial.

T. Bartalena[1], M.F. Rinaldi[2], E. Pravatà[3], A. Cianfoni[3], E. Rimondi[4], G. Rossi[5], D. Bartalena[1]
[1]Radiologia, Poliambulatorio Privato Zappi Bartalena, Imola/ITALY, [2]Radiologia, Policlinico S.Orsola-Malpighi, Bologna/ITALY, [3]Neuroradiology, Neurocenter of Italian Switzerland, Lugano/SWITZERLAND, [4]Radiologia Diagnostica e Interventistica, Istituto Ortopedico Rizzoli, Bologna/ITALY, [5]Radiologia Interventistica Angiografica, Istituto Ortopedico Rizzoli, Bologna/ITALY

Introduction: SPACE (Sampling Perfection with Application-optimized Contrast with different flip-angle Evolutions) is a novel 3D FSE sequence that can be used for isotropic T2-weighted imaging of the spine. Source images may be further reprocessed in any plane using multiplanar reconstructions (MPR) and maximum intensity projections (MIP).
Cases: This pictorial review shows a selection of spine MRI studies performed with SPACE T2 sequences. The spectrum of pathologies and tips and trick about post-processing are explained. Images are acquired in the sagittal plane with isotropic resolution of 0.9 mm in the cervical spine and 1 mm in thoracolumbar tract. Total acquisition time is 2 minute and 48 second. Post-processing include axial and sagittal oblique MPRs, coronal curved MPRs and radial MIPs, and requires no longer than 2 minutes by experienced MRI technologists or radiologists.
Discussion: Axial MPRs allow evaluation of disc spaces with exquisite detail of nerve roots without CSF flow artifacts. Sagittal oblique MPRs allow assessment of the neuroforamina in the cervical spine and of the pars interarticularis in the lumbar tract in cases of suspected spondylolysis. Coronal and sagittal curved MPRs can be used to assess scoliosis and analyze nerve roots extraforaminal course. MIP myelography nicely depicts central canal stenosis. Due to the limited acquisition time and valuable amount of anatomical informations, isotropic SPACE T2 sequences can be proficiently included in routine MRI spine protocols.

References:
Meindl T, Wirth S, Weckbach S, Dietrich O, Reiser M, Schoenberg SO.
Eur Radiol. 2009; 19: 713-721.
Kwon JW, Yoon YC, Choi SH.
Clin Radiol. 2012; 67:106-113.

Naraghi A, White LM.
AJR. 2012; 199:W283-W293.
Tins B, MD, Cassar-Pullicino V, Haddaway M, Nachtrab U.
Br J Radiol. 2012; 85:480-489.

675

Interobservor variability of femoro-acetabular impingement (FAI) measurements in MRI hip arthrograms

A. Char, A. Sorani, S. Patel
Radiology, Royal Derby / Nottingham University Hospitals, Nottingham/ UNITED KINGDOM

Introduction:
Aim: To see whether objective measurements in assessing suspected FAI are reproducible and can improve accuracy of reporting MR hip arthrograms.
Background: Published literature suggests that using objective measurements in MR hip arthrograms in suspected FAI is useful. We wanted to ascertain whether those measurements were reproducible between 3 radiologists trained in musculoskeletal (MSK) radiology. The three radiologists were of differing levels of experience with one having just started MSK subspecialty , the second coming to the end of is training and the third a consultant with close to 2 years of subspecialty experience.
Methodology: Retrospective analysis of the radiology information system (CRIS) revealed 30 cases of MR hip arthrograms performed at Royal Derby Hospital between February 2012 to March 2013. These cases were analysed independently on PACS using the Alpha angle and acetabular depth as objective measurements. An abnormal angle was taken as >55 degrees and abnormal depth was any depth that was <0mm. Concordance for alpha angle was taken as anything more than 55 degrees but within a range of +/- 5 degrees. Similarly concordance for acetabular depth was taken as any negative measurement (less than 0mm).
Cases:
Alpha angle: >55 Degrees is abnormal.
Acetabular depth: Negative measurement due to over coverage.
Discussion:
Femoroacetabular (FAI) impingement occurs when there is excessive contact between the acetabular rim and the proximal femur. This can result in changes to the femoral neck, acetabulum and labrum. Ultimately cartilage damage and osteoarthritis can result if not treated.
Types: 2 types of FAI impingement can be identified. Cam type -abnormal shape at the femoral head-neck area which causes abutment on the acetabular rim and Pincer type where the abnormality is due to acetabular overcoverage.
Imaging: Over time both types of impingement can lead to labral degeneration, labral tears, ossification of the labrum paralabral cysts. Articular cartilage damage and subchondral osseous changes may occur in more severe cases. In addition to the above changes we were particularly interested in evaluating the utility of both alpha angle and acetabular depth measurements which help to diagnose Cam and Pincer type FAI respectively.
Conclusion: There was significant interobserver variability between the 3 radiologists. Although published literature suggests these measurements are useful, in our experience the high rate of interobserver variability precluded satisfactory reproducibility.
References:
August 2005 Radiology, 236,588-592.
September 2006 Radiology,240, 778-785.
The MRI Mentor: Volume 4, Number 6 – August 24, 2010

Clinical Review Poster

Clinical neuro MRI

676

WITHDRAWN

677

Case report of hidradenitis suppurativa: MRI features and review of the literature.

P.P. Arcuri[1], S. Roccia[2], A. Pingitore[3], V. Arcuri[4], G. Fodero[4]
[1]U.O. Radiology, A.O. Pugliese-Ciaccio, Catanzaro/ITALY, [2]INPS, INPS, Lamezia terme/ITALY, [3]Radiology dept, King's College Hospital NHS Foundation, London/UNITED KINGDOM, [4]A.O. Pugliese-Ciaccio, Radiology, Catanzaro/ITALY

Introduction: We describe a case of hidradenitis suppurativa in a 56-year-old woman with Crohn's disease, diagnosed by MRI and confirmed histologically. This disorder is rare; is a chronic disease manifest by recurrent abscesses, sinus tracts, and scarring.This disease typically affects the genitofemoral area in women or axillae in both sexes. It is also known as Verneuil's disease.Three previous cases are described in the radiology literature, with only two reports describing the MRI findings and only one describe the MRI features within the skin and subcutaneous tissues of the typical form. The imaging findings include marked thickening of the skin, induration of the subcutaneous tissues, and formation of multiple subcutaneous abscesses.
Cases: Our patient had Crohn's disease that was diagnosed 15 years earlier. She had multiple pus-filled lesions discharging into her groin.She was referred for MRI because of her history of Crohn's disease to evaluate for perineal abscess formation. MRI was performed on a 1.5-T scanner using the following sequences:coronal TSE T2, axial FFE T1, axial and sagittal STIR T2, axial and sagittal SPIR before and after contrast administration.MRI revealed thickening of the skin of the subcutaneous tissues of the perineum, and mons pubis, which were of low signal on T1 and high signal on T2 and STIR images. In addition, multiple small areas of low signal on T1 and of high signal on T2 and STIR images were shown in the subcutaneous tissues.After IV contrast administration, many of these small subcutaneous areas showed rim enhancement compatible with multiple abscesses.No communication with the bladder, urethra, or rectum was detected and the abscesses were distinctly remote from the rectum and anus.These findings are not compatible with the fistulous tracts associated with Crohn's disease.
Discussion: Perianal hidradenitis suppurativa mimics the presentation of Crohn's disease, anal fistula, pilonidal sinus, or perianal abscess. Crohn's disease and hidradenitis suppurativa may coexist, as in our patient, making diagnosis difficult. Because our patient did not have sinus tract formation extending to the bowel, distinguishing the cutaneous and subcutaneous manifestations of Crohn's disease from those of hidradenitis suppurativa was easier.
References:
Aine M. Kelly1 and Paul Cronin. MRI Features of Hidradenitis Suppurativa and Review of the Literature AJR. 2005;185:1201-1204.
Simpson RC, Dyer MJ, Entwisle J, Harman KE. Positron emission tomography features of hidradenitis suppurativa. Br J Radiol. 2011 Aug; 84(1004):e164-5.
Yazdanyar S, Miller IM, Jemec GB. Hidradenitis suppurativa and Crohn's disease: two cases that support an association. Acta Dermatovenerol Alp Panonica Adriat. 2010 Oct; 19(3):23-5.

678

MRI findings of an atypical course of herpes simplex encephalitis

L. Gubskiy[1], **D. Namestnikova**[1], A. Gazanchyan[2]
[1]Department of Fundamental and Clinical Neurology, The Russian National Research Medical University named after N.I.Pirogov, Moscow/RUSSIAN FEDERATION, [2]Department of Radiology, Russian Medical Academy of Postgraduate Education, Moscow/RUSSIAN FEDERATION

Introduction: Herpes simplex encephalitis (HSE) is a sporadic, necrotizing viral infection of the CNS caused by HSV-1/HSV-2. It is usually localized in temporal, frontal lobes and limbic regions. Typical clinical presentation includes flu-like illness, fever, headache, seizures, cognitive impairment, focal neurological signs [1]. HSE should be recognized as soon as possible because of its potentially high mortality [2]. Among with clinical examination and lumbal punction, MRI is the diagnostic modality of choice showing pathognomonic features of HSE. In our study we report a case of HSE with an atypical localization of brain lesions, MRI and clinical findings.
Cases: Woman 76 y/o long-suffering from arterial hypertension admitted to hospital with nausea, non-systemic dizziness, decreased and blurred vision, "rainbow" in front of the eyes. Six days before patient complained for headache, subfebrilitate, cough and weakness, which regressed rapidly without specific treatment. Month before she had pulpitis and teeth extraction, 14 years before – ischemic stroke with mild left-sided hemiparesis, 72 years before – unclear neural infection. On neurological examination the patient appeared horizontal nystagmus and mild left-sided pyramidal symptoms, no abnormalities in standard clinical and laboratory examination were found. CT and MRI (fig.1) of the brain were performed – lesions in the right occipital lobe were hypothesized as ischemic. Patient had been managed conservatively for vertebrobasilar stroke for several days. From 10th day of onset gradually began to appear double vision, headache, ataxia, dysarthria, disorientation and progressive depression of consciousness, hyperthermia, meningeal signs. MRI (fig.2) and lumbal punction were performed. CSF analysis showed lymphocytic pleocytosis, lower glucose concentrations and HSV-1,2 DNA detected by PCR. MRI findings have also allowed to suspect HSE, but with atypical localization. Due to prolonged acyclovir therapy with antibiotics clinical conditions began to improve. After 8 month the patient remained minimal neurological deficit in the form of reduced vision, left-sided hemianopia, mild left-sided hemiparesis and had a residual changes in the brain tissue (fig.3).

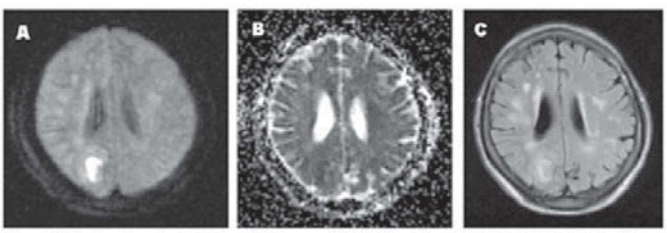

Figure 1. MR imaging performed on day 8 of illness. DWI shows very high signal intensity (so called "lightbulb sign") in the right occipital lobe (A). The region of increased DWI signal demonstrates low signal on ADC map (B), which is typical for true restricted diffusion, and hyperintensity on the FLAIR image (C). This appearance corresponds to cytotoxic edema being found in several conditions such as acute stroke and herpes encephalitis, however occipital lobe is not typical localization of latter one.

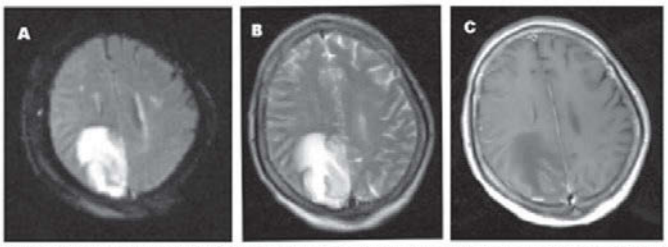

Figure 2. MR imaging performed on day 15 shows extension of the pathologic changes; heterogeneous increased signal on DWI (A) referes mainly to T2 shine-througt effect, T2/WI (B). Contrastenhanced T1 weighted images demonstrates meningeal and subtle intraparenchymal enhancing (c). On the basis of the MR imaging findings, examination of CSF a diagnosis of herpes encephalitis was considered.

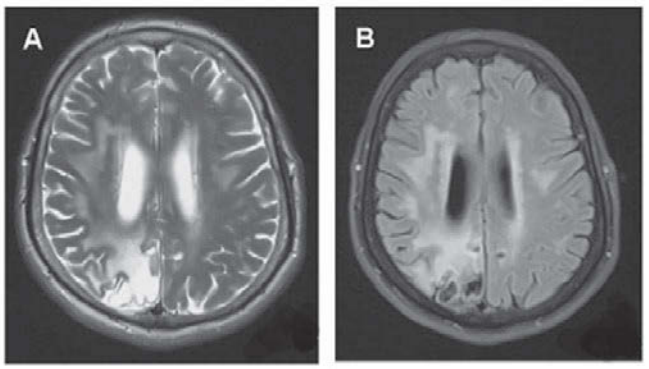

Figure 3. T2-weighted (A) and FLAIR (B) images performed after 8 months shows residual changes of brain tissue as cavitation and gliosis of the right occipital lobe.

Discussion: We presented a case report of HSE with atypical localization and clinical history, which was at first misdiagnosed as ischemic stroke. Physiological reasons for such localization is not completely clear, but may be related to increased permeability of the blood-brain barrier in this area (the effects of neural infection in childhood), and decreased immunoreactivity. MRI itself and its correlation between PCR and clinical finding made possible the correct diagnosis.

References:

[1]Gkrania-Klostas E., 2008, J Med Case Rep, 387-391; [2]Gurgone G., 2012, ACTA MEDICA MEDITERR, 25-28.

679

Processing Speed Relates to White Matter Integrity in Multiple Sclerosis

O. Rilo[1], **A. Cabrera Zubizarreta**[2], J.M. Ontaños Garcés[2], J. Peña[1], N. Ojeda[1], A. Antiguedad Zarranz[3], M. Mendibe Bilbao[4], N. Ibarretxe-Bilbao[1]

[1]Department of Methods and Experimental Psychology, Deusto University, Bilbao/SPAIN, [2]MR Unit Hospital Galdakao, OSATEK, Galdakao/SPAIN, [3]Neurology, Hospital Basurto, Bilbao/SPAIN, [4]Neurology, Hospital Cruces, Barakaldo/SPAIN

Introduction: Multiple sclerosis (MS) is associated with multiple and complex cognitive function impairments, but processing speed (PS) is considered as the main and most common cognitive deficit in this disorder. PS has been related to white matter (WM) integrity in MS, other neurodegenerative pathologies and in healthy aging in several brain areas. While results obtained in some studies point out influence of specific tracts in different brain areas, other studies sustain influence of whole-brain WM in PS. The aim of the study is to investigate relationship between performance on PS tasks and whole brain WM fractional anisotropy (FA).

Cases: We recruited 29 patients with MS (mean age=43). Participants were given an extensive battery of neuropsychological tests and a DTI on a Philips Achieva 3T. Total correct responses on the Symbol Digit Modalities test, Letter Portion of the Salthouse Perceptual Comparison Test, and Words and Colors Portions of the Stroop Color-Word Test were considered indicative of PS and were united in a composite score (α= .91). Whole-brain voxel-wise regression analysis of this composite score and cerebral WM FA data was performed controlling influence of gender and age using TBSS (Tract-Based Spatial Statistics) as implemented in FSL.

Discussion: A positive correlation between the composite score of processing speed and FA in a cluster of voxels (n=55397, $p_{corrected} < .001$) was found. It WM of several lobes including the following cerebral white matter tracts bilaterally: inferior cerebellar peduncle, middle cerebellar peduncle, superior cerebellar peduncle, cerebral peduncle, medial lemniscus, corticospinal tract, inferior longitudinal fasciculus, superior longitudinal fasciculus, inferior fronto-occipital fasciculus, superior fronto-occipital fasciculus, cingulum WM, corpus callosum (genu, body and splenium), fornix, anterior thalamic radiation, posterior thalamic radiation, posterior corona radiate, sagittal stratum, corona radiate, forceps major, forceps minor, uncinate fasciculus and internal capsule.

References:

Processing speed interacts with working memory efficiency in multiple sclerosis. Legenfelder J, Bryant D, Diamond B, Kalmar j, Moore NB, deLuca J. Archives of Clinical Neuropsychology 2006;21:229-238.

Is Speed of Processing or Working Memory the Primary Information Processing Deficit in Multiple Sclerosis? DeLuca J, Chelune GJ, Tulsky DS, Legenfelder J, Chiaravalloti ND. Journal of Clinical and Experimental Neuropsychology 2004;26: 550-562. Processing speed is correlated with cerebral health markers in the frontal lobes as quantified by neuroimaging. Kocuhnov P, Coyle T, Lancaster J, Robin DA, Hardies J, Kochunov V, et al. Neuroimage 2010;49:1190-1199. Regional DTI differences in multiple sclerosis patients. Roosendaal SD, Geurts JJG, Vrenken H, Hulst HE, Cover KS, Castelijns JA, et al. Neuroimage 2009;44:1397-1403.

680

Altered White Matter Connectivity Relates to Processing Speed in Parkinson Disease´s patients

L. Olabarrieta[1], **A. Cabrera Zubizarreta**[2], J.M. Ontaños Garcés[2], O. Rilo[1], J. Peña[1], N. Ojeda[1], M.Á. Gomez Beldarrain[3], I. García Gorostiaga[3], N. Ibarretxe-Bilbao[1]

[1]Department of Methods and Experimental Psychology, Deusto University, Bilbao/SPAIN, [2]MR Unit Hospital Galdakao, OSATEK, Galdakao/SPAIN, [3]Neurology, Hospital Galdakao, Galdakao/SPAIN

Introduction: Parkinson Disease (PD) has been traditionally considered a motor disorder, but cognitive functions such as processing speed (PS), memory, language, executive and visuospatial/constructive functions are also impaired. Diffusion tensor imaging (DTI) gives estimations of neuronal changes in patients with neurological diseases. DTI is used to assess the integrity of white matter (WM) tracts in the brain assessing, among others, fractional anisotropy (FA) values. In the specific case of PD, the significance of WM tract microstructure alterations for motor and cognitive function disease is still in debate. In this study we aimed to investigate the relationship between performance on PS and cerebral WM FA in PD patients

Cases: We recruited 35 non-demented PD patients (mean age=69.03, mean of illness duration=6.51). Patients underwent a neuropsychological battery and were scanned with an imaging protocol that included DTI on a Philips Achieva 3T. PS was measured with Salthouse Perceptual Comparison Test´s (PCT) total correct score. Whole-brain voxel-wise regression analysis of PS and cerebral WM FA data was performed using TBSS (Tract-Based Spatial Statistics), part of FSL software.

Discussion: The group´s mean score in PCT was 19.94 (SD=12.24). A significant positive correlation (pcorrected =.04) was found between PS and a cluster including WM areas of right external capsule and right inferior-frontooccipital fasciculus. Other tracts found were right superior longitudinal fasciculus (temporal part), right anterior thalamic radiation, right acoustic radiation, right corticospinal tract white matter, right optic radiation, right uncinate fasciculus, anterior corona radiata and callosal body. Our results show correlations between WM FA and performance on PS in PD patients. We conclude that those specific WM tracts contribute to PS in PD patients.

References:

Smith, S.M., Jenkinson, M., Johansen-Berg, H., Rueckert, D., Nichols, T.E., Mackay, C.E, et al. Tract-based spatial statistics: Voxelwise analysis of multi-subject diffusion data. NeuroImage 2006;31:1487-1505. Smith, S.M., Jenkinson, M., Woolrich, M.W., Beckmann, C.F., Behrens, T.E.J., Johansen-Berg, H, et al. Advances in functional and structural MR image analysis and implementation as FSL. NeuroImage,2004;23(S1):208-219. Tracy R. Melzer TR, Watts R, MacAskill MR, Pitcher TL, Livingston L, et al. White matter microstructure deteriorates across cognitive stages in Parkinson disease. Neurology 2013;80:1841-1849.

Matsui H, Nishinaka K, Oda M, Niiwaka H, Kubori T, Udara F. Dementia in Parkinson Disease: diffusion Tensor imaging. Acta Neurologica Scandinavica 2007;116:177-181.Kerchner GA, Racine CA, Hale S, Wilheim R, Laluz V, et al. (2012) Cognitive Processing Speed in Older Adults: Relationship with White Matter Integrity. PLoS ONE 7(11): e50425. doi:10.1371/journal.pone.0050425

681

Diffusion-weighted imaging as a method for evaluation of risk of malignant intracranial hypertension development in children with severe traumatic brain injury.

I. Melnikov, M. Ublinsky, O. Lukovkina
Radiology Department, Children's Clinical and Research Institute of Emergency Surgery and Trauma, Moscow/RUSSIAN FEDERATION

Introduction: Diffusion-weighted imaging (DWI) and consequent apparent diffusion coefficient (ADC) maps are an extremely sensitive for detection of brain tissue edema regardless of its etiology. Brain swelling is one of the most dangerous complications of primary traumatic brain injury (TBI), which leads to rise of intracranial pressure (ICP). In most severe cases, when intracranial hypertension cannot be managed medically, the only way to keep the brain from further injury is to perform decompressive craniectomy (DC). We propose that DWI can be a useful tool for evaluating the risk of malignant intracranial hypertension development and can be used to determine the need of DC in patients with severe TBI.

Cases: We retrospectively evaluated clinical and MRI data of 34 pediatric patients with severe TBI. The severity of clinical condition of each patient was evaluated with the use of the Glasgow Coma Scale (GCS). Parenchymal ICP gauge placement was performed in all patients for adequate ICP monitoring. Patients were categorized into three groups: (1) high ICP managed conservatively; (2) malignant ICP managed with DC; (3) normal ICP. MRI was performed to all patients not later than in 2 days from the moment of trauma. Four pairs of symmetrical regions of interest (ROIs) were manually drawn on ADC maps that were grouped for analysis of deep white matter of frontal, temporal, parietal and occipital lobes. All ROIs excluded areas that appeared abnormal on T2-weighted images (T2WI). Average ADC values in the deep white matter of frontal lobes were significantly increased in children with severe TBI with following DC (851.5+/-54.3x10(-3) mm2/sec) compared to those with severe TBI and conservatively controlled ICP (756.4+/-40.5x10(-3) mm2/sec; $p<0.05$).

Discussion: Assessment of DWI and ADC values in severe pediatric TBI is a useful tool for evaluating the risk of malignant ICP development. Early identification of children at high risk for this complication may assist in earlier aggressive (surgical) clinical management of pediatric TBI patients.

References:

1. Prieto-Valderrey F, Muñiz-Montes JR, López-García JA, Villegas-Del Ojo J, Málaga-Gil J, Galván-García R. Utility of diffusion-weighted magnetic resonance imaging in severe focal traumatic brain injuries. Med Intensiva. 2012 Sep 22. pii: S0210-5691(12)00231-8.

2.Weiss N, Galanaud D, Carpentier A, Naccache L, Puybasset L. Clinical review: Prognostic value of magnetic resonance imaging in acute brain injury and coma. Crit Care. 2007;11(5):230.

682

Congenital Intraventricular Teratoma

G. Okur, J.E. Lim-Dunham
[1]Radiology, Loyola University Medical Center, Maywood/IL/UNITED STATES OF AMERICA

Introduction: Intracranial teratomas diagnosed in the prenatal period and presenting at birth are rare overall but they are the most common intracranial tumor in newborns. We present a case of a female infant with intraventricular teratoma who underwent surgical excision and is currently doing well on 5.5 year follow-up.

Cases: An intracranial mass was diagnosed by second trimester prenatal ultrasound in a female fetus and confirmed on fetal MRI. She was born via normal vaginal delivery with an APGAR score of 9/9/9 at 38 weeks gestation. After birth ,neonatal cranial MRI confirmed the presence of a large expansile mass orginating from the left lateral ventricle measuring 6.6 cm. The lobulated mass revealed mixed signal intensity on T1/T2W sequences with cystic and fat areas. She underwent left craniotomy with biopsy and resection of the tumor. Histopathology of resected mass revealed intraventricular teratoma composed of mature and immature elements. The follow up CT scan of the head revealed a residual enhancing mass. Subsequently, a second surgical resection with ventricular shunt placement was performed. On follow up MR scans, no residual tumor was shown. The patient's most recent follow up MRI, which shows atrophy of the cerebrum and corpus callosum on the affected side, was performed at 5 years of age in September 2012. Apart from mild cognitive dysfunction and seizures which are well-controlled by medication, she is currently doing well. Her bone age is compatible with chronologic age.

Discussion: Intraventricular origin is a rare location for intracranial teratomas, which are increasingly recognized in prenatal ultrasound and fetal MRI (1). Depending on the various elements (fatty elements,calcifications,cysts) present in the tumoral mass, mixed signal intensities or densities can be seen on MRI and CT. Despite their benign cytopathologic features, the tumors can grow rapidly and can replace all brain tissue. With complete resection, chemotherapy may delay the re-growth of these tumors (2). In the literature,survival rates are low with few reports of prolonged survival beyond 4 years after resection(3). To our knowledge, the 5.5 year survival in this patient is unusual.

References:

1.Yu L, Krishnamurthy S, Chang H, Wasenko JJ.Congenital maturing immature intraventricular teratoma.Clin Imaging. 2010 May-Jun;34(3):222-5.

2.Mehrotra N, Shamji FM, Vassilyadi M, Ventureyra ECG. Intracranial tumors in first year of life.The CHEO experience Childs Nerv Syst 2009;25:1563–156.

3.Lanzino G, Kaptain GJ, Jane JA, Lin KY.Successful excision of a large immature teratoma involving the cranial base: report of a case with long-term follow-up.Neurosurgery.1998 Feb;42(2):389-93.

683

Fiber tractography of the abnormal thick corpus callosum – a case report.

S.K. Rączkowska[1], K. Kotulska[2], K. Nowak[1], S. Chełstowska[1], E. Jurkiewicz[1]
[1]Radiology Dept., The Children's Memorial Health Institute, Warsaw/POLAND, [2]Neurology Dept., The Children's Memorial Health Institute, Warsaw/POLAND

Introduction: Thick corpus callosum (CC) is a very rare congenital brain malformation. Recently, only few cases have been reported. We describe diffusion tensor imaging (DTI) and diffusion tractography in a child with corpus callosum thickening.

Cases:

We report a patient who was admitted at the age of 6 years, because of delayed psychomotor development and spastic tetraparesis. She was born to healthy parents, the pregnancy was uneventful. Delay in development was observed from birth. The most affected function was speech. She was able to walk only with support.

MR brain examination was obtained on the 1.5T scanner using 8-channel phased-array head coil. The routine protocol consists of T1, T2-weighted images with axial and sagittal planes, FLAIR images in axial plane, T2-weighted in coronal plane. Diffusion weighted imaging (DWI), diffusion tensor imaging (DTI) and 3D isotropic T1-weighted sequences were also performed additionally. DTI was performed by single-shot spin-echo echo-planar imaging (SE-EPI) acquired in the axial plane, in 12 directions with b values of 0 and 800 s/mm2 (TR/TE, 7400/92 ms; field of view: 240x240mm; matrix: 256x256; slice thickness 4mm).

Discussion:

Conventional MR imaging showed that corpus callosum was significantly thicked and shortened in anteroposterior dimension. Agenesis of rostrum was also observed. Within corpus callosum expanded perivascular spaces were visible. There was also anterior commissure thickening and abnormal, tortuous course of the anterior part of the longitudinal cerebral fissure. No other malformations occurred.

Diffusion tensor imaging and diffusion tractography showed abnormal, longitudinal tract located dorsally to the corpus callosum. On DTI, the body of the CC contained an abnormal longitudinal bundle. According to the previously published data these fibers may represent a congenital heterotopic cingulum, indusium griseum or aberrantly oriented callosal axons.

The morphology of the corpus callosum should be accurately estimated, especially in children with facial dysmorphism or motor and/or mental developmental delay.

References:

Koob M, Weingertner AS, Gasser B,et al. Thick corpus callosum: a clue to the diagnosis of fetal septopreoptic holoprosencephaly?Pediatr Radiol 2011 Oct 18 42:886-890

Rollins N.K. Diffusion Imaging of the Congenitally Thickened Corpus Callosum AJNR Am J Neuroradiol 2012 Aug 16

Sato N, Ota M, Yagishita A,et al. Aberrant Midsaggital Fiber Tracts in Patients with Hemimegaloencephaly AJNR Am J Neuroradiol 2008 Apr 29:823-27

WahlM, Lauterbach-Soon B, Hattingen E, et al. Human motor corpus callosum: topography, somatotopy, and link between microstructure and function. J NEUROSCI 2007;27:12132-38

Hori A, Stan AC. Supracallosal longitudal fiber bundle:heterotopic cingulum, dorsal fornix or Probst bundle? Neuropathology 2004;24:56-59

684

Diffusion tensor imaging in early amyotrophic lateral sclerosis at 3T MRI

A. Sarsilmaz[1], B. Sarikaya[1], **Z. Firat**[1], A.M. Ulug[1], G. Karlikaya[2], C.A. Bingol[2], M. Cihangiroglu[1], I. Kovanlikaya[1, 3]
[1]Radiology, Yeditepe University, Istanbul/TURKEY, [2]Neurology, Yeditepe University, Istanbul/TURKEY, [3]Radiology, Cornell University, New York/UNITED STATES OF AMERICA

Introduction: Amyotrophic lateral sclerosis (ALS) is a multisystem disorder with impairment of white matter, corticospinal tract and frontotemporal functions such as cognition and behavior. The purpose of this study was to perform the diffusion tensor imaging for the detect white matter microstructural abnormalities in ALS at 3T MRI.

Cases: We investigated 12 patients (7 male, 5 female) with sporadic ALS and 10 control subjects (7 male, 3 female) using voxel-based analysis of diffusion tensor images (DTI) at 3T MRI. DTI region of interest (ROI) and tractography techniques were used to compare fractional anisotrophy (FA) and apparent diffusion coefficient (ADC) values along the brain corticospinal tracts between ALS subjects and healthy controls.

Patient group's results of FA and ADC measurements were, respectively, 0.638±0.041 and 0.350±0.01 ($p<0,001$), healthy group's results of FA and ADC measurements respectively 0.701±0.054 and 0.288±0.027 ($p<0.05$). DTI revealed reduced fractional anisotropy in the bilateral corticospinal tracts, internal capsule posterior crus. The FA reductions in this region correlated with the disease severity in ALS patients.

Discussion: In conclusion, longitudinal DTI study captures progression of upper motor fiber degeneration in ALS. DTI can be useful for monitoring ALS progression and efficacy of treatment interventions.

References:

1. Cirillo M, Espesito F, Tedeschi G, Caiazzo G, Sagnelli A, Piccirillo G, Conforti R, Tortora F, Monsurro MR, Cirillo S, Trojsi F. Widespread microstuctural white matter involvement in amyotrophic lateral sclerosis: a whole-brain DTI study. AJNR 2012: 33; 1102-8.

2. Zhang Y, Schuff N, Woolley SC, Chiang GC, Boreta L, Laxamana J, Katz JS, Weiner MW. Progression of white matter degeneration in amyotrophic lateral sclerosis: A diffusion tensor imaging study. Amyotroph Lateral Scler. 2011: 12; 421-9.

685

Comparison between Proton MR spectroscopy and MIB-1 labeling index of brain tumors

Y. Fushimi[1], T. Okada[1], A. Yamamoto[1], M. Kanagaki[1], T.M. Mehemed[1], E. Morimoto[1], R. Sakamoto[1], S. Nakajima[1], S. Okuchi[1], H. Yamada[1], T. Kakigi[1], A. Sakata[1], T. Dodo[1], Y. Kanazawa[1], K. Takakura[1], K. Fujimoto[1], A. Kido[1], N. Sakashita[2], K. Togashi[1]
[1]Department of Diagnostic Imaging and Nuclear Medicine, Kyoto University Graduate School of Medicine, Kyoto/JAPAN, [2]MRI Systems Development Department, Toshiba Medical Systems Corporation, Otawara/JAPAN

Introduction: Glioblastoma (GBM) is the most malignant brain tumor in adults and is heterogeneous in appearance and outcome. The survival for most patients remains dismal despite aggressive multimodal therapeutic strategies. MIB-1 labeling has been assumed to be a surrogate marker of tumor proliferation and has association with prognosis.

Cases: 26 patients with brain tumor underwent MRS at 3T MR scanner (Toshiba Medical Systems, Otawara, Japan). Newly operated 14 patients with glioma (grade II 4, III 5, IV 5 patients) were enrolled in this study. MRS was analysed with LCModel (Version 6.3-0C). Calculated concentration of NAA, choline

(Cho), creatine (Cr) and lactate (Lac), NAA/Cr ratio and Cho/Cr ratio were compared with MIB-1 index. Positive correlation was seen in Lac vs. MIB-1 index (r=0.532), and Cho/Cr vs. MIB-1 index (r=0.646).
Discussion: Determination of proliferative activity using the monoclonal antibody MIB-1 LI has been investigated in malignant gliomas [1]. The information of MRS data prior to therapy may also be valuable in assessing recurrent sign of brain tumor. MIB-1 LI is correlated with the grade of malignancy, however, considerable overlap is seen among different grades [2]. MIB-1 LI having been determined from the resected tissue, therefore, sampling errors between MRS and MIB-1 LI are inevitable. Our findings of MRS suggest the possibility of preoperative survey of proliferative activity of brain tumors.
References:
[1] Johannessen AL, et al. Pathol Oncol Res. 2006
[2] Pirzkall A, et al. Neuro Oncol. 2009

686

Neurofibromatosis Type 1: MRI features

D.R.J.D. Nascimento[1, 2], M.R. Matos[1], R. Jogo[1], M.C. Barrueto[1], A. Nunes[1], E. Soares[1]
[1]Serviço de Radiologia- Hospital Dona Estefânia, Centro Hospitalar de Lisboa Central, Lisboa/PORTUGAL, [2]Serviço de Radiologia, Serviço de Saúde da Região Autónoma da Madeira, Funchal/PORTUGAL

Introduction: Neurofibromatosis type 1 (NF1) is a multisystemic disorder but is main features are neurocutaneous. It also has a frequent and important association with several tumours.
Using iconography and clinical data from NF1 cases, the present review first discusses its manifestations and establishes the importance of MRI. Management, prognosis and etiology are also considered.
Cases: Symptoms such as soft bumps on or under the skin, bone deformities and learning disabilities are frequent.
Lobulated masses along peripheral nerve course (localized neurofibromas) were seen in multiple locations such as head and neck, costal grid and paravertebral location. We found neurofibromas in craneal nerves, along the mastigator space and causing intracraneal anomalies such as widening of the pterygopalatine fossa.
MRI also revealed many frequently associated skeletal abnomalities, such as ribbon rib and rib notching deformities and scoliosis.
Diffuse, tortuous, rope-like expansion lesions (plexiform neurofibromas) were seen in the neck.
Localized cutaneous and diffuse subcutaneous neurofibromas were also evident in MRI.
Some patients had bright spots on T2-weighted images of the cerebellum, called unidentified bright objects (UBOs) which are believed to represent benign hamartomas.
One case had also stenosis of the aqueduct of Sylvius,with widening of the third and lateral ventricles.
Discussion: NF1 affects over 1:2500 individuals. In half of cases, the disease is inherited as an autosomal dominant condition. The remaining is due to a new mutation.
The NF1 gene product (neurofibromin) is tumour suppressor. Inactivation of this gene thus predisposes to tumour development.
Tumours include pheochromocytoma, ganglioneuroma, neurofibroma, malignant peripheral nerve sheath tumour, Wilms tumour, rhabdomyosarcoma, renal angiomyolipoma, glioma and carcinoid.
Neurofibromas are very typical of this disease. There are three types: localized (cutaneous), diffuse (subcutaneous) and plexiform (considered pathognomonic).
It is important to keep in mind that NF1 can be multissistemic: many anomalies occur in central nervous system (UBOs, craneal ossification anomalies, gliomas), skin (café au lait spots and neurofibromas), skeleton (kyphoscoliosis, posterior vertebral scalloping, rib deformities) and vessels (aneurysms/arteriovenous malformations, renal artery stenosis).
A combination of supportive and surgical therapies are employed depending on the tumours and anomalies present.
Prognosis is variable, but patients have a life expectancy of approximately half that of non affected individuals.
References:
- Neurofibromatosis fact sheet. National Institute of Neurological Disorders and Stroke.
- Torpy JM, et al. Neurofibromatosis. Journal of the American Medical Association. 2009;302:2170.
- Plon SE. Neurofibromatosis type 1 (von Recklinghausen's disease). http://www.uptodate.com/index. Oct. 12, 2012.
- Schwannomatosis. Neurofibromatosis Network. Oct. 16, 2012.
- Ferner RE. The neurofibromatoses. Practical Neurology. 2010;10:82.

687

Pronostic value of multimodal MR imaging in pseudoprogression of globlastomas.

V. Cazzola[1], A. Benouaich-Amiel[2], F. Aubry[3], I. Catalaa[1], C. Cognard[1], F. Bonneville[1]
[1]service de neuroradiologie, CHU toulouse, toulouse/FRANCE, [2]service de neurologie, CHU toulouse, toulouse/FRANCE, [3]UMRS 825, INSERM, Toulouse/FRANCE

Introduction:
Standard treatment protocol for glioblastomas (GBM) is based on temozolomide concurrent with radiotherapy (STUPP regimen). MRI performed within 12 weeks after radiotherapy may show an increase in contrast enhancement, termed pseudoprogression (psPD) which may suggest, sometimes mistakenly, progressive disease. Follow up after this 12 weeks period is needed to assure this diagnosis. PsPD may evolve in a true tumor progression (TP) or may stabilize, being a true psPD. The aim of this study was to determine early MR imaging parameters, that can differentiate, on the MRI performed one month after radiotherapy, patients with true progression (TP) from stable patients (true psPD).
Cases:
69 patients with newly diagnosed glioblastoma, treated using the STUPP regimen between March 2009 and January 2012 are retrospectively include in this study. In all cases a multimodal MRI was performed (including spectroscopy, MRI perfusion and diffusion séquences) preoperatively, one month after radiotherapy (RT+1) and 3 months after radiotherapy. Therapeutic response was evaluated according to the RANO criteria. On the MRI RT+1, we studied apparent diffusion coefficient (ADC), cerebral blood volume (rCBV), and ratios of choline/NAA, choline/creatinine and NAA/creatinine.
Out of 69 patients, 38 (55%) had MRI consistent with pseudoprogression according to the RANO criteria on the MRI RT+1. Subsequent MRI at 3 months confirmed progression in 18 patients (TP), while 20 were considered stable (true psPD).
On MRI RT+1, mean choline/NAA ratio was lower in true psPD patients than in TP patients (1,16 vs 2,15 respectively). The estimated cut-off to differentiate psPD and TP was 1,73 (sensitivity 80%, specificity 78%).
True psPD patients had also a significant decrease of rCBV, between preoperative MRI and MRI RT+1 compared to the TP group (39% vs 8% respectively, p = 0,019).
The median survival in true psPD patients was 661 days compared with 374 days for TP patients (p = 0.014).

Discussion:
Choline/NAA ratio < 1.73 and decrease of 40% of rCBV appear to be pertinent criteria that could help to differentiate pseudoprogressions from early true progressions on the brain MRI performed 1 month after radiotherapy.
References:
Wen PY, Macdonald DR, Reardon DA, et al. Updated response assessment criteria for high-grade gliomas: response assessment in neuro-oncology working group. J Clin Oncol 28 (11): 1963-72.
Grand S, Kremer S, Le Bas JF, et al. Perfusion-diffusion 1H spectroscopy: role in the diagnosis and follow-up of supratentorial brain tumours in adults. Rev Neurol (Paris). 2006 Dec; 162(12):1204-20.
De Wit MC, de Bruin HG, Eijkenboom W, et al. Immediate post-radiotherapy changes in malignant glioma can mimic tumor progression. Neurology. 2004 Aug 10; 63(3):535-7.

688

The role of MR Imaging and its advancement in the diagnosis of ischemic and hemorrhagic stroke.

M. Kasam[1], **S. Arjuna**[2]
[1]Radiology, Mayo Clinic, Rochester, Rochester/UNITED STATES OF AMERICA, [2]Dept of Radiology and Imaging, Fortis Memorial Research Institute, Gurgaon/INDIA

Introduction: PURPOSE/AIM
Among all cerebrovascular accidents, Stroke is the most devastating and affects around 1 million people each year in the United States. It's is a medical emergency and may result in permanent neurological damage, complications including death. Apart from that, it is the major cause of adult disability around the world. The aim of the presentation is to discuss the role of MR Imaging and its advancement in the diagnosis of both Ischemic and Hemorrhagic stroke (ICH).
Cases: Review
Discussion: CONTENT ORGANIZATION
1: Introduction - The evolution and resolution of ischemic and ICH stroke. How the MRI became the key role for the diagnosis.
2: Review of the principles of diffusion, functional and Spectroscopic MR and their role on the diagnosis of acute ischemic stroke and ICH.
3: Detailed discussion on advantages and limitations of the above techniques.
4: Necessity for the development of more sensitive tools.
SUMMARY
The principles of conventional and non-conventional MR to study the evaluation and resolution at different stages of both ischemic and ICH stroke have been reviewed to gain further understanding in the pathophysiology after ischemic stroke
References:
List will be provided at the time of poster presentation

689

Application of MRI for non-invasive estimation of cerebral ferritin levels and the activity of microglia in Intra cerebral hemorrhagic.

M. Kasam[1], **S. Arjuna**[2]
[1]Radiology, Mayo Clinic, Rochester, Rochester/UNITED STATES OF AMERICA, [2]Dept of Radiology and Imaging, Fortis Memorial Research Institute, Gurgaon/INDIA

Introduction: To enhance the knowledge about MR Imaging to the treating clinician about noninvasive estimation of cerebral ferritn levels and microglia activity and the recent updates in intracerebral hemorrhage (ICH) patients research.
Cases: Review
Discussion: Organization of methods, results and updates
1) In-situ monitoring of the cerebral ferritin levels and microglia activity of ICH patients using MRI.
2) Correlate and establish the literature till date and explore the relationship between the serum ferritin levels and perihematomal ferritin levels at each stage of ICH stroke.
Conclusion:
Noninvasive monitoring of both ferritin levels and the microglia activity using MRI may help the clinician in selecting a proper iron chelating drug and its dosage to control the secondary injury, thus affecting the mortality and disability in ICH population.
References:
Will be provided at the time of presentation.

690

Brain Nuclear Magnetic Resonance findings associated with iodine deficiency. A Systematic Review

M.C. Valdes Hernandez[1], K.L. Wilson[2], E. Combet Aspray[3], J.M. Wardlaw[1]
[1]Neuroimaging Sciences, University of Edinburgh, Edinburgh/UNITED KINGDOM, [2]College of Medicine and Veterinary Medicine, University of Edinburgh, Edinburgh/UNITED KINGDOM, [3]Human Nutrition, University of Glasgow, Glasgow/UNITED KINGDOM

Introduction: Iodine deficiency (ID) is a common cause of preventable brain damage and mental retardation worldwide, according to the World Health Organisation. European countries are usually assumed to be iodine sufficient, however, several pockets of insufficiency have been described (including UK, Italy, Belgium), with no official data available for several countries[1]. ID may adversely affect brain maturation processes that potentially result in structural and metabolic brain abnormalities, visible on Nuclear Magnetic Resonance (NMR) techniques. However, there the appearance of these brain changes on NMR methods has not been reviewed. We systematically reviewed the literature up to May 2013 using 3 online search databases (Medline, Embase and Web of Knowledge) and multiple combinations of the search terms: iodine, iodine deficiency, magnetic resonance, MRI, MRS, brain, imaging and iodine deficiency disorders.
Cases: Of the 1673 related papers found, 37 studies confirmed their findings directly using Positron Emission Tomography, Single Photon Emission Computed Tomography, MRI and/or Magnetic Resonance Spectroscopy. Of them, 36 were in humans and involved 327 subjects, 46 of whom had primary hypothyroidism, 97 had congenital hypothyroidism, 3 had endemic cretinism, 12 had subclinical hypothyroidism and on 151 the subtype of hypothyroidism was not specified. The studies were small, with a mean relevant sample size of 9, median 5, range 1-94, while 15 studies were individual case reports. T1-weighted was the most commonly used MRI sequence(24/37 studies) and 1.5 Tesla the most commonly used magnet strength(6/11 studies that provided this information). Pituitary abnormalities (18/37 studies) and cerebellar atrophy(5/37 studies), followed by decreased hippocampal and parietal metabolic activity(4/37 studies) were the most prevalent brain abnormalities found. Only fMRI studies (4/37) reported cognition-related abnormalities but the brain changes found were limited to a visual description in all studies.
Discussion: This review fills a void in the literature and provides a starting point for researching on the macroscopic structural brain changes caused by ID using NMR methods. Our findings suggest ID may contribute to pituitary abnormalities, aberrant development of the cerebellar hemispheres and vermis or be associated with mechanisms that cause reduced blood flow mainly in the cerebellum, and regions of the temporal and parietal lobes leading to atrophy.

More studies that use NMR methods to identify changes on brain volume or other global structural abnormalities are required. This will improve the understanding of the pathophysiological mechanisms related with the effects of ID in the brain and hence cognitive damage.

References:

[1]Andersson M et al.J Nutrition 2012;378:129-133

691

The use of dynamic contrast-enhanced MRI to study permeability of the blood-brain barrier – A systematic literature review

A.K. Heye[1], R.D. Culling[2], M.C. Valdes Hernandez[1], J.M. Wardlaw[1]
[1]Division of Neuroimaging Sciences, University of Edinburgh, Brain Research Imaging Centre, Edinburgh/UNITED KINGDOM, [2]University of Edinburgh, School of Medicine and Veterinary Medicine, Edinburgh/UNITED KINGDOM

Introduction: Many brain pathologies cause a malfunction of the blood-brain barrier (BBB). Permeability imaging using dynamic contrast-enhanced MRI (DCE-MRI) has been widely used in the assessment of such diseases, in particular tumours [1], multiple sclerosis [2] and acute ischemic strokes [3]. This review aimed to summarise the state-of-art of dynamic contrast enhanced MRI methods and their application to study changes in BBB permeability with disease. We systematically reviewed the existing literature up to February 2013. We sought studies that assessed BBB integrity using T_1-weighted DCE-MRI techniques in animals and humans in normal or abnormal brain tissues. We analysed studied pathologies, MRI scanning protocols and methods for data analysis to determine the range of available methods and their likely reliability.
Cases: The literature search provided 47 studies that were eligible for inclusion, overall involving 243 animals and 1203 human subjects. The pathologies most studied were intracranial neoplasms in humans (19 publications, 453 patients) and induced focal ischemia in animals (five publications, 148 subjects). Eight studies investigated pathologies associated with subtle BBB disruption, such as cerebral small vessel disease or diabetes. We found large variations in DCE-MRI scanning procedures regarding imaging sequences, duration and contrast agent details. Studies used a variety of different methods for data analysis, mainly based on model-free measurement, Patlak's graphical approach or Tofts compartmental model. Five studies attempted to validate estimated permeability parameters by comparing values obtained by different analytic methods or performing simulation experiments.
Discussion: This systematic review demonstrates that DCE-MRI has been successfully applied for several clinical purposes, such as differentiation of brain tumour types and evaluation of treatment response. Moreover, it shows the clinical potential of DCE-MRI in several application scenarios with more subtle BBB abnormalities as in ageing-related white matter disease [4]. However, this review also highlights the great diversity of studies using DCE-MRI to assess BBB permeability. In order to increase inter-study comparability and reliability of quantitative permeability estimates, a standardisation of clinical DCE-MRI methodology is urgently needed. For this purpose, further research investigating the influence of different analytic methods and scanning details such as MRI sequences and contrast agent doses is required.
References:

[1] Singh A, et al., 2007, J Magn Reson Imaging,26:871-880.
[2] Jelescu IO, et al., 2011, J Magn Reson Imaging,33:1291-1300.
[3] Kassner A, et al., 2009, AJNR Am J Neuroradiol,30:1864-1869.
[4] Wardlaw JM, et al., 2008, Stroke,39:1327-1332.

692

The possibilities of magnetic resonance perfusion in the differential diagnosis of post-radiation changes and recurrence of glial brain tumors

T. Gribanova, V. Fokin, E. Yuhno
of Radiology, Military Medical Academy, St Peterburg/RUSSIAN FEDERATION

Introduction: Radiation therapy has become an important addition to the surgical treatment of patients with glioblastomas. Such therapy can lead to radionecrosis. It is difficult to determine the accumulation of contrast material is associated with tumor recurrence or radiation necrosis, which is necessary for further patient management and prognosis of the disease. Magnetic resonance perfusion disorders in planning and monitoring of radiation therapy of gliomas of the brain to predict the likelihood of recurrence and differential diagnosis of recurrence and post-radiation change
Cases: Studies conducted 13 patients: 6 - with newly diagnosed glioblastomas before surgery and in the early postoperative period, 5 - with signs of disease recurrence after radiotherapy, 2 - in the postoperative period up to a deferred radiotherapy.
Discussion:
The data in the assessment of perfusion disorders in patients with primary brain glial formations after the surgery and post-radiation therapy allow you to set the criteria for differentiation between post-radiation changes and recurrence of the disease, which can help improve the quality of care for patients with glioblastomas.
References:

Ozsunar Y., Mullins M.E., Kwong K. et al. Glioma recur-rence versus radiation necrosis? A pilot comparison of arte-rial spin-labeled, dynamic susceptibility contrast enhanced MRI, and FDG-PET imaging // Acad. Radiol. 2010. V. 17. № 3. P.282—290.
Hu L.S., Baxter L.C., Smith K.A. et al. Relative cerebral blood volume to differentiate high-grade glima recurrence from posttreatment radiation effects: direct correlation be-tween image-guided tissue histopathology and localized dy-namic susceptibility-weighted contrast-enhanced perfusion MR imaging measurements // Am. J. Neuroradiolody. 2009. V. 30, № 3. P. 552—558.
Jain R., Narang J., Sundgren P.M. et al. Treatment induced necrosis versus recurrent/progressing brain tumor: going be-yond the boundaries of conventional morphologic imaging // J. Neurooncol. 2010. Epub ahead of print. DOI 10.1007/s11060-010-0139-3.
Kumar A.J., Leeds N.E., Fuller G.N. et al. Malignant glio-mas: MR Imaging spectrum of radiation therapy-and chemo-therapy-induced necrosis of the brain after treatment // Radi-ology. 2000. V. 217. P. 377—384.

693

Neurological emergencies in paediatrics secondary to oncological therapy

I. Rehman, K. Aftab
Radiology, Shaukat Khanum Memorial Cancer Hospital And Research Center, Lahore/PAKISTAN

Introduction: A large number of paediatric oncology patients on therapy present with diverse neurological symptoms and pose a challenge for oncologist as well as imaging interpretation. With improvements in treatment, side effects of oncology therapy are also being better known and evaluated. MRI is important in early recognition of critical side effects and is crucial in dictating further management.
Cases: A number of pediatric oncology patients present with variable neurological symptoms. Imaging features of these cases were retrospectively reviewed and reported by consultant radiologist in light of clinical information prior

to imaging and patient's labs e. g., CSF analysis and clinical follow up. Follow up imaging was reviewed where available.

Discussion: Paediatric oncology patients can have variable complications ranging from hemorrhage to venous thrombosis to infections with bizzarre clinical presentations. Imaging appearances can also be diverse. ER radiologist needs to have an indepth view of such cases.

Reversible posterior encephalopathy syndrome is being increasingly recognized at our set up after initial therapy and improves after simple preventive measures. Knowledge of key features of this non traumatic neurological emergency is imperative for a radiologist. Permanent neurological sequelae can be prevented if recognized early. Similarly neurotoxicity after chemotherapy and/or radiotherapy can also present in bizzarre manners.

We will be sharing our experience and understanding of neuroemergencies in paediatric oncology at a tertiary care cancer set up.

References:

1.) Vazquez E, Delgado I , Sanchez-Montanez A, Barber I, Sanchez-Toledo J, Enriquez G. Side effects of Oncologic Therapies in Pediatric Central Nervous System: Update on Neuroimaging Findings. Radiographics 2011; 31:1123-39.

2.) Vazquez E, Lucaya J, Castellote A et al. Neuroimaging in Pediatric Leukemia and Lymphoma: Differential Diagnosis. Radiographics 2002; 22:1411-28.

3.) Parisi MT, Fahmy JL, Kaminsky CK, Malogolowkin MH. Complications of Cancer Therapy in Children: A Radiologist's Guide. Radiographics 1999; 19:283-97.

Software Exhibits

694

Toolbox for co-registration and spatial normalisation of CBF maps acquired with ASL for group comparison studies

V. Mato Abad[1], F. Zelaya[2], P. García-Polo[1], O. O'Daly[2], J. Álvarez-Linera[3], J.A. Hernandez-Tamames[4]
[1]Neuroimagen, Fundación CIEN - Fundación Reina Sofia, Madrid/SPAIN, [2]Department of Neuroimaging, King's College London, London/UNITED KINGDOM, [3]Neurorradiología, Hospital Ruber Internacional, Madrid/SPAIN, [4]Tecnologia Electronica, Universidad Rey Juan Carlos, Mostoles/SPAIN

Purpose of the software: The availability of ASL as a routine method for assessment of resting state CBF data has provided the possibility of employing physiological markers to probe functional differences between groups. However, due to the lack of commercial packages, ASL methodologies have evolved independently and apart from a handful of packages [1][2], there are no well-established standards or normalising ASL data to a common frame of reference. This lack of a harmonised pre-processing pipeline contributes to the potential discrepancies in studies of resting state perfusion across different laboratories. We have developed an ASL processing toolbox with different analysis strategies depending on the ASL image and the type of structural scans available (T2-weighted and/or T1-weighted high-resolution scans). The toolbox can automatically process several ASL datasets by accessing both SPM-8 and FSL software, which are two of the most widely available image processing platforms for structural and functional MRI.
Methods/Implementation: The toolbox is written in MATLAB and includes a GUI, that mimic the SPM handling menus (Figure1) and a batch mode. The process is:
1. Rough skull-stripping of the CBF maps using the FSL Brain Extraction Tool (bet) for noisy CBF maps using a conservative threshold.
2. Skull-stripping of the structural scan by two options: the bet tool OR with a brain mask created from SPM segmentation routine.
3. Co-registration of the CBF maps to the skull-stripped structural scan using SPM-8.
4. Skull-stripping of the co-registered CBF maps using the brain mask obtained on (2).
5. Normalization of the structural scan and co-registered and skull-stripped CBF maps to the MNI space.
6. Smoothing of the final, spatially normalised CBF by a smoothing kernel.
Figure2 shows an example of the results: source CBF dataset (a) and the final normalised skull-stripped CBF (b, d). CBF shown in (b) is obtained using a T1-weighted scan (c) and SPM-8 routines. CBF shown in (d) is obtained using a T2-weighted scan (e) and FSL.
The software also offers facilities for rapid extraction of CBF values from anatomically or functionally ROIs. The results can easily be incorporated into statistical packages.
The toolbox has been tested on approximately 150 individual CBF maps obtained at the IOP/KCL Neuroimaging Department employing three versions of a pCASL sequence with a 3D Spiral readout (using a GE scanner).

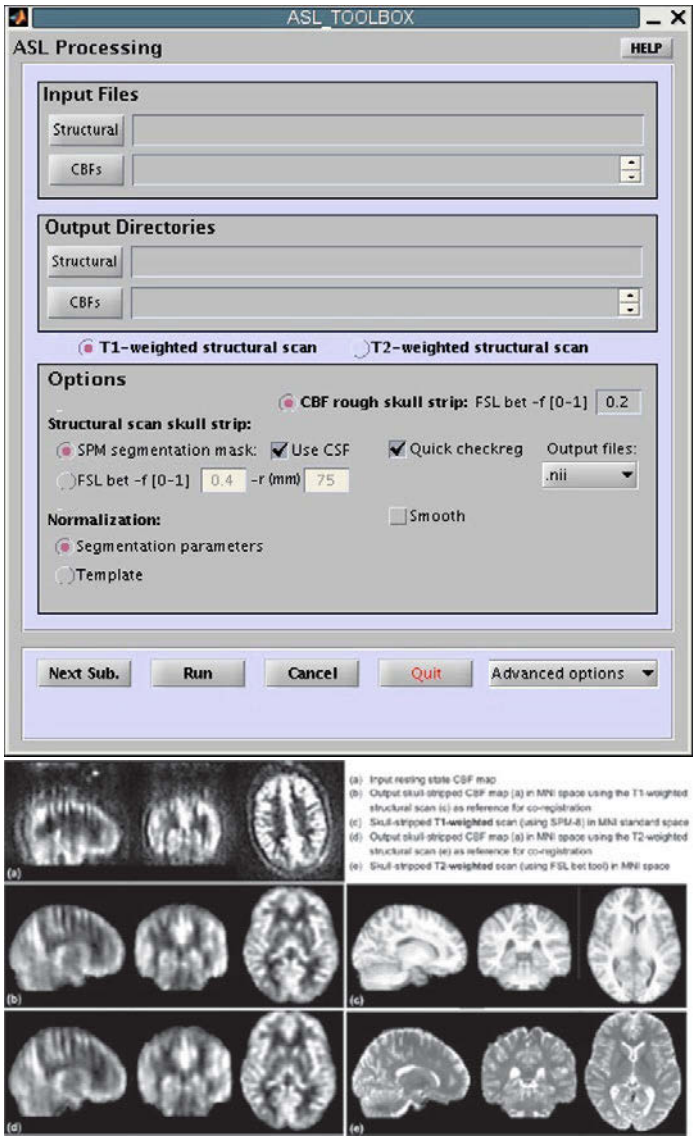

Features illustrated at the exhibit: The Toolbox will be illustrated at the ESMRMB exhibit.

References:

[1]Chappell MA et al, 2009, IEEE T Signal Proces 57(1):223-236
[2]Wang Z et al, 2007, Magn Reson Imaging, 26(2):261-9

695

My Therapy Response: A novel software tool to predict the response to antiangiogenic therapy in mouse glioma models.

A. Benítez[1], **G. Peláez-Brioso**[1], A.R. Borges[2], P. López-Larrubia[1], L. Lago-Fernández[3], S. Cerdan[1], M. Sánchez-Montañés[3]
[1]*Department of Experimental Models of Human Disease, Instituto de Investigaciones Biomédicas Alberto Sols CSIC-UAM, Madrid/SPAIN,* [2]*Radiology, Instituto Português de Oncologia Centro de Lisboa, Lisbon/ PORTUGAL,* [3]*Escuela Politécnica Superior, Departamento de Ingeniería Informática, Universidad Autónoma de Madrid, Madrid/SPAIN*

Purpose of the software: Clinical management of high grade gliomas (HGG) often involves antiangiogenic therapies using monoclonal antibodies, mainly against VGEF. Responses to this treatment are highly heterogeneous, with similar cohorts of patients behaving as "*responders*" or "*non-responders*". It would be then very useful to discriminate by non invasive criteria the two populations as early as possible, to tailor treatment accordingly.
Here we provide a software package to predict in vivo and automatically the treatment outcome of mice bearing implanted Gl621 tumors to anti-VGEF therapy, using DWI and T2w data sets.
Methods/Implementation: We evaluated treatment response in 13 mice bearing implanted Gl261 tumors on a 7T MR scanner (RECIST criteria [1], mAb against VEGF B20-4.1, 5mg/Kg twice weekly for 8 weeks). MRI studies included T2w and DWI performed sequentially at 3/4 day intervals until completion of treatment or obvious, treatment independent, tumor growth. Fisher's discriminant analysis [2] was then applied to Day-1 and Day-2 of treatment data set in order to find the linear projection that best discriminates the pixels as belonging to "*responder*" or "*non-responder*" animals to anti-VGEF treatment. The discriminant function obtained may be used later to classify additional data into one of the two classes.
Our package is implemented in MATLAB and is able to accept DWI and T2w data sets from mouse brains, providing automatically a prediction of the new image in a scale of "*response rate*" 0 (*non-responder*) - 100 (*responder*).
Features illustrated at the exhibit: We illustrate the operation of the program (Fig. 1) with a set of sample DWI and T2w images from the mouse brains using the data base described in Methods. The user may enter an external data base into the application or use preeexisting data base already configured in the software package. Features include: Data input, Data Exploration, Train new model (Fig. 2), Classify a subject, results expressed as "*response rate*" (Fig. 3), and Export report.
This software provides a protocol for the prediction of therapy response to antiangiogenic therapy in mouse glioma models, based on non invasive parameters as T2w and DWI.

Fig. 1. Initial GUI of *My Therapy Response* software package.

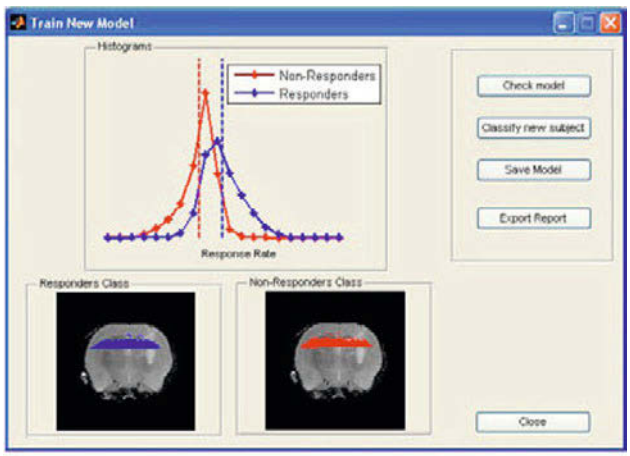

Fig. 2. Top panel: Representation of Fisher's projection ("*responders*" - blue dots / "*non-responders*" - red dots). **Bottom panels**: Images shown the regions where are change detected from the brain of "*responders*" mice (blue pixels) and "*non-responders*" mice (red pixels).

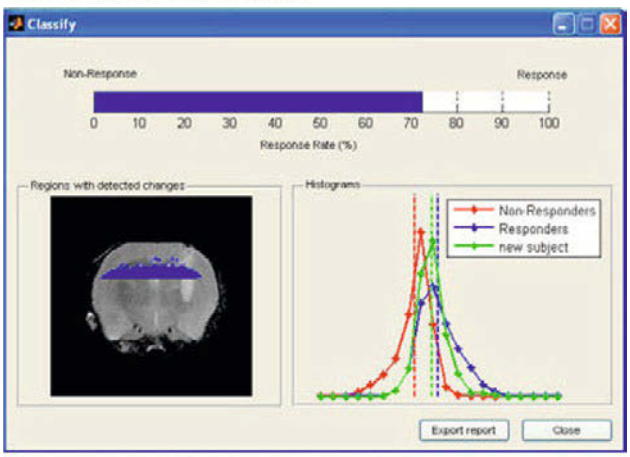

Fig. 3. Example of the "*response rate*" prediction to the antiangiogenic therapy for a mouse with glioma (top panel) and brain regions with detected changes (shown with red pixels) in "*responders*" class (left bottom panel). The Fisher's projection of the response rate is presented in the right bottom panel, with "*non-responders*" values (red dots), "*responders*" values (blue dots) and new mouse values to classify (green dots).

References:
[1] Therasse, P., et al. *New Guidelines to Evaluate the Response to Treatment in Solid Tumors*. Journal of the National Cancer Institute, Vol. 92, No. 3, February 2, 2000.
[2] Hastie, T., et al. J. *The elements of statistical learning. Data mining, inference, and prediction.* Springer Series in Statistics. New York, NY, 2001.

696

My Inflammation:An Intelligent Decision Support System to identify cerebral inflammation areas using multiparametric MRI data sets

A.B. Martin-Recuero, S. Cerdan
Alberto Sols, Consejo de Investigaciones Cientificas, Madrid/SPAIN

Purpose of the software: Cerebral inflammatory responses underlie the most morbid and prevalent neurological disorders, including cancer, ischemia, neurotrauma or neurodegeneration[1]. In most cases, current bioimaging methods are not able to discriminate unambiguously between the primary pathology and the associated inflammatory response. Here we provide s software package, an Intelligent Decision Support System (IDSS), to discriminate between inflamed and healthy mouse brain using Magnetization Transfer, T1, T2 and Diffusion Weighted Imaging (MT, T1W, T2W, DWI).
Methods/Implementation: Adult male mice C57BL/6 (n=6) received an i.p. injection of LPS from E. Coli Serotype 0127:B8 (5mg/kg). MRI studies of the mouse brain were carried out in a horizontal 7T/16 scanner. ADC in the head-foot (H-F), left-right (L-R) and the antero-posterior (A-P) directions with b=0, 100, 400, 800 s/mm^2, T1, T2, and MT maps were acquired before and three days after the LPS administration, when maximal inflammation develops[2,3]. For the present set-up, there were 70 different MRI feature sequences (image types) considered, however, the model may include any additional feature desired. IDSS was built as follows: Features for the IDSS were selected sequentially starting by the one with the highest R^2 value, as obtained from a linear regression analysis of a Fisher´s discriminant[4] model. Features were included until the adjusted Root Mean Square Error (RMSE) value became smaller than a limit ⊠. At this point, the selected features are those that contribute the best cost-effective model of inflammation classification. Gaussian distributions of the Fisher projections and distance criteria based on them were calculated and used to discriminate between «inflamed» and «healthy» subjects, as well as for the calculation of an "inflammation index".
Features illustrated at the exhibit: The operation of the program is illustrated in Figures 1-4. The user may choose the MRI datasets, either to automatically select the most relevant MRI features in the inflammation model, to train a different model or classify a subject and calculate a map of inflammation index. All these features are currently implemented for the segmentation of hippocampal regions. Further software improvements e.g. classification for the whole brain image (poster abstract 47081) will become available in the near future.

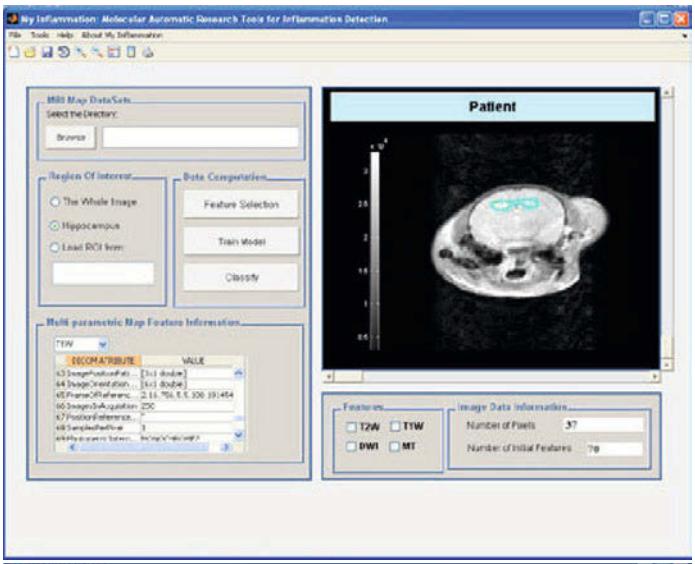

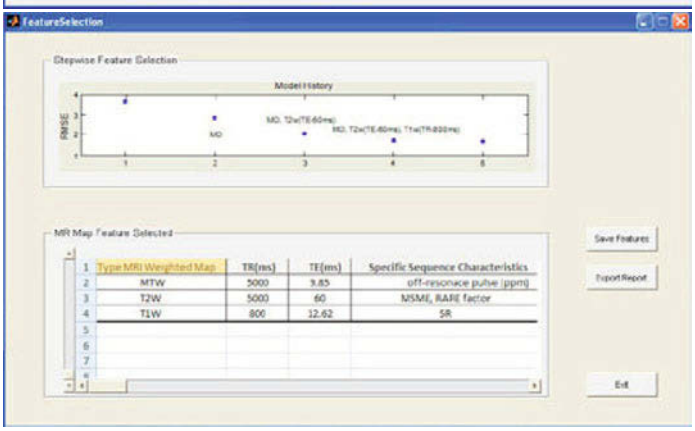

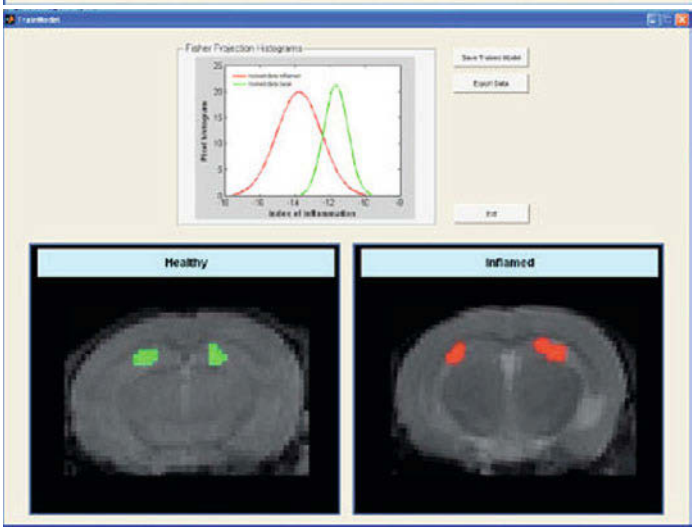

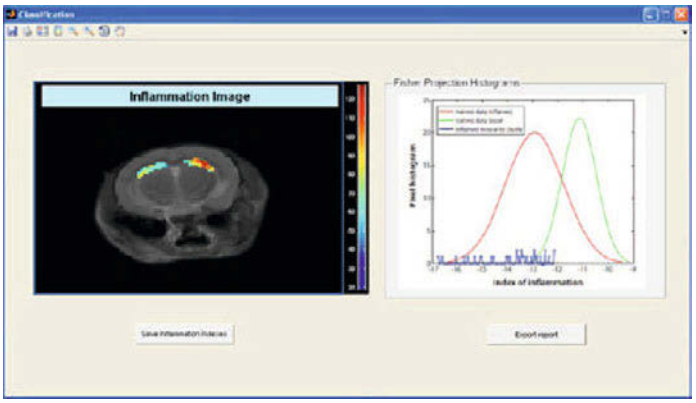

References:
(1) Scrivo R. et al. 2011, Autoimmun Rev. 10(7):369-74.
(2) Jeong HK, Jou I, Joe EH, 2010, Exp Mol Med. 31;42(12):823-32.
(3) Martin-Recuero AB, et al. ISMRM 2012
(4) McLachlan, G. J. Discriminant Analysis and Statistical Pattern Recognition. Wiley Interscience; 2004
(5) Martin-Recuero AB, et al. Submitted abstract 47081

697

iSix (Image Segmentation in OsiriX)

W. Valenzuela[1], P. Vermathen[2], C. Boesch[3], L. Nolte[1], M. Reyes[1]
[1]Institute for Surgical Technology and Biomechanics, University of Bern, Bern/SWITZERLAND, [2]DRNN & DKF / AMSM, University Bern, Bern/SWITZERLAND, [3]Dept. Clinical Research, AMSM, University and Inselspital Bern, Bern/SWITZERLAND

Purpose of the software: We developed a tool for the non-commercial version of OsiriX called iSix (Image Segmentation in OsiriX). This tool allows the user to create a segmentation from DICOM images with different labels and obtain for each one statistical information of voxels in the label. Also, the user can navigate through the segmented volume using 2D and 3D visualisation. We exemplify the use of our tool on the segmentation of spinal muscles, for which the tool also computes the muscle composition (fat/lean-muscle proportion) automatically.

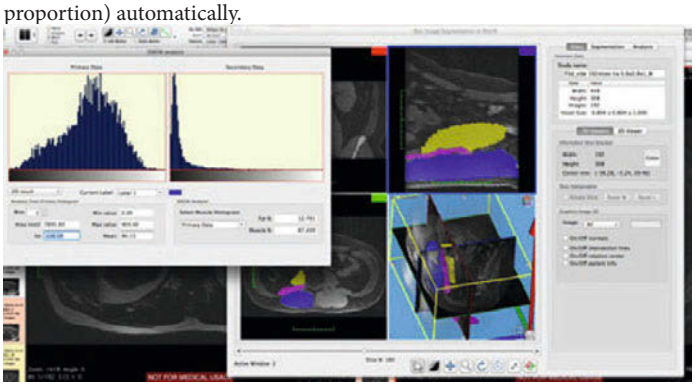

Methods/Implementation: The tool works on MRI images and allows the user to work on standard (axial, sagital, coronal) and user-defined plane orientations. In addition, using the output segmentation and DIXON images the tool computes the percentage of fat/muscle. For this we have implemented and extended the work of [1] to operate in 3D. This information can be used on clinical analyses to find correlations between disease and fat % in the muscle (e.g. sarcopenia), and also for mechanical simulations of muscles.

Currently the iSix tool is available as a plug-in for OsiriX, which enables users to easily install it and make use of all functionalities available in Osirix. However, the architecture of the tool would enable us in the future to make it available to Linux and Windows users.
In this version of the plugin we implemented three type of segmentation algorithms: - Region growing (semi-automatic): Implemented using the ITK library [3]. - Livewire (semi-automatic): here we use the algorithms developed in [2]. - Manual segmentation: We included two features, (1) Brushes to draw and erase with the mouse, (2) segmentation through closed polygons created by mouse clicks. Furthermore, segmentations on an specific slice can be propagated as an stencil to other slices and edited in place, reducing the manual work.
Features illustrated at the exhibit: At the exhibit we will show the full software running on a Mac Machine. Here the audience will see the 2D and 3D visualisation of segmented muscles and we will show how to use the interface to perform segmentation and automatic quantification of fat/lean-muscle content.

References:
[1] MichaelA Fischer, Daniel Nanz, Ann Shimakawa, and Gustav Andreisek. Quantification of Muscle Fat in Patients with low Back Pain : Comparison of Multi- Echo MR Imaging with Single-Voxel. Raiology, 2013.
[2] Steven Marx and Chris Brown. Progressive Livewire for Automatic Contour Extraction. In Western New York Image Processing Workshop, page 6, 2000.
[3] "The Insight Segmentation and Registration Toolkit", www.itk.org.

698

Image Analysis Software for MRI, PET and CT data

H. Merisaari[1], S. Piirola[1], T. Laitinen[1], S. Nesterov[1], C. Han[1], I. Jambor[1,2], H. Xiaoming[1], M. Teräs[1], J. Knuuti[1]
[1]Turku PET Centre, University of Turku, Turku/FINLAND, [2]Department of Diagnostic Radiology, University of Turku, Turku/FINLAND

Purpose of the software: Medical image analysis workflow contains multiple steps that need to be done before quantification of imaging data sets. Our aim was to allow a user to perform common procedures related to image analysis and interpretation with an easy-to-use GUI. As new methods are constantly being developed in the field of medical imaging research, it is crucial to allow inclusion of custom features to the main framework of the software.
Methods/Implementation: The Carimas software (1, 2) has been developed at Turku PET Centre (Turku, Finland) by a cross-functional team consisting of researchers from various fields and computer engineers that have contributed to the design of the software. The source code is in C# language running on .NET 2.0 framework. The .NET framework allows executing the software on all Windows platforms. In addition, preliminary tests conducted in Linux and OS X operating system suggest that the Carimas binary files can be used on those platforms as well when run on Mono framework. The software runs in .NET 2.0 runtime environment, and is freely available for academic use. It can be downloaded from www.pet.fi/carimas
Images of many conventional imaging formats— DICOM, Analyze75, Nifti, etc.—can be loaded to Carimas. After loading, the imaging data sets are visualized in three standard projections— transaxial, sagittal, and coronal—and in a 3D view. In order to allow fusion of MRI data with other modalities, a co-registration tool for rigid alignment has been implemented.The tool allows use of the most common goodness-of-fit values for rigid co-registration such as Normalized Mutual Information (NMI). Extensive ROI tools are readily available, allowing a user to extract quantitative values from imaging data sets. Depending on the dimensionality of the data, statistical measures can be calculated within the ROIs, or curves of the mean values of ROIs can be plotted and further processed using modeling tools. In addition to ready made features, the software offers also plug-in interfaces for developing specialized custom models and image filters.

Features illustrated at the exhibit: - Fusion of different imaging data sets including co-registration of PET to MRI
- VOI/ROI drawing on fusion images
- Visualization of images, Time Activity Curves in 4D data and statistical values in 3D data
- Adding a custom model plugin to the software, performing modeling

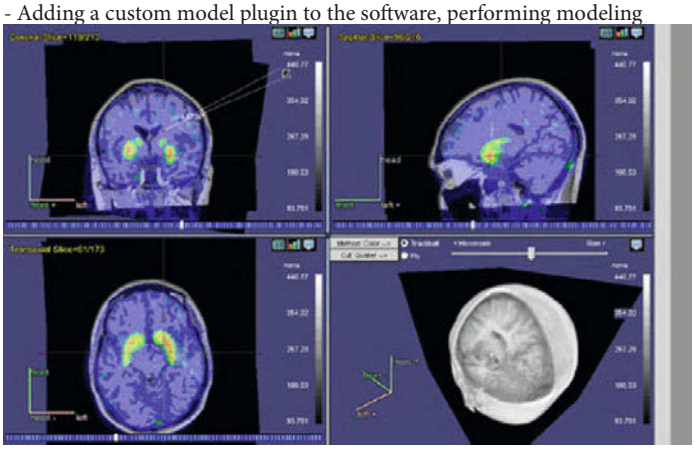

References:
1. Nesterov SV et al. Eur J Nucl Med Mol Imaging 2009; 36:1594-1602.
2. Jambor I et al. Eur J Radiol 2012; 81:2966-2972.

699

MouseMorph: A complete, automatic pipeline for processing preclinical µMRI subjects for morphometric phenotyping

N. Powell[1], M. Modat[2], M.J. Cardoso[2], D. Ma[3], M.F. Lythgoe[4], S. Ourselin[2]
[1]Centre for Advanced Biomedical Imaging & Centre for Medical Image Computing, University College London, London/UNITED KINGDOM, [2]CMIC, University College London, London/UNITED KINGDOM, [3]CMIC & CABI, University College London, London/UNITED KINGDOM, [4]Centre for Advanced Biomedical Imaging, Div of Medicine, University College London, London/UNITED KINGDOM

Purpose of the software: Statistical morphometric analysis techniques such as Voxel- and Tensor-Based Morphometry (V/TBM) are used clinically with tools such as SPM/FSL. They are ideal for investigative phenotyping – determining the morphometric effects of genes, disease, drug treatment and behaviour in animal models [1,2,3] – but few specialised tools exist for processing preclinical µMRI images (resolution <150µm). Consequently, despite being non-invasive and omitting the time-consuming requirements for manual delineation of regions of interest or naive histology [4,5], uptake of these techniques in preclinical studies has been slow.
Here we demonstrate *MouseMorph*, a new, completely automated image processing pipeline for preclinical datasets (mouse brain/embryo), designed to ease this image processing burden. The software is customised for high-throughput, large-cohort studies not encountered in the human MRI paradigm, in which multiple subjects may be scanned simultaneously, requiring separation and orientation to a standard space. We introduce a skull-stripping method based upon registration to prior atlases and tissue classification with accurate prior maps.
We have used this pipeline on over 10 mouse datasets comprising brain (*in-* and *ex-vivo*) and embryo (*ex-vivo*) images and show the results as proof-of-principle.
Methods/Implementation: The *MouseMorph* pipeline follows the following modular steps (see figure):
1) Multiple subject separation from single µMRI scans
2) Orientation correction to standard space, employing subjects' principal axes and symmetry
3) Skull stripping by registration of atlas masks
4) Non-uniformity correction (N3, [6])
5) Tissue classification based upon a Gaussian Mixture Model, using tissue prior maps (WM, GM shown) with *NiftySeg* [7], implementing an iterative Expectation Maximisation algorithm
6) Intensity normalisation [8]
7) Iterative groupwise registration (12 degrees-of-freedom affine, using a block-matching approach, followed by many-DOF non-rigid, following a Free-Form Deformation technique) with *NiftyReg* [9]
8) Deformation field transformation [4]
9) Statistical maps generated via the General Linear Model (in-vivo results shown)
The pipeline is implemented in Python 2 (Windows/Unix/Mac OS) and uses the NIfTI-1 data format. *NiftySeg* and *NiftyReg*, both C++, are available from http://cmic.cs.ucl.ac.uk, where we will also release *MouseMorph* this year. All steps run on a contemporary desktop computer, but we recommend a parallel environment for groupwise registration.

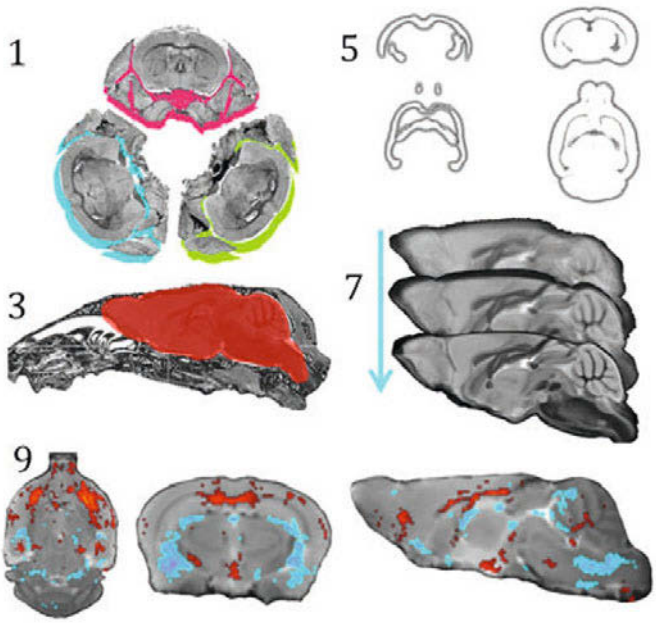

Features illustrated at the exhibit: We show each stage of our pipeline, from scanner to statistical parametric map, with results from both *in-vivo* (brain) and *ex-vivo* (brain and embryo) µMRI mouse data before and after processing. We also show the software interface, relevant sections of our code, documentation, screen-shots and animations illustrating the process.

References:
[1].Austin,C.,2004,*Nat.Genet.*,*36*(9),921-924
[2].Holmes,H.E.,2013,ISMRM.E-Poster.(3679)
[3].Nieman,B.J.,2007,*Human.brain.mapping*,*28*(6),567-75
[4].Ashburner,J.,2000,*NeuroImage*,*11*(5),S465
[5].Cleary,J.,2012,Thesis,http://discovery.ucl.ac.uk/1347518
[6].Sled,J.G.,1998,*IEEE.trans.on.med.imaging*,*17*(1),87-97
[7].Cardoso,M.J.,2011,*NeuroImage*,*56*(3),1386-97
[8].Nyul,L.,2000,Med.Imaging,IEEE,19(2),143-150
[9].Modat,M.,2010,*Comp.methods.and.progs.in.biomed*,*98*(3),278-84

700

NMRScopeB Plugin for jMRUI – A Versatile Simulator for Spectroscopic Quantitation and Method Development

J. Starcukova[1], D. Graveron-Demilly[2], **Z. Starcuk Jr.**[1]
[1]Magnetic Resonance and Cryogenics, Institute of Scientific Instruments of the ASCR, v.v.i., Brno/CZECH REPUBLIC, [2]Laboratoire CREATIS-LRMN, CNRS UMR 5220, Inserm U630, Universite Claude Bernard Lyon I, INSA Lyon, Villeurbanne/FRANCE

Purpose of the software: High-field MR scanners make it possible to acquire spectroscopic signals of coupled spin systems of up to about 20 metabolites, and motivate development of faster spectroscopic acquisition schemes. Quantitation of metabolites often requires a basis set of measured or simulated metabolite spectra, which may be prone to artifacts due to measurement errors or model simplification. Voxel inhomogeneity due to selective excitation and B_1 inhomogeneity, steady-state formation, consequences of specific pulse sequence timing and RF pulse shapes are factors affecting spectral patterns but hardly ever taken into account. Realistic simulation may improve metabolite quantitation, or support method development and artifact analysis. The software presented has been developed as a versatile tool addressing most spectroscopist's needs – calculation of implementation-specific basis spectra, method development, study and teaching, without distracting the users from their problems by immersing them deep into programming or restricting their freedom of task definition.
Methods/Implementation: The calculations are based on density operator algebra (Liouville - von Neumann equation enriched by Redfield model of relaxation) [1]. Coupled spin systems of up to about 11 spins can be handled thanks to sparse representation of most operators and propagator reuse whenever possible. As a part of jMRUI [2], the interface has inherited much of NMRScope, traditionally included in the same package, but many new features have been added, such as relaxation, gradients, spatial distribution, arbitrary quantum-mechanical observables, arbitrary setup of observation points, option to define variables among spin system or pulse sequence parameters, forming arrayed or integrated experiments, design of protocols controlling low-level pulse sequences, defining own RF and gradient shapes, support for heteronuclear experiments, pulse sequence display etc. The simulation has been implemented in Python (code available to inspection), control and display functions are implemented in java in a jMRUI plugin module. Several data viewing possibilities exist. Windows version has been tested, Linux implementation is in progress.

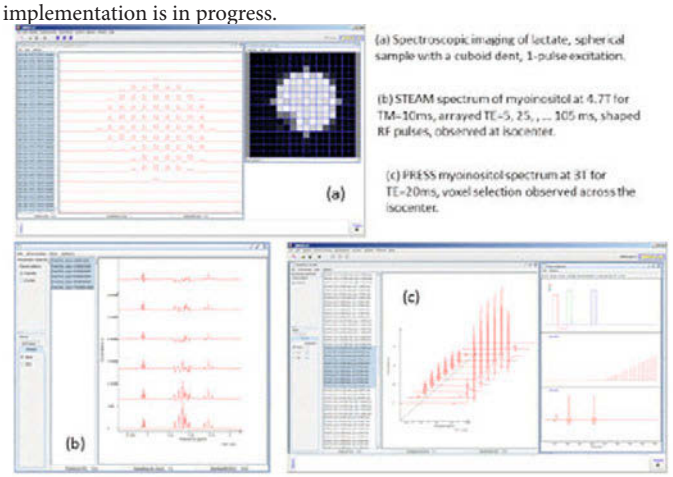

Features illustrated at the exhibit: Pulse sequence definition and display, spin system definition, calculation of basis spectra with a predefined protocol, use of variables (B_1, B_0, TE etc.) for optimization, spectral editing by selective excitation, spatial selectivity, spectroscopic imaging, 2D spectroscopy.
References:
The authors acknowledge the support by EU Marie-Curie FP7-PEOPLE-2012-ITN grant TRANSACT PITN-GA-2012-316679, EC and MEYS CR project CZ.1.05/2.1.00/01.0017 and by EU Marie-Curie grant MRT-NCT-2006-035801.
[1] Stefan, D. et al., 2009, Meas. Sci. Technol. 20, 104035. [2] Starcuk Jr., Z. et al., 2009, Meas. Sci. Technol. 20, 104033.

701

A simple and low-cost optical fiber response system for fMRI studies

A.R. Amorim, A. Santos Ribeiro, H.A. Ferreira
Institute of Biophysics and Biomedical Engineering, Lisboa/PORTUGAL

Purpose of the software: Electronic devices are a major concern in MRI, because they are negatively affected by the high magnetic fields present in the MR suite. Consequently, specially designed MRI-compatible devices based on shielded electronics and/or optical systems are required for monitoring subjects' responses during fMRI studies. In particular, existing response systems are somehow expensive and may be complex to setup. Therefore we developed a simple and low-cost fiber optic response system.
Methods/Implementation: The device consists of a clothespin fiber optic switch, which functions by interrupting the connection between the extremities of two fiber optic bundles attached to the clothespin's tips. Light emission and detection are accomplished respectively by light emitting diode (LED) and light dependent resistor (LDR) based electronic circuits, connected to a prototyping platform, such as Arduino. The subject contacts only with the clothespin, distanced from the system electronics, which are placed outside of the MR room. The data can be analyzed with any data processing software (ex: MATLAB; Python application).
Parts needed:

- A 5 meter 64 fiber optic bundle (~15€)
- A clothespin with connected tips and the metal spring removed (<1€)
- A strong elastic band to replace the metal spring (<1€)
- Two rigid ~2mm diameter tubes to enclose the optic fiber bundle and fix it against the clothespin tips (<1€)
- Electronics (~3€): a high-powered LED (ex: OSW57L5111P), a LDR (ex: VT935G) and resistors (33Ohm, 2* 100kOhm)
- An Arduino platform (~20€)
- A housing for the electronics (5€)

Total costs: <50€
Features illustrated at the exhibit: The detection unit is fed by the prototyping platform and no pre-processing electronics are needed, allowing readily data acquisition with suitable temporal resolution, which can also be adjusted by the software. We tested the system with a chosen resolution value of 5ms and plotted the voltage detected against time, showing the inverse proportionality between voltage and the degree of aperture of the clothespin, with the voltage varying between 4.5V and 2V. Finally, the device is extremely portable, easy to use and to set up.
Applications: The system was initially designed for monitoring subject responses during fMRI experiments, i.e "yes/no" button. However, the proportionality between the voltage and degree of aperture of the clothespin may be used for grasping tests or muscle strength measurements, for rehabilitation medicine applications.
References:
Sommer, J. et al., 2004, Brain

702

Delayed-enhancement analysis software with left ventricle segmentation in cardiac magnetic resonance

A.S. Gaspar[1], S.R. Tecelão[1, 2], R.G. Nunes[1], A.M. Ferreira[3]
[1]*Institute of Biophysics and Biomedical Engineering, Faculty of Sciences, University of Lisbon, Lisbon/PORTUGAL,* [2]*Escola Superior de Saúde, Universidade Atlântica, Lisbon/PORTUGAL,* [3]*Cardiology Department, Hospital da Luz, Lisbon/PORTUGAL*

Purpose of the software: Cardiac magnetic resonance protocols usually involve the acquisition of cine and delayed-enhancement (DE) images. DE images are acquired after paramagnetic contrast injection that accumulates in lesion areas and can be used to evaluate acute myocardial infarction. Unfortunately, as most processing packages available for this analysis only provide tools for manual segmentation, the results can be highly operator dependent. The developed software provides a tool capable of performing semi-automatic left ventricle (LV) segmentation and DE image analysis with a graphical user interface.
Methods/Implementation: The software was developed in Matlab environment. LV segmentation was implemented with manual and semi-automatic options. Using the semi-automatic segmentation, the endocardium and epicardium contours are manually delineated on the first cine image of the slice under study and the contours automatically propagated to the following time frames. Affine registration is used to align the DE and Cine images, in order to overlap the LV contours on the DE images [1]. Using the manual segmentation option, it is only necessary to delineate the LV myocardium contours on the DE image. This process is performed for all slices allowing calculation of the total LV mass [2]. DE delineation involves defining a healthy myocardium region of interest (ROI) on the DE image and a seed point on the hypersignal region. Additionally, an intensity threshold is chosen above which infarct is assumed, based on the standard deviation of the signal within the healthy ROI. The DE region is delimited applying a region-growing algorithm [3]. The DE mass and percentage are calculated and displayed.
Features illustrated at the exhibit: LV segmentation and DE delineation will be presented and applied to example images. The main interface allows the user to preview all image groups and choose which of them will be studied (Fig. 1). The other interfaces present a set of options that allow the user to analyse the images (Fig. 2) and evaluate the final results.
This investigation was supported by FCT grant PEst-OE/SAU/UI0645/2011 and Foundation Amadeu Dias.

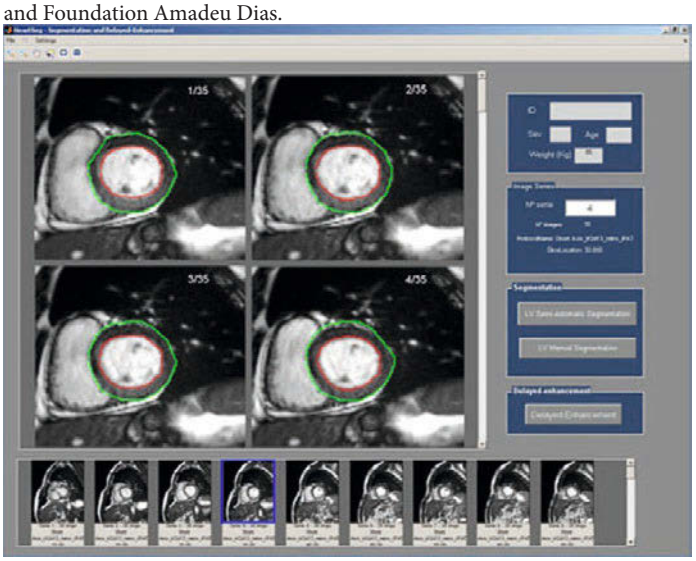

Fig. 1 –LV semi-automatic segmentation results.

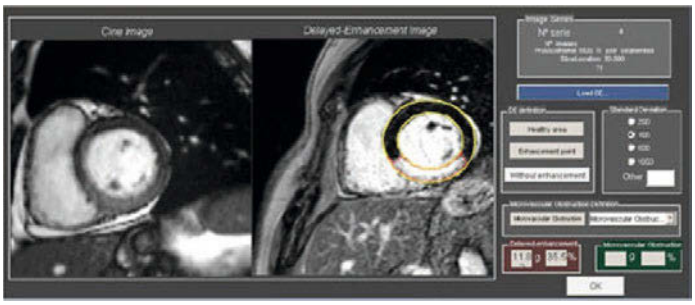

Fig. 2 – DE analysis.

References:
1. Chenoune, Y. et al. *Computing in Cardiology.* 2010, 37:161–164.
2. Shapiro, E. et al. *Circulation.* 1989, 79:706-711.
3. Gonzalez, Woods and Eddins. *Digital Image Processing Using MATLAB.* s.l. : Gatesmark Publishing, 2009.

703

Updated qMapIt, an ImageJ-plugin, for quantitative multi-parametric analysis

M.G. Kaul, G. Adam
Department of Diagnostic and Interventional Radiology, University Medical Center Hamburg-Eppendorf, Hamburg/GERMANY

Purpose of the software: QMapIt offers an operation system independent platform for multi-parametric analysis of MRI data in a framework embedded in the image processing software ImageJ [1]. This has the main advantage that tasks can be modulized and the stored results can be piped to further tools to analyse more complex processes [2, 3]. Now we want to present further improvements.
Methods/Implementation: All quantitative tools can by assessed by an interactive graphical user interface. The selective import of DICOM data is managed by DicomSort'n'Select (DSnS) [2]. The configurable DSnS provides technical information about the scans to further ImageJ plugin tools. Several sessions can be imported, processed [3], and stored as DICOM files using the DCM4che libraries [4]. A session can consist on several image stacks which are grouped images that belong together like time-series.
qMapIt is now featuring the alignment of stacks to a reference concerning the geometric properties of the scans. The properties are the x-, y-, z-location and the image resolution. The user can initiate the alignment by the user interface. But the alignment is now also an integrated part of the analysis modules for the calculation of concentration maps from quantitative T1 and contrast enhance times series or for vessel size imaging. One major benefit of a alignment is that drawn regions of interest can be easily copied from one image to the same location (x,y,z) in another image stack.
All incorporated plugins (T2RelaxIt, T1RelaxIt, ADCIt, IVIMIt, VSIIt, DCEIt and the new AglingIt) are developed in Java using Eclipse [5] and are also running as standalone plugins in ImageJ.
Features illustrated at the exhibit:
* Selective import of DICOM files with DicomSort'n'Select (DSnS)
* Calculation of various parametric maps
* Aligning and merging of 3D or 4D datasets
* Pharmacokinetic modelling (Tofts model)
* Plugins available for mapping of T1, T2 (also with T2Prep), T2*, ADC, IVIM, VSI, and DCE

References:
[1] rsbweb.nih.gov/ij
[2] Kaul MG, Ernst T, Adam G. DicomSort´n´Select, an ImageJ-plugin, for sorting, selecting of DICOM images and providing a technical data interface. ESMRMB (2011)
[3] Kaul MG, Adam G. QMapIt, an ImageJ-plugin, for quantitative multi-parametric analysis of DICOM images
[4] dcm4che.org
[5] eclipse.org

704

Codeare - Common Data Exchange and Reconstruction Framework

K. Vahedipour[1], N.J. Shah[1, 2]
[1]INM-4 Medical Imaging Physics, Forschungszentrum Juelich, Juelich/GERMANY, [2]Department of Neurology, Faculty of Medicine, JARA, RWTH Aachen University, Aachen/GERMANY

Purpose of the software: With the recent advances in high performance computing, the real-time use of notoriously expensive algorithms for MR imaging is in reach. Mostly, this kind of computationally extensive work is performed off-line in easy-to-program toolboxes like MATLAB etc. Processing speed is low, acceptance with medical investigators is limited and real-time manipulation of sequence or image reconstruction is impractical. However, such toolboxes bring along the advantage that prototyping of algorithms is very easily accomplished close to textbook notation. Thus, the design goal for codeare was to build a framework, which satisfies the aforementioned missing performance while retaining as much of the ease-of-implementation as possible and embed it into a dependable, multi-threaded client-server application and framework.
Methods/Implementation: codeare's core language is C++ for speed and flexibility with interfaces to other languages like FORTRAN, Python etc. The core entity is an n-dimensional data-template, Matrix<T,R>, where the first template parameter depicts the precision while the second hides from the user the traited/templated complexity of handling GPU and distributed memory systems. Vectorisation capabilities like SSE2-AVX2 are exploited for accelerating floating-point operations. Moreover, multiple datatypes are handled for IO of binary (HDF5, MATLAB, Nifti, etc) and meta data (XML).
The currently existing toolbox for the above nd-matrices entails FTs (FFT, SENSE[1], and GRAPPA[2] both Cartesian/non-Cartesian), DWT operators, finite differences operators, 1-3D interpolations, arithmetic functions (sin, cos, exp, log, …), linear algebra routines (eig, svd, inv, pinv, chol, …), statistical tools (cov, mean, stddev, nrmse, …), etc (Fig.1).

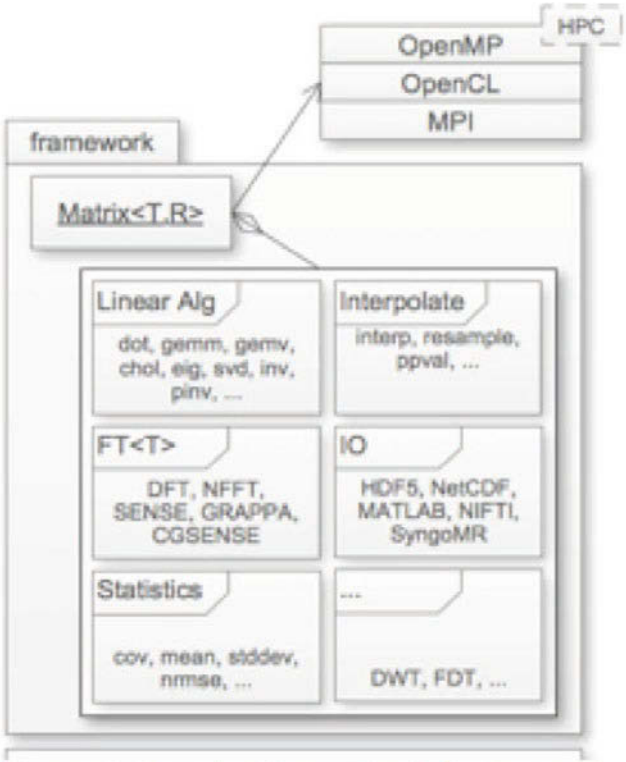

Figure 1: Rough schematic of the internal data structure of codeare. The header-only matrix library abstracts from the underlying hardware and precision in a unique way. The workspace offers easy memory management and allows users to grant and restrict access to memory objects.

External high-performance libraries were used wherever possible to integrate a wide range of numerical and linear algebraic operations on data [3-7]. The code of atomic operations is highly optimised allowing one to use prototypical algorithms in production.
codeare integrates with runtime processes of scanners over network to bypass/extend the functionality of vendor services. The network communication is transaction-safe and has been tested to up to 10GB/s.
Features illustrated at the exhibit: codeare's entire scope of operation is presented at the meeting. Image reconstruction and pulse-design algorithms as well as the network functionality are detailed and demonstrated.
References:
[1] Pruessmann et al, MRM 1999 vol. 42 (5) pp. 952-962 [2] Griswald et al, 2002 vol. 47 (6) pp. 1202-1210 [3] Anderson et al, SIAM, 1999, ISBN 0-89871-447-8 [4] Blackford et al, SIAM, 1997, ISBN 0-89871-397-8 [5] Frigo et al, IEEE, 1998, ISBN 0-78034-428-6 [6] Galassi et al Network Theory Ltd., 2006 2nd Ed, ISBN 0-95416-173-4 [7] Yoo et al, Proc. of Medicine Meets Virtual Reality, IOS, 2002, pp586-92

705

SEQfMRI: batch for sequential analysis of ictal fMRI data

C. Falcon[1, 2], B. Marti-Fuster[2], X. Planes[2]
[1]Medical Image Platform, IDIBAPS, Barcelona/SPAIN, [2]GIB-UB, CIBER-BBN, Barcelona/SPAIN

Purpose of the software: The EEG/fMRI registration of partial epileptic episodes is becoming an approach to localize the epileptogenic area in refractory epilepsy when there is not evidence of lesion in conventional MRI. Usually, fMRI analyses are EEG-informed (fMRI events obtained from EEG). The resulting activation/deactivation maps are static and hence, information about propagation and possible differences between epileptic events are hidden.
A sequential model free analysis has been proposed to obtain complementary information [1-2]. The aim of such analysis is to calculate a sequence of continuous activation/deactivation maps covening the epileptic episodes recorded with EEG/fMRI. The epileptogenic area location is not automatic but supervised by the clinician according the EEG data (timing, onset channel and propagation channels). In return, it gives dynamic information about brain activity that could be very valuable.
Methods/Implementation: SEQfMRI is a fully automated script that uses SPM and home-made functions. It includes all required steps from image preprocessing to the final results.
SEQfMRI determines activation/deactivation areas in a short part of the serie (temporal window) using fixed-size blocks as activation periods. The analysis is repeated moving the temporal window one scan further until the end of the period to be analyzed is reached. SEQfMRI offers two statistical analysis: 1) the rest period is the same for all the analyses (BB: blocked baseline) 2) the rest period is part of the analysis window, so it is different for each analysis (CF: continuous forward). The BB method gives absolute activation/deactivation areas relative to the predefined baseline. Instead, CF is a kind of temporal smoothed derivative since it shows activation/deactivation patterns between consecutive blocks.
Features illustrated at the exhibit: The output is a folder for each temporal analysis and a postcript file with their results (display) in separated pages. The tittle of each page contains the time (hh:mm:ss and seconds from the begin of the run) of the corresponding activation period. This allows an easy synchronization with simultaneous EEG data. Figure shows the activation/deactivation maps of the analysis of a run.

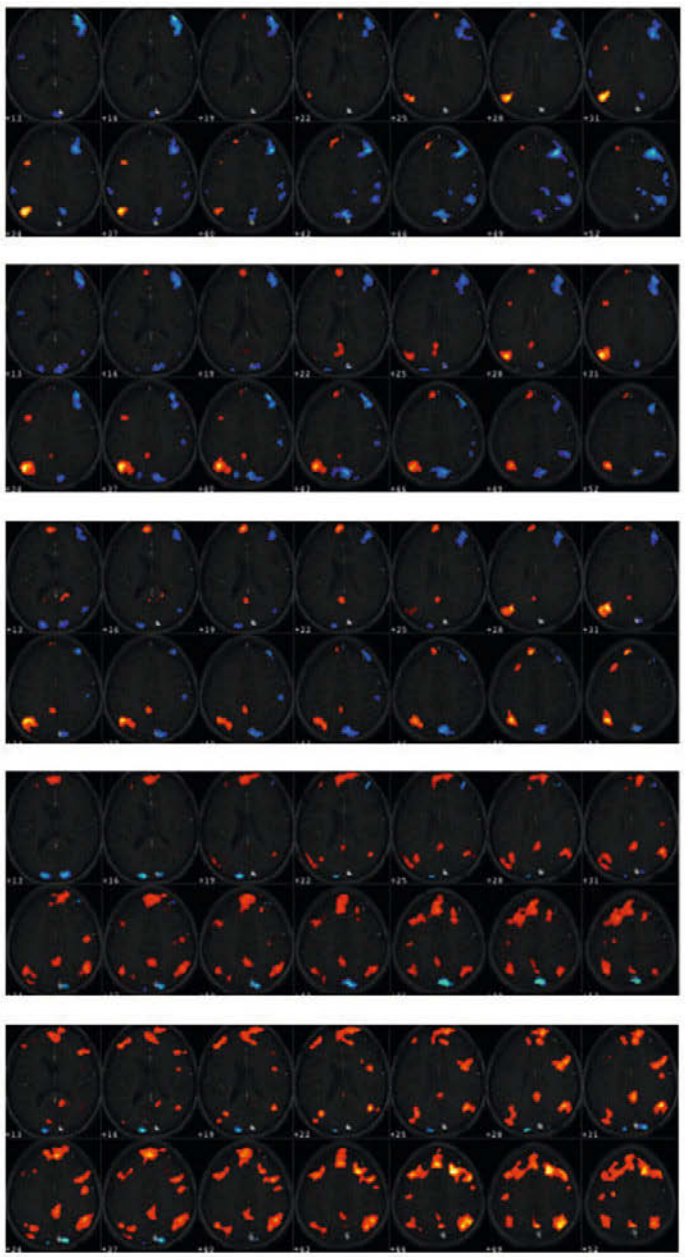

References:
1-Donaire A, **Falcón C** et al.. Sequential analysis of fMRI images: A new approach to study human epileptic networks. Epilepsia. 2009 50(12):2526-37.
2-Donaire A, Bargallo N, **Falcón C**, et al. Identifying the structures involved in seizure generation using sequential analysis of ictal-fMRI data. Neuroimage. 2009. 47(1):173-83.

706

JEMRIS 2.7: new features and use cases of the general-purpose MRI simulator

T. Stöcker[1], K. Vahedipour[2], D. Pflugfelder[2]
[1]*MR Physics, German Center for Neurodegenerative Diseases (DZNE), Bonn/GERMANY,* [2]*INM-4 Medical Imaging Physics, Forschungszentrum Juelich, Juelich/GERMANY*

Purpose of the software: The open-source C++ software project JEMRIS is a versatile multiplatform MRI simulation environment (www.jemris.org). General Bloch equation-based modeling of a large spin system is combined with the most important off-resonance effects, parallel receive and transmit, nonlinear gradient fields, and spatiotemporal parameter variations at different levels, e.g. to simulate object motion or tissue contrast agent uptake [1]. The software provides a highly flexible module for sequence design. The newest version of JEMRIS is presented, which includes important extensions such as simulation of spin diffusion, eddy currents, as well as improved data I/O to support compatibility with third-party software.
Methods/Implementation: Recent extensions are bundled in the new software release 2.7. The physical concepts now include a general Monte-Carlo based approach of spin-diffusion in dedicated microstructure compartments such as crossing or kissing fibers. Further, modeling of eddy currents with a user-defined system response can be either utilized on a low-level or only for specific events in the sequence timing. Additionally to the extension of physical concepts, data I/O was redesigned taking advantage of the HDF5 library (www.hdfgroup.org) providing more flexible and efficient data handling. The sequence design module was extended by an automated storage of k-space trajectory with minimal user interaction. According to the goals of JEMRIS, the implementations utilized object orientated design patterns and code encapsulation, to provide a general, flexible, extensible and modular environment to the community.
Features illustrated at the exhibit: The software will be introduced as a general-purpose tool for MRI physicists, with special focus on the new features such as the simulation of realistic diffusion MR-data. Different use cases are discussed, such as investigation of spin-echo BOLD signals at high field [2] or generation of ground-truth MRI data for image analysis [3]. The capabilities for rapid method development and sequence prototyping will be presented, e.g. to use JEMRIS in combination with other software tools for image reconstruction [4] or EM simulations of RF transmission (www.cst.com). JEMRIS 2.7 will be officially released at the conference.
References:
[1] Stoecker T et al. High Performance Computer MRI Simulation. MRM, 2010; 64:186–193.
[2] Pflugfelder D et al. On the numerically predicted spatial BOLD fMRI specificity for spin echo sequences, MRI, 2011 , 29(9):1195-1204.
[3] Nieuwstadt H et al. Numerical Simulations of Carotid MRI: How Accurately Can We Quantify Atherosclerotic Plaque Components in vivo? ISMRM Mtg. 2013
[4] Hansen MS, Sørensen TS. Gadgetron: An open source framework for medical image reconstruction. MRM 2013 69(6):1768-76.

707

Simple Motion Simulation for MRI - A basic MATLAB Framework

M. Völker[1], F. Breuer[1], P.M. Jakob[1, 2]
[1]*Magnetic Resonance Bavaria e.V (MRB), Research Center, Würzburg/GERMANY,* [2]*Experimental Physics 5, University Würzburg, Würzburg/GERMANY*

Purpose of the software: Cartesian MRI is prone to severe motion artifacts mainly in phase-encoding direction. However, Cartesian acquisition allows to freely vary the acquisition order of k-space lines. Time-dependent systematic errors in the data are distributed according to the sampling pattern, thereby affecting the Point-Spread-Function (PSF) of the object. For given motion types it can be useful to study the PSF originating from the sampling pattern and sequence parameters in a controlled environment. We present a simple MATLAB framework to simulate a moving point signal and allowing to incorporate arbitrary motion models with basic MATLAB skills.
Methods/Implementation: If the 3-dimensional displacement of a point source is known, the equivalent k-space data can be calculated according to the Fourier-Shift-Theorem:
$S(t,k) = e^{2\pi i \cdot dx \cdot k}$
The proposed MATLAB framework[1] defines the function getMotion() to calculate coordinates (x,y,z) for each sequence cycle, having already implemented basic motion models (constant/random/periodic/respiration/heartbeat). Further equations are easy to integrate for everyone with basic MATLAB knowledge. For simplification, no motion is assumed to happen during readout of k-space lines. The function getReorderLinesCartesian() implements different reordering strategies that can be queried using memorable aliases. Predefined reorderings are "linear" (gradual increase of phase-encoding gradients, the clinical standard), "shuffle" (random permutation of the lines) and "random" (pure random sampling, no consideration for already sampled lines). The function simCartesianMRI() accepts a binary mask of time bins at which the sequence should aquire data, the TR, and matrix size. The mask allows to sample an arbitrary number of lines and also to skip individual lines, by setting values zero, allowing to simulate the effect of retrospective gating. 2D and 3D is possible, signal averaging is done point-by-point in k-space.
Features illustrated at the exhibit: For demonstration, a point moving on an ellipse at 3Hz was simulated. Three 2D-MRI experiments were simulated, using the described reordering methods and common parameters: TR=5ms, 512×512Px matrix, 5120 sampled lines, equivalent to 10-fold averaging. The resulting PSF is shown in Fig.1. Coherent ghosting is seen in the standard linear approach. Both irregular reorderings exhibit mainly localized blurring. The randomly distributed phase errors in k-space produce a stripe of noise-like signal in phase-encoding direction, only. The desired object is clearly visible.

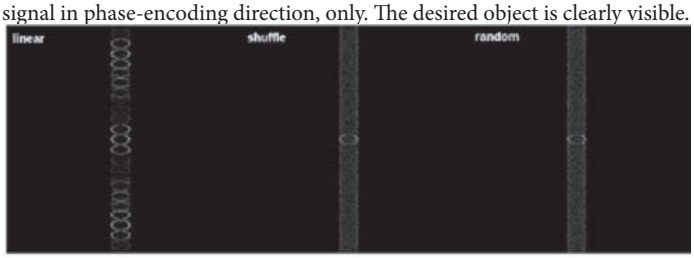

Fig. 1: *A point moving on an ellipse at 3Hz was simulated. Three 2D-MRI experiments were simulated, using TR = 5 ms, 512 × 512 Px matrix size, 10 averages. Phase encoding was in the up-down direction.*

Available full-featured MRI simulation packages like JEMRIS[2,3] are too complex for non-computer-scientists to allow for custom modifications. The proposed framework is easy to read, modify, and optimized for speed.
References:
[1] http://www.mathworks.com/matlabcentral/fileexchange/41920
[3]Stöcker, Vahedipour: Advances in Parallel Computing, 2008,15(1),155-164
[3]Vahedipour et al: Proc. ESMRMB 2008